

12-2017

## Laser-assisted processing of multilayer films for inexpensive and flexible biomedical microsystems

Rahim Rahimi  
*Purdue University*

Follow this and additional works at: [https://docs.lib.purdue.edu/open\\_access\\_dissertations](https://docs.lib.purdue.edu/open_access_dissertations)

---

### Recommended Citation

Rahimi, Rahim, "Laser-assisted processing of multilayer films for inexpensive and flexible biomedical microsystems" (2017). *Open Access Dissertations*. 1623.  
[https://docs.lib.purdue.edu/open\\_access\\_dissertations/1623](https://docs.lib.purdue.edu/open_access_dissertations/1623)

This document has been made available through Purdue e-Pubs, a service of the Purdue University Libraries.  
Please contact [epubs@purdue.edu](mailto:epubs@purdue.edu) for additional information.

**LASER-ASSISTED PROCESSING OF MULTILAYER FILMS FOR  
INEXPENSIVE AND FLEXIBLE BIOMEDICAL MICROSYSTEMS**

by

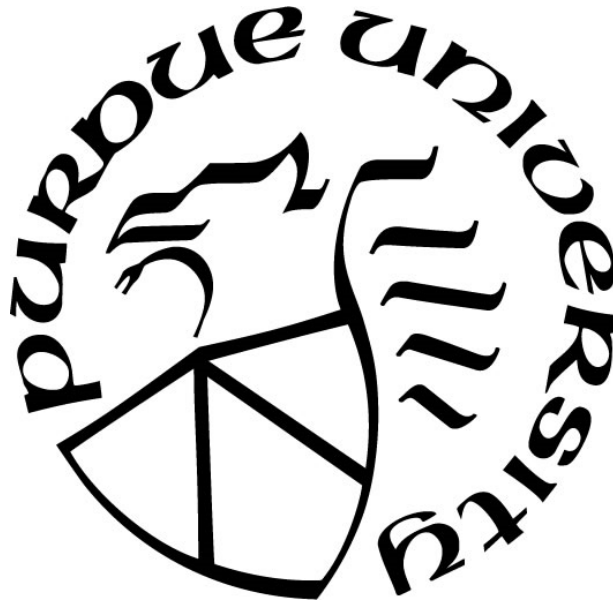
**Rahim Rahimi**

**A Dissertation**

*Submitted to the Faculty of Purdue University*

*In Partial Fulfillment of the Requirements for the degree of*

**Doctor of Philosophy**



School of Electrical & Computer Engineering

West Lafayette, Indiana

December 2017

**THE PURDUE UNIVERSITY GRADUATE SCHOOL**  
**STATEMENT OF COMMITTEE APPROVAL**

Dr. Babak Ziaie, Chair

Department of Electrical & Computer Engineering

Dr. Saeed Mohammadi

Department of Electrical & Computer Engineering

Dr. Çağrı Savran

Department of Mechanical Engineering

Dr. Dimitrios Peroulis

Department of Electrical & Computer Engineering

**Approved by:**

Dr. Venkataramanan Balakrishnan

Head of the Graduate Program

*To my wife and parents.*

## ACKNOWLEDGMENTS

Throughout my graduate life, I have truly enjoyed working with many wonderful people. This dissertation could not have been completed without the advice, guidance, and support from many people. At first I would like to express my sincere gratitude towards my academic advisor and mentor, Prof. Babak Ziaie, for his invaluable guidance and support which made my dissertation possible. His enthusiasm and inspiration allowed me to accomplish more than I ever would have expected as a graduate student at Purdue.

I would also like to express my sincere appreciation to my thesis committee members, Prof. Saeed Mohammadi, Prof. Çağrı Savran, and Prof. Dimitrios Peroulis for their interest in my research, and for their time and inputs on my thesis. I am very appreciative of the staff and director of the Birck Nanotechnology Center Prof. Ali Shakouri for their constant help and assistance in my research and also creating a wonderful multicultural environment of enthusiasm and learning. It was a place where I spent most of my time at Purdue finding wonderful people and close lifelong friends. I would also express utmost appreciation to the wonderful people who I had the honor of collaborating during my graduate studies. In particular, the wonderful NSF EFRI team from Harvard Medical School and Tufts University, including Prof. Ali Khademhosseini, Prof. Sameer Sonkusale, Dr. Mehmet R. Dokmeci, Dr. Ali Tamayol, Dr. Pooria Mostafalu, Dr. Xin Zhao, Dr. Iman K. Yazdi, Dr. Alireza Hassani Najafabadi, and Dr. Nasim Annabi. I am also grateful to Prof. Sophie Lelièvre, Prof. Mukerrem Cakmak, Dr. Siamak Shams Es-haghi, Prof. Rodolfo Pinal, Dr. Rajiv Sood, and Dr. Michael Zieger for their continued support throughout various other interdisciplinary projects.

My special thanks to my senior colleagues and friends from ZBML, beginning with Dr. Manuel Ochoa who was one of the first members of the group that I met when I joined ZBML and has always been a tremendous helpful friend and colleague. Many thanks also to my other senior colleagues Dr. Charilaos Mousoulis, Dr. Nithin Raghunathan, Dr. Seung Huyn Song, Dr. Jun Hyeong Park, Dr. Albert Kim, Mr. Marcus Brown, Mr. Zachariah Hughes, and Dr. Girish Chitnis who I collaborated with in the different projects and helped me learn various skills in the lab. I also want to thank current members of ZBML for being such a good company in conference travels and their invaluable assistance in different projects, including Mr. Wuyang Yu, Mr. Jiawei

Zhou, Chang K. Yoon, Mr. Tejasvi Parupudi, Mr. Hongjie Jiang, Ms. Tiffany L. Huang and all my other lab colleagues.

Outside of the academic world, I most first acknowledge the tremendous sacrifices and constant support of my parents for my education. For this and much more, I am forever in their debt. Sincere thanks to all my friends at Purdue for making the graduate school a wonderful and enjoyable experience. Last, but certainly not least, I want to thank my loving wife, Tahereh for her understanding, patience, and encouragement, without her I would not have succeeded this far.

I would also like to take this opportunity to thank those who provided financial support as I pursued this academic endeavor including: Purdue Department of Mathematics, and Electrical and Computer Engineering, for the teaching opportunities and financial support, National Science Foundation grant EFRI-BioFlex #1240443, Department of defense, NextFlex PC 1.0 Program, and the educational research grants from Eli Lilly, Indianapolis, Indiana, USA.

## TABLE OF CONTENTS

LIST OF FIGURES .....	ix
ABSTRACT.....	xix
1. INTRODUCTION .....	1
1.1 Research motivation.....	1
1.2 Background.....	4
1.3 Overview of thesis .....	12
2. LASER MATERIAL PROCESSING.....	13
2.1 Laser systems.....	13
2.1.1 Solid state lasers: Fiber laser .....	14
2.1.2 Gas lasers .....	15
2.2 Laser-material interaction .....	15
2.2.1 Physical material alterations via laser.....	16
2.2.2 Laser activated chemical processes .....	18
3. LASER CARBONIZATION OF POLYMERIC FILMS.....	19
3.1 Laser-induced porous carbon from polyimide film .....	20
3.1.1 Results and discussion .....	21
3.2 Porous-carbon/silver nanocomposite .....	24
3.2.1 Fabrication process .....	25
3.2.2 Results and Discussion .....	27
3.3 Stretchable carbon–polyaniline composite.....	31
3.3.1 Fabrication process .....	32
3.3.2 Results and discussion .....	34
4. LASER ABLATION OF MULTILAYER POLYMERIC FILMS .....	42
4.1 Laser ablating hydrophobic paper.....	42
4.1.1 Materials and method .....	43
4.1.2 Results and discussion .....	45
4.1.2.1 Surface wettability and morphology.....	45
4.1.2.2 Mechanical properties.....	47
4.1.2.3 Oxygen and medium permeability .....	48

4.2	Laser patterning ITO-coated PET .....	50
4.2.1	Materials and method .....	51
4.2.2	Results and discussion .....	51
4.3	Laser ablating metalized paper .....	57
4.3.1	Materials and method .....	58
4.3.2	Laser processing .....	60
4.3.3	Mechanical and surface characterization .....	64
5.	LASER ENABLED DEVICE MANUFACTURING .....	68
5.1	Mechanical sensors .....	68
5.1.1	Highly stretchable and sensitive strain sensor .....	68
5.1.1.1	Fabrication process .....	69
5.1.1.2	Results and discussion .....	70
5.1.2	Wireless pressure sensor .....	76
5.1.2.1	Fabrication process and measurement technique .....	76
5.1.2.2	Results and discussion .....	77
5.2	Electrochemical sensors .....	78
5.2.1	Flexible and transparent pH sensor with NFC communication .....	80
5.2.1.1	Transparent pH sensor fabrication .....	81
5.2.1.2	Electronic readout circuit .....	83
5.2.1.3	Characterization of the sensor and wireless module .....	85
5.2.2	Highly stretchable pH sensor via direct laser-writing/machining .....	90
5.2.2.1	Fabrication process .....	90
5.2.2.2	Device Characterization .....	92
5.2.2.3	In vitro biocompatibility assessment .....	94
5.3	Paper-based environmental sensors .....	96
5.3.1	Humidity sensor .....	97
5.3.1.1	Results and discussion .....	98
5.3.2	Temperature sensor .....	102
5.3.2.1	Results and discussion .....	104
5.4	Paper based <i>in-vitro</i> model for respiratory system .....	105
5.4.1	Paper-based microfluidic ALI platform .....	107

5.4.2 Airway epithelial cells on the paper platform.....	110
6. CONCLUSION.....	114
6.1 Summary and Conclusions .....	114
6.2 Future Directions .....	116
REFERENCES .....	118
VITA.....	142

## LIST OF FIGURES

Figure 1.1. U.S. disposable medical sensors market by product, 2014 - 2025 (USD Million) .....	1
Figure 1.2. Laser processing market in China, 2014 - 2025 (USD Million) .....	3
Figure 1.3. Next-generation flexible electronics systems and the key relevant sectors [9].....	4
Figure 1.4. Disposable devices fabricated by conventional photolithography processes. (a) Optical images of temporary transfer tattoo with built-in electronics for measuring ECG, EMG, and EEG in conformal skin-mounted modes with- out conductive gels or penetrating needles[16]. (b) Optical image of multiplexed array of electro tactile stimulators in a stretchable, mesh geometry on the inner surface of an elastomeric finger-tub for measuring pressure created by physical contact [17]. (c) Optical image of multifunctional inflatable balloon catheter with integrated sensors for measuring temperature, flow, tactile, optical and electrophysiological data, together with radiofrequency electrodes for controlled, local ablation of tissue [18]. (d) Optical image of the wearable sweat analysis patch with a sweat-uptake layer and integrated flexible glucose, lactic acid, and pH sensors [19]. (e) Surgical sutures with built-in electronics for targeted wound monitoring and therapy [20]......	5
Figure 1.5. Long-term implantable devices fabricated by conventional photolithography processes. (a) Optical image of ultrathin and flexible silicon nanomembrane transistors into the electrode array for recording and stimulating the brain [21]. (b) Mechanically flexible silicon electronics for multiplexed measurement of cardiac electrophysiology[22]. (c) Fully implantable miniaturized optoelectronic systems for wireless optogenetics [23]......	6
Figure 1.6. Flexible electronic manufacturing approaches: (a) conventional photolithography, (b) printing and additive manufacturing, (c) laser processing. ....	7
Figure 1.7. (a) Transfer process of silicon nanomembrane in a ‘wavy’ herringbone layout, to an underlying piece of PDMS. (b) Photographs of a stretchable circuit with a non-coplanar mesh design transferred onto the tip of a finger on a plastic model of a human hand [5]. (c) Optical image of an array of interconnected photodetectors and junction diodes in a compressed, hemispherical geometry on an elastomeric transform element [29]. ....	8
Figure 1.8. Laser direct writing techniques: (a) laser ablation, (b) laser-driven micro transfer, (c) selective laser sintering of conductive nanoparticles, (d) laser carbonization. ....	10

- Figure 2.1. Schematic of laser components: 1) Gain medium capable of sustaining stimulated emission. 2) Energy source to pump the gain medium. 3) Total reflector to reflect energy. 4) Partial reflector. 5) Laser beam output (<https://www.ulsinc.com/learn>)..... 14
- Figure 2.2. Absorption of various metals at relevant wavelengths for industrial lasers ..... 16
- Figure 2.3. Interactions of laser with materials. (a) Physical interaction with thermoplastics causes material removal via melting and evaporation. Molten material can redeposit on the surface. High power results in through-hole features, but lower power allows controlled ablation/texturing. (b) Physical interaction with thermosets decomposes the material (pyrolysis) with redeposited debris. High power results in through-hole features, but lower power allows controlled ablation/texturing. (c) Very low power allows minimal material damage but alters the surface chemistry via interactions with atmospheric gasses ..... 17
- Figure 3.1. Porous carbon formed from commercial PI films using a CO<sub>2</sub> laser at an optimum combination of laser power (6.75 W) and speed (1.3 m/s). (a) Schematic of the synthesis process of porous carbon from laser carbonized PI film. (b) Photograph of final fabricated array carbon pattern on PI tape..... 21
- Figure 3.2. Electrical characterization of pyrolyzed carbon patterns. (a) Sheet conductivity of carbon trace on polyimide as a function of laser fabrication parameters (power and speed). (b) Power and speed required to achieve carbon traces with high sheet conductivity (low sheet resistance), (c) EDS spectra of the laser carbonized PI (d) Raman spectra before and after laser treatment. .... 22
- Figure 3.3. SEM of highly porous conductive carbon patterns. (a-c) images of 1 mm wide patterns. (d-f) images of smallest features with 90 $\mu$ m width..... 23
- Figure 3.4. Goniometric experiments with 10  $\mu$ l DI water droplet for measuring the surface wettability, (a) water droplet before depositing on the surface, (b) water droplet on polyimide sheet, (c) water droplet wicking immediately into the laser carbonized surface upon contact (super hydrophilic)..... 24
- Figure 3.5. (a-c) Fabrication process of carbon/silver nanocomposite using laser pyrolyzation and selective aqueous silver ionic solution trapping; (d) laser carbonized traces before and after decorating with silver nanoparticles: (i) silver ionic solution, (ii) pristine carbonized trace, (iii) carbon/silver nanocomposite; flexible laser carbonized traces (e) before and (f) after

- decorating with silver nanoparticles; (g) array of lit LEDs with flexible interconnect. All scale bars: 1 cm ..... 26
- Figure 3.6. Magnified optical image of (a) laser carbonized polyimide and (b) carbon-silver nanocomposite SEM image of (c, d) laser carbonized polyimide and (e, f) carbon-silver nanocomposite..... 27
- Figure 3.7. (a) XRD pattern of carbonized polyimide and carbon-silver composite, (b, c) EDS spectra of the nanocomposite, (d) high magnification SEM of carbon-silver composite, (e, f), EDS color mapping of silver (red) and carbon (green). ..... 28
- Figure 3.8. (a) Electrical sheet resistance of carbon-silver composite after annealing at different temperatures, (b) carbonized polyimide and carbon-silver nanocomposite resistances as a function of line width, (c) change in the carbonized polyimide resistance of various trace widths ranging from 0.2 mm to 2 mm as a function of radii of curvature, (d) schematic for the behavior of carbonized polyimide and carbon-silver nanocomposite under mechanical flexion, (e) change in the resistance of carbon-silver nanocomposite of various trace widths ranging from 0.2 mm to 2 mm as a function of radii of curvature, (f) resistances of carbonized polyimide and carbon-silver nanocomposite as a function bending cycles of  $180^\circ$  at 5 mm of curvature radius, with breaks at the first five and last five cyclic..... 31
- Figure 3.9. Schematic illustrations of the fabrication process and photographic images stretchable carbon–polyaniline composite interconnections: (a) polyimide sheet is silanized and placed on an air-plasma-treated Ecoflex substrate, (b) a  $\text{CO}_2$  laser is used to carbonize serpentine carbon traces on the polyimide sheet, (c) polyaniline is spray-coated onto the porous carbon, (d) the polyimide sheet is machined with the same  $\text{CO}_2$  laser at a higher power level, (e) excess polyimide is removed, (f) interconnects are insulated by another Ecoflex layer, (g) photograph of various stretchable PANI/C–PI interconnect designs, and (h) different trace widths. Scale bar in all images is 1cm..... 34
- Figure 3.10. Optical and SEM images of stretchable PANI/C–PI serpentine interconnects with the design parameters of one repetitive serpentine unit. Top views of serpentine structures with the widths of (a) 1.2 mm and (b) 0.3 mm. SEM top view of a single repetitive unit with 0.3 mm width at (c) low and (d) high magnification. Side view SEM image of PANI/C–PI composite structure and polyimide film (e) before and (f) after encapsulation with Ecoflex. .... 35

Figure 3.11. Top view SEM image of (a) pristine porous laser-carbonized polyimide and (b) PANI/C–PI composite. (c) Raman spectra of pristine porous carbon, PANI, and PANI/C–PI. (d–f) Optical image of  $5 \times 25$  mm PI and PANI/C–PI samples used for tensile testing. (g) Comparison of the tensile stress–strain curve of PI and PANI/C–PI. (h) Variation of resistance with line width before and after PANI deposition..... 37

Figure 3.12. (a) Optical images of serpentine traces with 0.3 and 1 mm width at 0%, 60%, and 120% elongation. (b) Relative change in electrical resistance of serpentine PANI/C–PI composites with difference widths as a function of strain. (c) Maximum elongation with less than 20% change in resistance versus trace width. (d) COMSOL simulation for displacement and stress distribution on serpentine traces with 0.3, 0.6, 0.8, and 1.2 mm width at 25% elongation; the stress concentration is in the crest of the serpentine interconnects. (e) Simulation results of maximum stress at the crest points of serpentine traces with different widths at various levels of strain. (f) Relative change in resistance of a 0.3-mm-wide serpentine trace versus the number of stretching cycles for 20%–80% elongation. .... 40

Figure 4.1. Basic structural characterization of different papers. (a–d) optical image of different papers: parchment paper, wax paper, filter paper, filter paper coated with PDMS, (e–l) low and high magnification SEM images of surface properties of different papers, (m–p) cross-sectional SEM image of different papers. .... 44

Figure 4.2. (a) Water droplet on different surfaces (i) before and (ii) after laser ablation, (b) comparison of contact angle of various hydrophobic surface before and after laser treatment, (c) SEM top-view of selective laser treated and untreated parchment paper, cross-section SEM image of (d) before and (e) after laser treatment of parchment paper, (f) selective cell attachment to circular hydrophilic patterns with 2mm diameter, Scale: 2 mm..... 46

Figure 4.3. (a) Optical image of test setup used for characterizing mechanical properties of paper. (b) Ultimate tensile strength for different papers as a function of wetting duration up to 7 days..... 47

Figure 4.4. Stress vs. strain of dry and wet paper films after 24 hours of PBS immersion (a) parchment paper, (b) wax paper, (c) paper-PDMS, and (d) filter paper ..... 48

Figure 4.5. (a) Schematic of setup used for characterizing diffusion of oxygen across various papers, (b) oxygen permeability and dissolution in water for different hydrophobic paper

- membranes as function of time, the inset in (b) shows a schematic of the oxygen permeability test setup, (c) schematic of setup used for characterizing diffusion of media across various papers, (d) diffusion of media across various hydrophobic films as a function of time..... 49
- Figure 4.6. (a) Schematic illustration of direct laser ablation of indium tin oxide thin using Nd:YAG laser. (b) Optical images laser ablated ITO film. (Inset shows the ablated trench at constant power of 10W and varying speed from 4 to 0.5 m/s..... 52
- Figure 4.7. Schematic illustration of indirect laser ablation of indium tin oxide thin using CO<sub>2</sub> laser. Different laser settings can result in either: (i) incomplete removal of conductive film, (ii) complete removal of conductive film, and (iii) cut through the PET substrate. .... 53
- Figure 4.8. (a) Electrical resistance changes of ITO layers with different laser power and scanning speeds. Optical images of the laser ablated trench at a laser power 3W and scanning speed of (b) 1m/s, (c) 0.8 m/s, (d) 0.4 m/s, and (e) 0.2 m/s..... 54
- Figure 4.9. Optimal laser power and speed required for complete remove the ITO thin film with minimal damage to the PET substrate. .... 55
- Figure 4.10. (a) EDX color mapping of Sn (red), In (green) and O (blue) on the ITO film after laser scrubbing with CO<sub>2</sub> laser beam, all scale bars are 100  $\mu$ m, (b) EDS spectra collected from the surface ITO film before and after laser ablation. (c) Optical image of laser ablated trench with different widths. (d) Cross-section profile of ablated trenches with different widths, (e) measurements of the resistances of laser ablated ITO electrodes with a length of 30 mm and widths from 0.5 mm to 4 mm. .... 56
- Figure 4.11. Process characterization of CO<sub>2</sub> laser ablating MP. (a) Combinatorial study for optimum laser power vs. laser scanning speed. (b) Microscopic pictures of laser ablated MP using constant power of 4.5W and different scanning speeds ranging between 0.2 to 4 m/s. (c) Resistivity and (d) mass change of 1×1cm samples at various laser powers and scanning speeds. .... 62
- Figure 4.12. Process characterization of Nd:YAG laser ablating MP. (a) Combinatorial study for optimum laser power vs. laser scanning speed. (b) Microscopic pictures of laser ablated MP using constant power of 4.5W and different scanning speeds ranging between 0.2 to 4 m/s. (c) Resistivity and (d) mass change of 1×1cm samples at various laser powers and scanning speeds. .... 63

- Figure 4.13. Mechanical characterization of MP before and after different etching processes. (a) Dumbbell-shaped samples used for the tensile strength test. (b) Force versus displacement graph of different samples. .... 65
- Figure 4.14. (a) Photograph image of simple LED circuit using optimized CO<sub>2</sub> laser ablation. (b) low and (c) high magnification SEM image of selective CO<sub>2</sub> laser ablated MP. (d) Photograph image of simple LED circuit using optimized Nd:YAG laser ablation. (e) low and (d) high magnification SEM image of selective Nd:YAG laser ablated MP. .... 66
- Figure 4.15. (a) Water droplet on different surfaces (i) pristine MP, (ii) CO<sub>2</sub> laser ablated MP, and (iii) Nd:YAG laser ablated MP. (b) Time-dependent water contact angle stability test of CO<sub>2</sub> and Nd:YAG laser ablated MP. .... 67
- Figure 5.1. (a) Schematic of the fabrication process for stretchable carbon nanocomposite using laser pyrolyzation of polyimide: (i) attach polyimide tape to a PET sheet; (ii) laser-carbonize patterns on the polyimide; (iii) pour and impregnate carbon traces with diluted uncured PDMS; (iv-v) peel off the PDMS sheet after crosslinking. (b) A carbon trace before and after transferring to the PDMS. (c) A twisted carbon trace. (d) A lit LED connected to carbon traces showing diminished brightness as a function of strain: (i) 0%, (ii) 2%, (iii) 4%, (iv) 6%. .... 71
- Figure 5.2. Surface and film architecture details. (a-b) Optical images of the carbonized polyimide before and after transfer to the PDMS. Scale bar 250  $\mu\text{m}$ . (c) SEM image of the aligned particles in the traces with the arrow showing the direction of laser ablation. (d) High magnification SEM image showing nanoparticles and fibers. (e) Cross section image of the carbon traces showing the porosity of the carbonized material. (f-g) SEM images of the carbon particles after transfer to the PDMS at different magnifications. (h) Cross section SEM of stretchable carbon traces embedded in PDMS. .... 72
- Figure 5.3. (a) Sheet conductivity of carbon trace on polyimide as a function of laser fabrication parameters (power and speed). (b) Sheet conductivity of carbon trace after transfer to the PDMS as a function of laser fabrication parameters (power and speed). .... 73
- Figure 5.4. Characterization of the stretchable carbon traces subjected to longitudinal and transverse strain. (a) Illustrations of carbon traces (i) in their relaxed state, (ii) under longitudinal strain, and (iii) under transverse strain. (b) Plot of the relative resistance change for different levels of longitudinal strain. (c) Plot of the relative resistance change for

- different levels of transverse strain. (d) Gauge factor of the stretchable carbon traces versus longitudinal strain. (e) The dynamic stretch-and-release cycle response of the sensor for various strains 0–25 %. ..... 74
- Figure 5.5. Human finger motion detection with stretchable carbon traces. (a-b) Photograph of five stretchable strain sensors attached to the finger joints on the glove. (c) Relative resistance change of the strain sensors at different bending stages over time; the corresponding finger configuration for each plot region (i-ix) is shown in the snapshots below the plot. .... 75
- Figure 5.6. (a) Fabrication process of wireless LC passive pressure sensor, (b) experimental setup and readout apparatus used for sensor characterization, (c) impedance phase versus frequency at several different pressures, (d) sensor resonant frequency vs. pressure. .... 78
- Figure 5.7. Flexible wireless wound pH monitoring system utilizing NFC communication. .... 81
- Figure 5.8. Fabrication process of (a) pH sensor on ITO film and (b) flexible battery-less NFC module ..... 83
- Figure 5.9. (a) Block diagram of the developed wireless NFC tag, black arrows represent data communication and red one represent power transfer, (d) photograph of completed wireless pH monitoring device and smartphone interface, images illustrating the flexibility of the (c) sensor and (d) wireless NFC module. .... 84
- Figure 5.10. UV-Vis. Spectra of different layers of the pH sensor in the range of 300–900 nm. The obtained spectra were measured in buffer solutions of (a) pH 4 and (b) pH 10, insets show emeraldine salt (green) and emeraldine base state (blue) of the electro-polymerized polyaniline. .... 86
- Figure 5.11. (a) Dynamic response of the pH sensor from pH 4 to 10, (b) EMF response of the pH sensor to various mechanical bending, inset schematic illustrates the bending mode and radius of curvature ( $r$ ) in the experiment. .... 87
- Figure 5.12. (a) Measured reflection coefficient, and (b) output voltage power supply of the wireless module versus frequency at various degrees of mechanical bending. .... 88
- Figure 5.13. Drift behavior of the pH sensors at pH 4, pH 6, pH 8 and pH 10. .... 89
- Figure 5.14. (a) Microfluidic test setup to emulated wound condition, (b) real-time recording of the pH changes in the hydrogel wound model, the corresponding color change of the emulated wound model for each region i-iv is shown in the snapshots above the plot. .... 89

Figure 5.15. Schematic illustrations of the fabrication process and photographic images of the stretchable pH sensor with serpentine interconnects: (a) polyimide sheet is silanized and placed on an air plasma treated Ecoflex substrate, (b) a CO<sub>2</sub> laser is used to carbonize serpentine carbon traces on the polyimide sheet, (c) polyaniline is spray coated onto the porous carbon, (d) the polyimide sheet is machined with the same CO<sub>2</sub> laser at a higher power level, (e) excess polyimide is removed, (f) interconnects are insulated by another Ecoflex layer followed by the deposition of Ag/AgCl and solid electrolyte, (g) photograph of various stretchable PANI/C-PI interconnect designs, (h-j) images illustrating an array of pH sensors being stretched and indented. .... 91

Figure 5.16. (a) Dynamic potential response of the un-stretched pH sensor to unit decrease and increase of pH, (b) potentiometric responses of the un-stretched pH sensor to pH changes, (c) optical image before and after longitudinal strain, (d) potentiometric responses of pH sensor to various longitudinal strain in different pH buffer solutions, (e) optical image before and after transverse strain, (f) potentiometric responses of pH sensor to various transverse strain in different pH buffer solutions. .... 93

Figure 5.17. (a) Microfluidic test setup to emulated wound condition, (b) optical image of microfluidic test setup with attached stretchable pH sensor, (c) optical image of microfluidic test setup with and without applied strain to the sensor, (d) real-time recording of the pH changes in the hydrogel wound model under 0% and 100% strain..... 94

Figure 5.18. Biocompatibility assessment of the materials used in the fabrication of the pH sensor using a culture of NIH 3T3 cells, a) micrographs demonstrating the live (green) and dead (red) cells cultured next to the samples, the majority of the cells are viable at day 4 of culture, b) metabolic activity of the cultured cells measured by PrestoBlue assay and compared to the control group. The results did not show immediate toxicity and the tested materials did not interfere with cellular growth as there were no statistically significant difference between the samples and controls. .... 96

Figure 5.19. Schematic illustration of the fabrication procedure for the paper based humidity sensor ..... 98

Figure 5.20. (a) Optical images of fabricated humidity sensors using CO<sub>2</sub> laser ablation, (b) capacitance variations versus relative humidity levels for the range 2–85%RH and (c) close up of capacitance variations versus relative humidity in range 2–50%RH. (a) Optical images

- of fabricated humidity sensors using Nd:YAG laser ablation, (b) capacitance variations versus relative humidity levels for the range 2–85%RH and (c) close up of capacitance variations versus relative humidity in range 2–50%RH..... 100
- Figure 5.21. (a) Comparison of response time performance of different capacitive sensor designs to RH between 2% to 40%. (b) Close up of capacitance variation during desorption procedure from 40% to 2%RH. (c) Repeatable capacitive responses of capacitive sensors during four cycles between 2% and 40% RH. (d) Comparison of response time performance of different capacitive sensor designs to RH between 40% to 85%RH. (e) Close up of capacitance variation during desorption procedure from 85% to 40%RH. (f) Repeatable capacitive responses of capacitive sensors during four cycles between 40% and 85% RH. .... 102
- Figure 5.22. Schematic illustration of the fabrication procedure for the paper based temperature sensor..... 103
- Figure 5.23. (a) Fabricated temperature sensors on the paper substrate through Nd:YAG laser ablating MP.(b) Electrical resistance of the four design temperature sensors and room temperature condition 21°C. (c) Resistance variation against temperature of four design RTDs sensors for temperature between -20°C to 80°C. (d) Sensitivity vs resistance curve. Stability test of four design RTDs continuously monitored at (e) 21°C and (f) 60°C conditions for 24h..... 105
- Figure 5.24. (a) Illustration of the respiratory epithelial tissue and paper-based microfabricated in-vitro lung device, (b) selective attachment of aqueous red dye on laser treated parchment paper, (c) schematic of the paper-based air-liquid-interface (ALI) platform, (d) photograph of components, and (e) assembled final device. All scale bars: 10 mm..... 108
- Figure 5.25. The procedure for airway cell culturing on the paper based platform; (a) cell seeding on the upper open chamber, (b) on day 3 the cells exhibit a confluent monolayer coverage on the laser ablated hydrophilic region on the parchment paper, (c) air-liquid interface is established by removing the medium from the top chamber while maintaining a constant flow of medium in the lower chamber for 7 days, (d) observation of ZO1 expression around the whole cell membrane that resembles the functional airway epithelium..... 109
- Figure 5.26. Assessment of cell viability of airway epithelium (CALU3) grown on parchment paper at day1 (a) and Day3 (b) by live-dead staining. CALU3 are stained with Syto10 (Live staining- green) and Ethidium Bromide (Dead staining- red). The images were captured

using Zeiss LSM710 confocal microscope under 20x objectives. (scale bar= 50  $\mu$ m, 20x objective) ..... 110

Figure 5.27. Comparison of airway epithelium integrity between paper-based ALI platform and conventional Transwell ALI. Tight junctional marker - ZO1 expression was compared between ALI platform (a,b,e,f) under flow condition and Transwell (c,d,g,h) under stasis at Day5 and Day7. The first column represents the ZO1 expression (green) at 60x magnification (scale bar = 20 $\mu$ m) and the second column represents the overlaid images of ZO1 (green) with DAPI nuclear staining (blue) at 40x magnification (scale bar =50 $\mu$ m). The images were representative from 3 set of independent experiments. (i) Comparison of thickness of ZO1 expression between paper platform and Transwell at Day5 and Day7. Thickness of ZO1 was measured at 200% zoom of original image using Image J software. Mean was calculated from 100 random measurements from images of 3 independent experiments. \*\*\*\*p<0.0001 and ns=not significant..... 111

Figure 5.28. Comparison of airway epithelium integrity between with (B, D) and without fibronectin coating (A, C) on conventional Transwell ALI culture. Tight junctional marker - ZO1 expression (green colour) was compared at Day 5 and Day7. (Scale bar = 20 $\mu$ m). ..... 112

Figure 5.29. Comparison of ZO1 expression on differentiated CALU3 cells at Air Liquid Interface under flow and static condition of new ALI platform for 5days (A,B) and for 7 days (C,D). The CALU3 cells were fixed and stained with tight junction marker ZO1 (Zona Occluden1 –green) (scale bar = 20  $\mu$ m)..... 113

## ABSTRACT

Author: Rahimi, Rahim. PhD

Institution: Purdue University

Degree Received: December 2017

Title: Laser-assisted processing of multilayer films for inexpensive and flexible biomedical microsystems

Major Professor: Babak Ziaie.

Flexible/stretchable electronics offer ideal properties for emerging health monitoring devices that can seamlessly integrate with the soft, curvilinear, and dynamic surfaces of the human body. The resulting capabilities have allowed novel devices for monitoring physiological parameters, improving surgical procedures, and human-machine interfaces. While the attractiveness of these devices are indubitable, their fabrication by conventional cleanroom techniques makes them expensive and incompatible with rapid large-scale (e.g., roll-to-roll) production. The purpose of this research is to develop inexpensive fabrication technologies using low-cost commercial films such as polyimide, paper, and metalized paper that can be utilized for developing various flexible/stretchable physical and chemical sensors for wearable and lab-on-chip applications. The demonstrated techniques focus on an array of laser assisted surfaces modification and micromachining strategies with the two commonly used CO<sub>2</sub> and Nd:YAG laser systems. The first section of this dissertation demonstrates the use of localized pulsed CO<sub>2</sub> laser irradiation to selectively convert thermoset polymer films (e.g., polyimide) into electrically conductive highly porous carbon micro/nano structures. This process provides a unique and facile approach for direct writing of carbonized conductive patterns on flexible polyimide sheets in ambient conditions, eliminating complexities of current methods such as expensive CVD processes and complicated formulation/preparation of conductive carbon based inks used in inkjet printing. The highly porous laser carbonized layer can be transferred to stretchable elastomer or further functionalized with various chemical substances such as ionic solutions, nanoparticles, and chemically conductive polymers to create different mechanical and chemical sensors. The second section of this dissertation describes the use of laser ablation for selective removal of material from multilayer films such as ITO-coated PET, parchment paper, and metalized paper to create disposable diagnostic platforms and *in-vitro* models for lab-on-chip based studies. The ablated areas were

analyzed using electrical, mechanical, and surface analysis tools to understand change in physical structure and chemical properties of the laser ablated films. As proof-of-concept demonstrations of these technologies, four different devices are presented here: mechanical, electrochemical, and environmental sensors along with an *in-vitro* cell culture platform. All four devices are designed, fabricated, and characterized to highlight the capability of commercial laser processing systems in the production of the next generation, low-cost and flexible biomedical devices.

# 1. INTRODUCTION

## 1.1 Research motivation

Disposable biomedical devices are identified as the cost-effective but powerful medical tools intended for one-time or temporary usage that can be used in monitoring health and diagnosing diseases as well as vital human parameters. A primary reason for using these devices is to prevent transmission of infection among patients. Although cost is an important factor in the design and manufacturing of such devices, there should be a careful balance between the cost of production and reliability of the device over its intended time of usage. A paradigmatic example of the trade-off between performance and cost of manufacturing, is the single use glucose monitoring strips. Standard electrochemical glucose strips on average cost about \$0.65 with a measurement accuracy of  $\pm 20\%$  of the actual blood glucose level. Increasing the accuracy in such sensors will result in higher cost and inconvenient for daily users. In contrast, manufacturing less expensive sensors using the same technology will require the use of less material (such as enzymes) and result in lower accuracy with inadequate level of performance for monitoring blood glucose levels. Based on a report published by Grand Review Research, the total market for such disposable biomedical sensors in 2016 was valued at 5.1 billion USD and is predicted to reach 12.3 billion USD by 2025 with a compound annual growth rate of 10.2%, Figure 1.1.

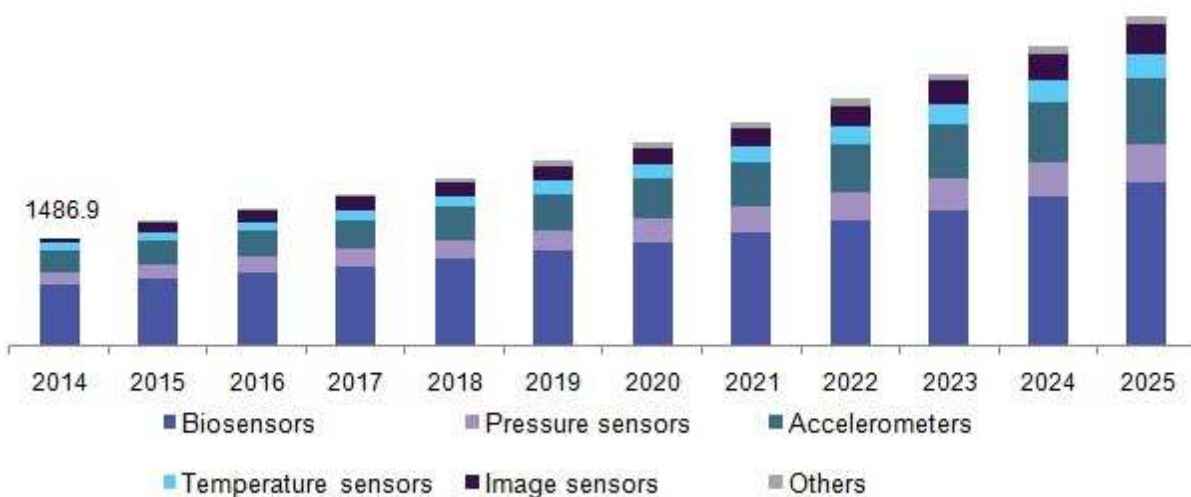


Figure 1.1. U.S. disposable medical sensors market by product, 2014 - 2025 (USD Million)

The increasing demand in healthcare, pharmaceutical, and food packaging are projected to be the primary driving markets over the forecast period. A growing population, and prevalence of infectious diseases, as well as increasing government initiatives towards innovating cost-effective medical devices for endemic diseases (e.g., malaria) are some of the key drivers to propel the market of disposable medical devices. Other factors such as the aging population with an increase in long-term chronic diseases coupled with rising awareness among people regarding wearable electronics and self-monitoring are also anticipated to fuel the disposable medical device industry in the area of wearable technologies over the coming years. This growing market, has resulted in extensive endeavors in both industry and academia to adapt conventional hard microelectronic manufacturing methods onto flexible and disposable substrates that can potentially use in the production of flexible and wearable health monitoring devices. Some of these examples include different wearable and adhesive based sensor that can monitor various physiological conditions in sweat and wound environment. Although such devices have shown great level of performance, time consuming and costly photolithography processes used in the design of such devices are some of the factors projected to challenge their potential growth and commercialization. On the other hand, recent advancements in scalable manufacturing processes such as inkjet printing and 3D printing have proven unpresented opportunities in development and manufacturing low-cost sensors. While printing technologies have been primarily used in publishing and packaging industries, they have recently re-emerged as a possible technology in the manufacturing of low-cost/disposable sensors and electronics. Development of different conductive and semiconducting inks in combination with high precision inkjet systems have demonstrated the possibility of printing a wide range of electronics with potential use in flexible and wearable applications including flexible displays, chemical and physical sensors. Despite the great advancements in the field of additive manufacturing, many challenges still remain, primarily with respect to the ink formulation. At the current technology status, silver, gold and CNT nano particles are the most practical materials in terms of both conductivity and printability; however, their performance is still insufficient and needs further improvements. Some of the major drawbacks of such inks include their high cost, limited shelf life, and need for multiple layers of printing (>12) to achieve acceptable levels of conductivity. One of the alternative approaches to inkjet printing technology is laser processing. Laser machining provides a unique set of capabilities beneficial to the development of low-cost and rapid manufacturing systems. Lasers provide a robust non-contact

method to selectively etch (ablate) materials, alter their surface morphology, and induce surface chemical changes, all of which can increase the functionality of the processed material. For example, lasers can be used to pyrolyze thermoplastic polymers (e.g Polyimide) to create active carbon materials, or (with proper wavelength settings) it can be utilized for selectively etching layers from a multilayer structure. Furthermore, the availability of commercial, reliable, and precise laser systems allows them to become part of large-scale (e.g., roll-to-roll) production lines. Surging advancements in laser technology with lowering cost of ownership is expected to increase the use of the laser technology in many sectors of manufacturing at a significant rate over the coming years. For example, Figure 1.2 shows an example of the fast growing laser processing market in China in the coming years which will significantly influence the cost and rate of production in the coming years. The purpose of the work in this dissertation was to investigate new design strategies to fabricate inexpensive biomedical microsystems on commercial flexible polymeric substrates with the focus of using low-cost laser processing techniques with two of the most commonly used laser systems (CO<sub>2</sub> and Nd:YAG) in industry. Systematical studies were performed on the laser interactions with different commercial film such as metalized paper, parchment paper and polyimide film using electrical, optical, and mechanical characterization methods as well as surface analysis with XPS, EDX and Raman spectroscopy. The laser characterization results were used in the development of different physical, and electrochemical sensors as well as *in vitro* models for cell culture applications.

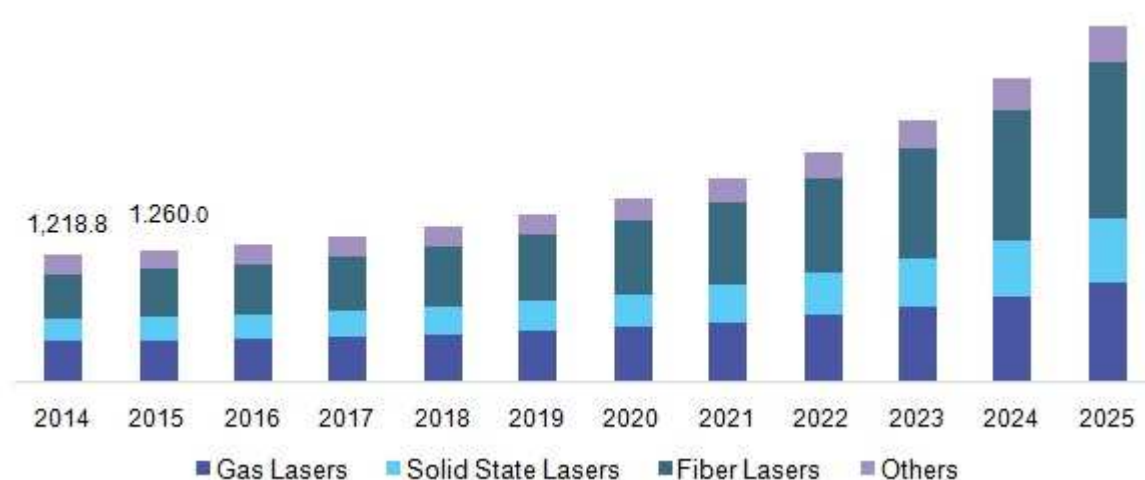


Figure 1.2. Laser processing market in China, 2014 - 2025 (USD Million)

## 1.2 Background

Over the past 50 years the vast majority of the work in electronics technology was focused on developing smaller transistors, in which improved the performance and speed of today's integrated circuit systems[1]. These electronic devices are fabricated on hard and brittle semiconductor substrates (e.g. silicon, glass, polysilicon) and are mounted on rigid printed circuit boards, both of which prevent intimate interaction with tissue or the human body[2]–[4]. Over the past few years with electronic systems becoming more personalized there has been an increasing demand to use future electronics in more human-friendly applications that requires flexibility and stretchability, which would be impossible with conventional rigid electronic systems[5]. This rising interest has evolved in the design and development of new forms of devices with novel mechanical and electrical characteristics that are capable of absorbing different mechanical deformations while maintaining their functionality, creating new classes of applications for food packaging[6][7], environmental/agriculture[8], displays[9] and inexpensive wearable/point-of-care diagnostics systems[10], Figure 1.3. Among the different potential use of flexible and stretchable electronics, wearable healthcare devices with an estimated market of 20.6 billion by 2019 has gained a considerable attention in both the scientific community and industry[11].

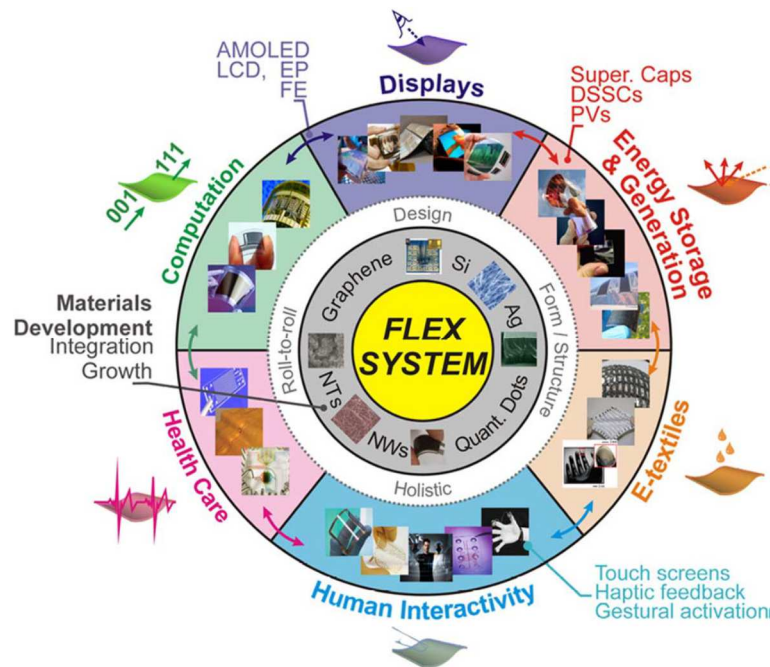


Figure 1.3. Next-generation flexible electronics systems and the key relevant sectors [9].

Depending on the applications, these devices can be classified into disposable and long term devices. Disposable devices are often used for diagnostic applications with a working time ranging from a few seconds to a few days for applications such as smart wound dressings, sweat diagnostic devices, wearable electrodes, surgical sutures for targeted wound monitoring and glucose sensing patches[12], [13]. Figure 1.4 shows some examples of such disposable biomedical devices. Long-term devices are often deployed in implantable health monitoring systems to continuously monitor the function of an internal organ as well as the general health condition of the individuals[14], [15], Figure 1.5. These devices can continuously monitor vital health information from the patient and provide them to the healthcare provider, which can open new paradigms to tissue implantation and prosthetics devices.

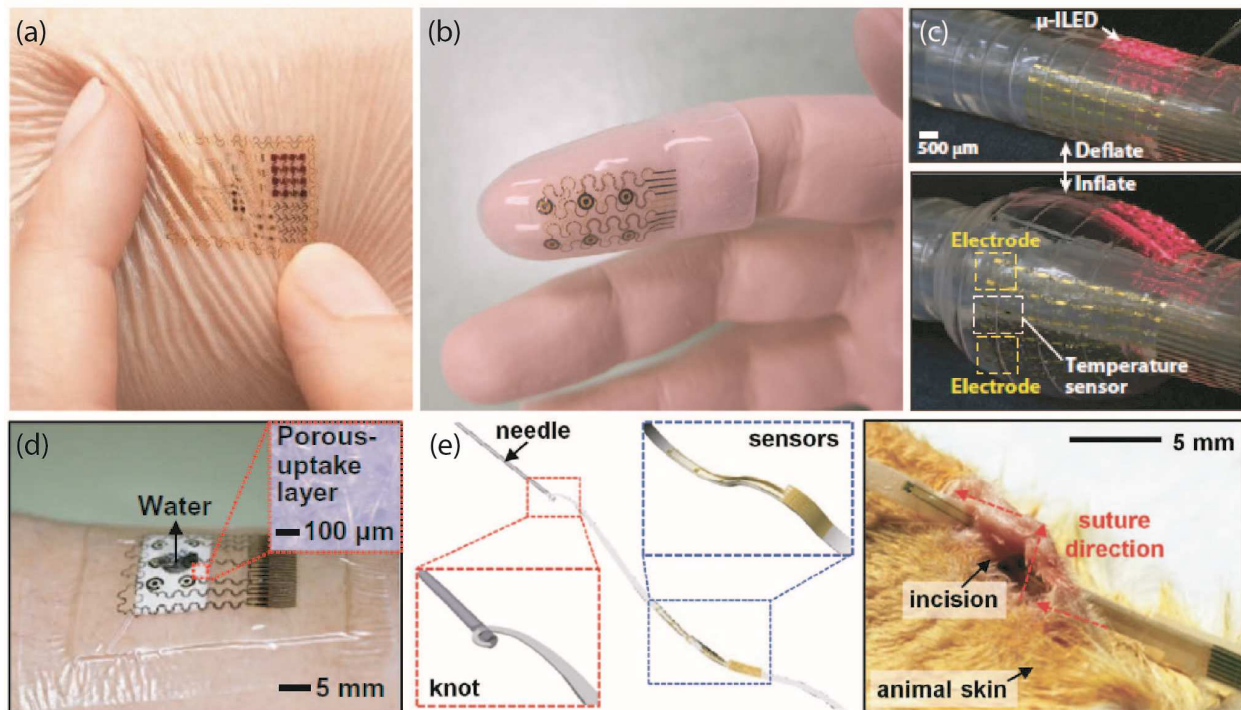


Figure 1.4. Disposable devices fabricated by conventional photolithography processes. (a) Optical images of temporary transfer tattoo with built-in electronics for measuring ECG, EMG, and EEG in conformal skin-mounted modes with- out conductive gels or penetrating needles[16]. (b) Optical image of multiplexed array of electro tactile stimulators in a stretchable, mesh geometry on the inner surface of an elastomeric finger-tub for measuring pressure created by physical contact [17]. (c) Optical image of multifunctional inflatable balloon catheter with integrated sensors for measuring temperature, flow, tactile, optical and electrophysiological data, together with radiofrequency electrodes for controlled, local ablation of tissue [18]. (d) Optical image of the wearable sweat analysis patch with a sweat-uptake layer and integrated flexible glucose, lactic acid, and pH sensors [19]. (e) Surgical sutures with built-in electronics for targeted wound monitoring and therapy [20].

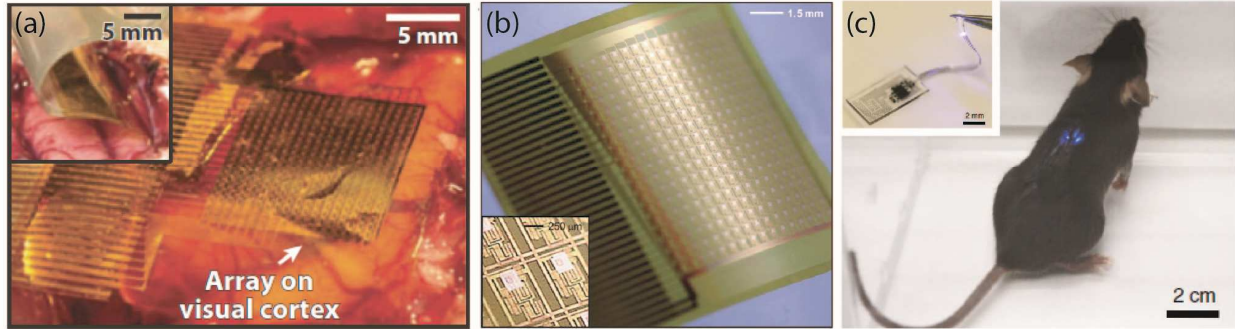


Figure 1.5. Long-term implantable devices fabricated by conventional photolithography processes. (a) Optical image of ultrathin and flexible silicon nanomembrane transistors into the electrode array for recording and stimulating the brain [21]. (b) Mechanically flexible silicon electronics for multiplexed measurement of cardiac electrophysiology[22]. (c) Fully implantable miniaturized optoelectronic systems for wireless optogenetics [23].

In either way, these devices hold considerable promise for more proactive response to patient's healthcare, helping to resolve potential issues before they become more severe clinical complications and burden on the healthcare service resources. In order to have proper functionality, these devices are required to be fabricated on elastic and plastic substrates. Over the past two decade, different biocompatible substrates have been used for fabricating health monitoring devices including elastic materials such as Polydimethylsiloxane (PDMS) and Ecoflex, plastic substrates such as Polyethylene terephthalate (PET), Polyimide, Parylene, and porous materials such as paper, and fabric[24]. However, the limited thermal budget and chemical restrictions associated with different plastic substrates often impose a significant challenge to the fabrication of these devices[25]. Different approaches have been developed for fabricating flexible and stretchable device which in general can be classified into two main techniques: (1) process based on conventional micromachining technology, and (2) new scalable manufacturing including printing and laser processing. Figure 1.6 shows a schematic illustration that compares of the sequential fabrication steps used in each approach.

Processes based on conventional microfabrication often require high temperate procedures (e.g. metal deposition, and thermal oxidation) and usage of harsh chemical reagents or etchants that can far exceed the tolerance of most plastic substrate. Therefore, the direct fabrication of devices onto flexible materials is often limited to a standard top-down photolithography techniques with low temperature metal deposition or lamination of very thin metal strips ( $\sim 10 \mu\text{m}$ ) on restricted plastic substrate (e.g. Parylene, Polyimide, and PDMS).

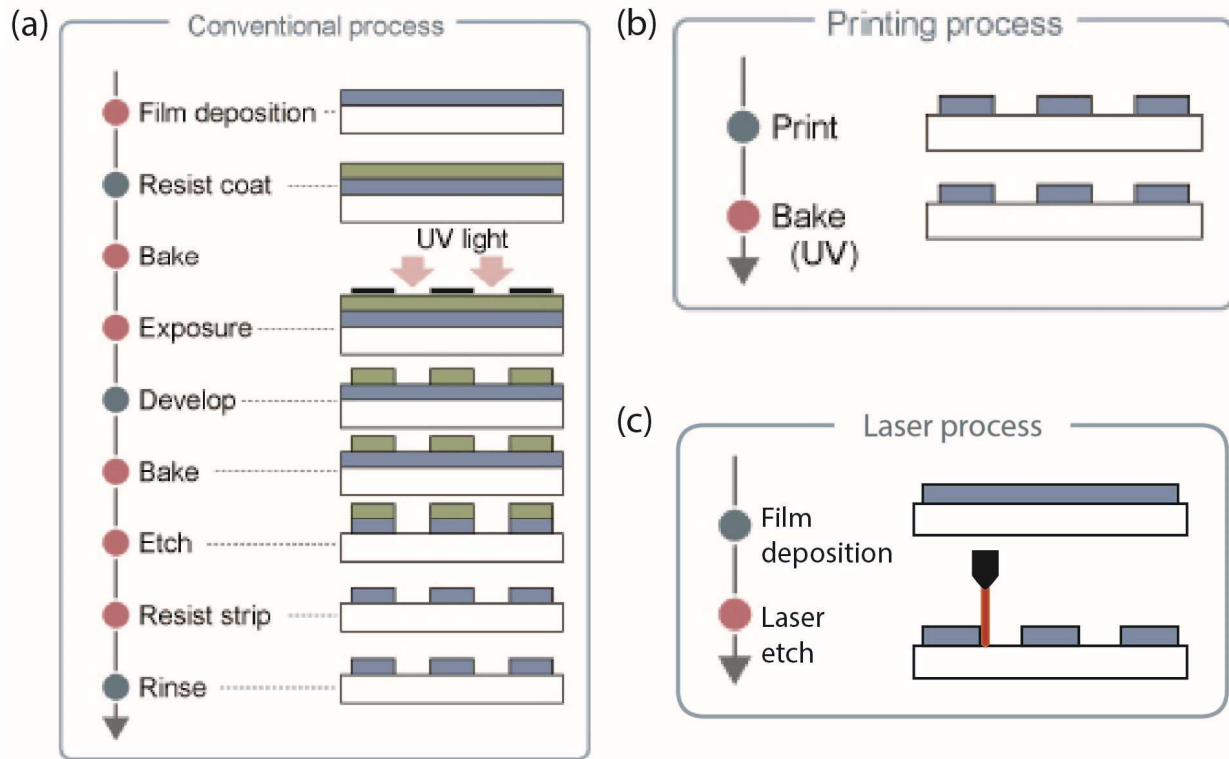


Figure 1.6. Flexible electronic manufacturing approaches: (a) conventional photolithography, (b) printing and additive manufacturing, (c) laser processing.

Examples of flexible circuit boards using this approach can be nowadays be seen in most light weight electrical appliances. This technology has reduced the weight and size of circuit board and allows them to fold and fit into more compact spaces. Although these circuits are pliable they can't be stretched, which limits their usage in wearable electronics that require to accommodate strain on arbitrary surfaces. The initial attempts in creating stretchable electronics with direct microfabrication process was pioneered by Whitesides and Hutchinson in 1998, where they investigated the effects of direct deposition thin films of gold onto the surface of pre-heated PDMS[26]. In later work by Wanger and Suo, stretchable interconnections were fabricated by thin films of gold deposited on pre-stretched PDMS[27], [28]. In the indirect approach, devices are first fabricated on rigid silicon wafers and finally transfer onto flexible/ stretchable substrates. In this process single-crystalline semiconducting materials can be prepared in the form of ribbons or plate with ultra-thin ( $< 1\mu\text{m}$ ) profiles by selectively etching away the underlying sacrificial layer or by utilizing the anisotropic etching characteristics of wet chemicals.

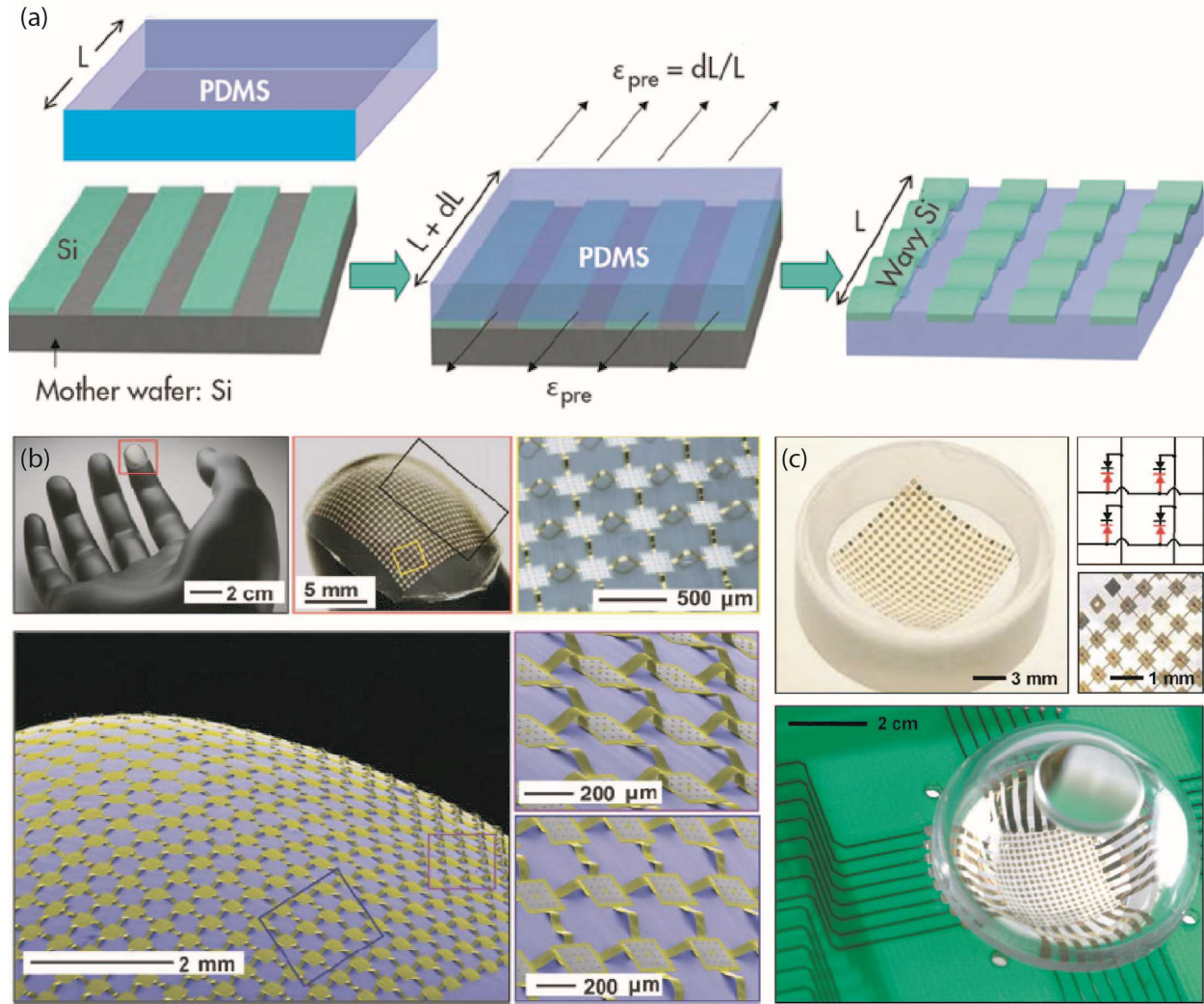


Figure 1.7. (a) Transfer process of silicon nanomembrane in a ‘wavy’ herringbone layout, to an underlying piece of PDMS. (b) Photographs of a stretchable circuit with a non-coplanar mesh design transferred onto the tip of a finger on a plastic model of a human hand [5]. (c) Optical image of an array of interconnected photodetectors and junction diodes in a compressed, hemispherical geometry on an elastomeric transform element [29].

In this process thin membranes (e.g. ribbons or plates) can be transfer-printed onto foreign substrates, such as plastic, using elastomeric stamp (e.g. PDMS) as a carrier[30], [31], Figure 1.7(a). Flexible electronics using this approach have reveal in high performance electronic devices with great mechanical flexibility. The use of thin films semiconductor in this approach allows the use of standard complementary metal-oxide semiconductor (CMOS) technology for creating multiple complex microsystems including transistors, logic gates, and oscillators in an amazing small footprint on flexible/stretchable substrates. The primary applications and driving forces for

such microsystems have been in the biomedical field, with the vision of developing a fully integrated wearable and implantable devices with various units including physical and chemical sensors with wireless communication that can conformably be mounted on the tissue or organs inside the body. The high flexibility and mechanical properties close to biological tissue provides less physical damage at the interface of the tissue and can enable a more conformable feeling for the user. The most sophisticated, and recent, examples involves the work by Rogers group where they took this method a step further by bonding thin strips of silicon ribbons to a pre-strained PDMS, thus creating buckled/wavy silicon ribbons, enabling full utilization of microfabrication capabilities offered by silicon processing to develop functional flexible and stretchable integrated systems. Using this method, various stretchable devices have been reported; these include fingertip electronics, medical balloon catheters and noninvasive electronics for brain, heart, skin and electronic eye[17], [32]–[35], Figure 1.7(b, c). Though these processes have shown great performance with highly compacted integrated circuits, their fabrication involves multiple complex, expensive, and time consuming processing steps, which may lead to higher cost and incompatibility with large scale manufacturing. This is an important consideration for many biomedical and sensing devices that are intended to be low-cost and disposable. More economical fabrication techniques with abundantly available and low cost materials (e.g. polymers, and paper) can significantly reduce the cost of production. Additionally, the manufacturing techniques should be economical, customizable, and adaptable for moderate-volume production (e.g., roll-to-roll). Among different approaches inkjet printing and laser-assisted processes are two of the two of the most particularly suited methods in the production of flexible electronic due to their scalability and ease of implementation. Inkjet printing provides a unique non-contact and mask-less patterning process that has been widely used for depositing an extensive number of materials in a solution form; these include, conductive polymers[36], ionic conductors [37], CNT[38], graphene[39], and various metallic nanoparticles[40]. Despite its promise, there are still important fabrication challenges associated with synthesis and printing of conductive inks. Currently, most such inks are based on the suspension of metallic nanoparticles that often exhibit good levels of conductivity only after multiple printing cycles accompanied by high sintering temperatures at 200–350 °C [41], [42]. In addition, suspended nanoparticles tend to agglomerate over time, influencing the print quality and clogging of the equipment nozzle.

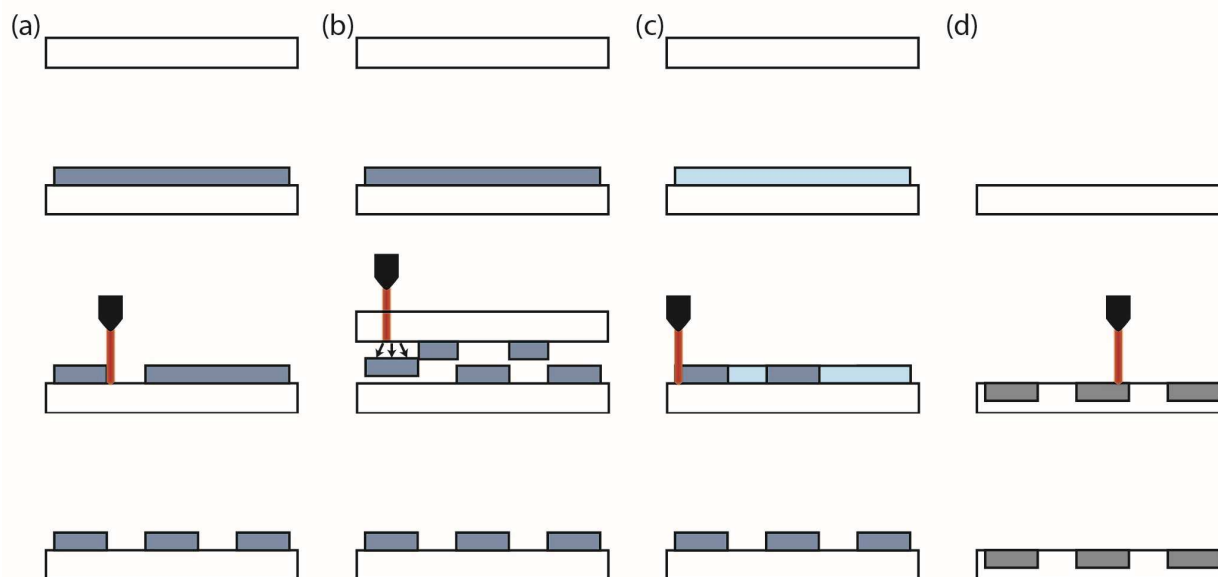


Figure 1.8. Laser direct writing techniques: (a) laser ablation, (b) laser-driven micro transfer, (c) selective laser sintering of conductive nanoparticles, (d) laser carbonization.

Laser processing can be considered as a high intensity beam of photons that can be accurately deliver into confined regions of a material in order to achieve a desired response. This control is exercised through the proper selection of laser processing parameters including wavelength, power, speed and the processing materials absorptivity. Depending on the laser beam parameters (e.g. wavelength, power, and speed) and material characteristic (e.g. structure and absorptivity), portions of the laser beam can be reflected, absorbed, diffused or transmitted. The absorbed energy is utmost the important parameter that determines the thermal effects on the material induced by the laser. The ability to precisely control the rate and location of energy delivered to the materials has resulted in wide range of laser ablation and deposition methods. Figure 1.8 shows a schematic illustration of different method of laser assisted direct writing techniques. Laser ablation is the process of removing material from a solid surface in a controlled fashion with using a laser beam, Figure 1.8(a). The irradiated material is heated by the absorbed laser energy and evaporated from the bulk substrate. The ablated features on the material are strongly influenced by the laser scanning speed and power. Laser ablation can be used on different polymeric and metallic based materials for a wide range of application. This type of fabrication allows the rapid production of a variety micro patterns without the need time-consuming photomasks processing and use of hazardous chemical etchants. Hence, laser ablation offers the

possibility to create complex microstructures in materials ranging from polymers to metallic films using a rapid single step-process. Many researchers have used this ability to create different low-cost devices for various applications such as microfluidics, microelectrodes and antennas. The second laser processing approach is for depositing different types of materials. This method can be further classified into laser-induced deposition (LID) and selective laser sintering (SLS). In LID processes, the substrate is placed in contact with a liquid or gas metalorganic precursor, and localized deposition is initiated with a focused laser beam at the precursor-substrate interface [43], [44]. The LID process has been used for the deposition of a wide range of metals such as Cu, Ni, Au, and Ag on several kinds of hard and flexible polymeric substrates such as polyimide (PI) [45]–[49]. However the high reactivity and toxicity of the precursors have made this processes impractical for scalable manufacturing. An alternative LID method, referred to as laser-induced forward transfer (LIFT) or laser driven release, uses laser imparted energy to transfer materials from a transparent supporting substrate onto an acceptor substrate[50], [51], Figure 1.8(b). The heat induced by the laser beam changes the phase of the film on the supporting substrate providing the propulsion required to drive the material from the holder onto the receiving substrate. This process faces challenges such as the preparation needed for transferring materials with the correct thermal matching, and oxidation or decomposition of materials during transfer[52], [53]. The selective laser sintering (SLS) process of conductive metal powder or nanoparticles (NP) has been explored as an alternative approach to inkjet printing [54], [55], Figure 1.8(c). The NP sintering for typical inkjet printing processes is usually implemented by exposing the whole printed substrate to elevated temperatures. SLS is often combined with inkjet printing to selectively localize the heat[56], thus enhancing the printing resolution and minimizing the substrate thermal exposure [57], [58]. Nonetheless, this method is associated with challenges regarding formulation of the binder materials and NP synthesis.

In addition to the aforementioned laser processing techniques, one can utilize the localized high temperature induced by laser irradiation to selectively convert organic thermoset polymers into conductive carbon materials, Figure 1.8(d). This can generate unique conductive carbon micro-patterns with highly porous micro/nano structures [59], [60]. The overall aim of this doctoral research is to propose new design and fabrication strategies to construct flexible and stretchable electronics by using laser carbonization and selective ablation of commonly used polymeric films. The second goal for my doctoral research is to develop novel strategies to implement these laser

processing techniques to biomedical applications ranging from point of care wearable electro-mechanical sensors to low cost *in-vitro* models for lab-on-chip based studies.

### 1.3 Overview of thesis

This thesis is organized into four main chapters. Chapter 2 briefly discusses laser technologies with an emphasis on commonly used laser systems for material processing in industry. Chapter 3 demonstrates the use of direct laser carbonization of thermoset polymers such as polyimide to create highly porous and conductive carbon traces. The localized heat induced by pulsed laser irradiation in ambient conditions rapidly converts the surface of polymer film into a highly porous and super hydrophilic structures of carbon. This chapter also includes the characterization of selective deposited silver nano particles and polyaniline into the laser induced porous carbon structures. Chapter 4 presents the selective laser ablation of multilayer films (e.g., parchment paper, ITO films) with two laser wavelengths (1.06 $\mu\text{m}$  (Nd:YAG), and 10.6 $\mu\text{m}$  (CO<sub>2</sub>)). Chapter 5 demonstrates the used of the laser carbonization and ablation strategies in the fabrication of low-cost mechanical and electrochemical sensors for healthcare monitoring applications as wells as *in vitro* models for on-chip investigation of the human respiratory system.

## 2. LASER MATERIAL PROCESSING

Laser processing provides an attractive method for fabricating inexpensive micro-systems by delivering a confined controlled energy onto the surface of the material without altering the bulk. The absorbed energy can be used to alter the surface chemistry, etch the material, or change the chemical structure of the material, all on a wide range of soft and hard materials from paper to metal alloys. The specific effect on the material is dictated by the laser processing parameters, which are controllable to high specificity in modern systems. This section briefly discusses the principles of two commercial lasers systems and their interactions with various materials.

### 2.1 Laser systems

A laser consists of three major parts: an energy pumping source, a gain medium (or lasing medium), and an optical set up. The lasing process is initialized by pumping some energy (electrical, light or other forms) into the gain medium, resulting in excitation of atoms in gain medium. An optical set up is needed to make sure that the laser beam is produced only in the desired direction and guided to the work space. Figure 2.1 shows a configuration with two mirrors and a photon-based pumping source. Depending on the active medium used, lasers can be classified into semiconductor lasers, dye lasers, solid-state lasers, and gas lasers. The medium and resonator determine the wavelength of the laser beam and the power of the laser. In this section, we discuss the two most commonly used laser (solid-state, and gas) processing systems for the fabrication of flexible devices. Commercial laser engraving systems offer good resolution, control, and processing speed. These systems consist of a laser module connected to a machining enclosure that contains a working stage and a software-controlled lens. The substrate is placed on the stage and the lens module guides the laser beam on the surface of the substrate to cut or ablate regions as defined in a CAD drawing. Most commercial systems use either a 10.6  $\mu\text{m}$  CO<sub>2</sub> laser (typical powers of up to 150 W) suitable for cutting polymers and wood or a 1.06  $\mu\text{m}$  fiber laser (typical powers of up to 40 W) that can mark metals and cut thin foils [61]–[63]. These systems have a linear scanning speed of a few meters per second and the output power and laser spot size/focus can be adjusted by software.

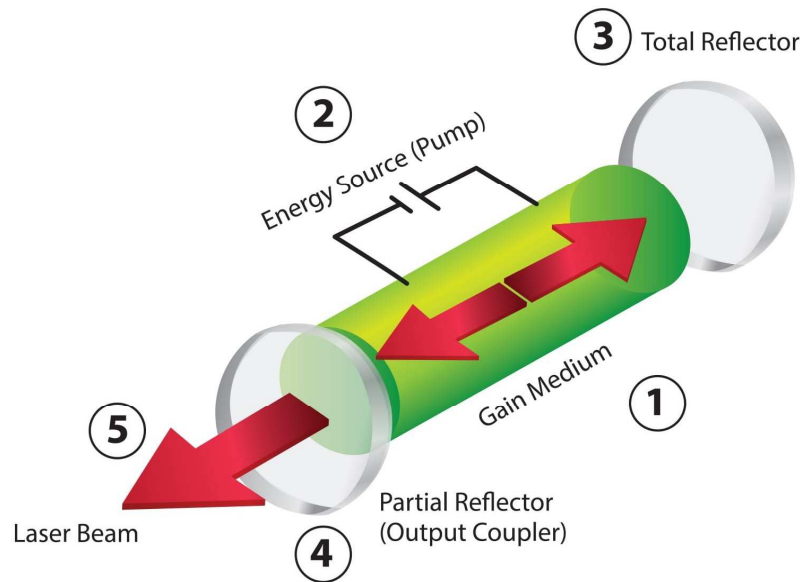


Figure 2.1. Schematic of laser components: 1) Gain medium capable of sustaining stimulated emission. 2) Energy source to pump the gain medium. 3) Total reflector to reflect energy. 4) Partial reflector. 5) Laser beam output (<https://www.ulsinc.com/learn>)

### 2.1.1 Solid state lasers: Fiber laser

The laser medium for Nd:YAG laser consist of Yttrium-Aluminium-Garnate cubic crystal ( $\text{Y}_3\text{Al}_5\text{O}_{12}$ ) where approximately 2% of the  $\text{Y}^{3+}$  ions sites in the lattice are replaced by  $\text{Nd}^{3+}$  ions. The photonic emissions are generated by the transition between the excited and ground energy levels of the Nd ion. Commercial Nd:YAG laser systems typically operate at the wavelength of  $1.06\text{ }\mu\text{m}$ , which is sufficiently small for creating device features with micrometer resolution. Additionally, the wavelength is more easily absorbed by metallic materials, allowing for processing of metal films. The output beam of the Nd:YAG laser can be operated in continued, pulsed, or Q-switching mode. A typical commercial Nd:YAG system is the PLSMW from Universal Laser Systems, Inc., which offers pulsed frequencies of up to 100 kHz, powers of up to 45 W, and scanning speeds of up to 4 m/s, with optics allowing for laser spot size as small as  $12\text{ }\mu\text{m}$ .

### 2.1.2 Gas lasers

In gas lasers, the active medium consists of gas molecules, offering advantages such as lasing media homogeneity, ease of cooling and replenishment, and low cost. The wavelength of the emitted light depends on the primary gas used; for instance, Xenon Chloride (XeCl) produces 308 nm, Xenon Fluoride (XeF) produces 351 nm, Argon Fluoride (ArF) produces 191 nm, Argon produces 488 nm, and carbon dioxide (CO<sub>2</sub>) produces 10.6  $\mu\text{m}$ . Of these, CO<sub>2</sub> is the most common in industrial engraver systems. During the operation, the CO<sub>2</sub> molecules are excited by vibrational excitation of nitrogen (intermixed with the CO<sub>2</sub>) using high voltage electrical discharge. The excited nitrogen molecules correspond to highly unstable (001) vibrational levels of CO<sub>2</sub>. The transition between (001) and the ground level of (100) results in a 10.6  $\mu\text{m}$  laser radiation. The properties of CO<sub>2</sub> laser is mainly determined by the gas flow in the discharge tube and can be operated in both pulsed as well as continuous wave (CW) mode. An example of a commercially available CO<sub>2</sub> laser system is the Universal Laser System, Inc., Professional Series, with a maximum power of 120 watts, a maximum speed 4 m/s, wavelength of 10.6  $\mu\text{m}$ , and continuous laser processing mode, with optics allowing for laser spot size as small as 30  $\mu\text{m}$ .

## 2.2 Laser-material interaction

Nd:YAG and CO<sub>2</sub> laser systems are routinely used for modifying materials in various ways, such as cutting, marking, welding, and chemical alteration. The specific result is determined by the interactions caused by the thermo-physical properties of the material and the electromagnetic radiation of the laser. During these interactions, a portion of the light is reflected, another transmitted, and the rest absorbed. The absorbed energy causes thermal effects (e.g., local heating, melting, vaporizing, or pyrolyzing). When laser-machining materials, the absorptivity,  $A$ , (or reflectivity,  $R=1-A$ ) of the material is of utmost importance. The absorptivity of some common metallic materials at different wavelengths is shown in Figure 2.2. In general, metals have a higher reflectivity (less absorption) at larger wavelengths. For instance, copper has a very low light absorption of 0.005 at 10.6  $\mu\text{m}$  (CO<sub>2</sub> laser) and slightly higher absorptivity of 0.03 at 1.06  $\mu\text{m}$  (Nd:YAG laser). Hence, Nd:YAG lasers are often used as the primary laser processing tool for metallic materials. The resulting effect of laser absorption can be classified into two categories: physical and chemical, as described below.

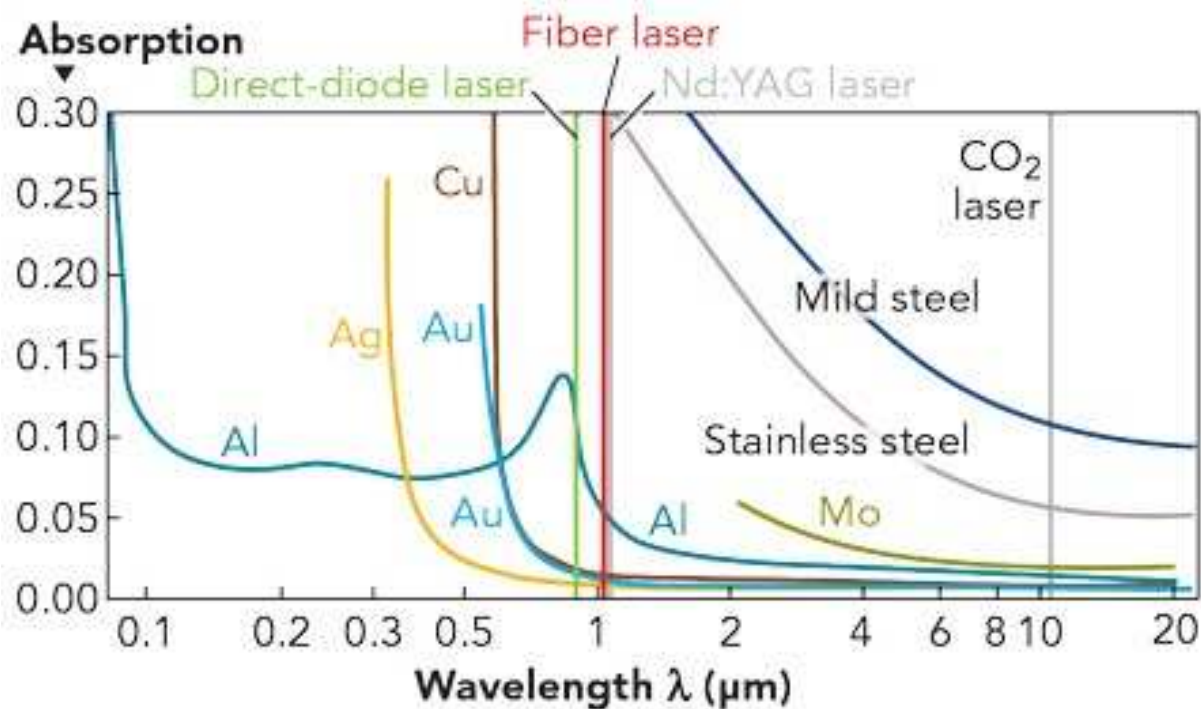


Figure 2.2. Absorption of various metals at relevant wavelengths for industrial lasers

### 2.2.1 Physical material alterations via laser

Physical changes to the material include removal of material (i.e., for through-hole cutting or surface ablation) and texturing (e.g., surface roughness). Both processes result from thermal effects and are a function of the laser fluence [64]. The optical energy delivered by the laser per surface area of the material is known as the fluence. Ablation occurs at energy densities greater than the material's fluence threshold, which is between 1 and 100 J/cm<sup>2</sup> for metals and between 0.1 and 10 J/cm<sup>2</sup> for organic materials [65]. In thermoplastics, this process locally melts the material, causing some to evaporate away [66], Figure 2.3(a). The amount and rate of material removal can be precisely controlled by the laser scanning speed and its intensity. High intensity (or lower scanning speed) can result in deep material removal which is commonly used for cutting materials whereas lower intensity (or higher scanning speed) can be used for surface texturing. During this process, some of the molten material can re-deposit on the surface, creating local surface roughness. The power can be controlled to minimize ablation while still permitting re-

deposition to occur. In thermosets, laser treatment above the fluence threshold result in material decomposition (e.g., pyrolysis, or carbonization in organic materials) which can be used for ablation. This process also results in surface roughness due to non-uniform surface pyrolyzation as well as re-deposition of pyrolyzed material. Such laser surface texturing has been widely used for several applications such as improving adhesion and increase the gripping performance of steel sheets [67] [68]. In more recent developments, laser surface texturing has been use to create micro- and nano-scale super-hydrophobic roughness on different materials for self-cleaning applications [69]. In other applications, exposure of thermoset polymers to high energy laser beams can cause thermal decomposition of the molecular chains in the material without melting, resulting in material pyrolysis, Figure 2.3(b).

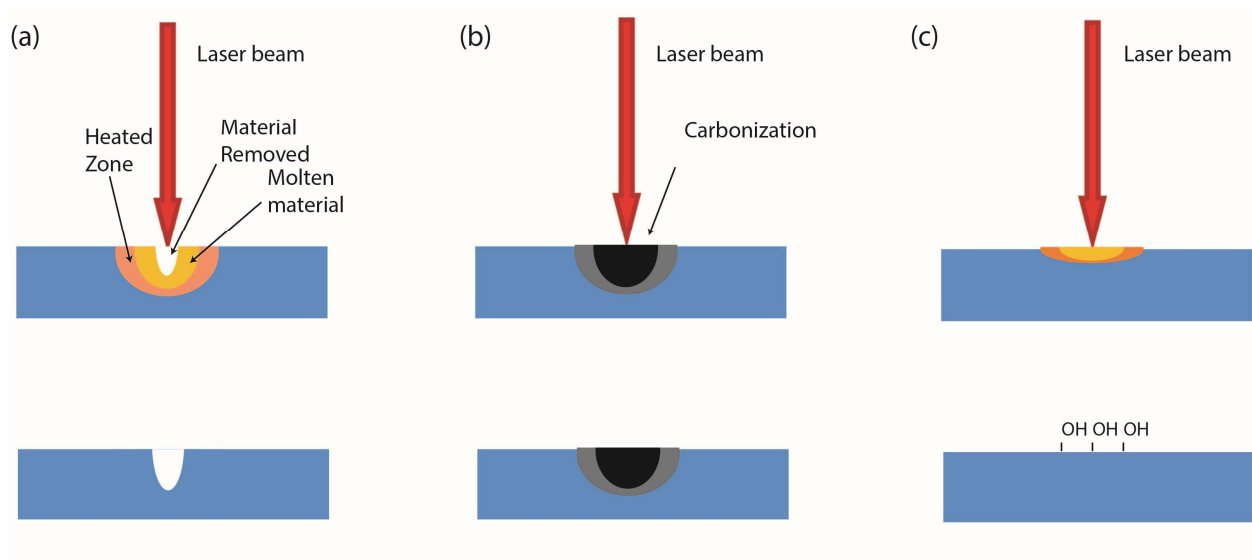


Figure 2.3. Interactions of laser with materials. (a) Physical interaction with thermoplastics causes material removal via melting and evaporation. Molten material can redeposit on the surface. High power results in through-hole features, but lower power allows controlled ablation/texturing. (b) Physical interaction with thermosets decomposes the material (pyrolysis) with redeposited debris. High power results in through-hole features, but lower power allows controlled ablation/texturing. (c) Very low power allows minimal material damage but alters the surface chemistry via interactions with atmospheric gasses

For example many molecular bonds such as C-N, C=O, C-O bonds in thermoset polymers can be dissociated with CO<sub>2</sub> laser (releasing the O and N atoms). The remaining material with high content of carbon bonds (C-C, C=C) results in porous and electrically conductive traces. These effects can then be used to create porous and conductive regions on polymeric or paper substrates which form the basis for fabricating a variety of passive and active components used in flexible devices.

## **2.2.2 Laser activated chemical processes**

In addition to physical surface modification, the laser process may also induce chemical modifications via a photo-thermal effect [70]. The high temperature generated by the laser can decompose the material and cause interactions with ambient gasses (e.g., oxygen, nitrogen) which can form additional functional groups, Figure 2.3(c). Often times, laser processing in such conditions results in the formation of hydrophilic functional groups, allowing laser to be used for controlling surface wettability[71], [72]. This technique is particularly useful when working with natively hydrophobic substrates such as parchment paper, and wax paper; processing techniques for these are described in the following chapters.

### 3. LASER CARBONIZATION OF POLYMERIC FILMS

Nanoscale carbon (carbon nanotubes and graphene) has unique chemical and electrical properties which have garnered significant attention over the past two decades [73]. In addition to their use in nano-electronics, carbon nanoparticles printed onto flexible substrates or loaded onto various polymeric binders have been used to fabricate flexible and stretchable systems [74]. Examples of these include carbon-based pastes for screen printing conductive films [75], carbon inks for inkjet printing [76], carbon-PLA filaments for extrusion-based 3D printers [76], and carbon-loaded elastomers[77]. These manufacturing materials are suitable for creating medical microsystems which can interface conformably with the human body and living tissue using rapid prototyping technologies. Using carbon-based composites, researchers have been able to create a variety of electrical and mechanical sensors and actuators which are applicable for monitoring or treating cutaneous wounds. For example, carbon-based inks have been used to define electrically-conductive traces on ceramic and polymeric substrates using screen printing techniques [78], [79]. The natural biocompatibility and chemical stability of carbon allows these traces to be used as electrical conduits on wearable devices/systems, including smart tattoos [80]. Meanwhile, materials comprising carbon nanoparticles embedded in stretchable binders (e.g. carbon-loaded PDMS or carbon-loaded PLA) have been used to create soft, elastomeric arrays strain/pressure sensors[81], [82]. Despite numerous reported carbon-based devices and sensors, few have been commercialized. This is primarily due to challenges with scaling the production of carbon-based nano-materials. For example, many of the nano/micro particles used in these systems are not economical to mass-produce for practical use in medical devices since they must typically be made into (possibly non-biocompatible) inks/pastes with general applicability (rather than specifically for medical applications) [83]. It would be more economical to create the carbon composites directly on the substrate without the use of additional binder materials (e.g., for inks) which may interfere with the biocompatible aspects of the material. One approach is to fabricate devices using carbonizable material. Many thermoset organic polymers can be pyrolyzed by raising their temperature to above 1000°C [84]. The result is pure carbon which is electrically conductive. Researchers have used this idea to create conductive carbon traces by pyrolyzing photoresists using a high temperature furnace [85]. Such materials have been used to fabricate supercapacitors [86], batteries [87], electrodes and biosensors for biomedical applications[88]. While the process is

economical and straightforward, it does not allow precise patterning of the material in a straightforward process. Moreover, the various components of the device must be resistant to high temperatures, lest they too be thermally decomposed. An alternative approach is to selectively carbonize a thermoset polymeric substrate via lasers. In this technique, laser energy is imparted onto a substrate to locally heat the substrate to a sufficiently high temperature to induce carbonization. Unlike bulk pyrolyzation methods (e.g., furnaces), the laser-based technique offers unprecedented control over carbon nanoparticle deposition and patterning. In this section we will first demonstrate the process of laser carbonizing polyimide and discuss its functionalization with conductive fillers including silver and polyaniline.

### **3.1 Laser-induced porous carbon from polyimide film**

In this section, we demonstrate the production of porous carbon produced from laser carbonizing polyimide and its use for different unique applications. In this process samples of polyimide tape and sheets were laser treated using a computer-controlled CO<sub>2</sub> laser cutting and engraving system (PLS6MW, Universal Lasers, Inc., Scottsdale, AZ). The desired carbon patterns was generated using CorelDraw (Corel Corporation) and ablated onto the polymer by raster scanning the laser beam across the surface. The electrical resistance of carbon traces was measured using a digital multimeter (Agilent 34401A). Scanning electron microscopy (field-emission SEM, Hitachi S-4800) was used to assess the morphology and microstructures of the laser pyrolyzed traces before and after different surface modification. Chemical composition was determined with using X-ray diffraction (XRD) and electron diffraction spectroscopy (EDS) and analysis was carried out by D-8 Focus and Oxford INCA Energy 250 systems. A universal testing machine (eXpert 4000, Admet) was used to assess the electromechanical robustness of the conductive traces by subjecting them to different mechanical deformations. Surface properties of the laser carbonized polymer were analyzed using a goniometer to determine the water contact angle.

As shown in Figure 3.1 the laser irradiation of a commercial polyimide (PI) film by a CO<sub>2</sub> infrared laser under ambient conditions converts the film into porous graphene which is also referred to laser-induced graphene (LIG). The computer-controlled laser allows to easily create desired patterns into various geometries. Figure 3.1(b) shows an optical image of array of laser patterned porous carbon traces on the polyimide tape.

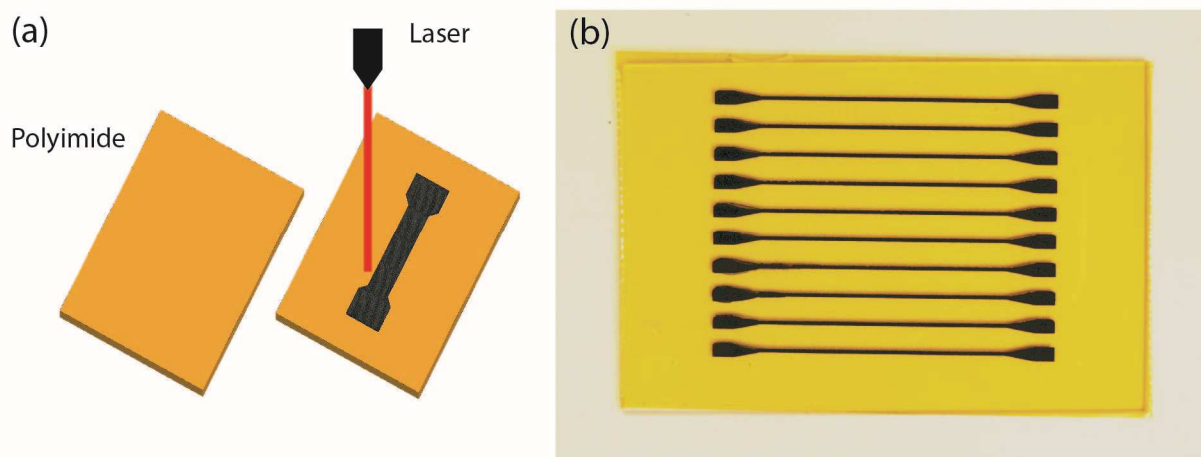


Figure 3.1. Porous carbon formed from commercial PI films using a CO<sub>2</sub> laser at an optimum combination of laser power (6.75 W) and speed (1.3 m/s). (a) Schematic of the synthesis process of porous carbon from laser carbonized PI film. (b) Photograph of final fabricated array carbon pattern on PI tape.

### 3.1.1 Results and discussion

The electrical conductivity of the carbon patterns before and after transfer to the elastomeric matrix was measured by four-point-probe technique. Figure 3.2 demonstrates the sheet conductivity of the carbon patterns as a function of the fabrication parameters, i.e., speed and power of the laser. The plots show the strong dependence of the sheet conductivity on both power and speed of the laser. In practice, the polyimide can be carbonized with the laser once the polymer reaches the threshold energy needed to initiate the pyrolyzation process. As the plots show, the threshold energy can be achieved at different laser powers and speeds. For example, with lower laser speeds, carbonization occurs at low power levels, whereas with higher laser speeds, carbonization requires a higher power. We observed that when the thermal energy is too large (high laser power and low raster speed) the polymer turns into a white ash, but when the thermal energy is too low, the polymer does not carbonize, both phenomena resulting in a low conductivity. The Gaussian shape of the conductivity plots in Figure 3.1(a) reflects this behavior, showing that there is an optimum combination of laser power (4.5 W to 8.25 W) and speed (0.5 m/sec to 1.9 m/sec) needed for producing high-quality, high-conductivity traces. The optimal setting corresponds to the maxima at each plot; these are plotted in Figure 3.2(b), showing a linear

relationship with speed and power (a maximum conductivity of 0.02 Mhos/ $\square$  with 6.75 W and 1.3 m/sec). The slope of the plot shows the optimal energy density (620 J/m<sup>2</sup>) needed to achieve low resistance carbon traces. Laser ablations with energy densities below or above this threshold will result in either insufficient energy for complete carbonization or burning of the polymer, respectively. The structural characteristics of the carbon nanomaterials were studied via EDS and Raman spectroscopy. The EDS spectra of the pristine carbonized polyimide shows a binding energy of 0.25 keV corresponding to high concentration of carbon material, Figure 3.2(c).

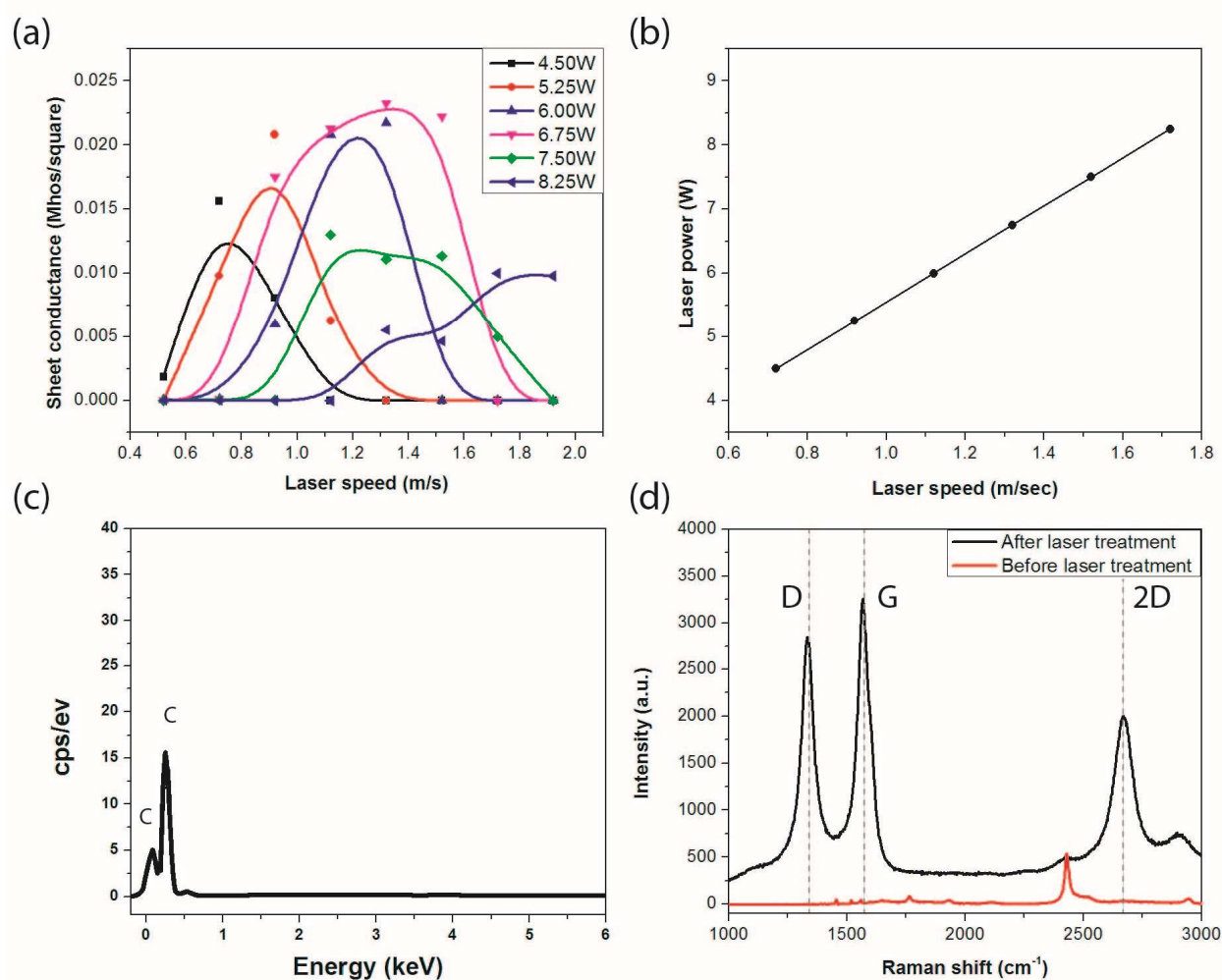


Figure 3.2. Electrical characterization of pyrolyzed carbon patterns. (a) Sheet conductivity of carbon trace on polyimide as a function of laser fabrication parameters (power and speed). (b) Power and speed required to achieve carbon traces with high sheet conductivity (low sheet resistance), (c) EDS spectra of the laser carbonized PI (d) Raman spectra before and after laser treatment.

Figure 3.2(d) shows the Raman spectra recorded from the center of the carbon patterns in the range of  $1000\text{--}3000\text{ cm}^{-1}$  using an excitation laser source at  $532\text{ nm}$ . The data clearly show three distinctive Raman spectra peaks at  $1350\text{ cm}^{-1}$  (D-band),  $1580\text{ cm}^{-1}$  (G-band), and  $2700\text{ cm}^{-1}$  (2D-band) after laser carbonization, which suggest the presence of CNT and graphite in the carbonized material. The peak located at  $1580\text{ cm}^{-1}$  (G-band) is the primary phonon arising from lattice stretching in the C–C bonding in the graphitic plane. The D-band observed at about  $1350\text{ cm}^{-1}$  corresponds to the disorder and defects in the graphitic lattice. The ratio of the peak intensity ( $I_D/I_G$ ) of the D and G bands is a parameter used to quantify the amount of defects in the graphitic material. The  $I_D/I_G$  ( $\sim 0.8$ ) ratio analyzed from the Raman spectra shows a reasonable amount of defect in the graphitic materials. The 2D-band is due to a secondary phonon vibration of the C–C bonding. This band provides information about stacking layers in the carbonized material (such as CNT, graphene). The ratio between the 2D and G bands ( $I_{2D}/I_G \approx 0.7$ ) calculated for the Raman data indicates that the graphitic material is composed of mostly three carbon layers.

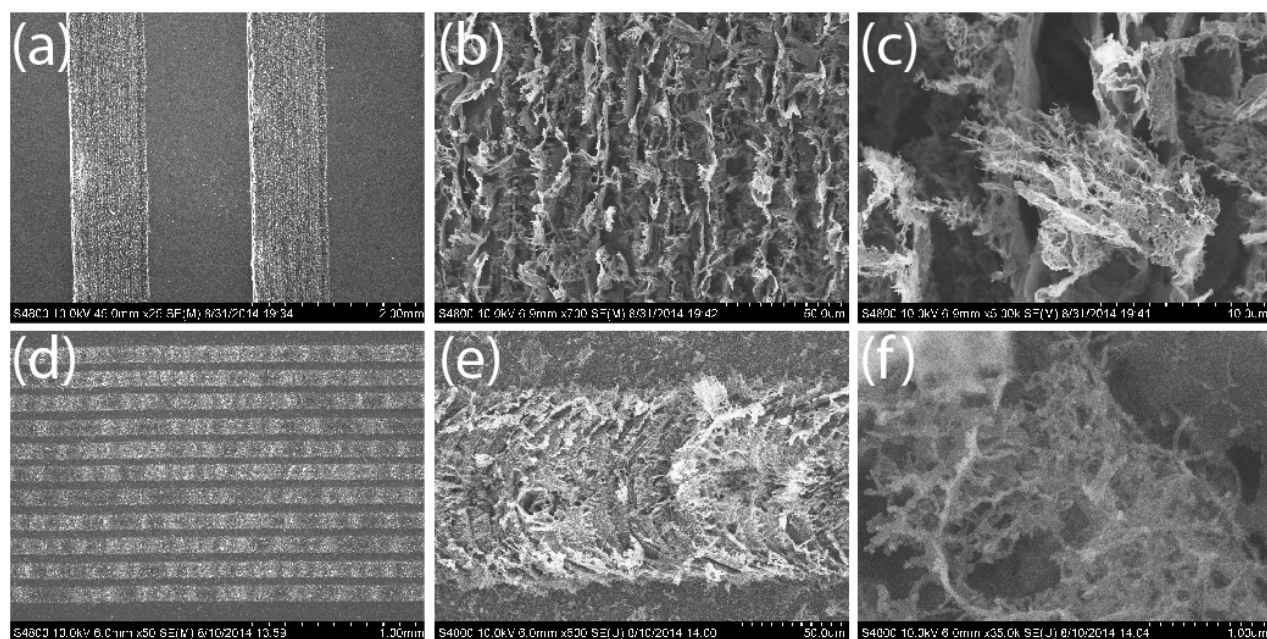


Figure 3.3. SEM of highly porous conductive carbon patterns. (a-c) images of 1 mm wide patterns. (d-f) images of smallest features with  $90\mu\text{m}$  width.

The morphology of the carbon patterns was investigated by scanning electron microscopy (SEM). The SEM images in Figure 3.3 (a-c) reveal a high degree of alignment and porosity as well as uniformity among the conductive carbon traces. Figure 3.3 (d-e) shows SEM images of the smallest features (width  $\times$  pitch = 90 nm  $\times$  120  $\mu$ m) achievable with our laser system, which is limited to the beam size of the laser. Figure 3.3 (f) shows a high-magnification top view of the carbon nano particles intertwining. The pristine Kapton film has a high contact angle and water droplet slides off when tilted. However, after carbonization the carbonized surface is super-hydrophilic and the water droplet immediately is wicked into to the carbonized material upon contact. Therefore changes in surface wettability of the laser carbonized region allows the selective trapping of aqueous solution into the carbonized patterns, Figure 3.4. In the next section we will discuss permeating the porous carbon with different materials including silver nano particles and polyaniline.

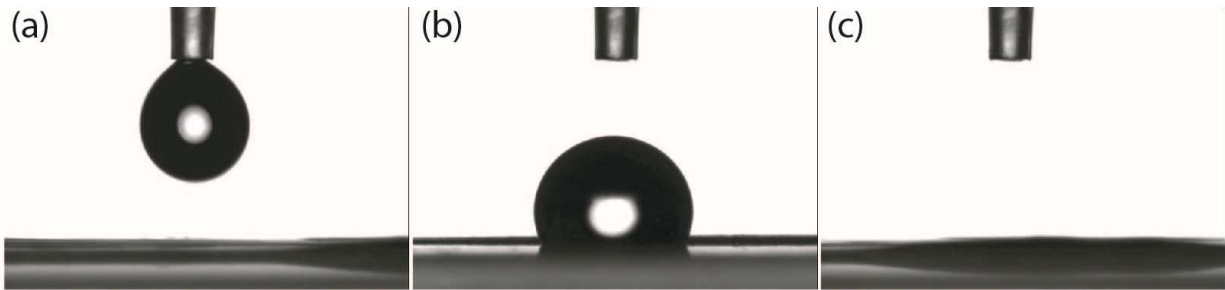


Figure 3.4. Goniometric experiments with 10  $\mu$ l DI water droplet for measuring the surface wettability, (a) water droplet before depositing on the surface, (b) water droplet on polyimide sheet, (c) water droplet wicking immediately into the laser carbonized surface upon contact (super hydrophilic).

### 3.2 Porous-carbon/silver nanocomposite

Despite the low cost of fabrication and stability of the laser carbonization process, they have a high electrical sheet resistance (typically between 15  $\Omega/$  to 1000  $\Omega/$  ) [59], [96] and sensitivity to mechanical deformations[97], limiting its use in flexible electronics, which often require highly

conductive and robust interconnections. In order to further advance the direct-writing laser-carbonization technique and overcome some of the shortcomings, we have developed a simple method that utilizes the super-hydrophilicity of the carbon traces to selectively synthesize and trap silver nanoparticles into the carbonized regions, significantly enhancing the electrical conductivity and robustness of the flexible interconnects.

### 3.2.1 Fabrication process

The presented patterning technique relies on the laser pyrolysis of a thermoset polymeric substrate serving as the flexible support to create highly porous network of conductive carbon traces. The traces are later selectively coated with an aqueous reactive silver ink, as shown in Figure 3.5(a-c). In this process commercially available polyimide (PI) sheets provided by DuPont (Kapton<sup>®</sup> HN, with a thickness of 60  $\mu\text{m}$ ) is used as the substrate for carbonization. Before the patterning process, the PI sheets are cleaned in an IPA solution for 30 min and rinsed with DI water and dried with nitrogen gun. The process begins by laser writing of highly porous carbon patterns into the surface of the PI sheet using a computer controlled CO<sub>2</sub> laser cutting and engraving system (PLS6MW, Universal Lasers, Inc., Scottsdale, AZ). The laser system characteristics include: maximum power of 100 W, maximum speed of 2 m/s, wavelength of 10.6  $\mu\text{m}$ , continuous wave (CW) mode, and beam spot size of 50  $\mu\text{m}$ . To carbonize the polymer substrate the laser beam should provide the threshold energy required to initiate the pyrolysis process, which can be achieved at different powers and scanning speeds. It should be noted that high thermal energies (high laser power and lower scanning speeds) result in cutting through the substrate while low thermal energies (low laser power and fast scanning speeds) will not effectively carbonize the polymer. For maximum conductivity, the laser is operated at 6.75 W with a scanning speed of 1.3 m/s. The laser ablates/carbonizes the surface of the polymer and creates porous super-hydrophilic carbon patterns, Figure 3.5(a). The electrical conductivity and robustness of the porous carbon trace is enhanced by filling the porous carbon them with silver nanoparticles. This is done by selective trapping of a reactive silver ionic solution in the traces, followed by an annealing step at 90 °C for 10 min, Figure 3.5(b, c). The silver ionic solution is only trapped in the laser-ablated areas (due to its super-hydrophilicity) and rolls away from the non-patterned regions. The silver ionic ink solution is prepared by a modified Tollen's process [98] in which 4 g of silver acetate (Alfa Aesar, 99 %) is mixed with 10 mL of ammonium hydroxide (Alfa Aesar, 28 %). To ensure

that the silver acetate powder is completely dissolved, the mixed solution is ultra-sonicated in a closed container for 30 min. Next, under continuous magnetic stirring, 1 ml of formic acid (Alfa Aesar, 97 %) is dropwise titrated into the mixture at room temperature (during the titration process the solutions change color from light yellow to light gray). The solution is stored at room temperature for 24 h to age, forming a clear solution. The final solution is composed of diammine silver (I) cations ( $\text{Ag}(\text{NH}_3)_2^+$ ), acetate ( $\text{CH}_3\text{CO}_2^-$ ) and formate anions ( $\text{HCO}_2^-$ ), containing 22 wt% silver[98]. Due to the rapid evaporation of the ammonia ligands and reactants, annealing at 90 °C results in silver nanoparticles formation in the porous carbon network.

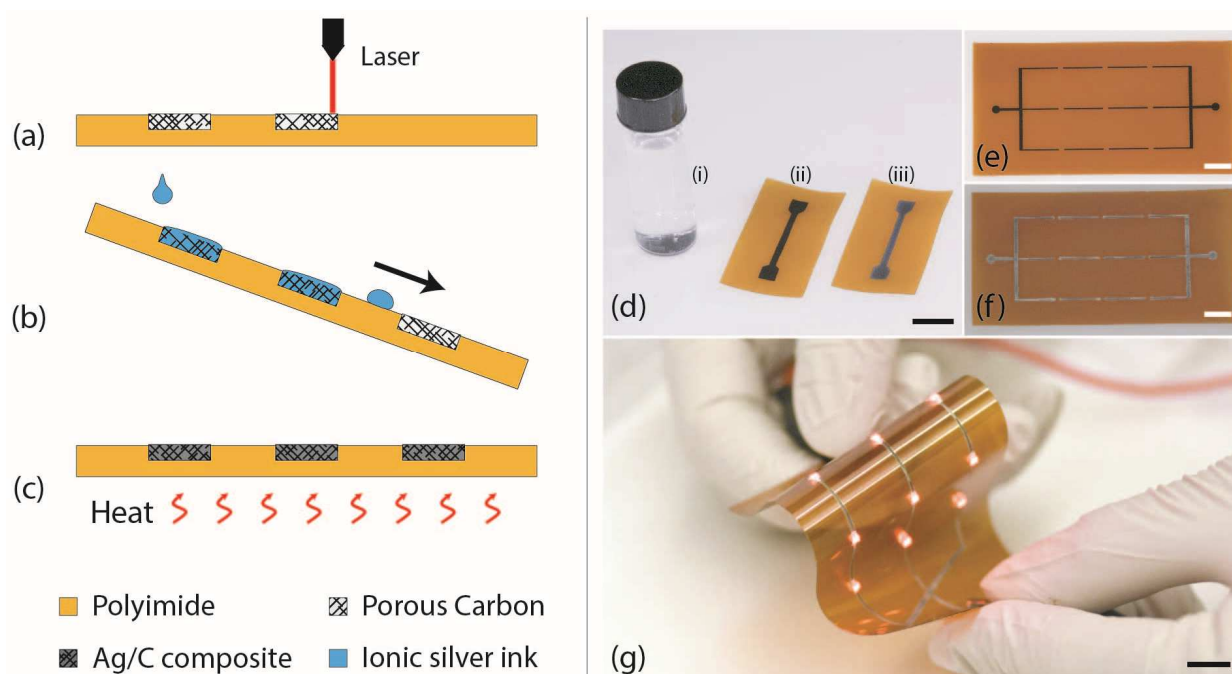


Figure 3.5. (a-c) Fabrication process of carbon/silver nanocomposite using laser pyrolyzation and selective aqueous silver ionic solution trapping; (d) laser carbonized traces before and after decorating with silver nanoparticles: (i) silver ionic solution, (ii) pristine carbonized trace, (iii) carbon/silver nanocomposite; flexible laser carbonized traces (e) before and (f) after decorating with silver nanoparticles; (g) array of lit LEDs with flexible interconnect. All scale bars: 1 cm

Figure 3.5(d-f) shows examples of different carbon patterns before and after coating with silver nanoparticles. Figure 3.5g shows a simple circuit lighting a  $3 \times 3$  array of LEDs using highly conductive Ag/C traces. The flexible substrate and LEDs can withstand mechanical bending and twisting while retaining the same illumination intensity.

### 3.2.2 Results and Discussion

Optical and SEM images were used to evaluate the morphology of laser carbonized microstructures before and after silver deposition, Figure 3.6. Microscopic images show a clear change in the color from black to silver after the selective silver coating, Figure 3.6(a, b). The SEM images show the creation of a highly-porous network of carbon micro/nano structures generated by laser carbonization of the polyimide substrate, Figure 3.6(c, d). The alignment of the carbon network is due to the scanning motion of the laser across the sample. Figure 3.6(e) is the top SEM image of the carbon trace after the precipitation of silver. High magnification SEM images illustrate the deposition of highly conductive silver nanoparticles on the porous carbon network, Figure 3.6(f). This is due to the low viscosity of the silver ionic solution and the strong capillary force of the carbonized traces, resulting in an easy percolation of the solution into the carbon network.

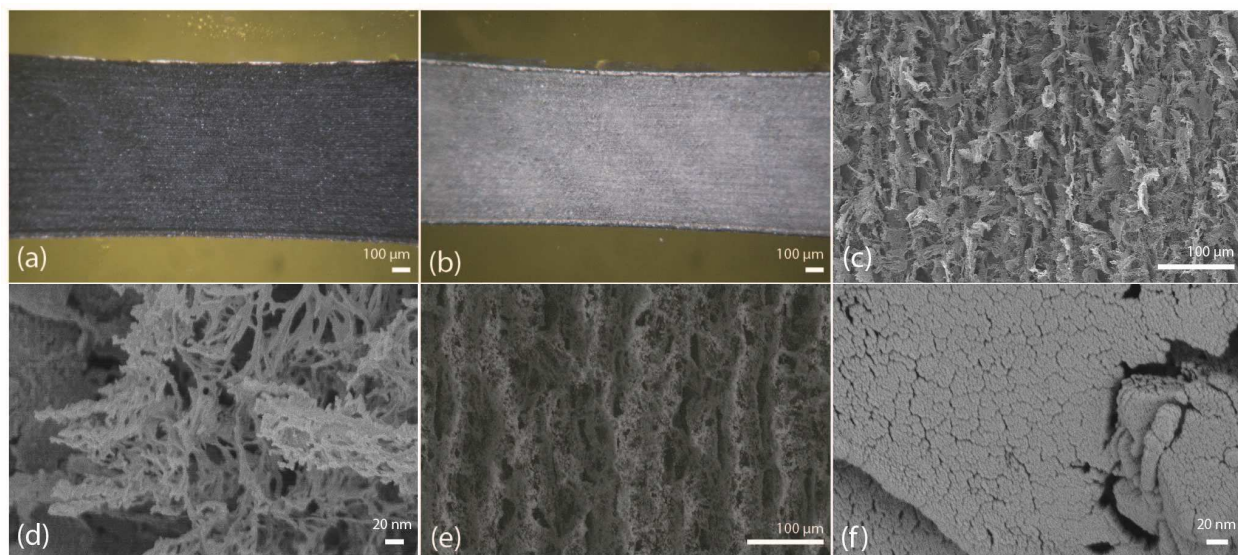


Figure 3.6. Magnified optical image of (a) laser carbonized polyimide and (b) carbon-silver nanocomposite SEM image of (c, d) laser carbonized polyimide and (e, f) carbon-silver nanocomposite.

In order to confirm the presence of silver and carbon in the conductive composite, material analysis was carried out by XRD and EDS measurements, Figure 3.7. Figure 3.7(a), shows the XRD pattern of the carbonized polyimide before and after silver coating. The broad diffraction peaks at  $26^\circ$  and  $43^\circ$  observed before and after silver coating can be attributed to the (002) and (100) crystal planes of graphitic carbon, which is assigned to the presence of low-degree-of-

graphitization and amorphous carbon [99], [100]. This was also confirmed by EDS measurements, which was performed before and after the laser carbonization of polyimide. The five distinct peaks observed after the ionic silver coating clearly reveal the formation of silver and the crystalline nature of the nanocomposite. The  $2\theta$  peaks obtained at  $38.1^\circ$ ,  $44.1^\circ$ ,  $64.4^\circ$ ,  $77.4^\circ$  and  $81.5^\circ$  correspond to the (111), (200), (220), (311) and (222) reflections of crystalline planes of the face-centered structure of silver [101], [102]. The quantitative presence of silver and carbon in the laser-carbonized composite before and after coating was further confirmed with EDS analysis, Figure 3.7(b, c).

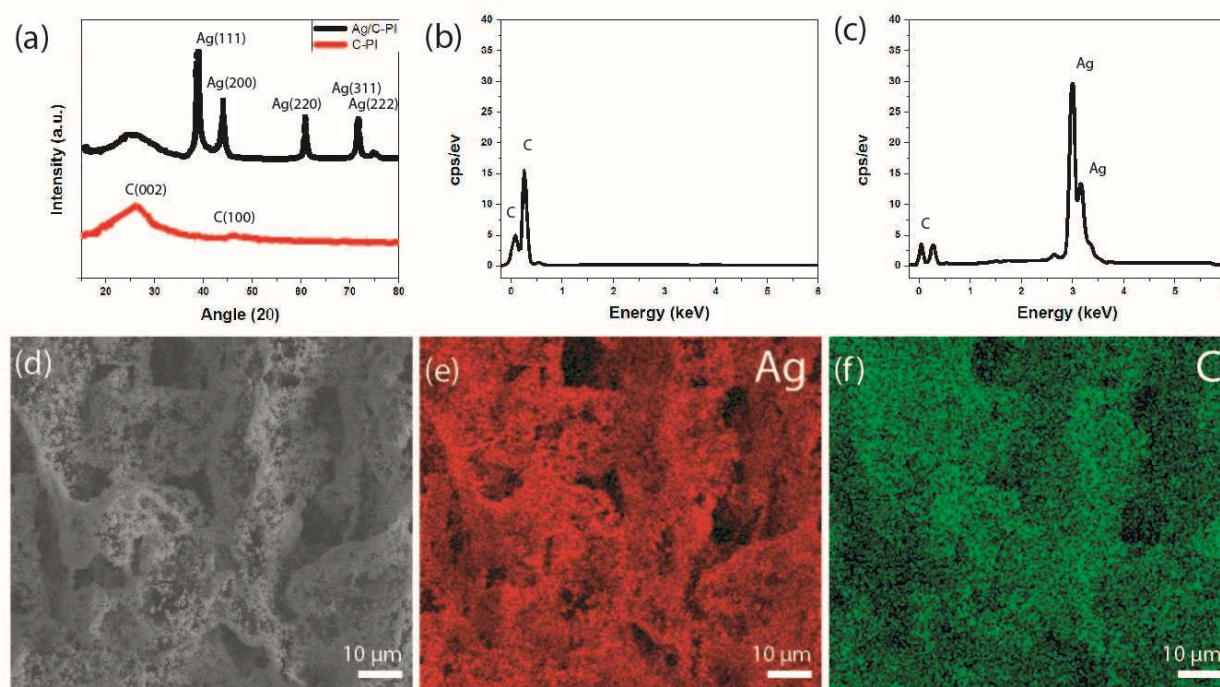


Figure 3.7. (a) XRD pattern of carbonized polyimide and carbon-silver composite, (b, c) EDS spectra of the nanocomposite, (d) high magnification SEM of carbon-silver composite, (e, f), EDS color mapping of silver (red) and carbon (green).

The EDS spectra of the pristine carbonized polyimide shows a binding energy of 0.25 keV corresponding to carbon, whereas the EDS spectra of the carbon-silver nanocomposite shows the addition of strong peaks at 3.0, 3.2 and 3.4 keV which correspond to the presence of the silver in the composite material. The percentage of carbon and silver in the composite is 17.41 % and

82.59 %, respectively. To investigate the distribution of the elemental silver throughout the composite, the samples were further studied by EDS element mapping. The red and green colored areas shown in Figure 3.7(d-f) correspond to the existence of silver and carbon elements in the material. The uniform distribution of the red dots shows the homogenous deposition of silver on the surface of carbon network.

Figure 3.8(a) shows the sheet resistance of the pristine carbonized polyimide and carbon-silver nanocomposite as a function of the annealing temperatures for samples of 3 cm length and 500  $\mu\text{m}$  width (annealing time was fixed at 10 min). The pristine carbonized polyimide exhibits the maximum sheet resistance of 52  $\Omega/\text{sq}$ , which is consistent with previous laser carbonization reports[59], [96]. As anticipated, the resistance of the silver-coated carbon traces decreases with increasing annealing temperatures. After drying the Ag/C nanocomposite at room temperature, the sheet resistance decreases slightly to 40  $\Omega/\text{sq}$ . Increasing the annealing temperature up to 90  $^{\circ}\text{C}$  improves the conductivity with the sheet resistance decreasing to 0.02  $\Omega/\text{sq}$ . After 90  $^{\circ}\text{C}$ , the effect of annealing on the conductivity was not significant (reactive silver ink is completely converted to bulk silver at 90  $^{\circ}\text{C}$ ). Figure 3.8(b), shows the change in the resistance of laser carbonized traces before and after silver coating as a function of traces widths ranging from 200  $\mu\text{m}$  to 2 mm at fixed annealing temperatures and times of 90  $^{\circ}\text{C}$  and 10 min. As can be seen, the composites traces show a resistance approximately three orders of magnitude lower than that of the pristine carbonized polyimide traces.

To assess the mechanical stability of the conductive traces upon bending, samples with different widths ranging between 200  $\mu\text{m}$  to 2 mm were subjected to flexion at curvature radii (CR) of 50 mm to 2 mm. The mechanical stability of the conductive composite was characterized with samples undergone the optimal annealing temperature of 90  $^{\circ}\text{C}$ . Figure 3.8(c) shows the change in the carbonized polyimide resistance as a function of CR. As can be seen, for small traces (200  $\mu\text{m}$ ), the change in a resistance starts at 30 mm CR with a relatively linear sensitivity coefficient of 0.35 ( $R/R_0$ ) per degree radius of curvature. However, with increasing width, the starting threshold decreases. For instance carbon traces of 2 mm width exhibit a resistance change starting at 10 mm of CR with a sensitivity of 0.04 ( $R/R_0$ ) per degree radius of curvature. This observation can be explained by the fact that the electrical conductivity between the two ends is provided by the connection between carbon particles throughout the material. Mechanical deformation separates the connection points in the material, resulting in an increase in resistance, Figure 3.8(d). However,

wider carbonized traces have abundant connecting points throughout their wide carbon network, and are less likely to be disconnected with mechanical deformation.

In addition to a significantly lower resistance, the carbon-silver nanocomposite shows greater robustness and lower sensitivity to mechanical deformation, Figure 3.8(e). For instance, after silver coating, a 200  $\mu\text{m}$ -wide trace with an initial resistance of 7.5  $\Omega$  shows less than 33 % change in response to CR as small as 2 mm; this translates to an 8.7 folds decrease in sensitivity to mechanical deformation as compared to a similar carbonized polyimide trace. Furthermore, for traces wider than 400  $\mu\text{m}$  carbon-silver nanocomposites have a high level of conductivity, with resistance smaller than 3  $\Omega$  and less than 9 % change in resistance at the maximum bending angles. This extreme level of conductivity and mechanical stability can be explained by the highly conductive Ag nanoparticles distributed throughout the carbon backbone structure. This structure provides multiple parallel electrical connections between particles, compensating for the change in the resistance of carbonized polyimide at high mechanical deformations, Figure 3.8d. Although Ag/C-P composite traces with short widths have much less sensitivity to mechanical defatation they are still composed of a sparse number of connections in the conductive carbon backbone network and can be disconnected at high levels of bending. In contrast, wider Ag/C-P composite can easily endure high degrees of mechanical bending with negligible change in the resistance due to the high degree of electrical pathways between the AgNP and carbon particles.

For flexible electronic applications, it is essential to maintain the electrical connections after multiple cycles of bending and mechanical deformations. In order to assess the robustness/reliability of the nanocomposite, the traces were subjected to multiple mechanical bending cycles, Figure 3.8(f). The response to mechanical bending cycles at 5 mm of CR was compared between carbonized polyimide and carbon-silver nanocomposites of 0.6 mm width. The resistance of the traces was continuously recorded during the cyclic test. As shown in Figure f, the pristine C-PI has an initial resistance of 2.5 k $\Omega$  with a sinusoidal variation in resistance with a peak-to-peak amplitude of approximately 2 k $\Omega$  (with a relative change of 80%) through a full bending cycle (from 0° to 180°). The maximum change in resistance occurs at the maximum bending angle (180°) and reduces by removing the applied flexure (return to 0°), this change in resistance is explained by the disconnections of the carbon macro/nano particles with bending. In addition to the high sensitivity of the C-PI to mechanical bending, the carbonized polyimide exhibits a large drift of 350  $\Omega$  (~14% of initial 2.5 k $\Omega$ ) after 15000 cycles. However, the carbon-

silver nanocomposite shows significant retention of its initial conductivity ( $3 \Omega$ ) after 15000 bending cycles with negligible drift. The Ag/C-PI shows less than  $0.6 \Omega$  ( $\sim 20\%$  of initial  $3 \Omega$ ) variation in resistance through a complete bending cycle after 15000 bending cycles. The relative change of resistance ( $R/R_0$ ) of C-PI and Ag/C-PI.

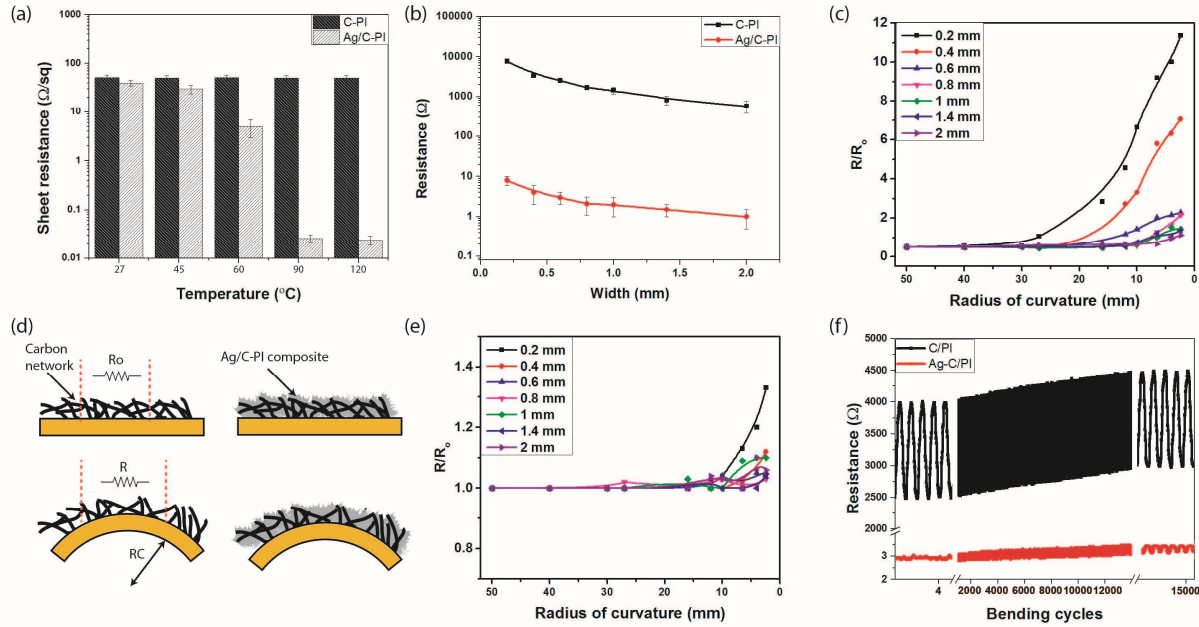


Figure 3.8. (a) Electrical sheet resistance of carbon-silver composite after annealing at different temperatures, (b) carbonized polyimide and carbon-silver nanocomposite resistances as a function of line width, (c) change in the carbonized polyimide resistance of various trace widths ranging from 0.2 mm to 2 mm as a function of radii of curvature, (d) schematic for the behavior of carbonized polyimide and carbon-silver nanocomposite under mechanical flexion, (e) change in the resistance of carbon-silver nanocomposite of various trace widths ranging from 0.2 mm to 2 mm as a function of radii of curvature, (f) resistances of carbonized polyimide and carbon-silver nanocomposite as a function bending cycles of  $180^{\circ}$  at 5 mm of curvature radius, with breaks at the first five and last five cyclic.

### 3.3 Stretchable carbon–polyaniline composite

Among various conductive particles, carbon-based nanostructures (e.g., CNT, graphene) are excellent candidates for use in conductive composites due to their unique properties such as high carrier mobility (conductivity), thermal stability, chemical inertness, large surface area, and ease

of functionalization[103]–[106]. Hence, carbon-based nanomaterials have been used in various stretchable devices including batteries, supercapacitors, speakers, and motion sensors[107]–[109]. Although carbon-based conductive inks and composites have shown promising results for fabrication of stretchable electronics, they are still limited by their printing challenges (optimal ink preparation). In addition, costly and complicated synthesis process of CNT and graphene nanoparticles also can potentially increase the fabrication cost of the targeted device[83]. The applications of carbon-based stretchable electronics would be greatly expanded if the conductive nanoparticles could be fabricated with precise patterning and integration into the elastic material using a facile and low cost process. A simple alternative approach to the synthesis of carbon-based micro/nano materials is pyrolyzation of thermoset polymers using a photo-thermal process with laser irradiation[60], [110]–[112]. These porous carbon-based materials can be easily converted to functional composites by impregnating the pores with organic and inorganic materials that are sensitive to different stimuli/parameters. Such simple functionalized/conductive nano-composites can potentially be used in the development of new low-cost/scalable sensors for wearable and other applications. In this section we investigate the functionalization of laser carbonized polyimide traces with polyaniline (PANI) and its potential use for stretchable electronic devices. In section 5.2 we will demonstrate the utilization of this technology in wearable pH-sensitive electrodes for wound monitoring applications.

### 3.3.1 Fabrication process

The fabrication process is illustrated in Figure 3.9 (a-f). The process begins by placing a thin film of silanized PI on a plasma treated Ecoflex. The 1 mm thick elastic substrate (Ecoflex) was prepared by mixing the Ecoflex pre-polymer at 1:1 ratio and curing at room temperature for 3 hours. The PI sheet surfaces were first cleaned with de-ionized (DI) water followed by isopropyl alcohol (IPA). Next, the APTES silanization process was used for irreversible bonding between the elastic substrate and PI (see supplementary material for detailed description). In this process, the PI sheet was treated with air plasma for 1 min followed by immersion in a 5 % APTES aqueous solution for 5 min. During the immersion process, the solution was placed on a hot plate set to 80 °C. Next, the PI was removed from the solution and rinsed with DI water and dried with nitrogen gun. The surface of the silicone and silanized PI were activated by 1 min and 10 s air plasma treatment, followed by immediately bring them into contact. Using a CO<sub>2</sub> laser engraver

at the optimal setting (6.75 W power,  $1.3 \text{ ms}^{-1}$  speed) that was previously reported by our group, highly porous conductive carbon patterns were directly pyrolyzed onto the polyimide side of the film. To enhance the mechanical stability and confer pH sensitivity to the electrodes, the porous carbon was coated with PANI. The coating was achieved by spraying a mist of PANI EB (polyaniline emeraldine base) dissolved in dimethyl sulfoxide (DMSO) onto the porous carbon traces, forming a PANI and carbon composite (PANI/C-PI).

The PANI EB solution was prepared by dissolving 100 mg of PANI emeraldine base (Sigma Aldrich,  $M_w \sim 50,000$ ) in 5 mL of DMSO and sonicating for 2 h. To remove any undissolved polymer and prevent clogging of the spray nozzle, the sonicated solution was maintained undisturbed for 1 hour and filtered through a syringe filter with pore size of  $0.2 \mu\text{m}$  (Whatman Filters, Anotop 25) prior to being sprayed onto the carbonized traces. PANI was chosen because of its biocompatibility, good electrical conductivity, and stability in different electrolytes. The reversible protonation and deprotonation of PANI in acid/base condition makes it an ideal material for pH sensors. After the PANI coating process, the extra PI was removed by laser cutting/machining the peripheral of the serpentine traces using the same laser machine at higher power level (15 W power,  $1.4 \text{ ms}^{-1}$  speed). The extra PI was removed and the device was annealed at  $80^\circ\text{C}$  for 30 min, for an irreversible strong Si-O-Si covalent bonds between the PI backing of the stretchable PANI/C-PI electrodes and Ecoflex substrate.

The PANI EB was converted to polyaniline emeraldine salt (PANI ES) by immersing the carbon traces into an acidic solution (1 M HCl) solution for 15 min. PANI ES has a higher conductivity than PANI EB which improves the conductivity and stability of the serpentine composite to applied stress. The electrodes were then washed with DI water and dried in room temperature. Next, a thin passivation layer of diluted Ecoflex was casted onto the PANI/C-PI interconnection traces leaving the contact pads and sensing areas exposed. To enhance the diffusion of the pre-polymer into the porous PANI/C-PI patterns, the Ecoflex pre-polymer was diluted with 10 wt% n-heptane. The insulating Ecoflex layer firmly and uniformly adheres onto the porous and rough PANI/C-PI composite and Ecoflex substrate. As shown in Figure 3.9 (g, h), the described technology can be used to fabricate different stretchable patterns such as zigzag, sinusoidal, and serpentine traces with various widths.

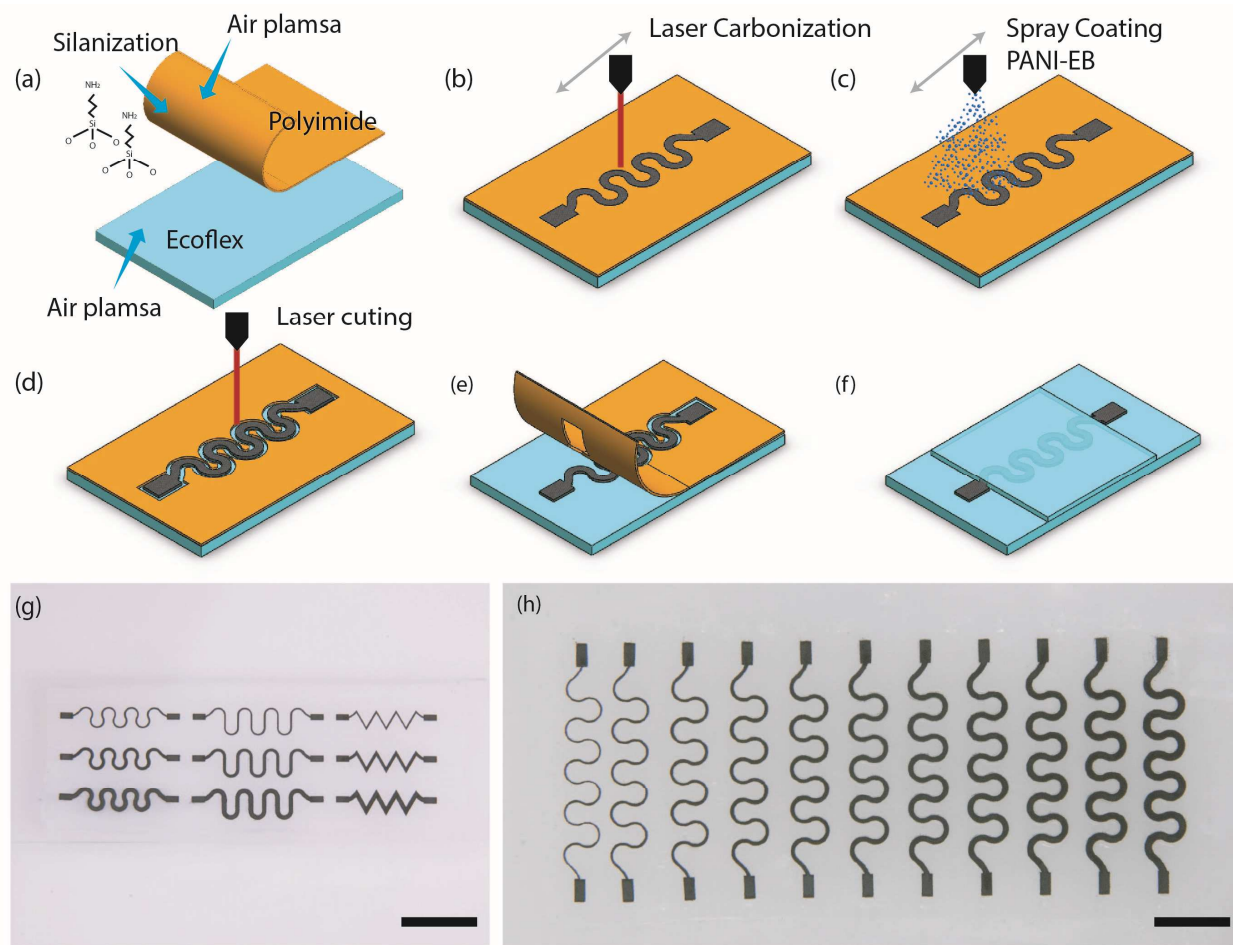


Figure 3.9. Schematic illustrations of the fabrication process and photographic images stretchable carbon–polyaniline composite interconnections: (a) polyimide sheet is silanized and placed on an air-plasma-treated Ecoflex substrate, (b) a CO<sub>2</sub> laser is used to carbonize serpentine carbon traces on the polyimide sheet, (c) polyaniline is spray-coated onto the porous carbon, (d) the polyimide sheet is machined with the same CO<sub>2</sub> laser at a higher power level, (e) excess polyimide is removed, (f) interconnects are insulated by another Ecoflex layer, (g) photograph of various stretchable PANI/C–PI interconnect designs, and (h) different trace widths. Scale bar in all images is 1 cm.

### 3.3.2 Results and discussion

Figure 3.10 (a) shows a repetitive unit of the serpentine patterns with the structural design parameters of radius ( $r$ ), width ( $W$ ), and angle ( $\theta$ ). Structures with different widths were characterized while the radius and angle of the traces were kept constant at 1 mm and 120°, respectively. Photographs of two serpentine traces with the widths of 300  $\mu$ m and 1.2 mm are shown in Figure 3.10(a, b). Figure 3.10(c) shows the top scanning electron microscopy (SEM) image of single repetitive unit of the serpentine traces with the width of 300  $\mu$ m.

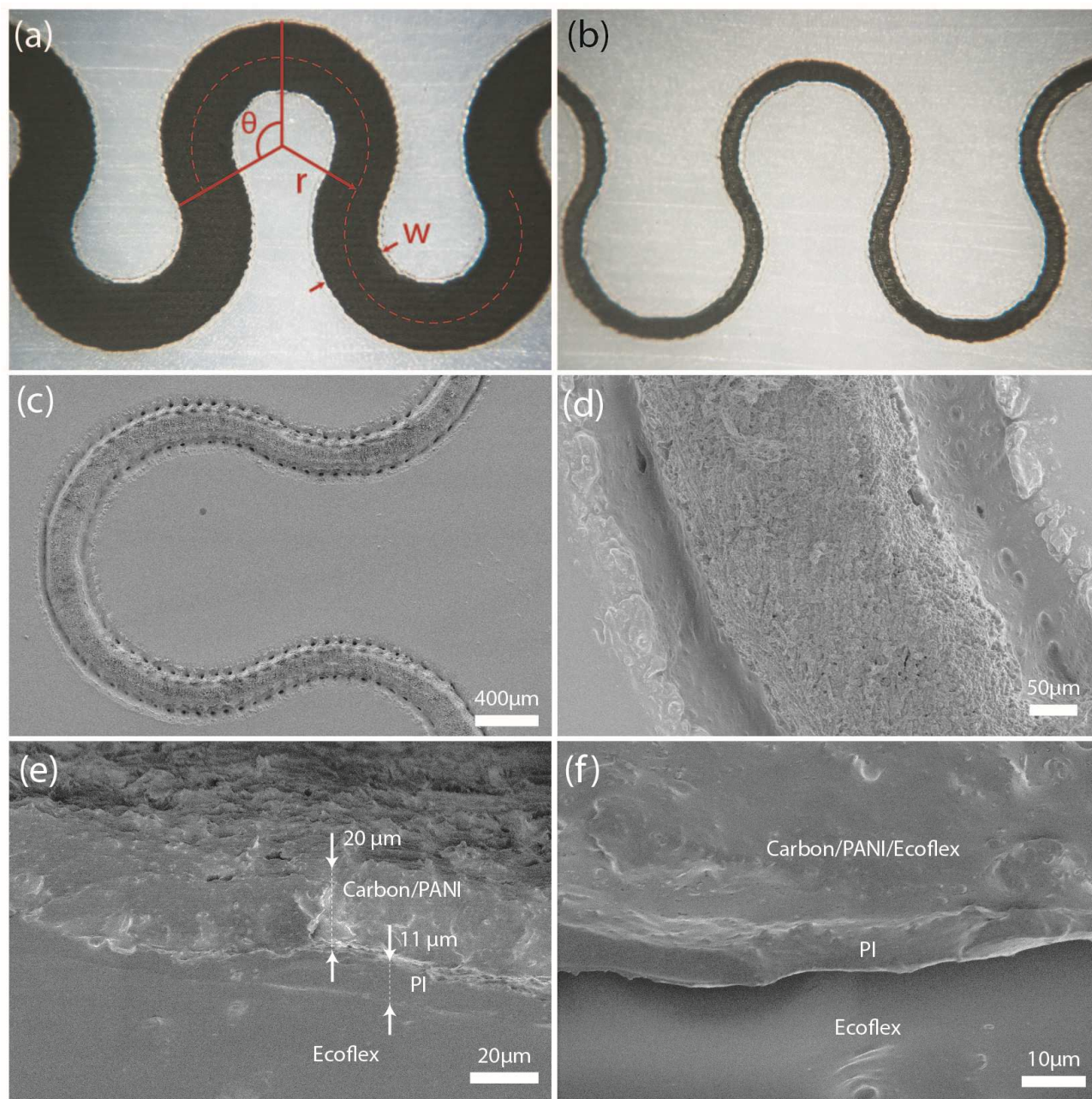


Figure 3.10. Optical and SEM images of stretchable PANI/C–PI serpentine interconnects with the design parameters of one repetitive serpentine unit. Top views of serpentine structures with the widths of (a) 1.2 mm and (b) 0.3 mm. SEM top view of a single repetitive unit with 0.3 mm width at (c) low and (d) high magnification. Side view SEM image of PANI/C–PI composite structure and polyimide film (e) before and (f) after encapsulation with Ecoflex.

Figure 3.10 (d) shows a magnified SEM image of the PANI/C-PI composite, illustrating the porous nature of the material (the 60  $\mu\text{m}$  trench visible around the perimeter of the carbonized traces is formed during the final cut through the PI sheet). This feature allows the liquid prepolymer of the insulating Ecoflex layer to penetrate into the material and form a strong mechanical bond. Figure 3.10(e, f) show the cross section SEM image of the patterns before and after encapsulating into the Ecoflex elastomer. Cross-section SEM images of fully encapsulated patterns show the diffusion of the top Ecoflex layer into the void spacing on the rough surface of PANI/C-PI composite electrode, Figure 3.10(f). The thickness of the PANI/C-PI composite and the remaining PI material are 20  $\mu\text{m}$  and 11  $\mu\text{m}$ , respectively. It should be noted that laser heating the PI film will cause explosive phase change in the PI material, which results in an increase in the total thickness of the material from 25  $\mu\text{m}$  to 31  $\mu\text{m}$  after carbonization. The SEM images clearly shows that no interfacial void is observed at the bonding interface between the PI and Ecoflex substrate.

Raman analysis at an excitation wavelength of 633 nm was used for further surface analysis of the laser carbonized PI before (Figure 3.11(a)) and after PANI deposition (Figure 3.11(b)). The laser carbonized polyimide (C-PI) spectra shows the three apparent 2D, D and G characteristic peaks attributed to graphitic materials with structure-derived G band and defect-derived D-band visible around 1590  $\text{cm}^{-1}$  and 1350  $\text{cm}^{-1}$ , respectively. The ratio intensity of the D and G band ( $I_D/I_G$ ) represents a measure of crystallinity or defect in the carbon material[113]. The 2D band observed at 2800  $\text{cm}^{-1}$  arises because of second-order zone boundary phonons. The ratio of G and 2D band intensity ( $I_G/I_{2D}$ ) is related to the number of layer of graphene in the material; a smaller ratio indicates an increased number of graphene layers[99], [114]. The pristine laser C-PI has  $I_D/I_G$  and  $I_G/I_{2D}$  ratio of 0.6 and 1, which indicates a multilayer graphene with good level of crystallinity. Compared to the pristine laser carbonized PI, the Raman spectrum of PANI and PANI/C-PI composite shows apparent new smaller peaks in the lower wave number regions with different intensities at 1167, 1350 and 1470  $\text{cm}^{-1}$ . These bands are ascribed to C–H bending, C–N<sup>+</sup> stretching, and C=N stretching vibration in PANI[115]. The Raman spectra confirms the deposition of PANI into the hybrid PANI/C-PI composite.

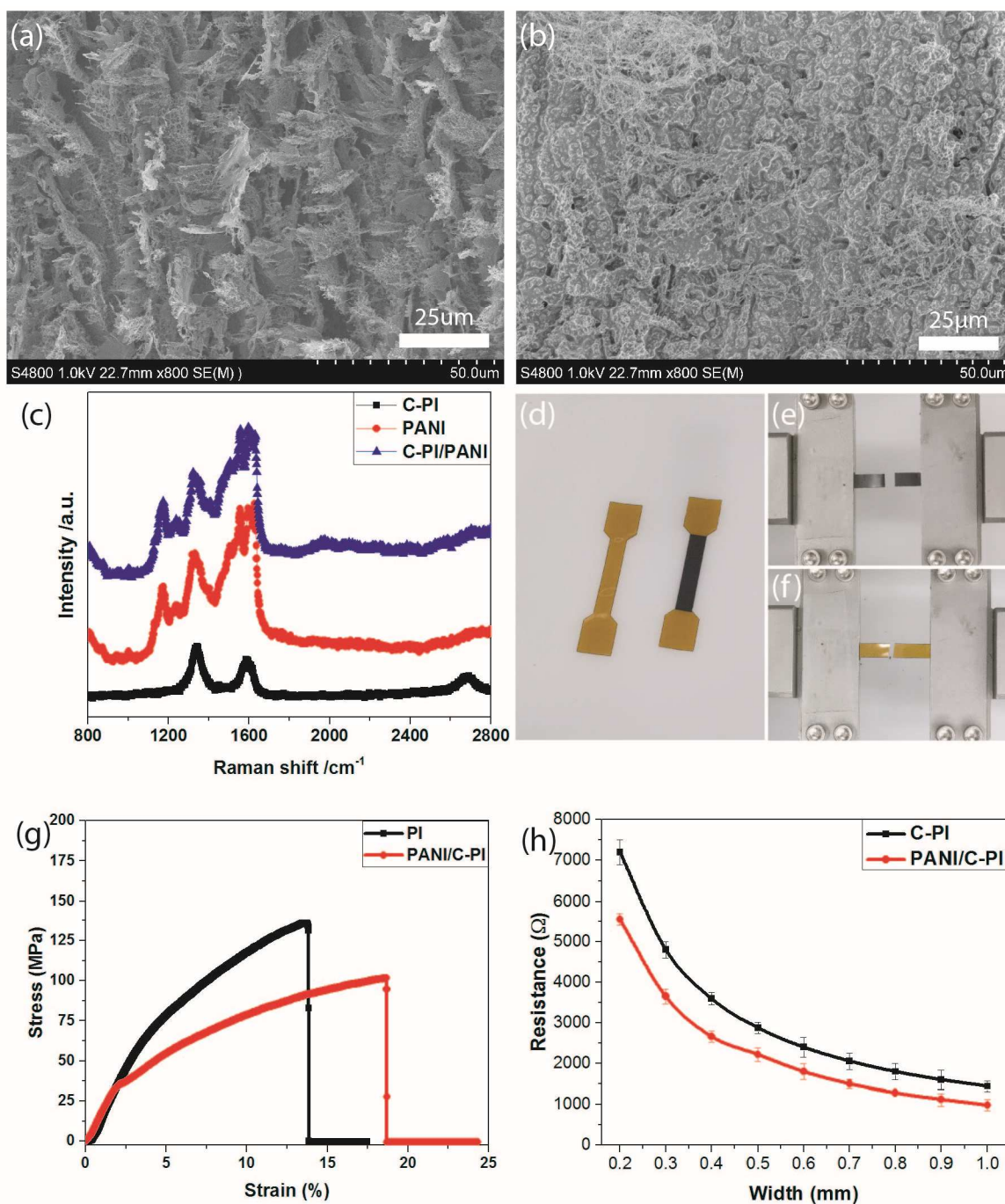


Figure 3.11. Top view SEM image of (a) pristine porous laser-carbonized polyimide and (b) PANI/C-Pi composite. (c) Raman spectra of pristine porous carbon, PANI, and PANI/C-Pi. (d-f) Optical image of  $5 \times 25$  mm PI and PANI/C-Pi samples used for tensile testing. (g) Comparison of the tensile stress-strain curve of PI and PANI/C-Pi. (h) Variation of resistance with line width before and after PANI deposition.

The mechanical properties of the PANI/C-PI and pristine PI film were measured from the stress-strain curve. The test samples ( $5\text{ mm} \times 25\text{ mm}$ ) were stretched to their breaking limit at a speed of  $50\text{ mm/min}$ , Figure 3.11(d-f). Using the results of the stress-strain curves presented in Figure 3.11(g), the modulus of elasticity ( $E$ ) and tensile strength of the pristine PI film is estimated to be  $1\text{ GPa}$  and  $135\text{ MPa}$ , respectively. It can be seen that the PANI/C-PI composite simultaneously exhibits a decrease in modulus of elasticity ( $650\text{ MPa}$ ) and tensile strength ( $105\text{ MPa}$ ). Moreover, the PANI/C-PI composite showed a  $34\%$  increase in elasticity before breaking. The electrical conductivity of PANI/C-PI composite was evaluated as a function of trace width before and after the deposition of the PANI filler, Figure 3.11(h). The plot shows a resistivity of  $0.096\ \Omega\cdot\text{cm}$  for the C-PI structures, which is close to previously reported values [116]. The PANI/C-PI composite after the protonation process of the PANI has an approximately  $32\%$  lower resistivity ( $0.065\ \Omega\cdot\text{cm}$ ) as compared to the pristine C-PI. The electrical characterization further confirm the contribution of the PANI filler to the binding and enhancement of the electrical properties of the PANI/C-PI composite.

The trace width is an important parameter that can strongly affect the performance of the stretchable interconnects. In order to assess the sensitivity of different laser carbonized traces to applied strain, we fabricated a range of serpentine interconnects with widths ranging from  $200\ \mu\text{m}$  to  $1.2\text{ mm}$  and fixed radius ( $1\text{ mm}$ ) and angle ( $30^\circ$ ). Figure 3.12(a) shows a sequence of *in situ* elongations from  $0$  up to  $120\%$  for serpentine interconnect samples with  $0.3$  and  $1\text{ mm}$  widths. The applied strain results in periodic out-of-plane deformation at the crest of the serpentine interconnects (more prominent for wider traces), resulting in higher stress and failure at smaller levels of strains ( $< 50\%$ ). However, the  $0.3\text{ mm}$  wide trace can tolerate extreme elongations ( $120\%$ ) with smaller out-of-plane deformation while still remaining conductive. Using a two-point probe measurement, the resistance of the various carbon traces was continuously recorded at different levels of strain. Figure 3.12(b) represents the relative change in resistance of each interconnection with applied uniaxial strain. The electrical resistance was continuously recorded until rupture. The sharp change in resistance represents the breaking point and disconnection in the trace. Wider traces such as  $1.2\text{ mm}$  showed a fast increase in resistance starting from  $15\%$  strain with a complete disconnection at  $52\%$  strain. However, traces with widths smaller than  $0.8\text{ mm}$  showed a near constant resistance for elongations up to  $65\%$  with gradual increase thereafter. This resistance change can be explained by the presence of micro-cracks in the

conductive PANI/C-PI composite that are initiated by the stress applied at crest of the serpentine patterns. These micro-cracks proliferate at higher strains and ultimately result in complete rupture in the composite.

Investigating the maximum stretchability of different interconnects showed that 300  $\mu\text{m}$  wide traces have the most stable electrical resistance for elongation up to  $\sim 100\%$  (ultimate elongation of 135 %). This is comparable to similar serpentine metallic traces created by micro-fabrication and photolithography[117]. Although narrower traces ( $\sim 200\ \mu\text{m}$ ) did have a slightly higher ultimate elongation before rupture ( $\sim 144\%$ ), it showed a higher sensitivity to the applied strain. This phenomenon can be explained by the limited amount of conductive (PANI/C-PI) material in the narrower traces, which results in its increased sensitivity to the micro-cracks propagation at crest points. Figure 3.12(c), summarizes the ultimate elongation and the stable electrical resistance region (with less than 20% change of its initial resistance) for different trace widths. Narrower traces ( $\sim 300\ \mu\text{m}$ ) had an ultimate elongation approximately 2.5 times that of the 1.2 mm traces. The observed longitudinal tensile measurements was also verified with COMSOL simulation. Figure 3.12(d) shows the stress distribution FEM simulation along different serpentine traces under 25 % elongation, assuming a Young's modulus and tensile strength of 650 MPa and 105 MPa, respectively. The values chosen for the simulation were the results obtained from the stress-strain curves in the material characterization section. As expected, the applied strain results in a non-uniform stress distribution across the length of the serpentine traces with concentration at every crest along the traces. The simulation results further confirm the presence of higher stress in traces with wider widths, making them more likely to exceed the tensile strength of the PANI/C-PI at higher levels of strain. Figure 3.12(e), shows the simulation results of the maximum stress at the crest point of different traces with strain levels up to 150 %. The plot shows an approximately linear increase in stress for all traces with the lowest and highest sensitivity for traces with widths of 300  $\mu\text{m}$  and 1200  $\mu\text{m}$ , respectively. The dashed line indicates the tensile strength (105 MPa) of the PANI/C-PI material. Tensile stresses that exceed this threshold will result in micro-crack formation and propagation in the conductive material. The simulation results for traces with width of 300  $\mu\text{m}$ , 600  $\mu\text{m}$ , 800  $\mu\text{m}$ , and 1200  $\mu\text{m}$  predicts micro-crack propagation and increased resistance at strain levels of 120 %, 80 %, 65 %, and 25 %, in good agreement with the experimental results.

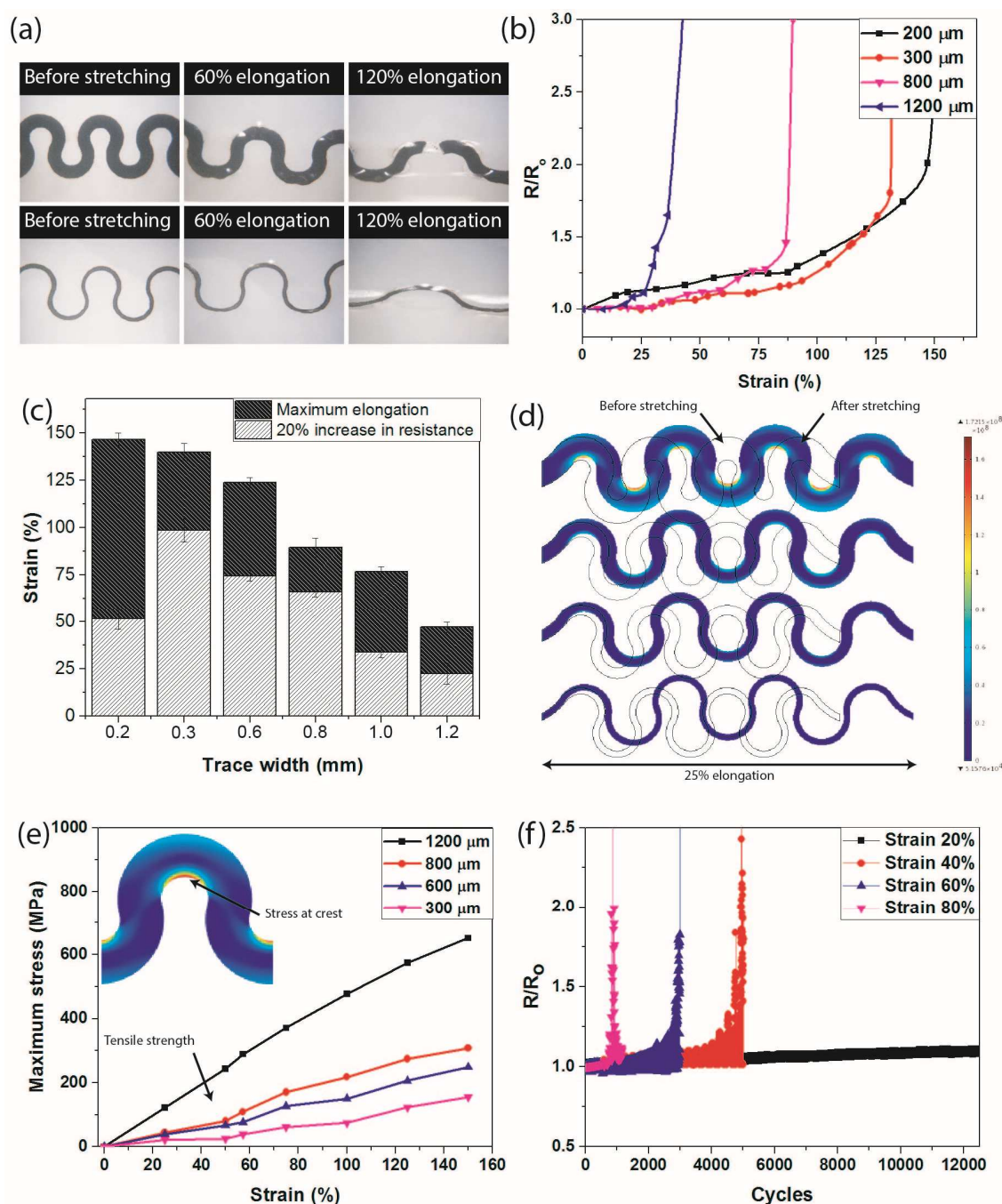


Figure 3.12. (a) Optical images of serpentine traces with 0.3 and 1 mm width at 0%, 60%, and 120% elongation. (b) Relative change in electrical resistance of serpentine PANI/C-PI composites with difference widths as a function of strain. (c) Maximum elongation with less than 20% change in resistance versus trace width. (d) COMSOL simulation for displacement and stress distribution on serpentine traces with 0.3, 0.6, 0.8, and 1.2 mm width at 25% elongation; the stress concentration is in the crest of the serpentine interconnects. (e) Simulation results of maximum stress at the crest points of serpentine traces with different widths at various levels of strain. (f) Relative change in resistance of a 0.3-mm-wide serpentine trace versus the number of stretching cycles for 20%–80% elongation.

The reliability of the serpentine traces with 300  $\mu\text{m}$  width was measured over 12,000 stretch cycles under various tensile strains (from 20 % to 80 %). Figure 3.12(f) shows the normalized resistance under various strain cycles. Results show that the 300  $\mu\text{m}$  PANI/C-PI serpentine trace could be stretched at 20 % strain over 12,000 cycles, without a notable change in the resistance. This level of stretchability and durability is comparable to several reported stretchable thin film metals, and conductive composites including metal NWs, CNT and graphene[117]–[121]. Interconnects that were subject to higher strain levels of 80 %, 60 % and 40 % withstood strain cycles above 1000, 3000, and 5000, receptively.

## 4. LASER ABLATION OF MULTILAYER POLYMERIC FILMS

Among different rapid fabrication technologies, laser machining offers a unique set of capabilities directly beneficial for the development of flexible/stretchable low-cost systems. Laser machining provides the ability to cut materials, etch (ablate) them, alter their surface morphology, without the generating high volumes hazardous chemical wastes that are often associated with photolithography processes. For example, laser can be used to tune the hydrophilicity of hydrophobic films such as wax and parchment paper, or it can be used for selective material removal from a multilayer substrates. Furthermore, the availability of commercial, reliable, and precise laser systems allows them to become part of large-scale (e.g., roll-to-roll) production lines. This chapter highlights the utility of CO<sub>2</sub> and Nd:YAG of laser systems in selective ablating and surface treating of commercial multilayer films including parchment paper, ITO-coated PET films and metalized papers.

### 4.1 Laser ablating hydrophobic paper

Paper is an attractive substrate for cell culture applications due to its naturally biocompatible 3D cellulose fiber composition and its webbed architecture for efficient cell attachment[122], [123]. However, the inherent hydrophilic nature and low mechanical strength, when moistened, prevents its prolonged use in aqueous environments[124]. Nevertheless, impregnating the paper with hydrophobic materials (e.g., wax, silicone) can resolve some of the abovementioned shortcomings (i.e., improve mechanical strength in aqueous environments) [125]. Such hydrophobic films (e.g., wax and PDMS), printed using inkjet or screen printing, form water-repelling barriers on paper substrates; these patterns create hydrophobic-hydrophilic structures which can replace existing cell culture plates. For example, wax printing was used by Whitesides group to generate a 3D, multilayer, paper-based assay for monitoring molecular and genetic response of different cells to oxygen and nutrition gradients[126]. Wang et al. reported the use of PDMS-stamped multi-wells on paper as biomaterial scaffold for direct differentiation of human induced pluripotent stem cells (iPSCs) into functional beating cardiac tissues[127]. However, among different types of commercially available papers, parchment paper offers several great advantages including wet and dry mechanical strength, high gas permeability, laser-process ability, and bio-compatibility

making it suitability substrate for different biomedical applications. This section demonstrates the key features of this paper before and after laser modification with a comparison to other common hydrophobic papers.

#### 4.1.1 Materials and method

Characterization were performed on several common hydrophobic papers and films in terms of their change in surface properties after laser treatment, wet strength (standard tensile strain tests as a function of wetting duration), and nutrition/gas permeability. These films were parchment paper (PP), wax paper (WP), filter paper (FP), PDMS, and a paper-PDMS (P/PDMS) composite prepared by placing a sheet of filter paper on a thin layer (50  $\mu\text{m}$ ) of PDMS pre-polymer spin-coated onto a silanized silicon wafer and cured at 80°C for 30 min. The performance of the papers were compared with the commercial polyethylene terephthalate (PET) transwell ALI culture membranes with 0.4  $\mu\text{m}$  pore size (Corning®). The micro structural properties of the papers were compared by SEM imaging, Figure 4.1. Previous studies have shown that the change in surface wettability with plasma and laser treatment often affects cell growth on different substrates. This method has been widely studied with different cells on various materials such as silk and polymers[128]–[130]. Therefore, as the first step, the surface properties of the films were characterized before and after laser treatment (at 10 W power with a scanning speed of 35 mm/s). The adjusted laser parameters were sufficient to change the surface properties of the films without completely cutting through the material. The surface wettability of samples were evaluated by measuring the static contact angle of a 10  $\mu\text{l}$  droplet of DI water before and after laser treatment using an optical contact angle measuring device (Rame-Hart goniometer, model 590). All experiments were conducted five times and the mean contact angle was calculated. High magnification surface and cross-sectional scanning electron microscopy (SEM) images were also obtained to assess the change in surface morphology before and after laser ablation. A standard tensile stress-strain test was used to characterize how well the fibers in different hydrophobic papers hold together when the paper is wetted/soaked for various times. In this test, the papers were submerged in buffer saline solution (PBS) for several durations (0-7 days), and the ultimate tensile strength (UTS) and Young's modulus were subsequently measured using a universal testing machine (Admet®, model eXpert 1000). All specimens were laser cut to the same dimensions

(5 mm × 20 mm). The tensile strength measurements were performed by fixing the two ends of the film and stretching from 0 % to 12 % strain at a constant extension velocity of 10 mm/min.

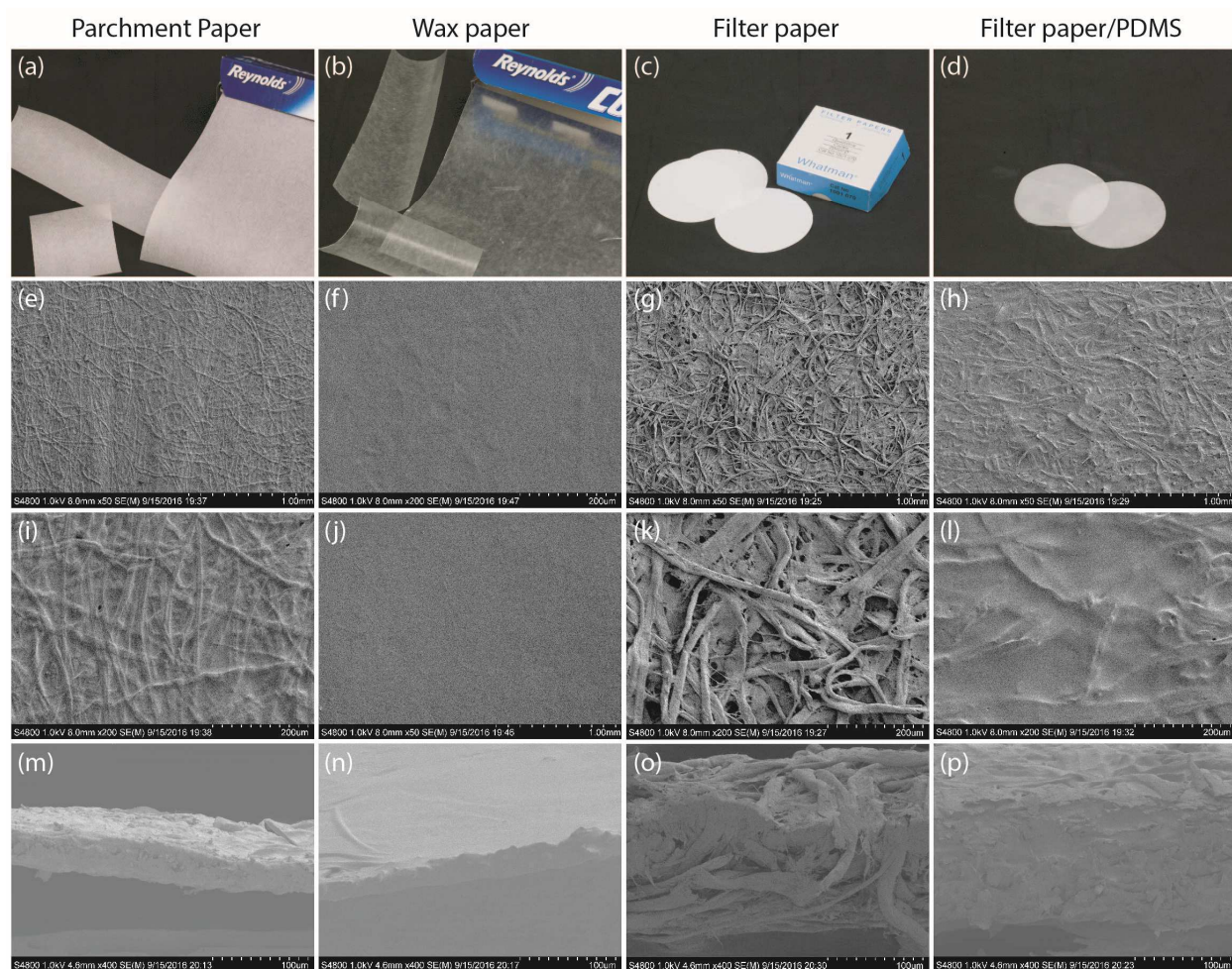


Figure 4.1. Basic structural characterization of different papers. (a-d) optical image of different papers: parchment paper, wax paper, filter paper, filter paper coated with PDMS, (e-l) low and high magnification SEM images of surface properties of different papers, (m-p) cross-sectional SEM image of different papers.

A customized setup was used to measure the gas permeability and oxygenation of the liquid medium through different films. The structure consisted of a cylindrical chamber filled with 20 mL of deoxygenated DI water and covered by 20 mm-diameter circular sample of the film. For all tests, the dissolved oxygen was removed by purging the water for 8 h with nitrogen gas. The oxygen permeability was confirmed with real-time measurements of the dissolved oxygen using

an optical oxygen sensor (NeoFox, Ocean Optics, Dunedin, FL) positioned in the DI water chamber. All measurements were performed at room temperature and atmospheric pressure. We evaluated the oxygen permeability of different membranes via the rate of dissolved oxygen increase in the water. The permeability of cell culture media through different substrates was assessed using a conductivity measurement setup. The setup consisted of two chambers filled with 20 mL of DI water and 20 mL of growth medium (Cell, P311-500) separated by the testing membrane. The conductivity of the chamber with DI water was measured using an LCR meter at 1 kHz (GW Instek LCR-819) for 24 h. For all measurements the initial conductivity of the DI water was close to zero ( $1.25 \times 10^{-6}$  S). The conductivity increased with time as a result of the diffusion of the ions from the medium to the DI water chamber.

## 4.1.2 Results and discussion

### 4.1.2.1 Surface wettability and morphology

The initial contact angle (CA) of the four surfaces (PP, WP, P/PDMS and PDMS) were measured to be 121°, 108°, 112°, and 94°, respectively. The P/PDMS and PDMS showed an increase in the contact angle following laser-treatment (to 115° and 126°, respectively). This increase can be explained by the Wenzel theory, which predicts a higher CA for water droplets on rough hydrophobic surfaces in contrast to homogeneous surfaces (both P/PDMS and PDMS become rougher after laser treatment) [131]. In contrast, the commercial PP and WP papers showed a significant decrease in CA to 21° and 39°, respectively, Figure 4.2(a,b). This increase in surface wettability is due to the creation of exposed micro/nano cellulose fibers and addition of hydrophilic –OH, =O groups on the laser-ablated areas[72]. Figure 4.2(c) shows a high magnification SEM image of selective laser-ablated parchment paper. The image show a clear change in morphology with exposed micro/nano fibers on the surface of the paper after laser treatment. The thickness of the paper was measured by cross-sectional SEM images before and after laser ablation, Figure 4.2(d, e). While the initial thickness of the paper is 60 µm, the laser-ablated region was protruded out of the plane by 15 µm over the original surface. This is due to the decomposition/re-deposition of the silicone coating in the paper upon laser exposure, leading to the generation of higher-volume porous micro/nano roughness. Figure 4.2(f) shows an example of how cells attach to hydrophilic regions (2 mm diameter circles) and proliferate over time.

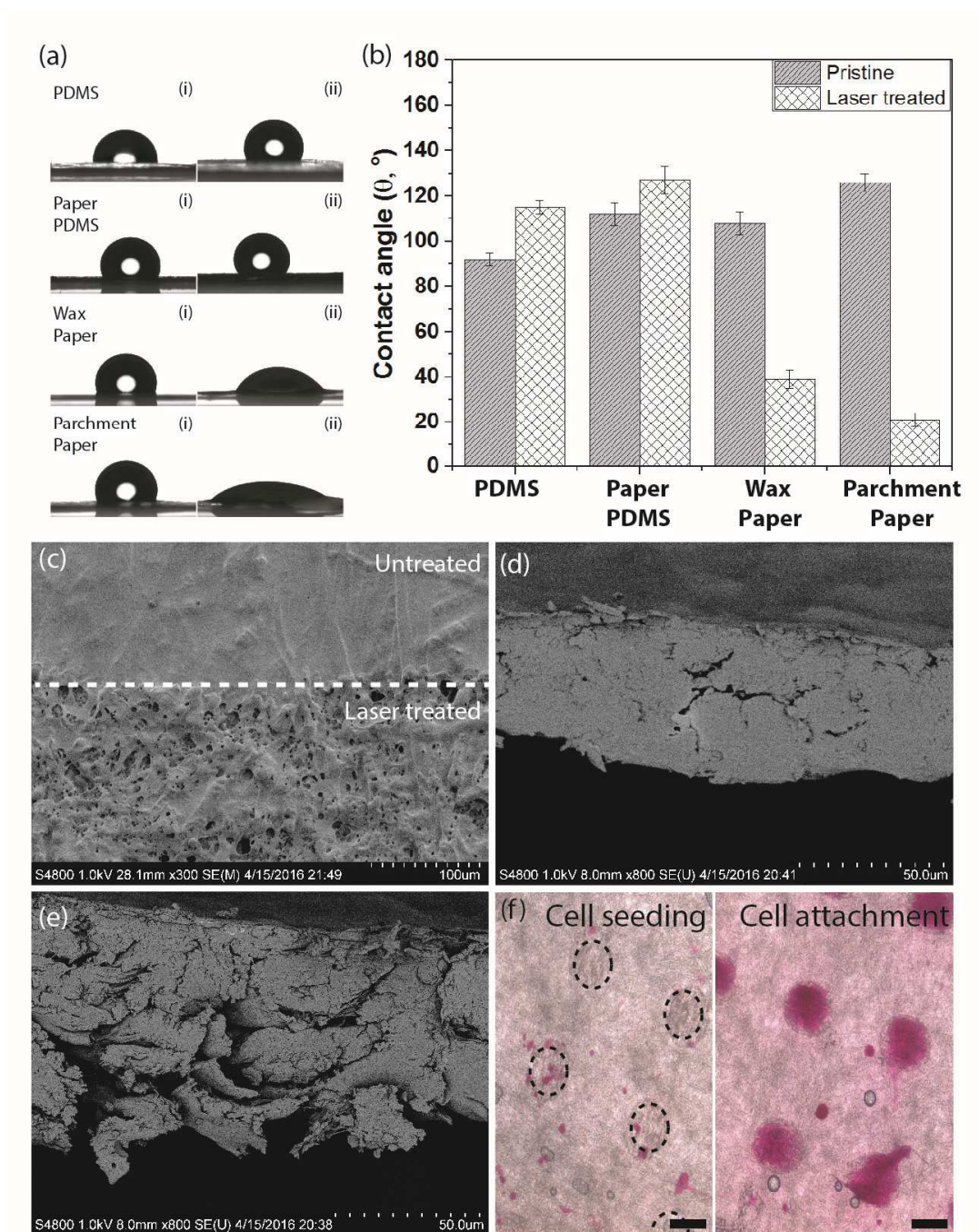


Figure 4.2. (a) Water droplet on different surfaces (i) before and (ii) after laser ablation, (b) comparison of contact angle of various hydrophobic surface before and after laser treatment, (c) SEM top-view of selective laser treated and untreated parchment paper, cross-section SEM image of (d) before and (e) after laser treatment of parchment paper, (f) selective cell attachment to circular hydrophilic patterns with 2mm diameter, Scale: 2 mm.

#### 4.1.2.2 Mechanical properties

Figure 4.3 shows the change in UTS for filter paper and various other hydrophobic papers/films before and after submersion in PBS. All the samples in dry states showed a linear stress-strain profile with a small strain (2.5 %) before rupture, Figure 4.4. In dry state the commercial PET transwell membrane had the highest UTS with 187 MPa followed by the commercial parchment and wax papers with the UTSs of 124 MPa and 129 MPa, respectively. Filter paper impregnated with PDMS had a dry UTS of 21.4 MPa, which is three time higher than the pristine filter paper (7.6 MPa). This increase in mechanical strength was explained by the presence of the PDMS filler in the network fiber of the paper forming a stronger composite film. Wet tensile strength results, for all the paper-based specimens, showed an increase in the elasticity and a decrease in the mechanical strength. Unlike the PET membrane that retained a stable UTS, the wet papers showed a decrease in their mechanical strength. This was due to the diffusion and plasticizing effect of water molecules in the paper films. The results show that the hydrophobic papers retained some of their mechanical strength after 24 h submerging in PBS, whereas the wet filter paper UTS drastically decreased to 1.1 MPa and started to disintegrate in the solution. Among the investigated hydrophobic papers, parchment paper retained more than 48 % of its original dry UTS strength followed by PDMS/paper and wax paper with retentions of 31% and 14 %. The parchment and wax papers showed a stable retention of mechanical strength (UTS) of 58 MPa and 11 MPa for 7 days. For filter paper and PDMS/paper, a longer wetting duration reduced the mechanical strength (UTS) down to 0.4 MPa and 5.4 MPa.

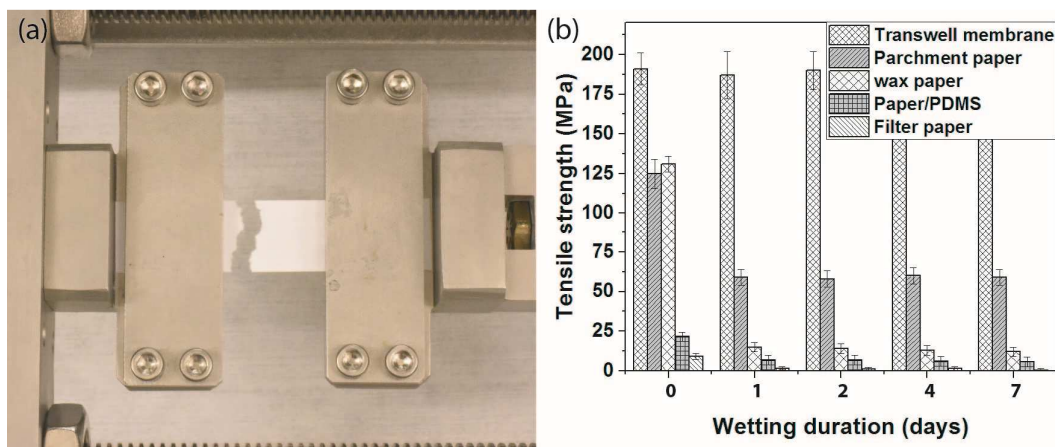


Figure 4.3. (a) Optical image of test setup used for characterizing mechanical properties of paper. (b) Ultimate tensile strength for different papers as a function of wetting duration up to 7 days

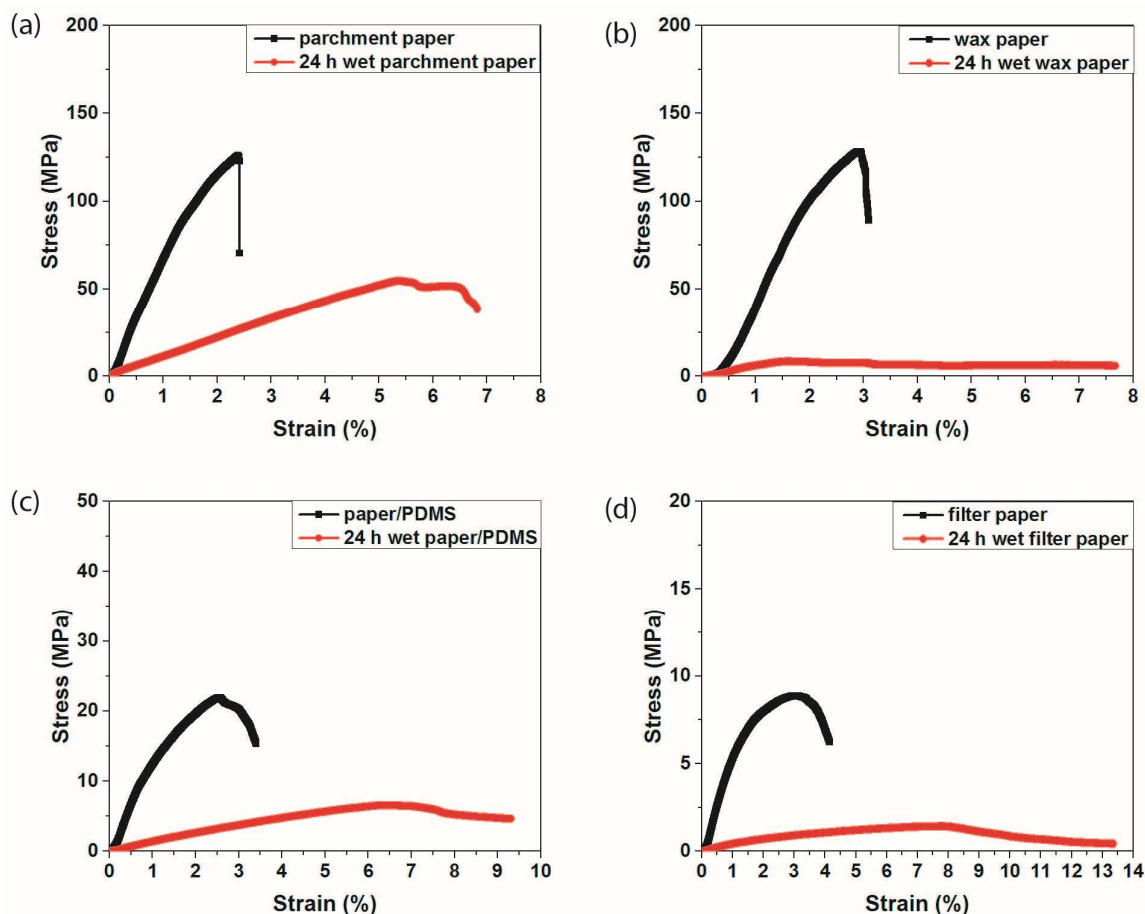


Figure 4.4. Stress vs. strain of dry and wet paper films after 24 hours of PBS immersion (a) parchment paper, (b) wax paper, (c) paper-PDMS, and (d) filter paper

#### 4.1.2.3 Oxygen and medium permeability

Figure 4.5(a, b) show the gas permeability setup and results for different films using the aforementioned setup (inset). For all measurements the initial dissolved oxygen of the DI water was close to zero ( $\sim 0.5$  ppm) and increased with time up to the oxygen saturation level in the water (8 ppm). The increase was due to the diffusion of the oxygen gas in ambient condition through the membrane and its dissolution in the water. Without any membrane, the water equilibrates to its steady-state saturation level of about 8 ppm in less than 140 min. However, when the chamber was covered, the time required for oxygen saturation increases. The results showed the longest oxygen equilibration time occurred for a pristine 100  $\mu\text{m}$  membrane of PDMS (720 min). The transwell membrane and PDMS/paper showed a similar oxygen permeability results with an average time of 650 min to oxygen equilibration. Parchment paper had a 3 fold larger oxygen permeability (time

to saturation of 210 min, with an average rate of 2.4 ppm/h) as compared to the commercial transwell membrane. No signs of water leakage were observed with the hydrophobic films during any of the measurements. The mechanical strength and gas permeability results showed the superior performance of the parchment paper, providing a suitable substrate for the proposed ALI platform. Furthermore, although in the described study the cell-culture was performed on only one side of the paper (with the basal surface of the cells attached to the paper and in contact with the liquid medium, and the apical expose to air), this platform is not limited to only such setups. A more complex pulmonary *in-vitro* system, for example, might feature a co-culture environment with epithelial cells and microvascular endothelial cells on the opposite sides of the cell culture membrane, which requires gas exchange with the cells in the basal lumen. Therefore the gas permeability characterization results further show that the presented system can also be easily used for co-culture *in-vitro* pulmonary studies.

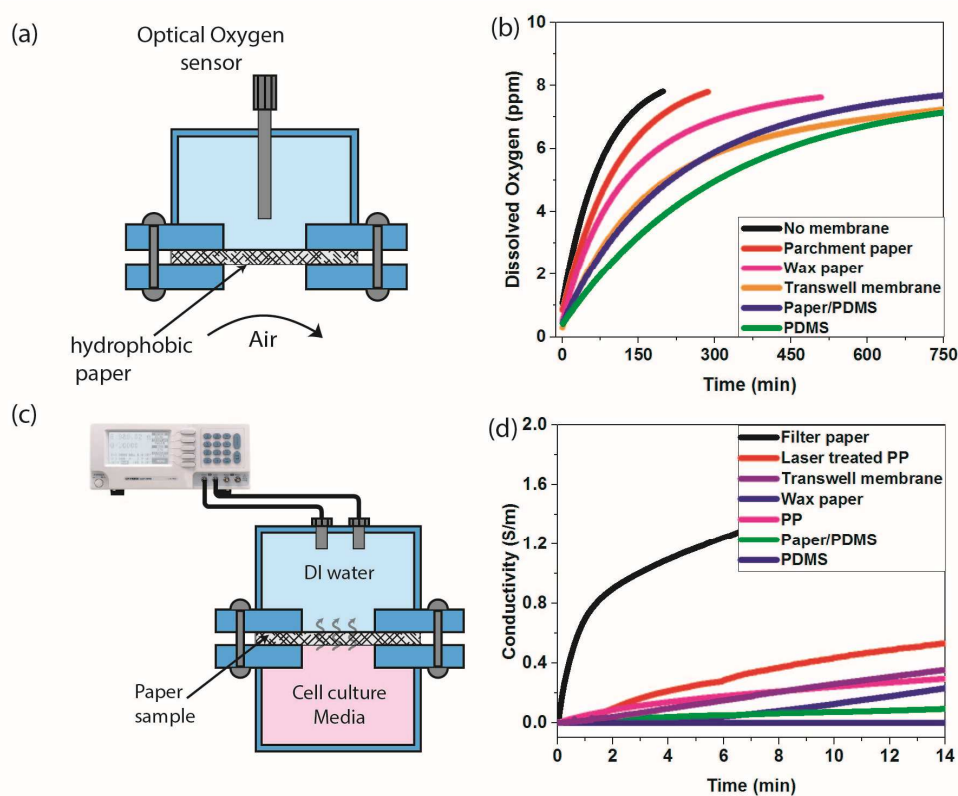


Figure 4.5. (a) Schematic of setup used for characterizing diffusion of oxygen across various papers, (b) oxygen permeability and dissolution in water for different hydrophobic paper membranes as function of time, the inset in (b) shows a schematic of the oxygen permeability test setup, (c) schematic of setup used for characterizing diffusion of media across various papers, (d) diffusion of media across various hydrophobic films as a function of time.

Figure 4.5(c, d) show the diffusion of medium across the different papers and change in electrolytic conductivity of the receptor media (starting with low conductivity DI water). The pristine hydrophilic filter paper showed the fastest change in electrolytic conductivity (1.75 S/m after 14 h). This sharp increase was due to immediate transmission of ions and media through the filter paper. The hydrophobic films (PDMS, P/PDMS, WP, PP) showed significantly smaller changes of 0.001 S/m, 0.075 S/m, 0.31 S/m, and 0.32 S/m, respectively. The low permeability of media through the hydrophobic films was due to the low permeability of wax and silicone to water and various ions present in the media<sup>17</sup>. The commercial PET transwell membrane also showed relatively low permeability, 0.335 S/m after 14 h with a linear increase rate of 0.023S/mh. Laser-treated PP showed a 75% increase in the permeability (0.55 S/m after 14 h, with an average rate of 0.04S/mh) as compared to an untreated sample, this was due to the porosity induced by the laser treatment.

## 4.2 Laser patterning ITO-coated PET

Transparent Indium tin oxide (ITO) film is one of the essential components in various optoelectronic devices, organic solar cells, touch screens, and digital displays such as organic light emitting devices and liquid crystal displays. ITO is typically deposited through large scale physical vapor deposition (PVD) and sputtering on different rigid and flexible films including glass and polymeric films such as Polyethylene terephthalate (PET). PVD deposited ITO films offers uniform high quality films with dense structures and benchmark electrical and optical properties (e.g. 4-60  $\Omega/\text{sq}$  and transparency > 85%). However device fabrication on these substrates requires the selective removal of the ITO layers to form the desired transparent and isolated electrodes. This process is generally carried out by photolithography and wet etching processes that consists of five steps of photoresist coating, optical lithography, photoresist developing, etching, and resist removing. However, these technique has several disadvantages, such as high cost, use of toxic and non-ecofriendly chemicals, large number of process stages which can be costly and time consuming. Therefore, alternative processes such as direct laser etching of desired conductive patterns into the ITO film would replace the challenges associated wet etching processes. Moreover, it provides a non-contact, high-speed, accuracy and flexibility in the production. Over the past few years different laser sources have been applied to various ITO coated substrates to investigate there ablation behavior and potential use in the fast growing market of flexible

electronics with the focus of optoelectronics and displays. More recently however, ITO electrodes have also found a great number of interest in the development of optically transparent bioengineering devices such as ion sensors and biosensors. Due to the fast growing market in flexible and wearable health monitoring devices the development of new cost-effective manufacturing processes is necessary. In this section we study the laser ablation of ITO thin film on flexible polyethylene terephthalate (PET) substrate two using CO<sub>2</sub> and Nd:YAG lasers.

#### **4.2.1 Materials and method**

The laser patterning were all preformed on a commercial ITO coated flexible PET substrate (130 nm ITO on 120  $\mu\text{m}$  PET) purchased from Sigma Aldrich. Two laser wavelengths (10.6  $\mu\text{m}$  produced by CO<sub>2</sub> lasers, and 1.06  $\mu\text{m}$  produced by Nd:YAG fiber lasers) at different operating powers and speeds were used to find the optimum ablation quality of the ITO film. Electrical resistance was measured using a digital multimeter (Agilent 34401A). Scanning electron microscopy (field-emission SEM, Hitachi S-4800) was used to assess the morphology and microstructures of the laser ablated ITO films. Electron diffraction spectroscopy (EDS) elemental analysis was carried out using Oxford INCA Energy 250 systems to confirm the complete removal of the conductive ITO coating. The depth and width of the laser ablated regions were measured using a surface profilometer (Alpha-Step IQ).

#### **4.2.2 Results and discussion**

Previous reports have shown that ITO films are excellent absorbers of fiber laser energy (wavelength=1.06  $\mu\text{m}$ ). Due to low absorption of glass at low wavelength ( $\sim 1.06 \mu\text{m}$ ) this method of ablation has widely been used in ablating thin layer of ITO coating on glass substrates. In this process laser energy is selectively absorbed by the ITO film and rapidly converted into heat. The localized elevated temperature results in vaporizing the conductive coating from the surface of the substrate. Low heat affected zone and high heat tolerance of the substrate will allow a more selective removal of the ITO coating without damage substrate. Figure 4.6(a) demonstrate a schematic illustration of the direct ablation process of the ITO coating using a Nd:YAG laser.

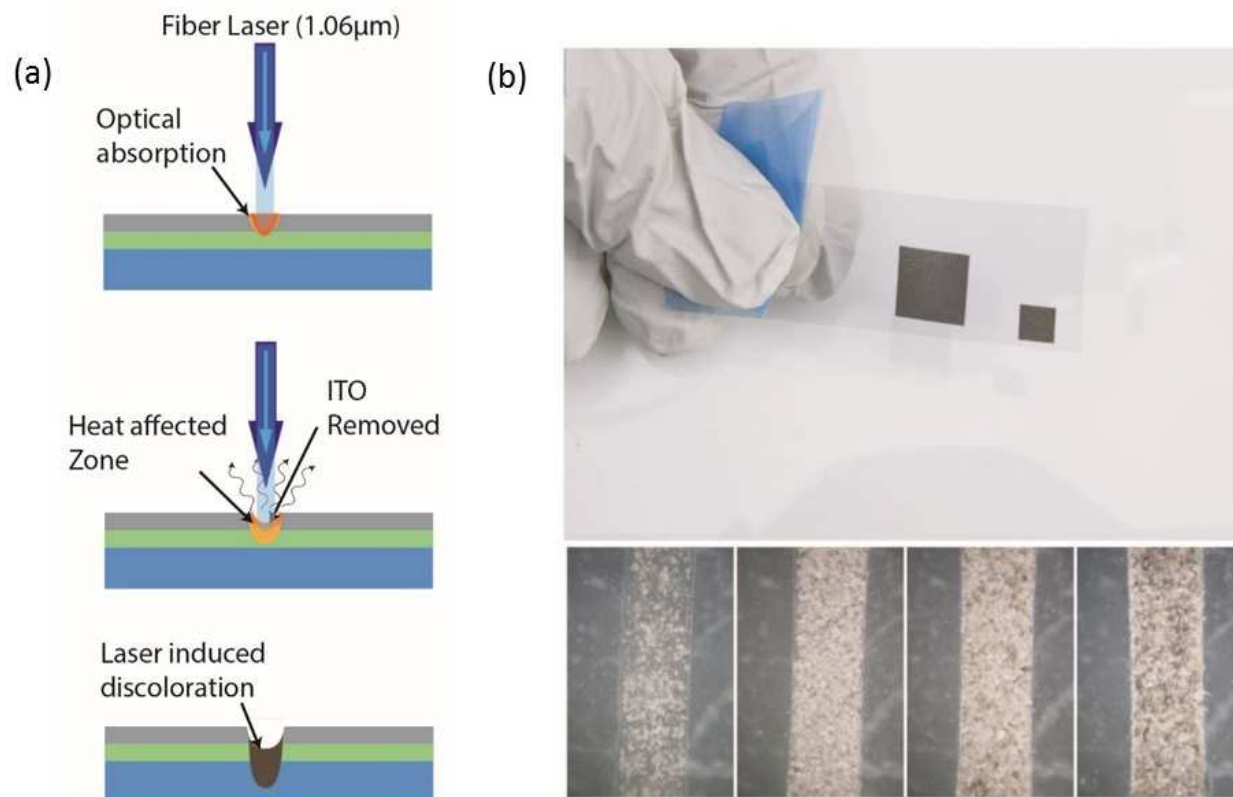


Figure 4.6. (a) Schematic illustration of direct laser ablation of indium tin oxide thin using Nd:YAG laser. (b) Optical images laser ablated ITO film. (Inset shows the ablated trench at constant power of 10W and varying speed from 4 to 0.5 m/s).

As shown in Figure 4.6(b) the laser processing results of the ITO coated PET was quite different than previous reported laser ablation processes of ITO film on glass substrates. In our laser ablated samples the PET substrate changed color to dark black with drastic reduction in optical transparency before complete electrical isolated ITO patterns was formed. This change in color is explained by the C-H, C-O and O-H groups being activated in the macromolecule chain can be activated in NIR radiation between 1000 and 2500nm. Which leads to chemical decomposition and color change in the polymer substrate. This is commonly used in laser marking PET plastics bottles in industry. Therefore the direct laser ablation of the ITO coating with our fiber laser (1.06 μm) wasn't successful and we further investigated the indirect laser ablation process using a CO<sub>2</sub> lasers with an operating wavelength of 10.6 μm. As illustrate Figure 4.7 the ITO film has a low absorption to the CO<sub>2</sub> laser and therefore it is mostly absorbed by the PET substrate. The laser energy is absorbed by excitation of molecular chain within the polymer which is converted

to molecular vibrations and heat within the structure of the PET substrate. Sufficient levels of localized heat leads to removal of the polymer substrate in the form of vapor and fine particles. The level of ablation can be tuned from partial removal of ITO coating to complete cutting through the substrate. The delivered energy is controlled by the scanning speed and power of the laser.

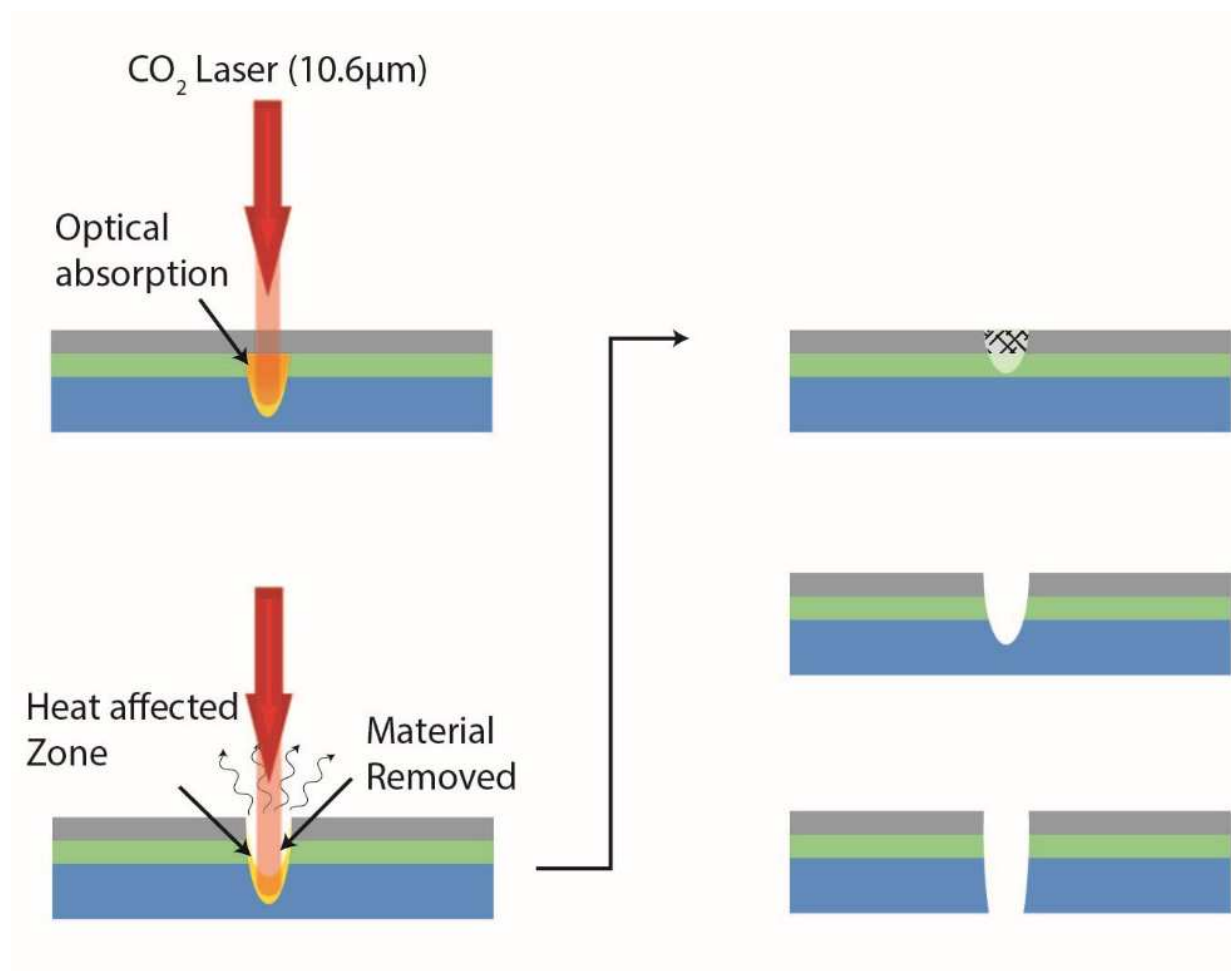


Figure 4.7. Schematic illustration of indirect laser ablation of indium tin oxide thin using CO<sub>2</sub> laser. Different laser settings can result in either: (i) incomplete removal of conductive film, (ii) complete removal of conductive film, and (iii) cut through the PET substrate.

The first step with the CO<sub>2</sub> laser ablation process was to characterize the laser setting required to completely remove the ITO layer with minimal ablation of the PET substrate. In this process we prepared 5 mm × 30 mm samples and laser ablated the center of the samples with a

single pass of laser. The optimal laser setting for minimal damage the plastic substrate were identified by microscopic imaging and electrical resistance measurement from the two ends of the laser ablated samples. Figure 4.8 shows electrical measurements with different laser ablation settings. Lower laser energies had higher risk of electrical interlinked path through the trench. As the energy increased, the ablation trench width and depth increased. The sharp increase in resistance reflects the optimum combination of laser power (0.75 to 3.75 W) and speed required for producing electrically isolated ITO electrodes with minimal damaging the PET substrate. As it's shown in Figure 4.8(a), the threshold energy can be achieved at different laser powers and speeds. Lower laser power required lower speed and higher laser power required higher processing speed. The optimal laser settings show a linear relationship with speed and power. The slope of the plot reflects the minimal energy density ( $6 \text{ J/cm}^2$ ) required to create electrical isolated ITO electrodes, Figure 4.9. Laser ablations with energy densities below or above this threshold will result in either insufficient energy for isolation or through-cut of the PET substrate, respectively.

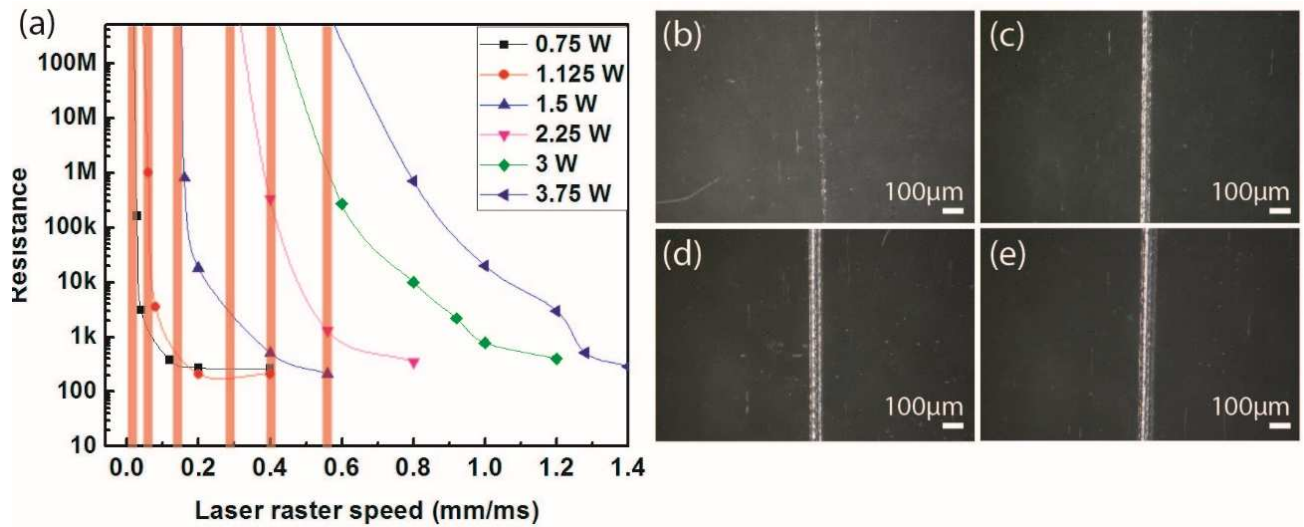


Figure 4.8. (a) Electrical resistance changes of ITO layers with different laser power and scanning speeds. Optical images of the laser ablated trench at a laser power 3W and scanning speed of (b) 1m/s, (c) 0.8 m/s, (d) 0.4 m/s, and (e) 0.2 m/s.

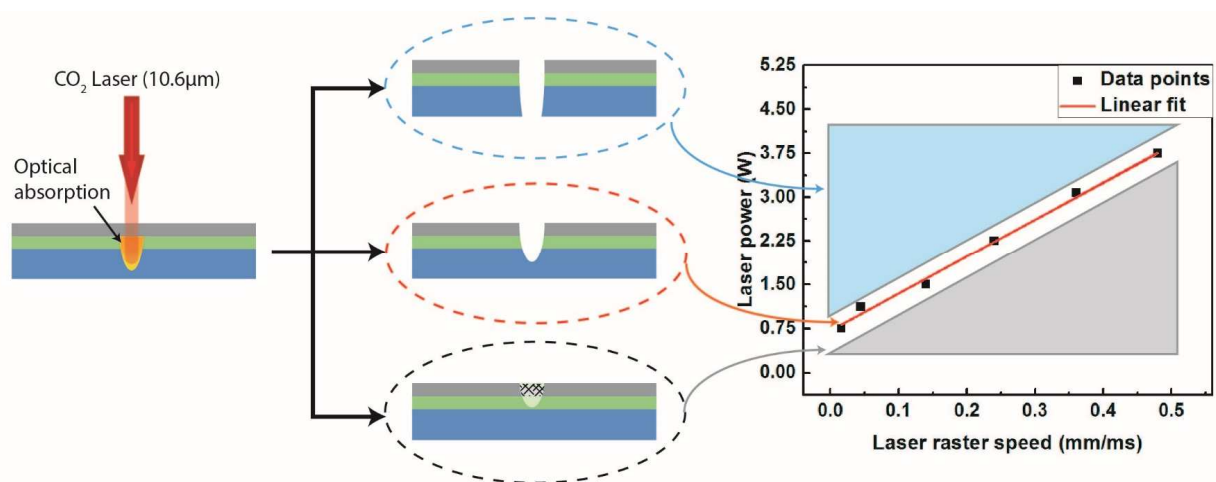


Figure 4.9. Optimal laser power and speed required for complete remove the ITO thin film with minimal damage to the PET substrate.

Figure 4.10(a) shows SEM image of a single laser ablated trench into the ITO film with an average width of 90 μm using the optimized laser setting (6 J/cm<sup>2</sup>). To investigate the elemental distribution on the surface, the samples were further studied by EDX mapping. The red and green areas correspond to the existence of indium and tin elements in the material while the blue areas shows the presents of oxygen. The clear difference in the red and green color contrast shows the complete selective removal of the conductive ITO layer from the surface of the film. Although both ITO and PET contain oxygen, the PET has more oxygen atoms per molecule, hence the darker blue color after ablation is another indication of complete removal of the ITO film. Figure 4.10(b) shows the EDS spectra along the lines on the laser ablated surface and pristine ITO film. EDS spectrum of pristine ITO film exhibits a strong intensity peak at 3.28 keV, which is characteristic of indium and smaller peak at 3.44 keV associated with tin. The percentage of elements on the ITO the films is as follows: Sn: 4.54%, In: 4.15%, O: 37.85%, and C: 53.46%. The excess carbon and oxygen are from the polymeric PET substrate. The spectra shows complete removal of the indium and tin elemental peaks after the laser ablation. Figure 4.10(d) shows the cross-section profile of ablated areas with different widths (laser speed and power kept constant). The profiles show an approximately constant depth of a 7.5 μm for different ablated areas. By measuring the electrical resistance of laser ablated ITO electrodes with different widths, the estimated sheet resistance of ITO film was calculated to be ~ 100 Ω/sq., Figure 4.10(e).

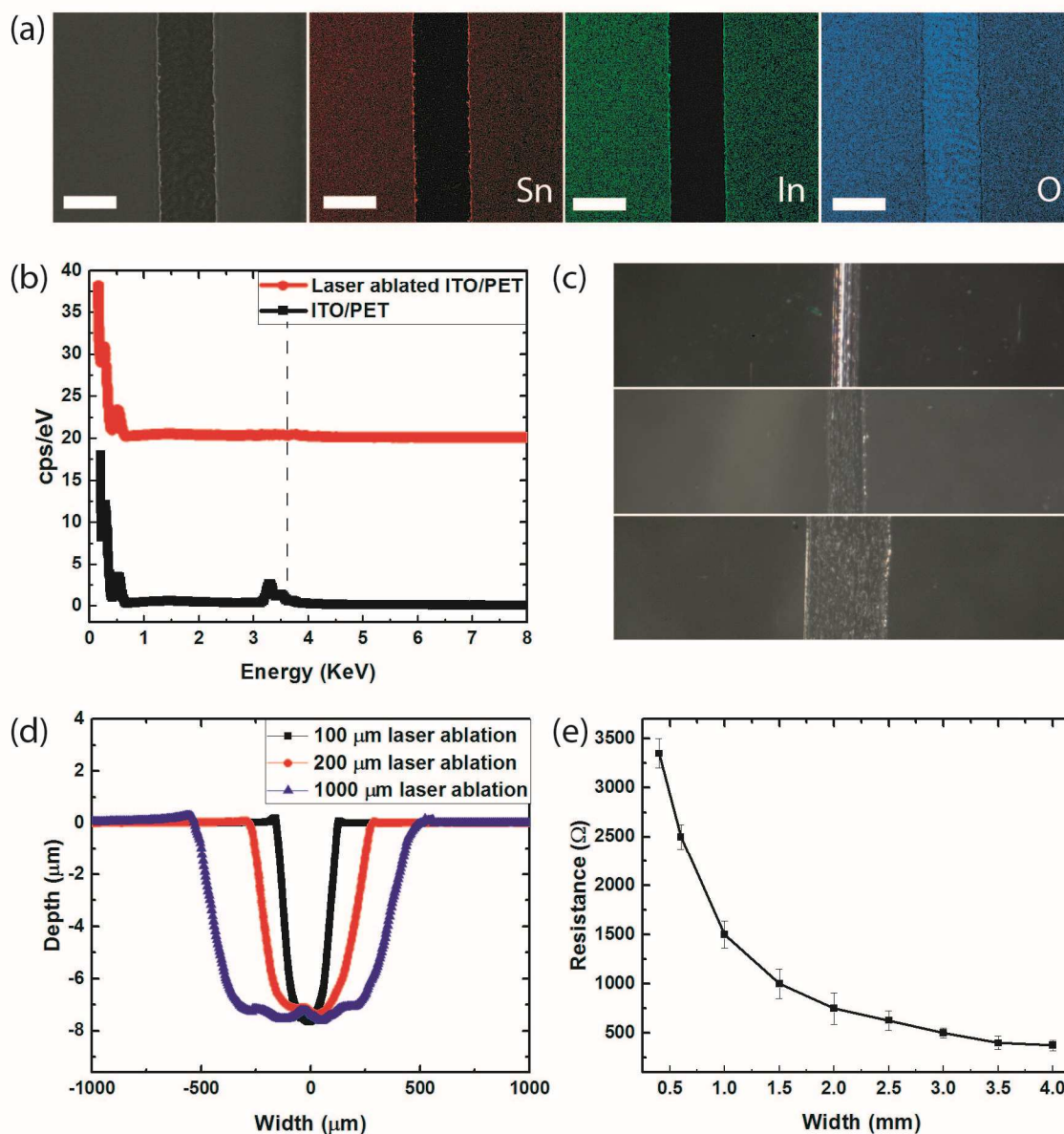


Figure 4.10. (a) EDX color mapping of Sn (red), In (green) and O (blue) on the ITO film after laser scrubbing with  $\text{CO}_2$  laser beam, all scale bars are 100  $\mu\text{m}$ , (b) EDS spectra collected from the surface ITO film before and after laser ablation. (c) Optical image of laser ablated trench with different widths. (d) Cross-section profile of ablated trenches with different widths, (e) measurements of the resistances of laser ablated ITO electrodes with a length of 30 mm and widths from 0.5 mm to 4 mm.

### 4.3 Laser ablating metalized paper

Paper is by far one of the most inexpensive and widely used materials found in our everyday lives due to its scalable processing capabilities (e.g., roll-to-roll[132]) as well as its ecological sustainability. While paper has been primarily used for printing and packaging, it has recently re-emerged as a promising substrate for many low-cost/disposable sensors and electronics[133]–[136]. One of the inherent characteristics of paper is its highly porous and hydrophilic fibrous nature which allows it to be impregnated with many functional materials including chemicals for colorimetric assays[137] (e.g., litmus paper) and highly conductive nano/micro fillers for use as paper-based electrodes[138]. Recent improvements in printing technologies have introduced the ability to print different functional and conductive nano-materials, thus drastically changing the landscape of paper-based devices and their integration into various kinds of devices including healthcare diagnosis[139][140], environmental monitoring[141], [142], and food quality assessment [143]–[145]. Recent examples of these include mechanical pressure and force sensors that can detect diverse human motions[146], and also portable chemical sensors that can monitor bioassays in, urine, tears, saliva, and wound blood[136], [147]–[149]. Despite the many advances in paper devices technologies, many challenges remain, primarily with respect to the ink formulations. The most commonly used inks in the paper-based devices are silver, carbon, and liquid metal alloys[106], [150]–[152]. Although carbon-based inks have a lower cost they exhibit a high electrical resistivity and high sensitivity to mechanical deformation[38][153]. At the current technology status, silver nano particles are the most practical material in terms of both conductivity and printability; however, their performance is still insufficient and needs further improvement. Some of the major drawbacks of silver-based inks include their high cost, limited shelf life, and need for multiple layers of printing (>12)[152], [154], [155] to achieve acceptable levels of conductivity. As a more economical alternative, researchers have tried to replace silver and other noble metal-based inks with less expensive and more abundant metals such as aluminum and copper. However, the challenge associated with aluminum and copper nanoparticle inks is their rapid oxidation in ambient conditions[156], [157]. For example, aluminum rapidly forms a native oxide layer that prevents the electrical contact between the NP, thus making it challenging to produce conductive aluminum based inks[158].

Metalized paper (MP) is a commodity in which a thin layer of aluminum offers both a decorative appearance and protective/controlled gas permeation. The thin (~25nm) aluminium

coating in these products are performed by using large-scale vacuum metallization which involves depositing a thin layer of aluminium using physical vapor deposition. The thin aluminium coating is a few tens of nanometers (25nm), which produces its reflective metal sheen. Although the initial intention of this product was for electronic applications, the aluminium coating on these film has a satisfactory level of electrical conductivity for potential use in low cost and active paper based devices. In order to create active device/circuit, the conductive coating on the paper has to be patterned into desired shapes. Functional circuits can be fabricated by etching chosen patterns into the aluminium layer of the paper. One of the well know approaches is by conventional photolithography and wet etching. Although this process allows the creation of high resolution patterns, it involves the use of many chemicals and materials that can significantly increase the cost of production and hazardous wastes that are harmful to the environment[159], [160].

Furthermore, etching chemicals used in such process can be disruptive to the paper substrate and result in mechanical damage and deformation of the paper. An alternative noncontact approach to patterning MP is the use of laser ablation to selectively remove the undesired materials from the surface. The advent of affordable lasers systems for various material processing have open doors for many novel applications with larger dimensions and in greater production volumes[161]–[164]. Coupling such laser system with commonly available commodities can offer unprecedented opportunities in the development of large-scale low-cost paper devices which can be used to capture clinical point-of-care information or deployed on the field for agricultural and environmental studies[165], [166]. In this section we present the results of our investigations on laser ablating MP using CO<sub>2</sub> and Nd:YAG lasers and their potential use in the production of low-cost sensors.

#### **4.3.1 Materials and method**

Here we used Vacumet Corp. (Franklin, MA) metallized paper. This aluminum-coated paper consists of a cellulose-based substrate, a thin conductive aluminum coating, and a final polymeric passivation layer. The cellulose film with an average thickness of 56  $\mu\text{m}$  provides a structural support for the  $\sim 25$  nm vacuum-deposited aluminum coating. The polymeric layer protects the metalized layer from scraps, scratches, and other environmental/handling damages. Although the aluminum and polymeric coatings are good barriers to moisture and gas, the cellulose substrate is hygroscopic and can readily absorb moisture and aqueous liquids. Here, we

demonstrate the patterning of the conductive coating on the paper into desired conductive regions using a universal laser engraver system (PLS6MW, Universal Lasers, Inc., Scottsdale, AZ). The discrete conductive regions on the paper can serve either as sensing electrodes or as conductive traces for electrical connections to external electronics. The desired conductive patterns were all generated using Corel draw software. The designed patterns were transferred onto the MP by raster-scanning the laser across the surface of the metal-coated paper. The optical energy delivered by the laser at selected locations ablates/removes the unwanted metal from the surface of the paper. The paper substrate is highly sensitive to laser processing parameters (e.g., wavelength, power, and scanning speed), so these had to be carefully selected. Improper settings can result either in creating through-holes in the paper (if too much energy is imparted) substrate or in incomplete removal of the metalized coating (if insufficient energy is imparted).

The efficacy of laser ablation in removing the conductive aluminum coating from the MP was evaluated using two of the most commonly used laser systems, CO<sub>2</sub> and Nd:YAG. The CO<sub>2</sub> laser operates in the infrared region (10.6  $\mu\text{m}$ ) and although not easily absorbed by metallic materials (mostly reflected) it is suitable for processing many organic and polymeric substrates such as wood, acrylic, rubber, etc. In contrast, the Nd:YAG laser operates at 1.06  $\mu\text{m}$ , which makes it ideally suited for absorption by most metals while its shorter wavelength inhibits its absorption by most organic and polymeric materials. The CO<sub>2</sub> laser systems used in our experiments is a continuous wave (CW) mode with a maximum power of 75 W and a maximum scanning speed of 4 m/s. The Nd-YAG fiber laser operates in the pulsed mode with pulse duration and repetition frequency of 10 ns and 30 kHz, respectively. The maximum scanning speed is 4 m/s and maximum average power is 40 W. CAD designed conductive patterns were ablated by raster scanning at proper laser setting (e.g., power and speed). The laser-treated/ablated samples using different laser systems were evaluated in various aspects before and after ablation, including optical, electrical, mechanical, water contact angle, and moisture absorption. The mechanical strength of the paper sample before and after laser ablation was compared with the wet etching process. Wet etched samples were prepared by removing the protective polymer and aluminum coating using an etching solution prepared by mixing a 10 ml of 0.1 M KOH with 10 ml acetone. The acetone dissolved the polymer coating while the aluminum coating was removed by the KOH solution.

### 4.3.2 Laser processing

CO<sub>2</sub> and Nd:YAG are two of the routinely used laser systems for modifying materials in various ways including ablating, drilling, cutting, and welding. Laser ablating of any material is determined by the interactions caused by the thermo-physical properties of the processed material and the photon energy of the well-defined laser. One of the utmost important parameters affecting laser-material interaction is the material's ability to absorb electromagnetic radiation of the laser beam. When a laser beam strikes the material, a portion of the light is reflected, another transmitted and the rest is absorbed. The absorbed portion of energy is strongly dependent on the photon energy. In general photons with energy above the material's band gap will be absorbed by the material. Such energies typically correspond to light frequencies below ultraviolet for polymers/insulator and below the infrared spectrum for metals/semiconductors. Aluminium typically has a relatively low absorbance (<0.03) at 10.6  $\mu\text{m}$  (CO<sub>2</sub> laser) and higher absorbance of (>0.3) at 1.6  $\mu\text{m}$  smaller wavelength (fiber laser). Hence, Nd:YAG fiber lasers are often used as the primary laser tool for processing aluminium based materials. Although the CW CO<sub>2</sub> laser in this process is not the ideal wavelength for processing the MP, it still was able to ablate the aluminium coating with properly adjusted power and scan speed settings. The thin aluminium coating on the paper allowed the CO<sub>2</sub> beam to pass through the conductive coating and absorbed by the cellulose supporting substrate. The absorbed energy can increase the localized temperature of the paper substrate which can cause an explosive phase change leading to hydrodynamic explosion/vaporizing the cellulose fiber which ultimately causes the removal of the conductive aluminium coating. In other words the laser patterning of the materialized coating with the CO<sub>2</sub> laser was achieved through an indirect ablating of the paper substrate. In contrast, the laser ablation with Nd:YAG provided more defined and selective removal of the aluminum layer with minimized thermal effect to the paper substrate. Figure 4.11 shows the results of the combinatorial study of the laser power and laser scanning speed for successful laser ablating the metal coating on the MP substrate using CW CO<sub>2</sub> laser. The optical images show a high sensitivity to laser processing scanning speed and power with narrow effective settings that could completely remove the conductive coating and have minimal damage to the substrate. Higher powers and lower speeds resulted in burning the paper substrate and in most cases complete removal of the paper substrate. Conversely, with lower power and fast scanning speeds the aluminium coating was undisturbed. Figure 4.11(b) shows an example of six samples utilized to measure change in electrical

conductivity with different laser ablation setting. The pictures show the four conditions of intact, partially removed, optimally removal, and burnt substrate using constant power (4.5W) and scanning speeds ranging between 0.2 to 4 m/s. The electrical characterization plot shows the complete removal of aluminium coating with minimal electrical conductivity between the two electrodes once the paper received a threshold energy, Figure 4.11(c).

This threshold energy was achievable at different laser powers and scanning speeds. For example, with lower laser speeds, complete removal occurs at low power levels, whereas with higher laser speeds, higher power was required. The optimal CO<sub>2</sub> laser setting (speed and power) corresponded to the laser fluence of 174 mJ/cm<sup>2</sup>. Laser ablation settings with energy densities above or below this threshold resulted in either insufficient energy for complete removing the aluminium coating or burning the paper substrate, respectively. Figure 4.11(d) shows the change in mass of the metallized paper after laser ablating on 1 cm × 1 cm samples using different CO<sub>2</sub> laser parameters (power and scanning speed).

The mass change measurements reflect an average decrease of 3.9 mg (~44.3%) in mass at the required threshold energy for complete electrical isolation between electrodes. Higher energies resulted in a more drastic decrease in mass (>90%). The measurements and optical images show minimal selectivity, color change (due to excess energy), and mass loss in the paper substrate. Successful metal patterning through laser ablation should satisfy both selective removal of conductive metal with minimal damage to the paper substrate. Figure 4.12 shows the combinatorial study of the laser power and scanning speed preformed using 10 ns pulsed Nd:YAG laser. As shown in Figure 4.12(a), significant difference in laser setting was required for ablating the metalized coating using pulsed laser ablation. Although aluminum has a higher absorption at wavelengths smaller wavelength (~1.06nm, Nd:YAG laser) it still required a critical laser energy to remove thin layers with minimized thermal effects to the paper substrate. As shown in the photograph, the ablation did not start until the average power was 3.6 W. Qualitative observation of also showed a much wider optimal setting of laser power and speed as compared to the CO<sub>2</sub> laser ablation. The ablation results showed a high laser scanning speed tolerance for powers between 4.4 to 10 W, i.e., it still was possible to regulate the delivered energy to the paper at high (>10W) and low (<4.4 W) laser powers.

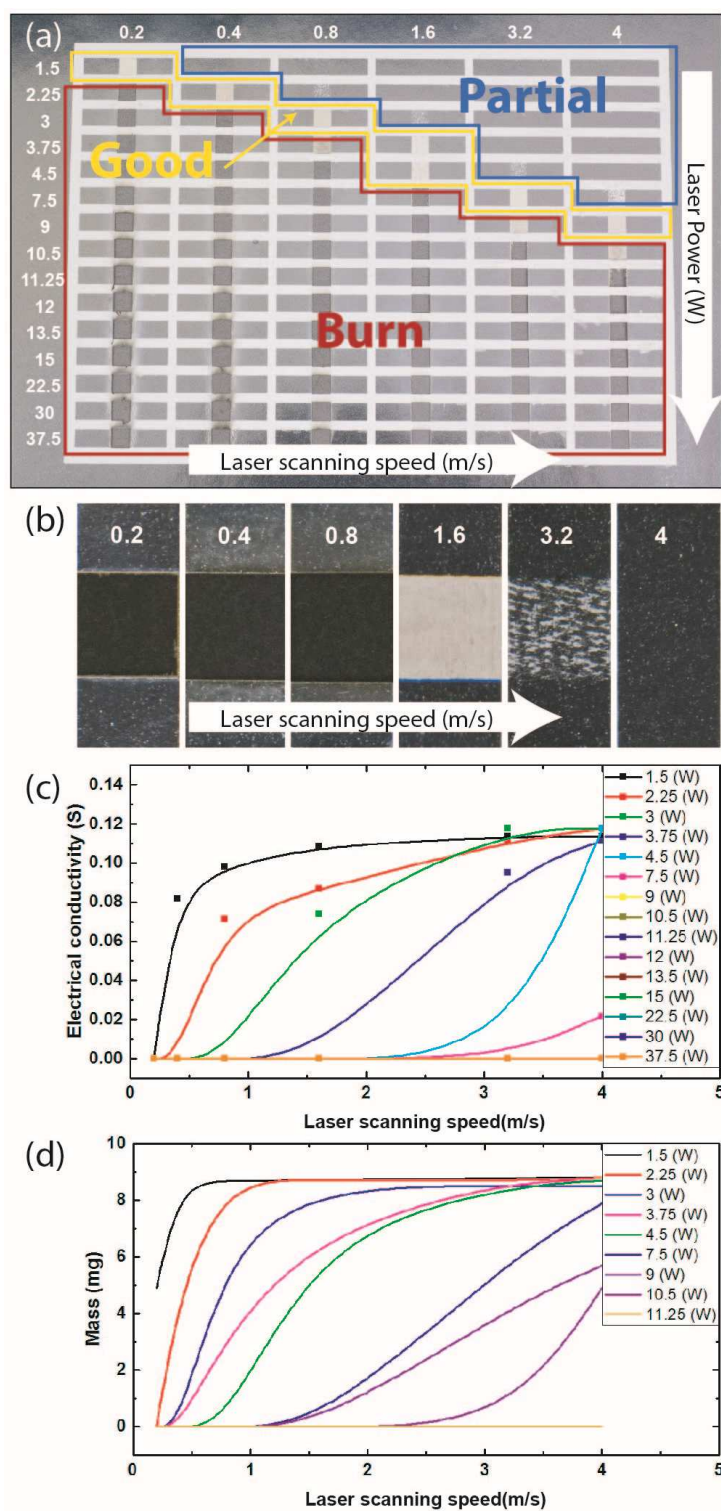


Figure 4.11. Process characterization of CO<sub>2</sub> laser ablating MP. (a) Combinatorial study for optimum laser power vs. laser scanning speed. (b) Microscopic pictures of laser ablated MP using constant power of 4.5W and different scanning speeds ranging between 0.2 to 4 m/s. (c) Resistivity and (d) mass change of 1×1cm samples at various laser powers and scanning speeds.

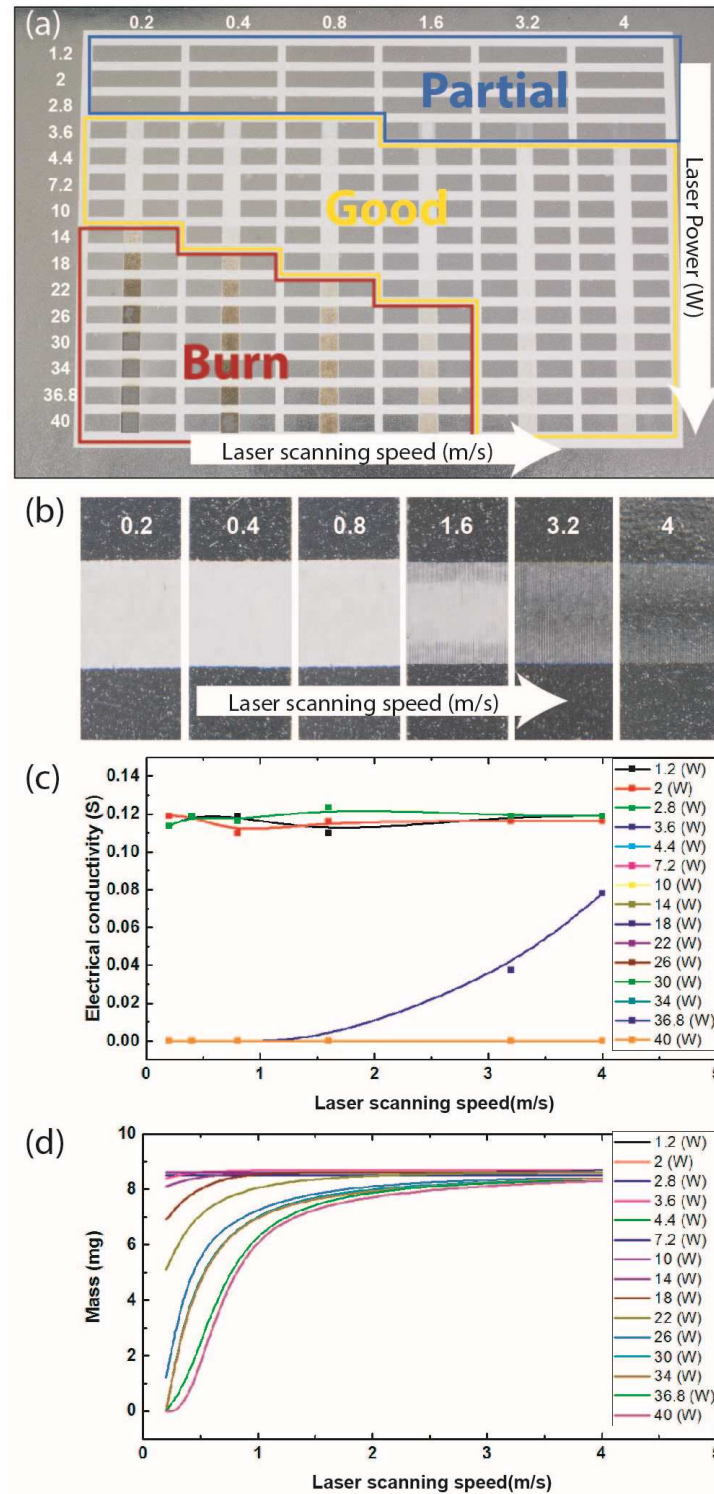


Figure 4.12. Process characterization of Nd:YAG laser ablating MP. (a) Combinatorial study for optimum laser power vs. laser scanning speed. (b) Microscopic pictures of laser ablated MP using constant power of 4.5W and different scanning speeds ranging between 0.2 to 4 m/s. (c) Resistivity and (d) mass change of 1×1cm samples at various laser powers and scanning speeds.

We observed that with high delivered energies (laser power  $>18$  W and raster speed  $<1.0$  m/s) the paper substrate started to burn and changed color. In contrast, at lower energies (laser power  $<3.6$  W and raster speed  $>1.6$  m/s), the metal coating was not completely removed. Figure 4.12(b) shows a close-up image of six laser ablated samples with 3.6 W power and scanning speeds ranging 0.2 to 4m/s. At high speed the energy was insufficient for complete removal of the metal coating. As shown in Figure 4.12(c), electrical isolation between two electrodes was achieved by a minimum power of 3.6 W and scanning speed of 0.8 m/s. At higher power setting ( $>10$ W) electrical isolation was always achieved, independent of the scanning speed of the laser. Weight lost measurements of the laser ablated samples showed a selective removal of the aluminum layer with minimal damage to the paper substrate at a weight loss of less than 0.1 mg (1.15% of original weight). The optical setting with minimal weight lost is shown as the “Good” regimes.

### 4.3.3 Mechanical and surface characterization

Figure 4.13 shows a quantitative mechanical characterizations of structural damages to the paper substrates as a result of ablation with CO<sub>2</sub> and Nd:YAG lasers. The mechanical test and further fabrication of paper based devices were done with using the fastest optimized process settings (power, speed). The CO<sub>2</sub> laser ablated samples were prepared using 9W of laser power and 4m/s raster speed while the Nd:YAG laser ablated samples were prepared with 7.2W laser power and 4m/s scanning speed. The Nd:YAG laser ablated samples showed a minimal change ( $<2.93\%$ ) in tensile strength of the paper, similar to the selective wet etched samples ( $<6.74\%$ ). However, the CO<sub>2</sub> laser ablated samples showed a dramatic decrease (64%) in tensile strength which is due to the structural damage in the cellulose fibers of the paper substrate.

Figure 4.14 shows a simple circuit lighting an LED using conductive aluminium traces prepared by optimal laser ablation setting with the CO<sub>2</sub> and Nd:YAG laser. Low and high magnification SEM images at the boundary of CO<sub>2</sub> laser ablated regions exhibit a clear destruction within natural microstructure of the paper. In contrast, the SEM images from the Nd:YAG laser ablated samples reveal successful metal removal and retention of highly porous fibrillary structure in the paper substrate.

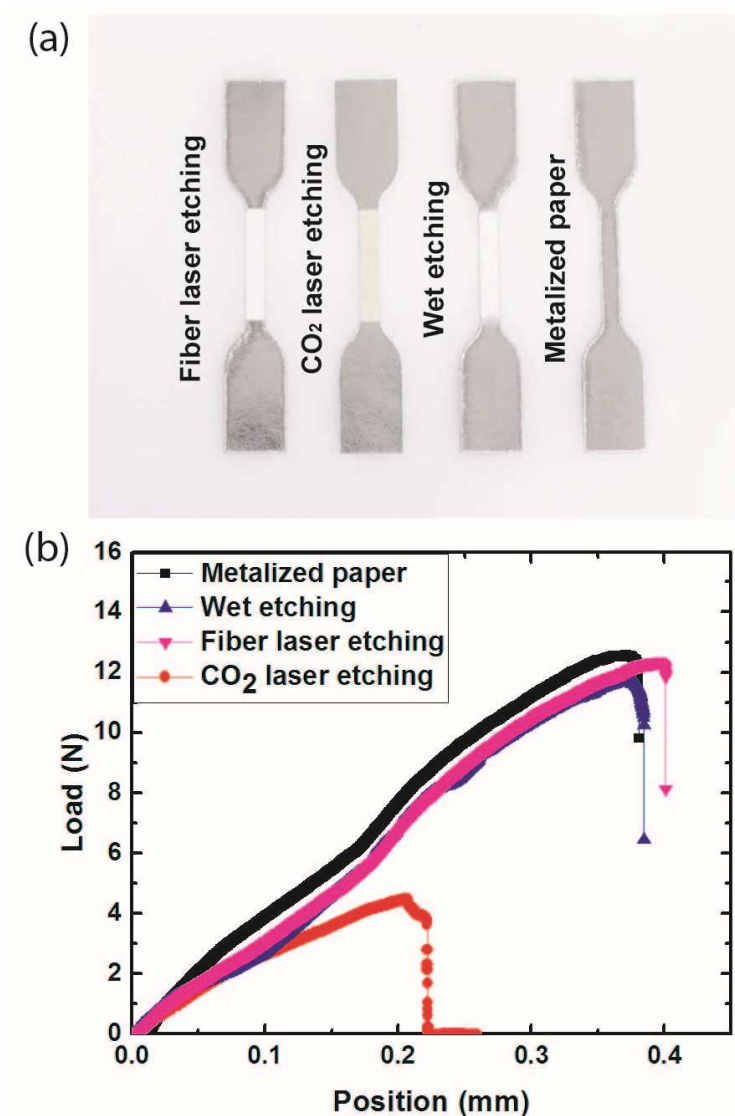


Figure 4.13. Mechanical characterization of MP before and after different etching processes. (a) Dumbbell-shaped samples used for the tensile strength test. (b) Force versus displacement graph of different samples.

The surface wetting characteristics of the laser ablated samples with the aforementioned optimized settings were evaluated with sessile droplet experiments. Figure 4.15 shows the results of the results water droplet contact angle (CA) measurements on pristine MP, CO<sub>2</sub> laser ablated MP, and Nd:YAG laser ablated MP, respectively. On the pristine MP the CA was measured to be approximately  $89.17 \pm 0.05^\circ$ , indicating a low surface energy due to the polymeric coating on the aluminum layer. The CA on the CO<sub>2</sub> laser ablated MP was measured to be approximately

$44.96 \pm 0.03^\circ$ , whereas on Nd:YAG laser ablated MP the CA was less than  $3^\circ$ , indicating the super hydrophilic nature of the laser ablated samples. These experiments indicate that the optimized Nd:YAG laser ablation process can selectively remove the metal/polymer coating from the pristine MP without damaging the super hydrophilic and nature capillary wicking nature of the paper substrate. Although the CO<sub>2</sub> laser ablated MP was expected to exposed the hydrophilic surface of the paper substrate, the contact angle measurements were significantly higher than the Nd:YAG laser ablated process. This can be attributed, to partially burning the paper substrate and distorting the natural wicking property within the micro porous structure of the cellulose substrate. Figure 4.15 (c) shows the time-dependent stability of water contact angle measurements over the course of 7 days. Regardless of the substrate type, the contact angle values were constant with negligible ( $< 8\%$ ) fluctuation throughout the measurement period.

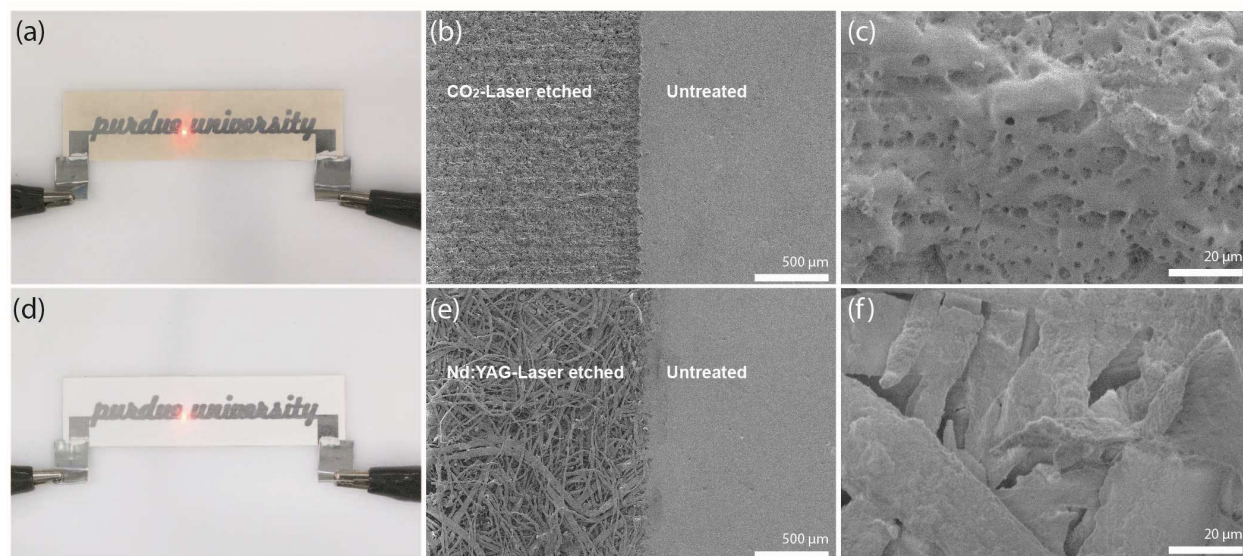


Figure 4.14. (a) Photograph image of simple LED circuit using optimized CO<sub>2</sub> laser ablation. (b) low and (c) high magnification SEM image of selective CO<sub>2</sub> laser ablated MP. (d) Photograph image of simple LED circuit using optimized Nd:YAG laser ablation. (e) low and (d) high magnification SEM image of selective Nd:YAG laser ablated MP.

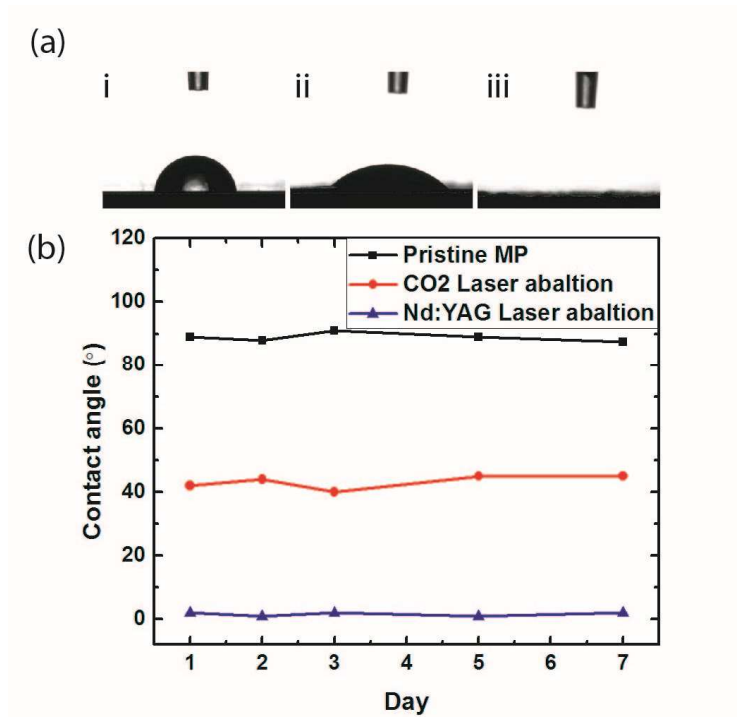


Figure 4.15. (a) Water droplet on different surfaces (i) pristine MP, (ii) CO<sub>2</sub> laser ablated MP, and (iii) Nd:YAG laser ablated MP. (b) Time-dependent water contact angle stability test of CO<sub>2</sub> and Nd:YAG laser ablated MP.

## 5. LASER ENABLED DEVICE MANUFACTURING

### 5.1 Mechanical sensors

Mechanical sensors have an important role in wide range of applications such as motion sensing, blood pressure monitoring, and mechanical vision in surgical robot arms. In this section we will demonstrate an inexpensive approach in fabricating a strain sensor and a wireless pressure sensor that can be potentially used in a variety of wearable biomedical applications.

#### 5.1.1 Highly stretchable and sensitive strain sensor

Stretchable and flexible sensors have attracted considerable attention for their potential applications in wearable electronics [167], smart textiles [168], soft robotics, [169] [170] and structural health monitoring [171]. Among the various types of transducers available for these applications, piezoresistive strain sensors are among the most investigated ones. These are often used for human motion analysis in applications such as athletic assessments [172], kinesiology [107], and interactive entertainment systems [173]. Traditional metallic and semiconducting strain sensors are not suitable for stretchable applications since they can only withstand very limited strain (<5%) before fracture [174] [175]. Today's most common approaches for fabrication of highly stretchable strain sensors are based on two main techniques: 1) conductive-liquid-filled elastomeric tubes or microchannels [176], and 2) polymeric blends or composites prepared by embedding conductive nanomaterials within an elastomeric network [177] [177]. The first method dates back to 1953 when Whitney used mercury-filled elastomeric tubes to measure blood volume in the limbs (mercury-in-rubber plethysmograph) [178]. When strained, the tube was stretched and narrowed, resulting in an increased resistance. More recently, several groups have reported on miniaturized variations of this technique using microchannels filled with eutectic gallium-indium [179] [180] or carbon grease [181]. Despite its attractive simplicity, this method suffers from various drawbacks, including small gauge factor, leakage of the liquid upon strain (mostly at the electrical connections ends), and technical challenges associated with filling a highly viscous fluid into microchannels. The second method relies on making elastomeric composites containing conductive nanomaterials (e.g., carbon nanotubes [107], graphene [182] [183], silver nanowires [184]) which are either embedded directly into the elastomeric material [185] [186] or deposited on the surface of a stretchable substrate using various methods such as contact transfer printing

[187], screen printing [188], and inkjet printing [189]–[191]. Recent examples of the latter method include screen printing of silver nanowire network onto a glass slide which are subsequently transferred to an elastic matrix [184] and mixing graphene with cellulose nanoparticles in a controlled ratio to create stretchable conductive nanopaper [192]. Although this method offers acceptable stretchability and sensitivity, the processes can be costly and do not always allow for precise patterning of the conductive traces.

As an alternative approach addressing some of the abovementioned problems, we present a simple and low-cost technique to create highly stretchable (up to 100 % strain) and sensitive (gauge factor of up to 20,000) strain sensors using laser-carbonized nanomaterials. The stretchable strain sensors consist of PDMS embedded with patterns of partially-aligned micro/nano carbon particles. The carbon nanomaterials are created by direct laser-pyrolization of a polyimide tape, resulting in highly porous carbon traces. The carbon particles are subsequently transferred to and encapsulated within an elastomeric material, yielding highly stretchable and unidirectional strain sensors.

#### **5.1.1.1 Fabrication process**

Figure 5.1(a) illustrates the fabrication process of the stretchable carbon traces. First, a piece of polyimide tape is attached to a PET sheet to provide handling rigidity during the process. Next, a CO<sub>2</sub> laser engraving system is used to inscribe highly-porous carbon patterns in the desired shape on the surface of the polyimide tape. This is achieved by locally carbonizing the surface of the polymer into carbon nanomaterials (e.g., CNTs, graphene). The traces are subsequently immersed in n-heptane for 20s; this improves the adhesion and increases the penetration of the elastomeric materials into the carbon network. In order to make stretchable sensors, the carbon patterns are then transferred to polydimethylsiloxane (PDMS). This is accomplished by pouring a diluted form of uncured PDMS (pre-polymer with 7 % n-heptane) over the carbon patterns, followed by degassing and crosslinking (at 70 °C for 2 hours). The use of diluted pre-polymer results in improved impregnation of the carbon patterns with PDMS during the vacuum degassing step. After crosslinking, the PDMS is peeled off the polyimide substrate. Figure 5.1(b-c) show photographs of the carbon patterns before and after transfer to the PDMS substrate. Figure 5.1(d-e) show an LED attached to a power supply through two parallel carbon traces of 1 mm width and 3 cm length. In an un-strained state, the LED is brightly lit, whereas at low strain levels (5 %) the

LED begins to dim. At higher strains ( $> 5\%$ ), the conductivity of the traces decreases significantly until the LED is eventually turned off.

#### 5.1.1.2 Results and discussion

The surface morphology of the carbon patterns, before and after embedment in the PDMS, was qualitatively investigated by scanning electron microscopy (SEM) (Figure 5.2). The top view of carbon traces clearly reveals highly-porous carbon micro- and nano-particles arranged in a parallel pattern. This phenomenon is related to the method by which the laser beam is scanned across the sample during the fabrication. Since the spot size (diameter) of the laser beam in our system is  $60\text{ }\mu\text{m}$ , ablation of areas larger than  $60\text{ }\mu\text{m}$  requires multiple sweeps of the laser beam over the targeted area; thus generating carbon particles in a parallel orientation to the direction of laser motion. Higher magnified pictures of the carbon particles in the pyrolyzed lines are shown in Figure 5.2(c-d). Partially-oriented carbon flakes and high aspect-ratio filaments (some of them as small as  $\sim 70\text{ nm}$  wide with lengths of up to  $\sim 2\text{ }\mu\text{m}$ ) can be seen on the carbon traces. A cross-sectional view of the carbon patterns shows that the entire thickness of the pyrolyzed carbon is comprised of highly porous nanomaterials. This enables the PDMS to penetrate deep into the carbon patterns (Figure 5.2(e)), resulting in a uniform transfer of carbon nanoparticles to the elastomeric matrix (Figure 5.2(f-g)). The thickness of the carbonized regions embedded in the PDMS is  $\sim 30\text{ }\mu\text{m}$  (Figure 5.2(h)), which is close to their original thickness on the polyimide (before transfer). The electrical conductivity of the carbon patterns before and after transfer to the elastomeric matrix was measured by four-point-probe technique. Figure 5.3 demonstrates the sheet conductivity of the carbon patterns as a function of the fabrication parameters, i.e., speed and power of the laser, before and after transfer to the PDMS. The carbon patterns exhibit a small dip in conductivity after transfer to the PDMS; this decrease can be attributed to an incomplete transfer where residual amounts of carbon particles remain on the polyimide surface (Figure 5.3(b)).

The performance of several prototype strain sensors consisting of four traces each  $2\text{ mm}$  wide and  $30\text{ mm}$  long was evaluated at room temperature by continuously recording the change in the resistance while the device was stretched by a micromanipulator. To ensure reliable electrical connections, silver paste was applied on the two ends of the device. The base-line resistance of the device (un-strained) was  $\sim 1\text{ k}\Omega$ , comparable to the reported piezoresistive strain sensors made with CNT ( $\sim 100\text{ }\Omega$ ) and AgNW ( $\sim 250\text{ }\Omega$ ) composites [184].

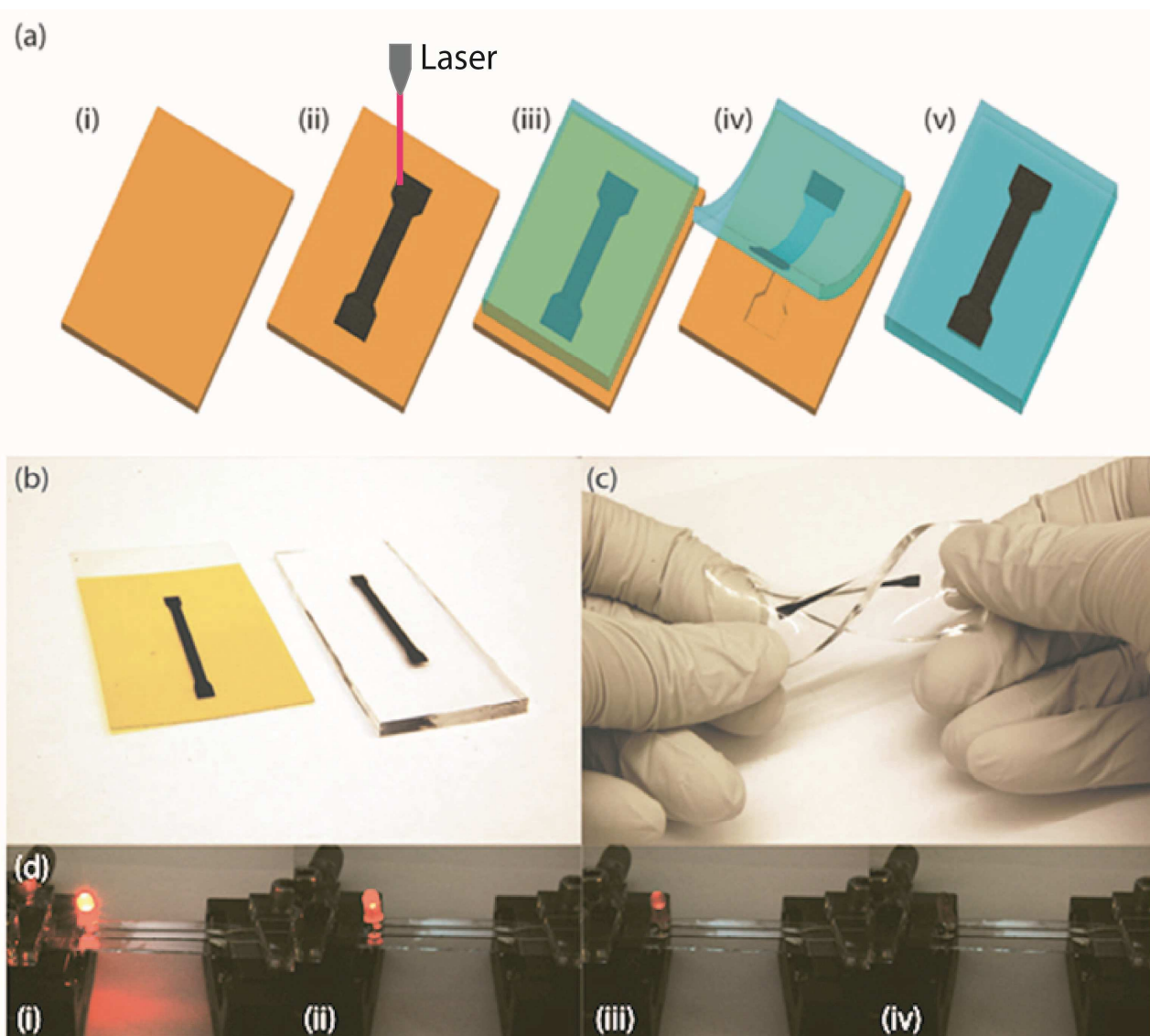


Figure 5.1. (a) Schematic of the fabrication process for stretchable carbon nanocomposite using laser pyrolyzation of polyimide: (i) attach polyimide tape to a PET sheet; (ii) laser-carbonize patterns on the polyimide; (iii) pour and impregnate carbon traces with diluted uncured PDMS; (iv-v) peel off the PDMS sheet after crosslinking. (b) A carbon trace before and after transferring to the PDMS. (c) A twisted carbon trace. (d) A lit LED connected to carbon traces showing diminished brightness as a function of strain: (i) 0%, (ii) 2%, (iii) 4%, (iv) 6%.

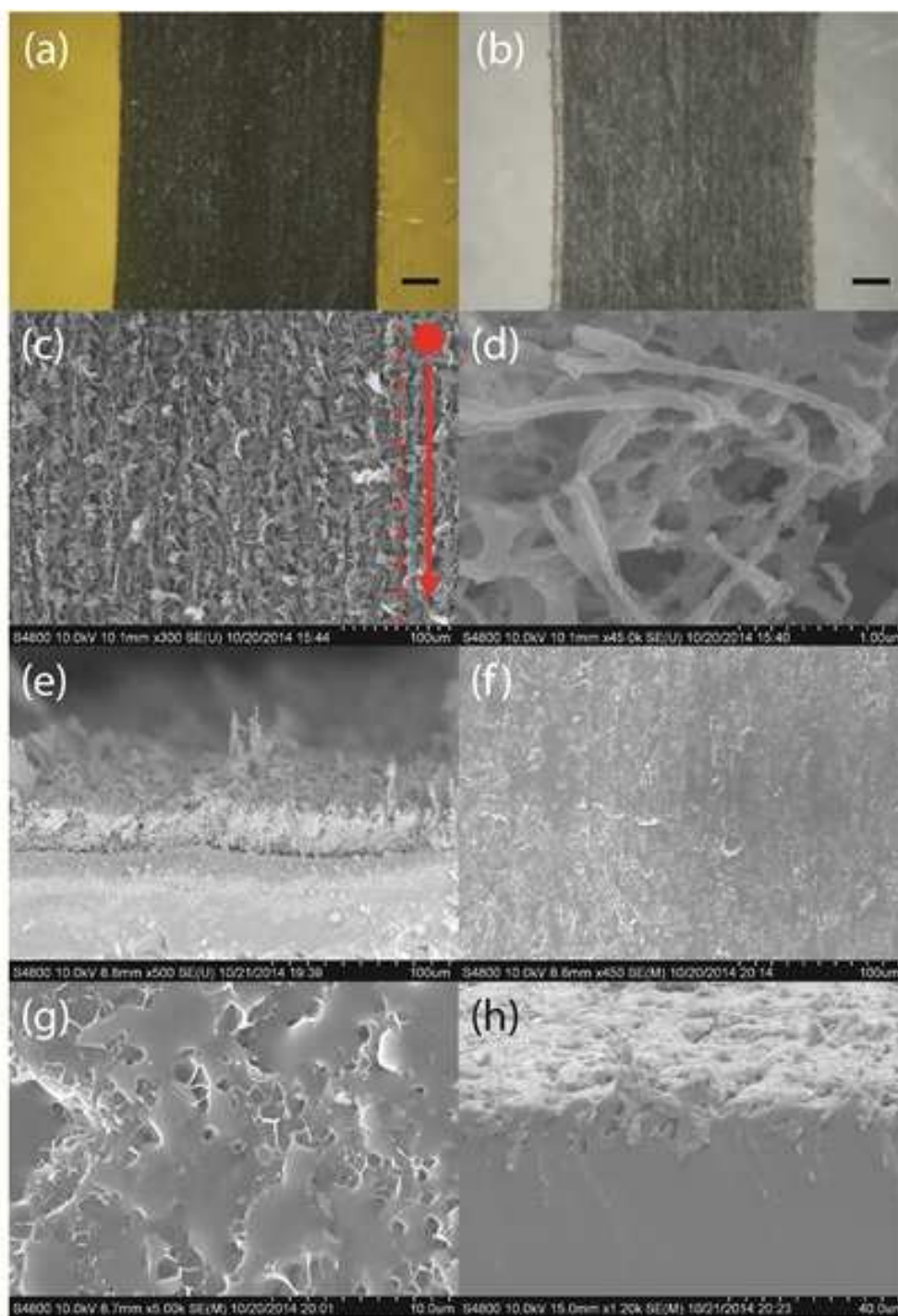


Figure 5.2. Surface and film architecture details. (a-b) Optical images of the carbonized polyimide before and after transfer to the PDMS. Scale bar 250  $\mu\text{m}$ . (c) SEM image of the aligned particles in the traces with the arrow showing the direction of laser ablation. (d) High magnification SEM image showing nanoparticles and fibers. (e) Cross section image of the carbon traces showing the porosity of the carbonized material. (f-g) SEM images of the carbon particles after transfer to the PDMS at different magnifications. (h) Cross section SEM of stretchable carbon traces embedded in PDMS.

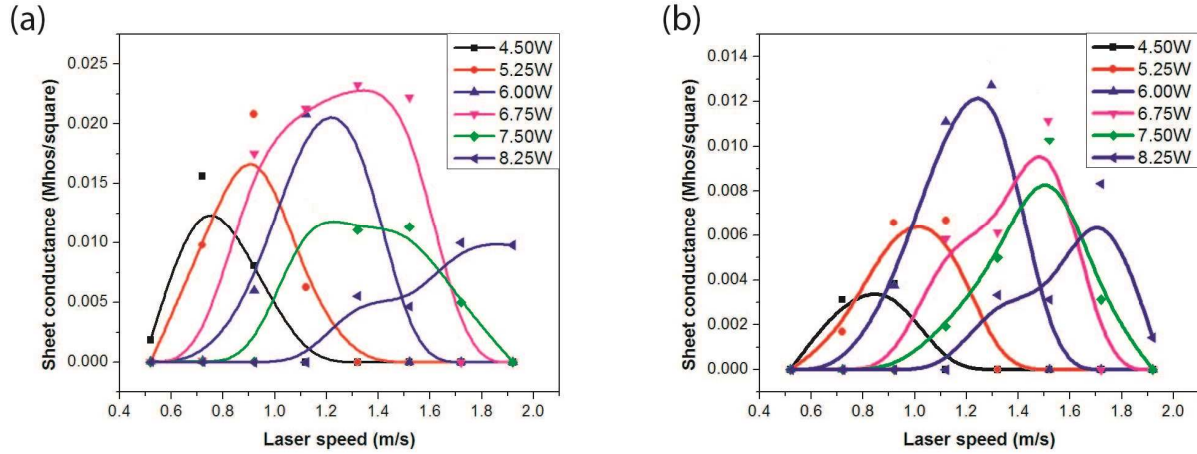


Figure 5.3. (a) Sheet conductivity of carbon trace on polyimide as a function of laser fabrication parameters (power and speed). (b) Sheet conductivity of carbon trace after transfer to the PDMS as a function of laser fabrication parameters (power and speed).

Figure 5.4(a) shows a series of pictures depicting the sensor under longitudinal (length) and transverse (width) strain. Unlike other composites in which the conductive nanoparticles are isotropically dispersed and oriented, the particles in our patterns possess an anisotropic orientation due to the abovementioned laser rastering process. This results in sensors with unidirectional sensitivity, i.e., conductivity is strongly affected by the longitudinal strain whereas remains essentially constant under transverse strain. The application of longitudinal strain increases the spacing between the conductive particles and lowers the number of contact points between the particles, resulting in an increased resistance. On the other hand, the number of contact points between the carbon particles does not change significantly when the device is stretched in the transverse direction. Figure 5.4(b-c) illustrates the relative change in resistance in response to the applied strain. The device exhibits a very large change in resistance ( $> 20 \text{ M}\Omega$ ) for 100 % longitudinal strain, Figure 4b, but its resistance changes negligibly ( $\sim 100 \text{ }\Omega$ ) in response to 100 % transverse strain, Figure 4c. The smaller decrease in the resistance for strain levels of  $< 40 \%$  (Figure 5.4(b)) can be attributed to the Poisson effect, which results in higher particle density in the middle of the trace (more contact points and increased conductivity). In both cases, the device showed no signs of failure for up to 100 % strain. Further stretchability is limited by the elastomeric properties of the PDMS substrate; however, this can be extended by using a more elastic material such as Ecoflex<sup>®</sup>. The uni-directionality of such sensors makes them suitable for

applications that require strain direction detection; for example, an orthogonal arrangement of three such sensors can form a coordinate system for measuring strain in three-dimensional space.

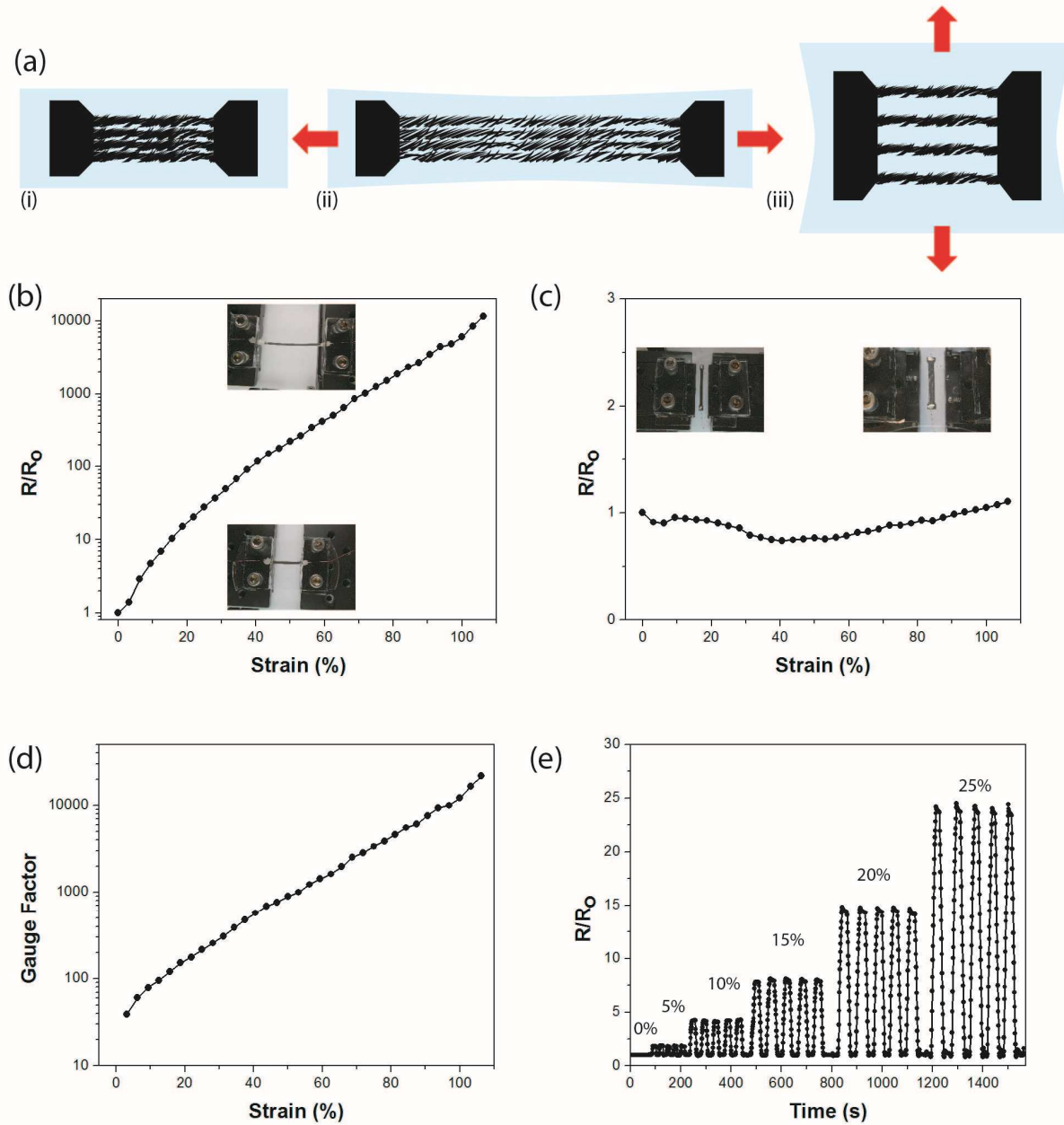


Figure 5.4. Characterization of the stretchable carbon traces subjected to longitudinal and transverse strain. (a) Illustrations of carbon traces (i) in their relaxed state, (ii) under longitudinal strain, and (iii) under transverse strain. (b) Plot of the relative resistance change for different levels of longitudinal strain. (c) Plot of the relative resistance change for different levels of transverse strain. (d) Gauge factor of the stretchable carbon traces versus longitudinal strain. (e) The dynamic stretch-and-release cycle response of the sensor for various strains 0–25 %.

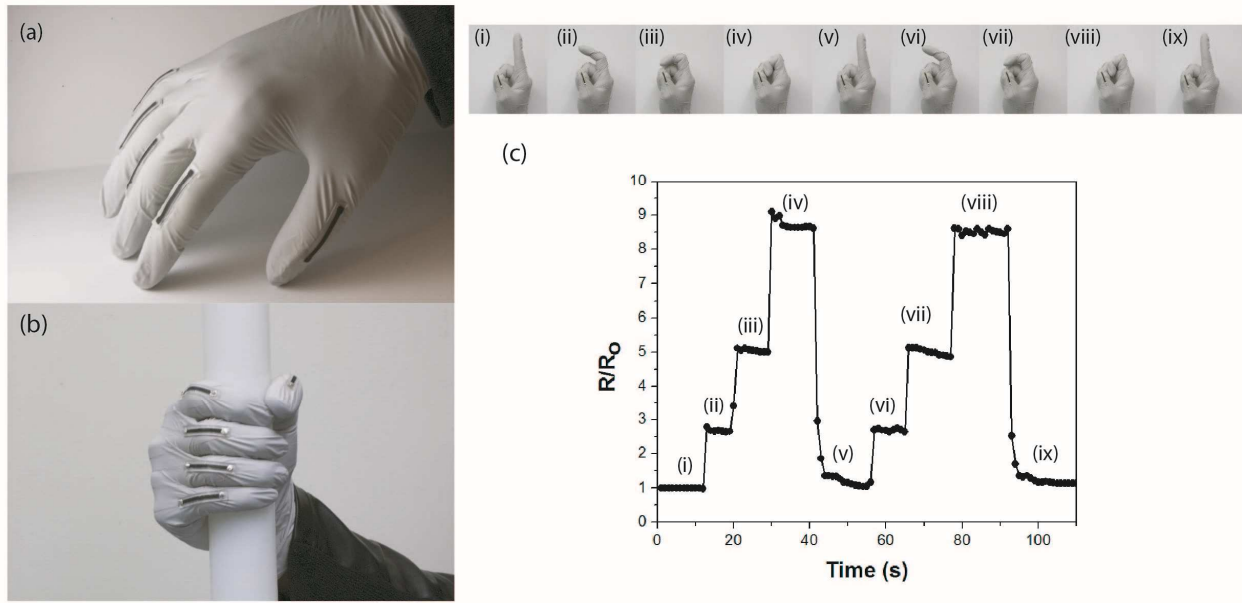


Figure 5.5. Human finger motion detection with stretchable carbon traces. (a-b) Photograph of five stretchable strain sensors attached to the finger joints on the glove. (c) Relative resistance change of the strain sensors at different bending stages over time; the corresponding finger configuration for each plot region (i-ix) is shown in the snapshots below the plot.

For comparison to other reported stretchable strain sensors, we calculated the gauge factor ( $G = \frac{R/R_0}{\Delta L/L}$ ) of our device from the measured data for both longitudinal and transverse strains. Figure 5.4(d) shows the longitudinal gauge factor (semi-log plot) as a function of strain. The exponential change in the gauge factor at higher strain levels is attributed to the drastic change in resistance at higher levels of longitudinal elongation (gauge factor of 50 at 5 % strain to a gauge factor of 20 000 at 100 % strain). This high gauge factor is significantly larger than those reported for conductive composites as well as metal strain gauges. The state-of-the-art graphene-based composites typically exhibit gauge factors within the range of 2–50, whereas CNTs and AgNWs sensors have an even smaller gauge factors 1–7<sup>20,28</sup>. In order to assess the dynamic performance of the device, the sensor was subjected to different levels of strain while the resistance was continuously measured. Figure 5.4(e) shows the results of five stretch-and-release cycles for strain levels of 0–25 %. The sensor shows a fast response (< 1 s) to the applied strain as well as a full recovery upon release. To demonstrate the utility of our technique as related to the fabrication of human motion sensors, we attached five strain sensors to a latex glove to detect the joint bending

motion, Figure 5.5(a-b). The sensors were attached to the glove by bonding their ends to the glove using a cyanoacrylate adhesive (Loctite® 420). Glove was subsequently donned and the bending angle (0–145°) of each finger at middle phalangeal joint was monitored by measuring the relative change in the resistance of strain sensors. The tests were conducted performing a stepped bending sequence in which the fingers were bent and held for a few seconds at each position. As Figure 5.5(c) shows the index finger at different bending angles and the time sequence of resistance change for two cycles ( $R/R_0 \approx 9$  for a completely bent joint).

### 5.1.2 Wireless pressure sensor

The described direct writing technology of carbon and silver in section 4.3 can be used to fabricate low-cost flexible sensors and actuators that require high electrically conductive traces. Here we have designed and fabricated a flexible passive wireless pressure sensor that can be used for wearable and implantable applications.

#### 5.1.2.1 Fabrication process and measurement technique

Figure 5.6(a,b) shows the fabrication process and working mechanism of the LC passive pressure sensor. The device consists of a pressure-sensitive capacitor with a variable spacing between its two electrodes that is connected in series with a planar spiral inductor. In this design, the coil provides an inductively-coupled link between the reader antenna and the LC passive pressure sensor, allowing wireless powering and information transfer. The resonant frequency of the sensor can be expressed as a function of the inductance (L) and capacitance (C) as follows[193], [194]:

$$f = \frac{1}{\sqrt{LC}} \quad (5.1)$$

When pressure is applied to the LC resonant circuit the gap between the two electrodes of the capacitor decreases, leading to an increase in the capacitance of the circuit. This change results in a reduction in the resonant frequency of the LC circuit that can be detected wirelessly by an external readout coil. We used a network analyzer to determine the resonant frequency of the sensor at various levels of pressure by measuring the location of the phase-dip in the impedance of the external coil. Passive LC resonant sensors require highly conductive traces for making the inductor and capacitor. The direct laser writing of carbon-silver nanocomposite described in this

section is uniquely suited for their fabrication (carbonized polyimide traces have large resistance, degrading the circuit electrical quality factor and making the readout challenging and not accurate).

Figure 5.6(a) shows the fabrication process using the presented conductive printing technique combined with a simple folding approach to make the inductor and capacitor used in the sensor. The inductor coil and the two capacitor electrode patterns were fabricated on a flexible polyimide substrate by using the aforementioned laser carbonized and silver deposition technique. Next, a 50  $\mu\text{m}$ -thick film of PDMS (Dow Corning Sylgard® 184, 10:1 ratio) was cast onto the conductive patterns and allowed to crosslink at 60 °C for 20 min. To fabricate the cavity needed for the pressure sensitive capacitor, a 300  $\mu\text{m}$ -thick film of PDMS with predefined hole-punched openings was bonded to the PDMS coating. The bonding between the two layers of PDMS was achieved by a standard PDMS-to-PDMS bonding procedure using corona treatment (BD-10A High Frequency Generator, Electro-Technic Products, Inc.) followed by annealing on a hotplate at 90 °C for 2 h. Finally, the substrate was folded in half and bonded to create the final wireless pressure sensor with the PDMS cavity between the two conductive patterns. For wireless measurements, the fabricated wireless sensor was coupled with a transceiver coil comprising a single 25 mm-diameter loop of wire that was used to detect the changes in the resonant frequency of the pressure sensor under different pressure levels, Figure 5.6(b).

#### 5.1.2.2 Results and discussion

The transceiver coil was fixed mechanically in close proximity to the sensor coil using an acrylic support and connected to a network analyzer. The pressure sensitivity of the sensor was measured by placing the sensor in a sealed chamber and applying pressurized air via an external syringe pump. The change in the resonant frequency was characterized by measuring the dip in the impedance phase for gauge pressures ranging from 0 to 97 kPa, Figure 5.6(c). As can be seen, increasing the pressure results in shifting the position of the dip to lower frequencies. The resonant frequency of the sensor as a function of applied pressure is shown in Figure 5.6(d). As expected, the resonant frequency decreases linearly with pressures up to 97 kPa, with an average sensitivity of  $-26 \text{ kHz/kPa}$ .

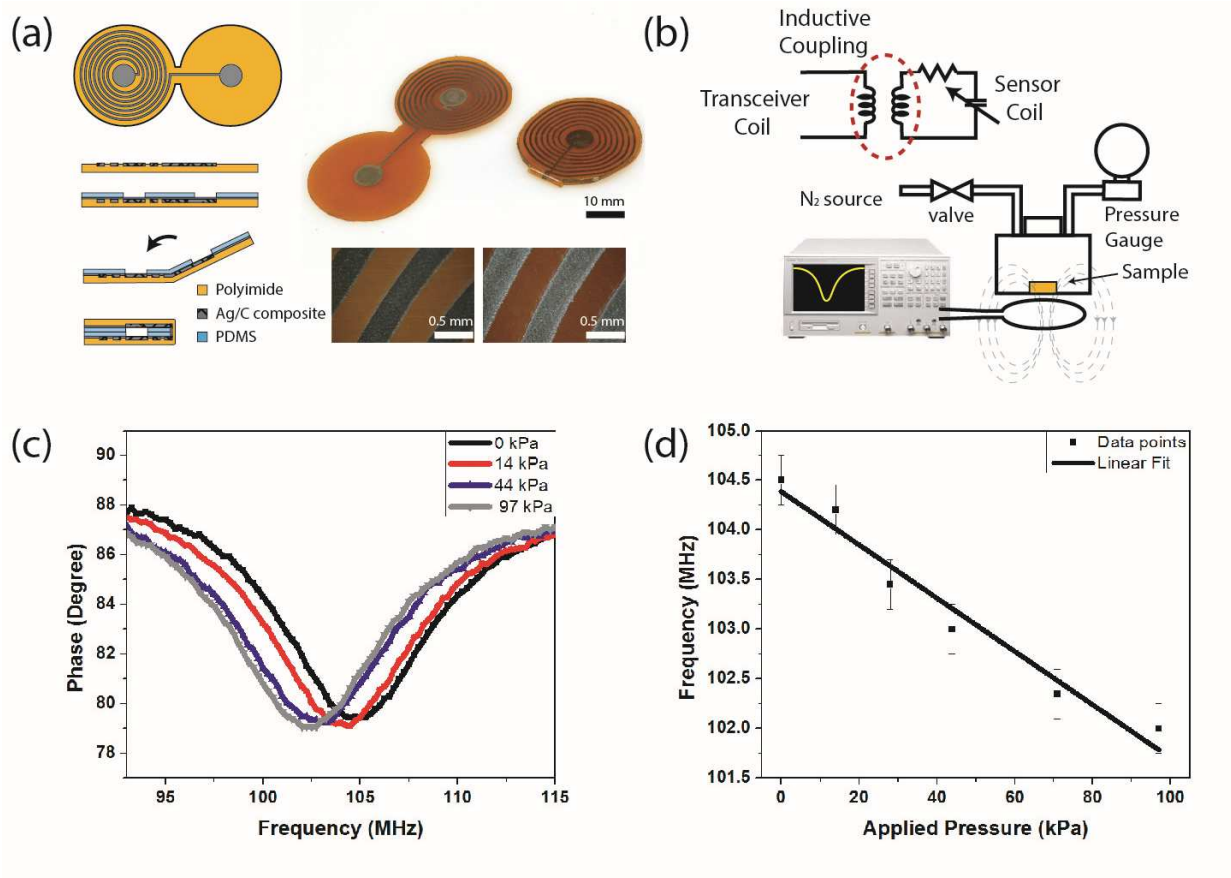


Figure 5.6. (a) Fabrication process of wireless LC passive pressure sensor, (b) experimental setup and readout apparatus used for sensor characterization, (c) impedance phase versus frequency at several different pressures, (d) sensor resonant frequency vs. pressure.

## 5.2 Electrochemical sensors

Normal acute wounds are cutaneous lesions that follow the four physiological healing phases of hemostasis, inflammation, proliferation, and remodeling in an appropriate length of time (usually a week or two) [195]. Pathological interferences with these pathways can result in non-healing chronic wounds [196], [197]. Chronic wounds, such as diabetic foot and bed sores, affect an estimated 6 million individuals in the United States and cost an estimated \$25 billion per year to treat and manage [198]. These numbers are expected to increase significantly with an aging population and recent epidemic of obesity and diabetes [199]. Current wound management is based on simple forms of intervention that require frequent change of the dressing with wound state

assessment relying on visual inspections that are often subjective and cannot provide correct insight into the status of the wound[200], [201]. Prompt detection of improper wound healing via sensor-embedded smart dressings can significantly improve the treatment efficacy[24].

The halt or slowdown in the healing processes can increase the likelihood of bacterial colonization, which in itself prohibits timely closure and result in added complexity to an already challenging clinical problem (in severe cases, bacterial infection can lead to amputations of the limb while unnecessary use of antibiotics can contribute to the spread of antibiotics resistant pathogens) [202], [203]. Infection can further delay the angiogenesis, collagen formation, and macrophage activity that are strongly dependent on the pH value of the wound-milieu. Under normal physiological conditions, the skin has a low pH value of 4-6 that is a result of the amino acids and fatty acids products secreted by the keratinocytes [204]. Most pathogenic microorganisms require a more alkaline environment to promote their growth and colonization [205]. In acute wounds, invading neutrophils reduce the pH to values that counteract the bacterial colonization, whereas chronic wounds are more alkaline (pH 7.15 to 8.9) and thus susceptible to infections [206]. In severe cases, increased pH is correlated to the formation of antibiotic-resistant biofilm on the wound, [207] requiring intensive antibiotic therapy and surgical intervention. Monitoring the wound pH can provide favorable insight into earlier identification of non-healing wounds and help the implementation of more effective treatment strategies.

Most reported wound pH measurements conducted in clinical studies have used flat glass membrane pH probes that require the removal of the wound dressing; these are impractical for patient management and can cause further disruption to the tissue [205], [208]. In recent years, several platforms have been proposed as alternative methods for sensing the pH of the wound. These measure the pH based on optical, chemo-mechanical, and electrochemical transduction methods. The simplest forms of optical-based sensors are the pH test paper strip that provide an inexpensive method to measure the pH of the wound environment. These, however, lack accuracy and can only be used for a single measurement [209]. Optical fiber pH sensors provide adequate accuracy, flexibility, and stability for *in-vivo* pH sensing. In this technique, pH sensitive materials are immobilized onto silica optical fibers connected to a spectrophotometric device that can measure pH-dependent absorption spectra [210]–[212]. These sensors are however expensive and require bulky optical spectroscopy instruments.

Chemo-mechanical sensing methods use pH-sensitive hydrogels which shrink or swell with the change in pH of the environment. A recent work by Sridhar and Takahata featured a wireless hydrogel-based pH sensor that consisted of an inductive transducer fabricated by folding a coplanar dual spiral coil with the pH sensitive hydrogel sandwiched between the folded substrates [213]. The swell/shrink behavior of the pH sensitive hydrogel results in a change of the device inductance, hence varying the resonant frequency of the device that can be detected using an interrogating antenna. Although the device provides wireless measurements, several difficulties limit the performance and application of this sensor. These include a slow response time, costly fabrication, and complex measurement equipment (e.g. network analyzer). Recent progresses in the fabrication of flexible and miniaturized electrochemical sensors have provided a compelling rationale for the integration of such pH sensing devices into the wound dressings. These, however, still face limitations associated with the required use of high-cost clean-room processes for their fabrication and wired electrical connection to bulky potentiostatic readout systems [214], [215]. Although considerable efforts have been devoted to the fabrication of the low-cost electrochemical sensors using rapid large-scale technologies such as inkjet and screen-printing, [149], [216], [217] these devices still require hardwire electrical connections. The ability to make more economical, optically transparent sensors with simple wireless read-out utilizing today's smartphone interface technology can significantly advance the care and management with chronic wounds [218].

In this section we present a practical, low-cost solution that consists of a disposable sensor module fabricated by laser ablating commercial indium tin oxide (ITO) films (for optical transparency) interfaced with a reusable flexible potentiostat circuit with wireless near field communication (NFC). In the next section we will demonstrate the use of laser carbonization and micromachining in fabricating stretchable pH sensors.

### **5.2.1 Flexible and transparent pH sensor with NFC communication**

Figure 5.7 shows an illustration of the wireless pH monitoring devices that can easily be integrated into standard wound dressings. The device consists of two major components: a flexible transparent pH sensor that is disposable and a flexible wireless NFC interface circuit that is reusable. The conductive transparent electrodes are fabricated by direct laser scrubbing commercial ITO films on a PET substrate. The pH measurement is based on open circuit potential measurement between an Ag/AgCl reference electrode and a pH-sensitive electrodeposited

polyaniline electrode. The battery-less NFC interface operates at 13.56 MHz (ISO15693) radio-frequency identification (RFID) band, compatible with Android smart phones. The data transmission between the pH sensing platform and the smart phone occurs by bringing the reader to within the 4 cm proximity of the NFC tag. The communication channel is based on the magnetic induction between two loop antennas located within the reader and the tag, effectively forming an air-core transformer. The reader emits a radio-frequency field that powers the NFC tag. The tag in turn uses the harvested energy to power the on-board chip, providing a rectified power supply for the pH sensing buffer circuit.

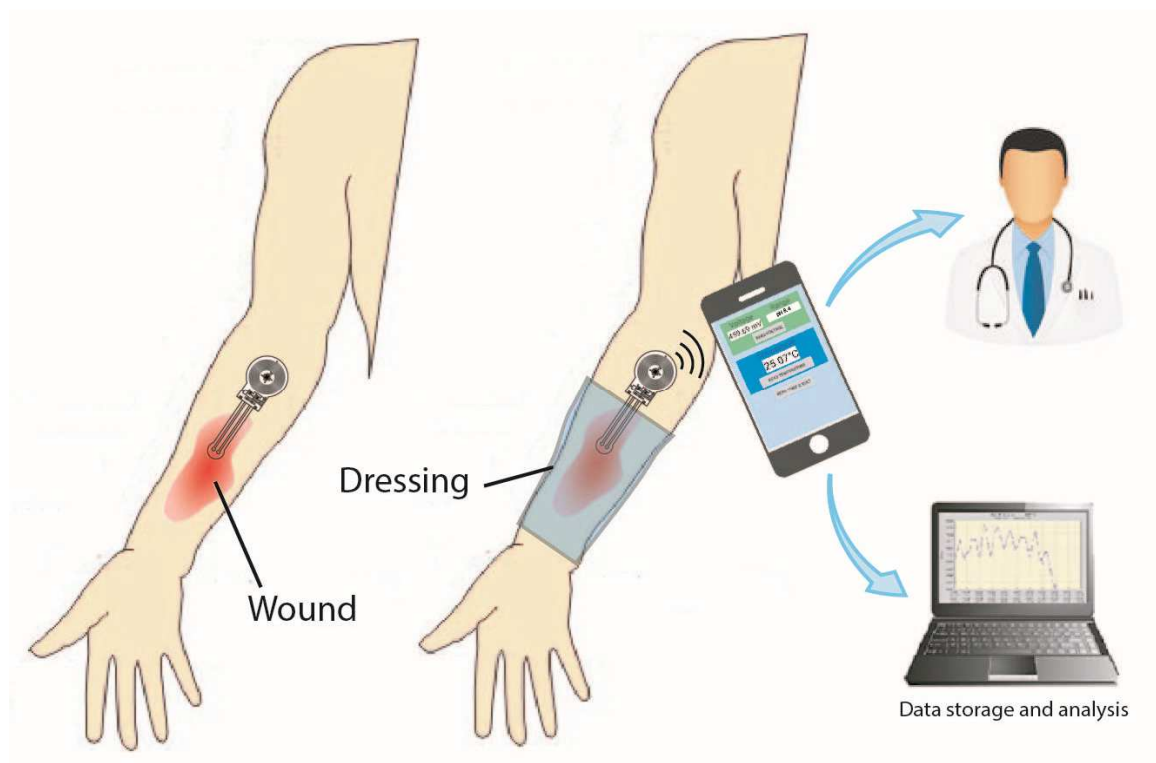


Figure 5.7. Flexible wireless wound pH monitoring system utilizing NFC communication.

### 5.2.1.1 Transparent pH sensor fabrication

The sensing electrodes and their electrical interconnects were fabricated on a commercial ITO coated flexible PET substrate (130 nm ITO on 120  $\mu\text{m}$  PET) purchased from Sigma Aldrich. The process of laser scribing/cutting and screen printing the potentiometric sensors are illustrated in Figure 5.8(a). The patterning of the ITO film was done by laser-scribing (Universal Laser Systems, Inc., Scottsdale, AZ) using an optimized energy density of 6 J/cm<sup>2</sup>, (Figure 5.8(a)i). The

ITO electrodes were separated from the ITO film by laser cutting the periphery of the sensor at higher energy density ( $14 \text{ J/cm}^2$ ), Figure 5.8(a) i, ii. The controlled laser machining process ablated the conductive ITO coating on the PET substrate leaving behind an isolated array of transparent and flexible tracings. To prevent the shorting of and reduce crosstalk between the interconnections in the aqueous environment, a transparent UV-curable adhesive (Henkel Loctite® 3105) was screen printed onto the conductive traces to define the active area and contact pads, Figure 5.8(a).iii. The insulator was cured under UV light for 10 min. In order to define the reference electrode, a silver overlaid layer was screen printed on one of the ITO electrode, Figure 5.8(a)iv. The screen printing stencils for these processes were prepared by laser cutting adhesive tape (3 M® MagicTape™) at a power and speed of 15W and 0.2m/s. The tape stencil was attached to the ITO film and silver ink (118-09, CreativeMaterials, Ayer, MA) was screen printed. The ink was then allowed to cure at  $70^\circ\text{C}$  for 15min. The silver electrode layer was then electrochemically chloridized in order to create the Ag/AgCl layer for the reference electrode. The chloridization process was performed using a constant current density of  $4 \text{ mA/cm}^2$  between the silver electrode and a Pt electrode in a solution of 1 M NaCl solution for 5min, forming a uniform dark grey layer of AgCl on the reference electrode. The electrode was then rinsed with DI water and blow-dried using nitrogen, Figure 5.8(a)v.

The working electrode, the  $\text{H}^+$  ion-selective membrane, was prepared by electropolymerization of aniline on the pre-defined ITO areas Figure 5.8(a)vi using a three electrode system (BASi Epsilon Potentiostat, Bioanalytical System Inc.). In this system, Pt wire was used as a counter electrode, Ag/AgCl as the reference electrode, and the ITO as the working electrode. The polymerization was performed at a constant potential of 0.8 V versus Ag/AgCl in a solution of 0.1 M aniline with 1 M HCl for 2min, forming a translucent green coating of PANI on the ITO electrode. The thickness of the deposited polymer can be controlled by adjusting the electropolymerization time. After polymerization, the electrodes were rinsed with DI water and blow-dried with nitrogen. The final step consisted of creating a solid-state reference membrane by mixing fine KCl powder with UV curable adhesive (Henkel Loctite® 3105), drop casting it onto the Ag/AgCl electrode, and curing under UV light for 10 min, (Figure 5.8(a)vii). During the UV exposure, the PANI film was protected with an aluminum film. After complete curing of the reference membrane, protective layer was removed and the sensor was ready to use.

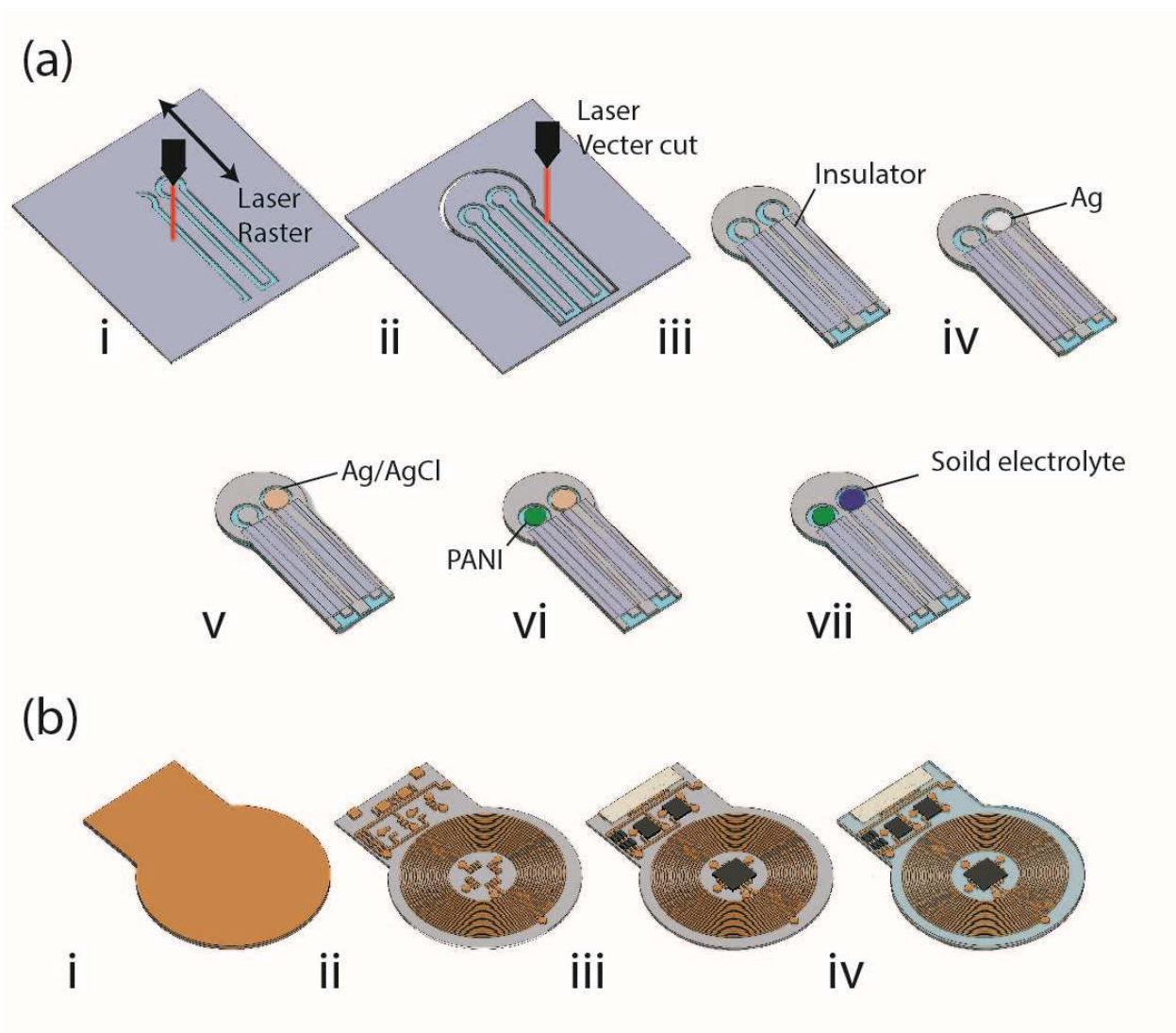


Figure 5.8. Fabrication process of (a) pH sensor on ITO film and (b) flexible battery-less NFC module

### 5.2.1.2 Electronic readout circuit

The NFC interface circuit was fabricated on a flexible polyimide sheet (PI) with copper laminated on both sides, Figure 5.8(b). The circuit was patterned using photolithography and the exposed copper was wet etched (CE-200, Transene), Figure 5.8(b)i, ii. Next, the NFC transponder microchip (SL13 from AMS) and the surface mount buffer components were soldered onto the flexible PCB, Figure 5.8(b),iii. PDMS pre-polymer (Dow Corning Sylgard® 184, 10:1 ratio) was then prepared, degassed under vacuum, poured onto the circuit, and cured at 70 °C for 2 hours;

thus, forming a  $\sim 500$   $\mu\text{m}$ -thick layer of passivation, Figure 5.8(b)iv. The low power analog buffer circuit (AD8603, Analog Devices Inc.) was designed to form dual-operational amplifiers with ultra-low input bias current.

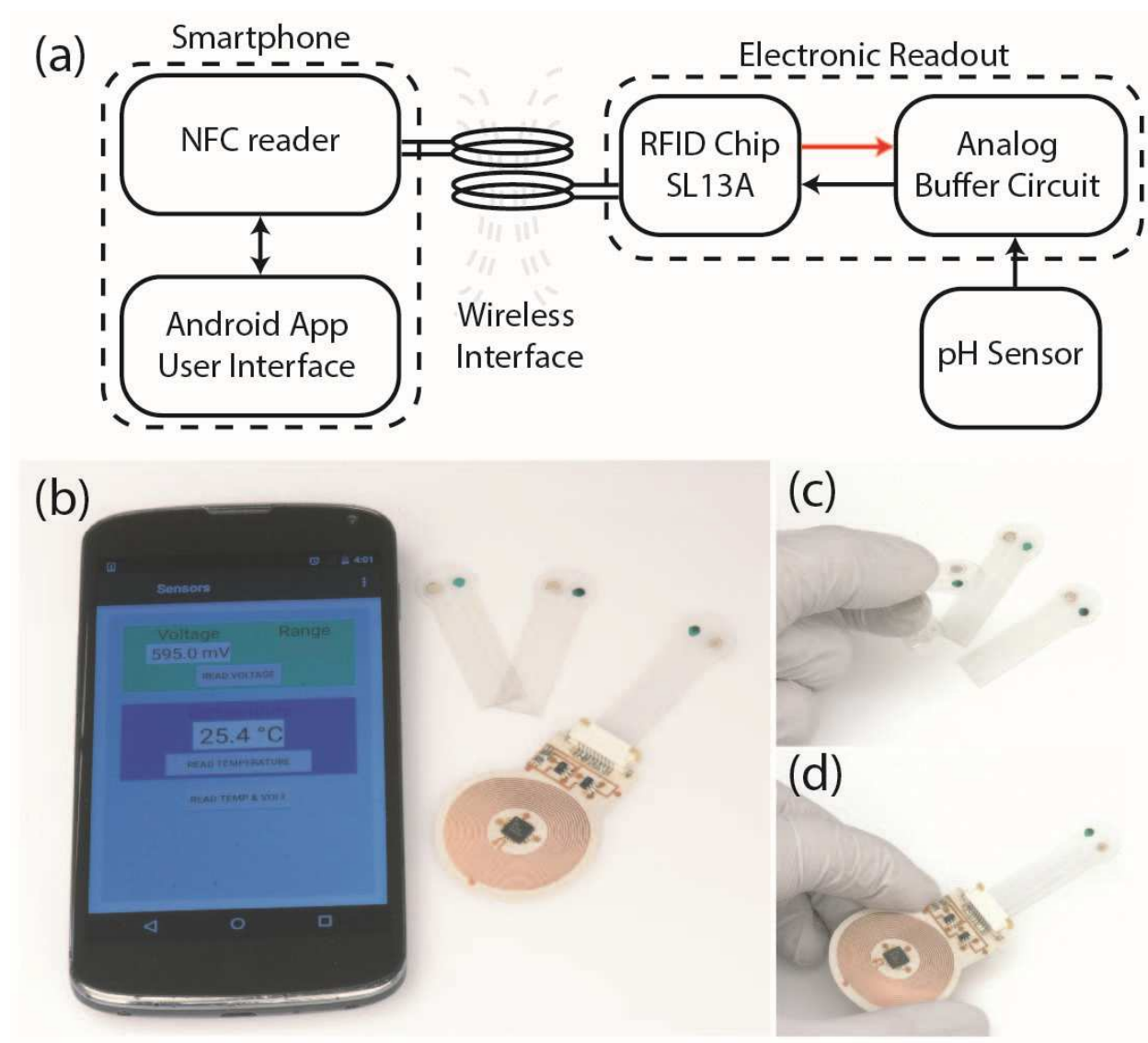


Figure 5.9. (a) Block diagram of the developed wireless NFC tag, black arrows represent data communication and red one represent power transfer, (d) photograph of completed wireless pH monitoring device and smartphone interface, images illustrating the flexibility of the (c) sensor and (d) wireless NFC module.

The pH sensors have high source impedances ( $10\text{ M}\Omega$  to  $1\text{ G}\Omega$ ) requiring low input current amplifiers. The SMD operational amplifiers with  $0.1\text{ pA}$  input bias current and  $40\text{ }\mu\text{A}$  supply

current was chosen for this application. The transponder has an integrated 10-bit A/D converter that can be multiplexed between its internal temperature sensor and the external flexible pH sensor. The NFC transponder allows wireless communication with either a smartphone (with Android operating NFC communication) or PC-based NFC reader (AS3911) by bringing the reader to close proximity of the tag (<4 cm). The Android app provides a simple user interface that allows wireless interrogation of temperature and pH in the wound bed. The block diagram of the wireless readout system is shown in Figure 5.9(a). Photographs of the disposable pH sensor (working areas of 2 mm in diameter) and the wireless NFC readout module (25 mm× 35 mm) are shown in Figure 5.9(b-d).

The optical transmittance for different films in buffer solutions of pH 4 and 10 are shown in Figure 5.10. The UV spectra shows the optical transparency of the ITO film before and after laser ablation in different pH solutions. However, as shown in the inset picture, the electrodeposited PANI shows a clear color change in different pH buffers (green in pH 4 and blue in pH 10). In acidic solutions, the polyaniline film has the green color of its emeraldine salt phase (less absorption at ~530 nm), while in an alkaline medium, it exhibits the blue color of its emeraldine base with a less absorption in the blue wavelength region of the spectra (~440 nm).

### 5.2.1.3 Characterization of the sensor and wireless module

The sensitivity of the pH sensor was evaluated by measuring the potential difference between the PANI working and Ag/AgCl reference electrodes at physiologically-relevant pH values of 4-10. Figure 5.11(a) shows the temporal response of less than 28 sec for increasing and decreasing pH steps. Figure 5.11(b) shows the potential values obtained from the cyclic titration measurements. The sensors exhibit a linear Nernstian response of -55 mV/pH with a correlation coefficient  $r^2=0.985$  across the pH range of 4-10.

For wound monitoring applications, it is essential that the sensor and the electronic interface maintains their performance under different mechanical deformations. The pH sensors performance was tested on a series of curved surfaces. The bending test showed less than  $\pm 4$  mV change in the output of the sensors and mechanical deformation had minimal affect the performance of the sensor, Figure 5.11(b). The working performance of the NFC module on different curved surfaces was also determined by measuring the RF reflection coefficient ( $S_{11}$ ). Figure 5.12(a) shows the  $S_{11}$  spectrum with the presence of NFC module on different curved

surfaces from flat to 2 mm radius of curvature. The unbent NFC modules display a resonant frequency of  $13.45 \pm 0.05$  MHz, where  $S_{11} = 12.2$  dB. Bending the tag shifts the minimum resonant frequency to higher values while at the same time decreasing and dip size (the dip was not noticeable at radius of curvatures smaller than 5 mm). The functionality of flexible circuit was also characterized by directly measuring the rectified output voltage on the NFC transponder. In flat and moderately bent conditions the RF signal on the receiver coil activated the tag providing a 3.4 V power supply for the circuit. However, at radii of curvatures smaller than 5 mm, the transmitted power was insufficient to activate the tag, Figure 5.12(b).

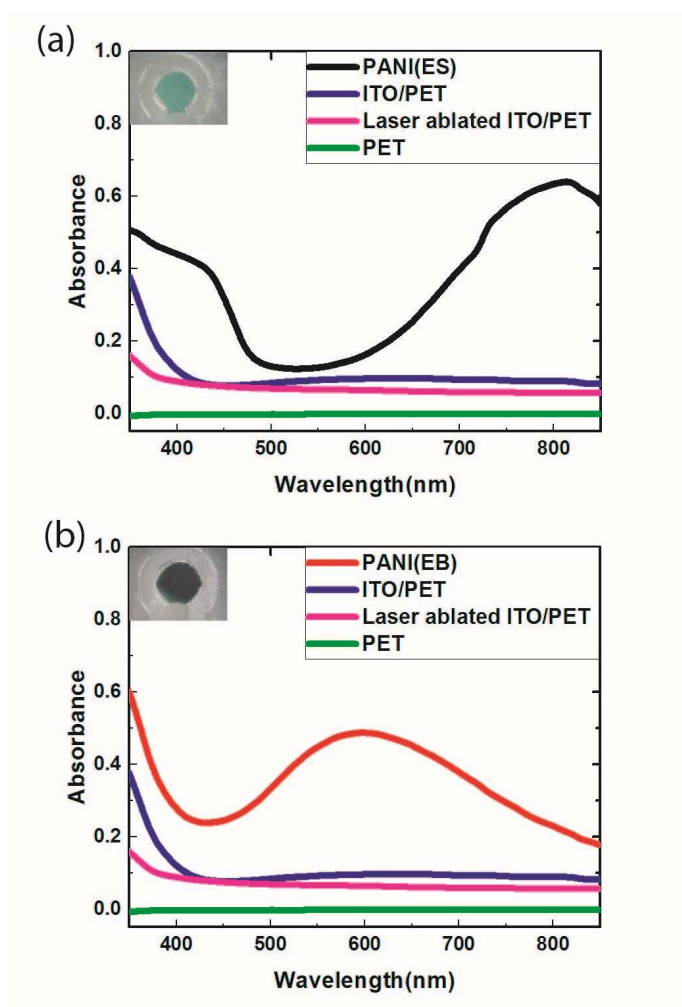


Figure 5.10. UV-Vis. Spectra of different layers of the pH sensor in the range of 300–900 nm. The obtained spectra were measured in buffer solutions of (a) pH 4 and (b) pH 10, insets show emeraldine salt (green) and emeraldine base state (blue) of the electro-polymerized polyaniline.

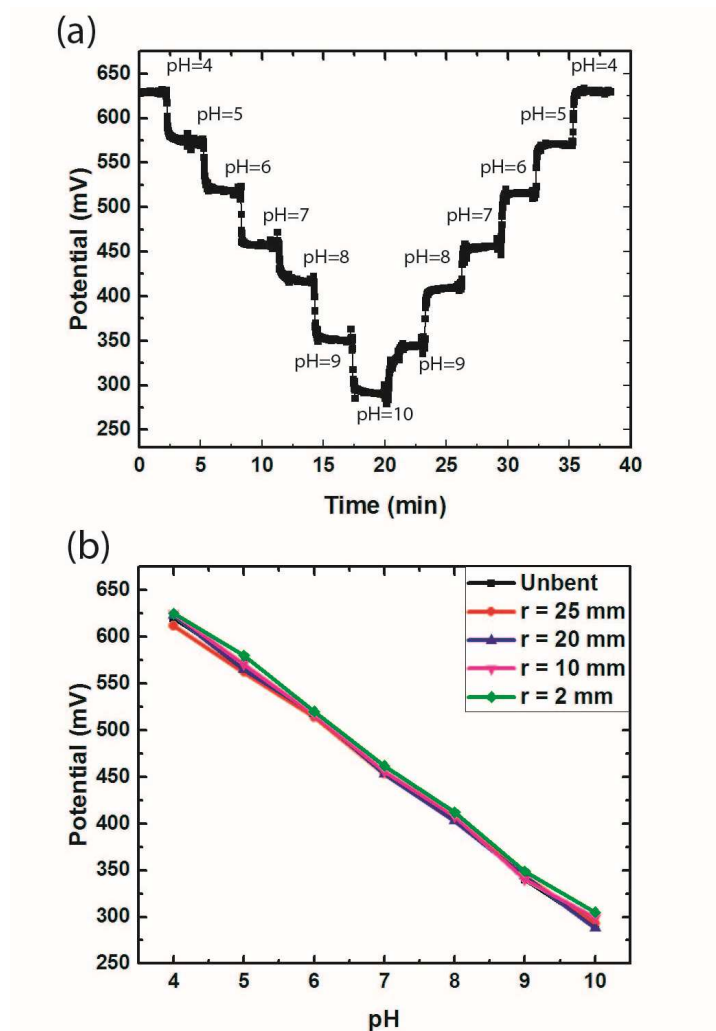


Figure 5.11. (a) Dynamic response of the pH sensor from pH 4 to 10, (b) EMF response of the pH sensor to various mechanical bending, inset schematic illustrates the bending mode and radius of curvature ( $r$ ) in the experiment.

Long-term stability is an important parameter for practical applications of electrochemical sensors since any significant drift require re-calibration which is not feasible in many situations. In order to evaluate the stability of the sensors, they were placed into standard pH buffer solutions and their output was monitored over a period of 24 h. Figure 5.13 shows continuous readings from the sensors in buffer solutions ranging from pH 4 to 10. As can be seen, the sensors had a noticeable but different drift characteristic in acidic and alkaline environments. In the alkaline solutions of pH 10 and 8 the sensors showed a drift of  $-0.63$  mV/h and  $-0.7$  mV/h, respectively (average drift of  $\sim 15$  mV or 0.2 pH unit over 24 hours). However, in the acidic solutions of pH 4 and 6 a lower drift of  $-0.38$  mV/h and  $-0.37$  mV/h was observed (average drift of  $\sim 9$  mV or 0.16 pH unit over

24 hours). In either conditions the sensors yielded an adequate level a stability suitable for application that require frequent (daily) replacement such as wound monitoring in which the sensor can be easily replaced during the daily change of the dressing. Figure 5.14(a) illustrates the microfluidic platform used to emulate the infected wound with the potentiometric-time trace measurements shown in Figure 5.14(b). The sharp change corresponds to the diffusion of ions into the gel which settles at 410 mV after approximately a 1 h, close to measurements observed in the buffer solution of pH 8. Furthermore, the inset in Figure 5.14(b) shows the optical transparency of the sensor and visible color change of the wound phantom (gel with pH indicator) from yellow to red over time sequences of 1h. This study demonstrates that presented sensor is able to detect pH fluctuations with in the physiologically relevant range of pH 5–8 as well as providing optical transparency for visual inspection of the wound.

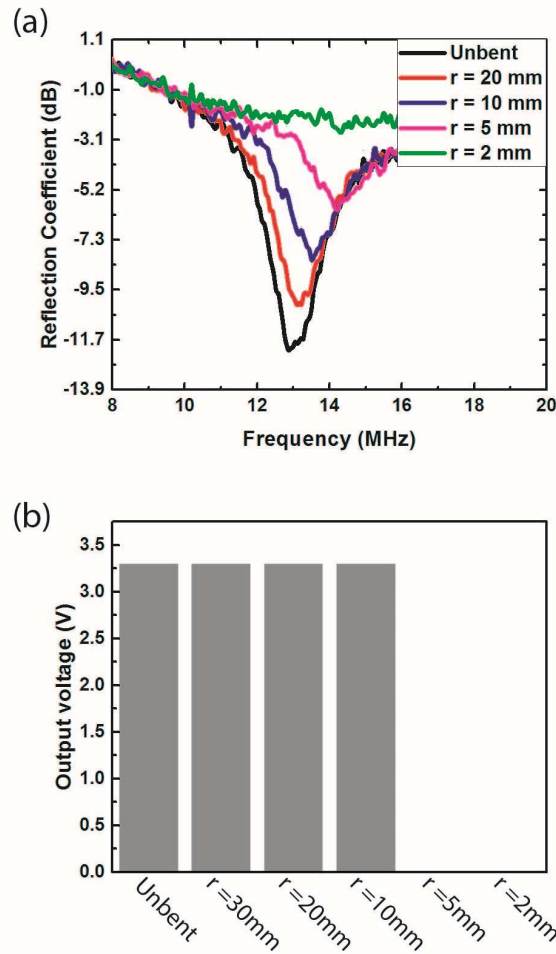


Figure 5.12. (a) Measured reflection coefficient, and (b) output voltage power supply of the wireless module versus frequency at various degrees of mechanical bending.

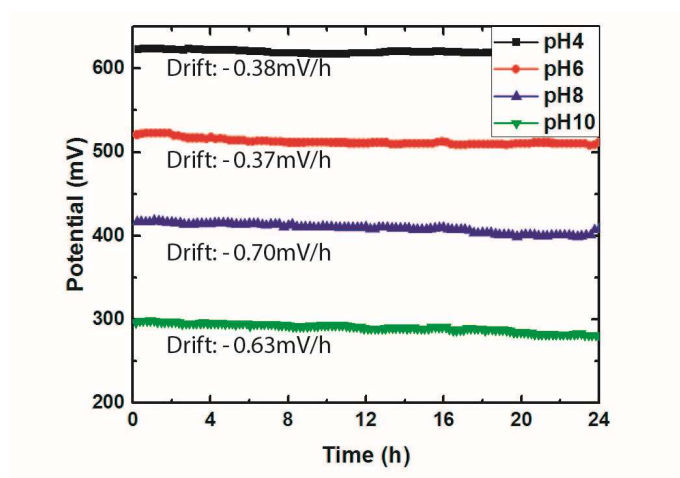


Figure 5.13. Drift behavior of the pH sensors at pH 4, pH 6, pH 8 and pH 10.

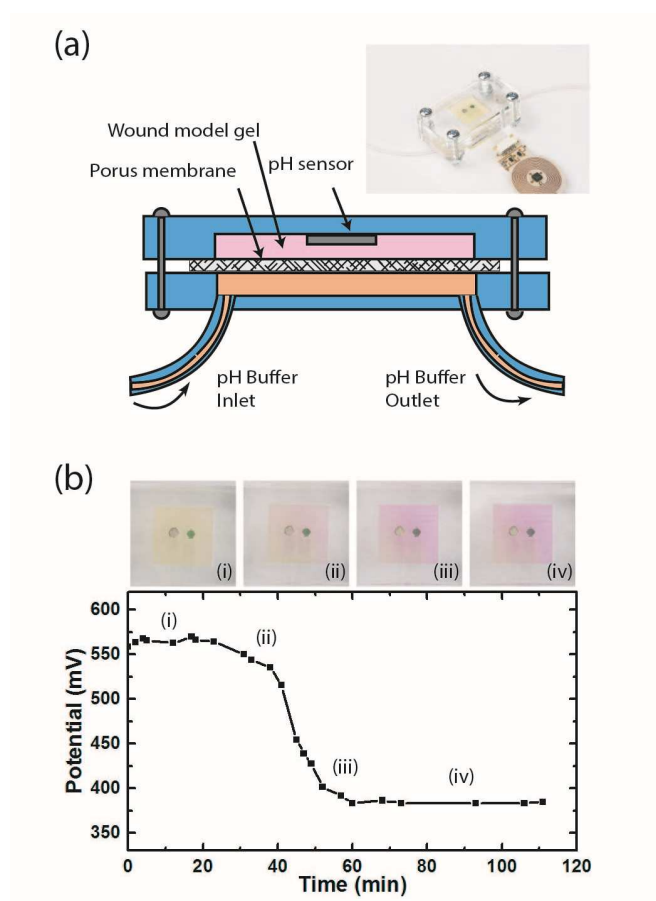


Figure 5.14. (a) Microfluidic test setup to emulate wound condition, (b) real-time recording of the pH changes in the hydrogel wound model, the corresponding color change of the emulated wound model for each region i-iv is shown in the snapshots above the plot.

## 5.2.2 Highly stretchable pH sensor via direct laser-writing/machining

Despite some effort towards the development of pH sensing devices for wound monitoring[219], [220] the majority of these sensors have several shortcomings such as structural weakness, limited stretchability (limiting their use over bending joints), and complicated fabrication processes. Herein, we report on a highly stretchable electrochemical pH sensor for wearable point-of-care applications that consists of a pH sensitive working and a liquid-junction-free reference electrode, in which the stretchable conductive interconnections are fabricated by laser carbonizing and micromachining of a polyimide sheet bonded to an Ecoflex substrate. This method produces highly porous carbonized 2D serpentine traces that are subsequently permeated with polyaniline (PANI) as the conductive filler, binding material, and pH sensitive membrane. The described method is based on CO<sub>2</sub> laser carbonization and functionalization with pH sensitive polymer (polyaniline) presented in section 3.3. Biocompatibility tests were also performed in order to evaluate the cytotoxicity of the materials utilized in the fabrication of the sensors and assess their safety for application that require direct contact with the wound tissue. The present process brings several major improvements to the production of stretchable electronic devices, including the combination of laser-induced generation of conductive carbon micro/nano material and substrate shaping into a single process. The described low-cost method eliminates the need for alignment and complications associated with printing conductive micro/nano material

### 5.2.2.1 Fabrication process

As illustrated in Figure 5.15 the fabrication process of the interconnection and working electrode of the sensor is similar to the process described in section 3.3.

The reference electrodes used in this sensor was prepared by screen printing a layer of silver ink on one of the PANI/C-PI electrodes. The ink was cured in an oven at 80 °C for 15 min. The silver electrode was then chloridated by immersing the electrode in a 0.1 M FeCl<sub>3</sub> solution for 15 min, transforming it into an Ag/AgCl reference electrode. In order to provide a stable potential, the Ag/AgCl electrode was covered by a solid electrolyte made by mixing KCl with of 20 % v/v Ecoflex. The Ecoflex binder is used to impart stretchability to the solid electrolyte.

Figure 5.15(h) shows an array of six pH working electrodes and two reference electrodes. The devices is robust and can withstand extreme mechanical deformations, Figure 5.15(i). The stretchability and pliability of the Ecoflex substrate enables the device to be conformably wrapped

around the complex non-planar surface of the human body, Figure 5.15(j). This allows the device to remain in contact with the skin even at joints with high degree of freedom such as elbows and knees.

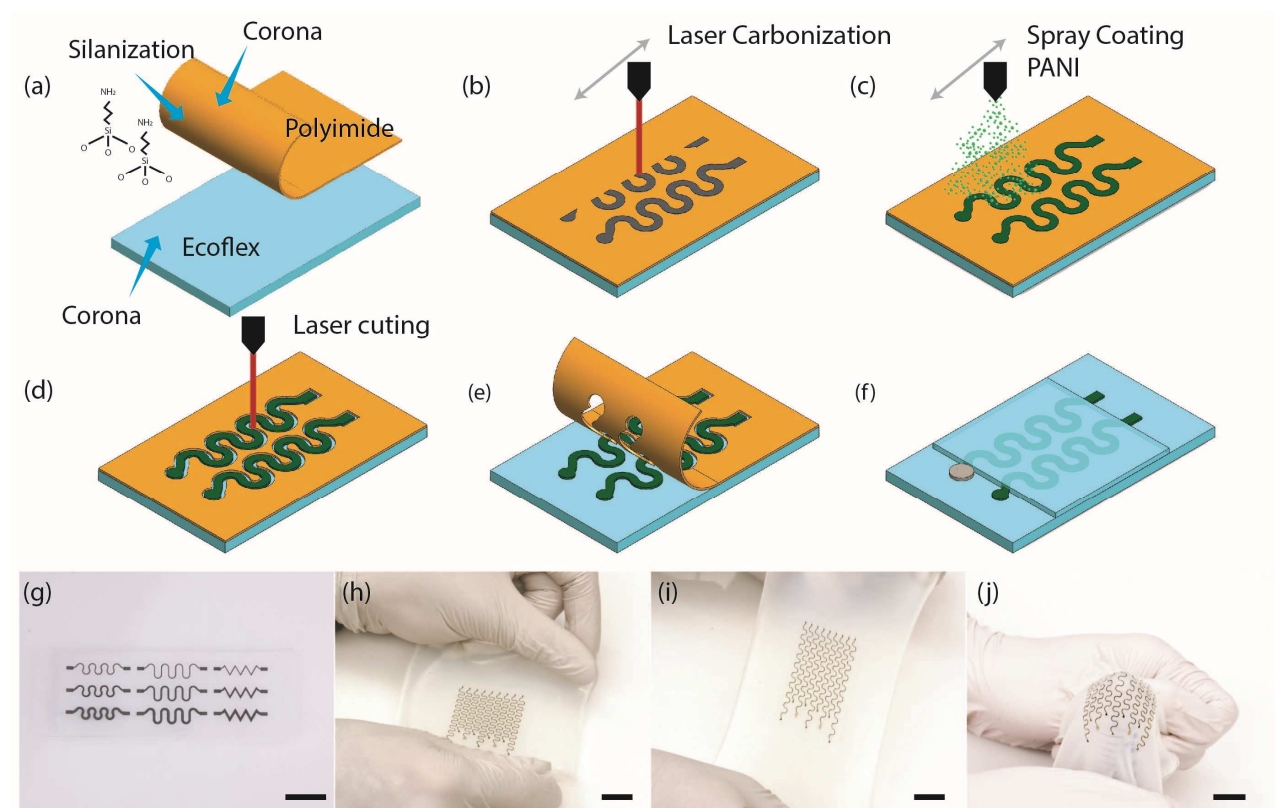


Figure 5.15. Schematic illustrations of the fabrication process and photographic images of the stretchable pH sensor with serpentine interconnects: (a) polyimide sheet is silanized and placed on an air plasma treated Ecoflex substrate, (b) a CO<sub>2</sub> laser is used to carbonize serpentine carbon traces on the polyimide sheet, (c) polyaniline is spray coated onto the porous carbon, (d) the polyimide sheet is machined with the same CO<sub>2</sub> laser at a higher power level, (e) excess polyimide is removed, (f) interconnects are insulated by another Ecoflex layer followed by the deposition of Ag/AgCl and solid electrolyte, (g) photograph of various stretchable PANI/C-PI interconnect designs, (h-j) images illustrating an array of pH sensors being stretched and indented.

### 5.2.2.2 Device Characterization

The performance of the pH sensor was examined by using potentiometric measurements between the working and reference electrode as a function of applied strain. All potentiometric measurements were performed using a unity gain buffer. The performance of the sensor was first probed in a pH titrated cycle without applying external strain. Figure 5.16(a) demonstrates the output voltage of the sensor in buffer solutions of pH 4, pH 10, and back to pH 4. The sensor exhibit distinct potential change at each pH level with an average response time of 58 s. The sensor response as a function of pH is plotted in Figure 5.16(b), showing a sensitivity of -53 mV/pH with a correlation coefficient  $r^2 = 0.976$ . Next, the sensor was tested under longitudinal strain in different pH buffer solutions (from pH 4 to 10), while the potential across the working and reference electrode was continuously recorded, Figure 5.16(c). Figure 5.16(d) illustrates the deviation in output of the sensor as a function of applied longitudinal strains up to 100 % in different buffer solution (pH 4 to 10). The output values stay relatively constant with a minimal deviation of less than  $\pm 4.2$  mV at 100 % strain, which is significantly smaller than the 53 mV potential changes at distinct pH levels. Subsequently, the device performance was tested under different levels of transverse strain, Figure 5.16(e). As depicted in Figure 5.16(f), the sensor shows negligible change of  $\pm 5$  mV in the output potential at different pH levels with applied transverse strain up to 100 %. We should mention that due to the potentiometric nature of the sensor, its stable output under high levels of strain is mainly the result of small changes in the resistance of the C/PANI interconnects (amperometric sensors will be more sensitive to the applied strain).

The sensor performance on the wound phantom was evaluated with and without 100 % applied strain, Figure 5.17(a-c). Figure 5.17(d) shows the real-time potentiometric measurements from the pH sensors before and after applying 100 % strain. The sharp decrease and increase corresponds to the diffusion of ions into the gel and settling after approximately 15 min. The stable potentiometric readouts of 210 mV and 52 mV were close to the measurements observed in the buffer solution of pH 5 and pH 8, respectively. Moreover, the sensor shows identical potentiometric measurements in both, strained and unstrained conditions. This test demonstrates that the presented sensor is able to detect pH fluctuations in physiological relevant range of pH 5 to pH8 over a time interval of 2 hours.

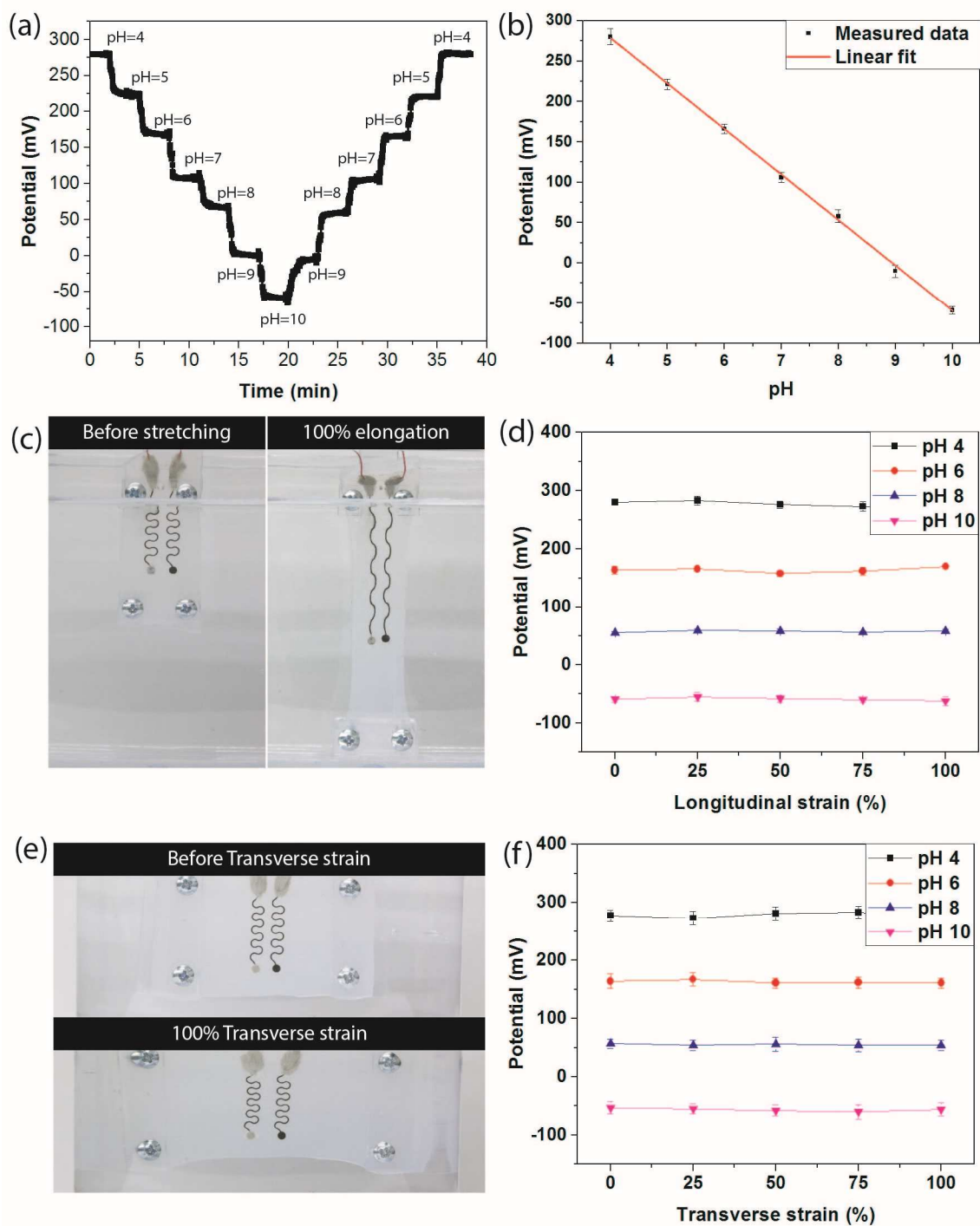


Figure 5.16. (a) Dynamic potential response of the un-stretched pH sensor to unit decrease and increase of pH, (b) potentiometric responses of the un-stretched pH sensor to pH changes, (c) optical image before and after longitudinal strain, (d) potentiometric responses of pH sensor to various longitudinal strain in different pH buffer solutions, (e) optical image before and after transverse strain, (f) potentiometric responses of pH sensor to various transverse strain in different pH buffer solutions.

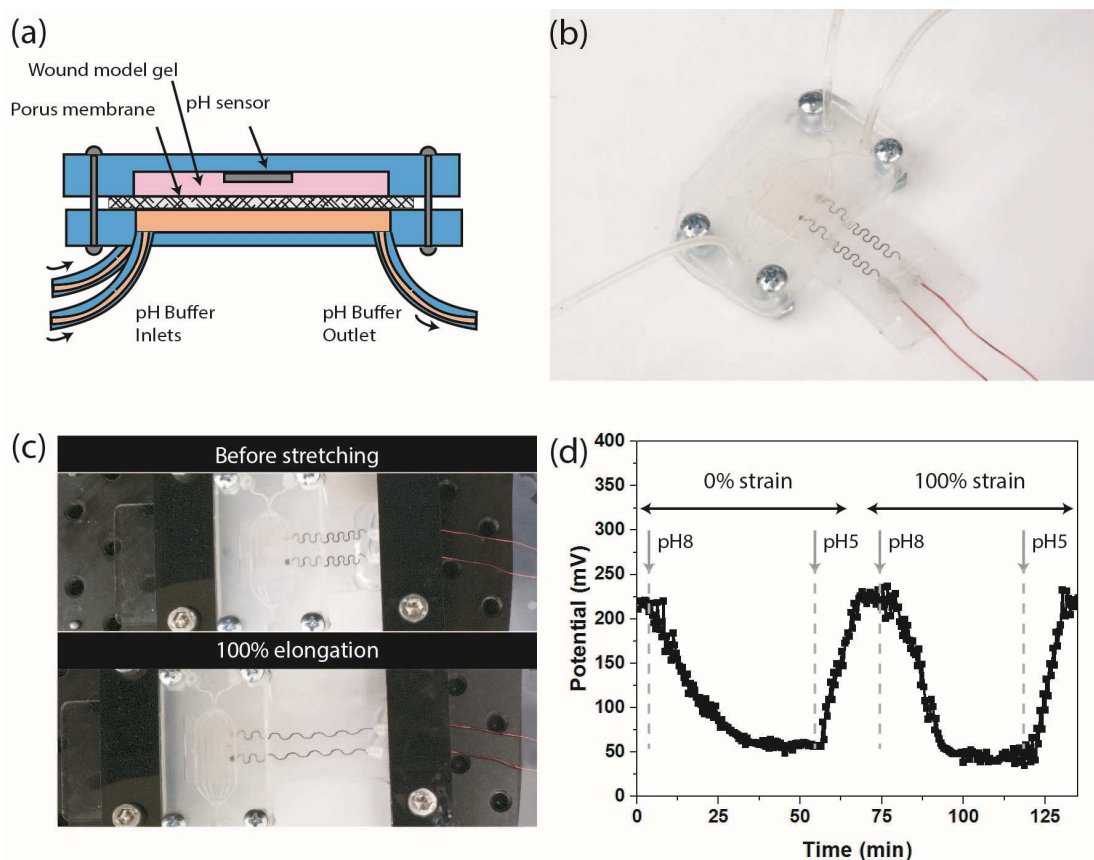


Figure 5.17. (a) Microfluidic test setup to emulated wound condition, (b) optical image of microfluidic test setup with attached stretchable pH sensor, (c) optical image of microfluidic test setup with and without applied strain to the sensor, (d) real-time recording of the pH changes in the hydrogel wound model under 0% and 100% strain.

### 5.2.2.3 In vitro biocompatibility assessment

One of the intended applications of the described pH sensor is its use as a wearable platform for monitoring the variation of the wound pH. In addition, such pH sensors can be integrated with in vitro culture models to form the next generation models for drug discovery and disease modeling that allow close monitoring of cellular environment. In all of such applications, the used materials should be biocompatible and non-toxic. The potential toxicity of the utilized materials was assessed on a culture of NIH fibroblast cells. Samples were fabricated in circular shape with a diameter of 10 mm and were placed at the bottom of 12-well plates. Cells were grown in Dulbecco's Modified Eagle Media (DMEM), supplemented with 10 % fetal bovine serum (Gibco) and 1 % penicillin–streptomycin (Gibco). At 70 % confluence cells were trypsinized and used for

toxicity assessment. 30,000 cells were seeded in each well and the viability and metabolic activity of cells were measured. For the cell viability tests, the cultures were washed with phosphate buffered saline (PBS) at specific time points and then calceinAM and ethidium homodimer were diluted into PBS as per manufacturer's protocol. 300  $\mu$ L of the solution was added to each well and the samples were incubated for 15 min. After 15 min the samples were washed and images were taken using an inverted fluorescence Zeiss microscope. In addition, to generate quantitative data from cellular viability and proliferation a PrestoBlue Assay (Invitrogen) was used to measure the metabolic activity of the cells. At each time point, cells were washed with PBS and PrestoBlue reagent was diluted in the culture media at a ratio of 1 to 9. The diluted reagent was added to each well and after 1hr the fluorescent intensity of the supernatant was measured using a BioTek multimode plate reader as per manufacturer guidelines. Two complementary assays were performed to assess the potential toxicity of the utilized materials. The Live Dead Assay (LDA) is commonly used for identifying the ratio of live to dead cells in a culture. In this assay, the live cells and dead cells uptake different colors and appear distinct under a fluorescent microscope. Representative micrographs of cells interfaced with different materials are shown in Figure 5.18(a). The results suggest that the majority of cells are viable as they appear in green. In addition, less than 10% of cells were dead, which is commonly observed in culture of cells. Another important aspect of cellular functionality is their metabolic activity, providing not only a measure of the number of viable cells, but also if performed over time it indicates cellular proliferation and growth. We used PrestoBlue Assay (Invitrogen), a fluorescence assay, to measure the metabolic activity of the cells. The reagents metabolized by healthy cells into a fluorescence byproduct, the intensity of which correlates with the number of healthy cells. An advantage of PrestoBlue assay over other assays is that it is non-toxic and can be performed on the same samples over the course of experiments to eliminate the sample to sample variability effect. The metabolic activity of the cells exposed to different compounds were measured at days 1 and 7 of culture using a PrestoBlue assay to assess acute toxicity of these compounds and their effects on cellular proliferation. The results were compared to values recorded for a control group which were not exposed to any material, Figure 5.18(b). As can be seen, none of the tested materials showed immediate toxicity as the recorded signal for all the compounds and control group are comparable. In addition, the materials did not interfere with cellular growth as there were no statistically significant difference between the values obtained for samples and controls on day 7.

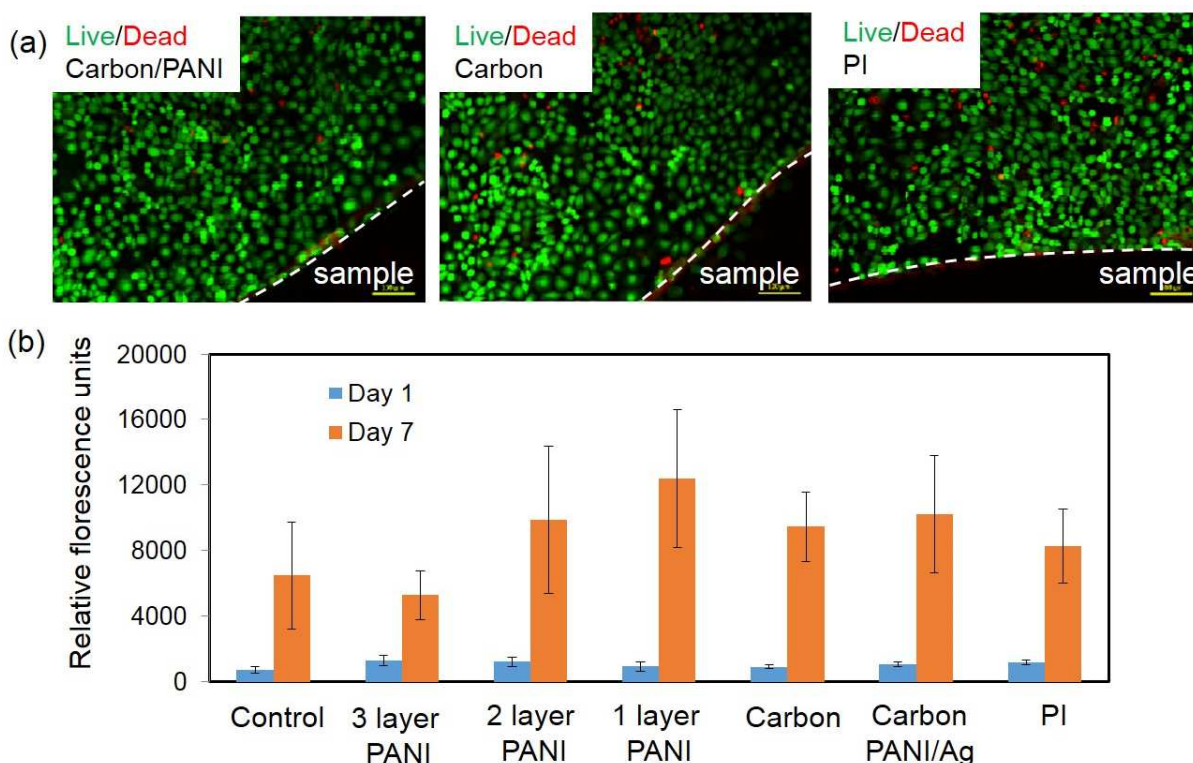


Figure 5.18. Biocompatibility assessment of the materials used in the fabrication of the pH sensor using a culture of NIH 3T3 cells, a) micrographs demonstrating the live (green) and dead (red) cells cultured next to the samples, the majority of the cells are viable at day 4 of culture, b) metabolic activity of the cultured cells measured by PrestoBlue assay and compared to the control group. The results did not show immediate toxicity and the tested materials did not interfere with cellular growth as there were no statistically significant difference between the samples and controls.

### 5.3 Paper-based environmental sensors

In this section, we present an inexpensive rapid process for creating mask-free and low-cost environmental sensors on paper substrates by laser ablating commercially available metallized paper. The process is based on the optimized laser ablation with CO<sub>2</sub> and Nd:YAG laser described in section 4.3. The facile laser patterning process of the metallized paper provides a simple, cost-effective, and scalable alternative to conventional photolithography-based processes and printing technologies.

### 5.3.1 Humidity sensor

The described humidity sensor exploits the hygroscopic characteristics of the cellulose paper substrate. The randomly distributed network of cellulose fibers are excellent low-cost and natural hygroscopic dielectric materials for sensing humidity. In general, papers have a low dielectric constant ranging between 2 to 4 which is often dependent on the structural properties and material used in its production. In contrast water has a much higher dielectric constant value of about 80. Therefore, absorption of moisture by the cellulose fibers can significantly change the effective dielectric constant of the paper substrate. At equilibrium conditions, the moisture content in the paper is proportional to the ambient relative humidity (RH).

The highly porous and spongiform surface of the cellulose fibers not only provides a high surface area, but also induces capillary condensation in the porous cellulose network. Capillary condensation is a process by which water vapor can condense into liquid within small process medium at lower humidity levels. The condensation of water vapor can cause a greater change in effective dielectric of the paper substrate. Change in dielectric properties of the hygroscopic paper can be measured by a pair of electrodes. The capacitance of a typical parallel plate electrode type for capacitive humidity sensing can be expressed as:

$$C = \epsilon_r \epsilon_0 A / d \quad (5.2)$$

where,  $C$  is the capacitance,  $\epsilon_r$  is dielectric constant of the material between the plates,  $\epsilon_0$  is permittivity of free space ( $8.854 \times 10^{-12}$  F/m),  $A$  and  $d$  are the area of each plate and the separation distance the two plates. The parallel plate design has disadvantages of relatively long response time and manufacturing difficulty in assembling the layers. However, the interdigitated type electrodes have high sensitivity and relatively easier fabrication. Therefore, in this work, the change in dielectric property of the paper was measured by utilizing a single step laser ablating interdigitated aluminium electrodes (IDE) onto the MP substrate.

The laser ablations were performed with two aforementioned laser systems (CO<sub>2</sub>, Nd:YAG) and sensing performance of sensors were compared. The sensors were designed in three IDE structures with different electrode widths ( $W$ ). In all designs the spacing gap between the electrodes were targeted to smallest possible pitch, which is limited to the effective metal removal with a single laser pass of the laser beam ( $G_{CO_2}=103 \mu\text{m}$  for CO<sub>2</sub> laser beam and  $G_{Nd:YAG}=64 \mu\text{m}$  for Fiber laser), Figure 5.19. By changing the electrode width the number of electrode covering the effective sensing area of  $8 \times 8 \text{ mm}^2$  was changed ( $n=2, 20$ , and  $40$ ) and denoted as IDE1, IDE2,

and IDE3, respectively. The sensors' response to RH were characterized in humidity chamber at constant temperature of 21 °C and varying relative humidity level from 2% to 85%. The humidity level in the chamber was accurately measured with commercial humidity sensor (Fluke 971) and controlled by supplying dry and humidified N<sub>2</sub> streams. The sample were place in the chamber with electrical feed-through. The change in electrical capacitance of the sensors were measured with a computer controlled LCR meter (GW Instek LCR-819) with 1VAC peak to peak excitation at 1 kHz. All humidity sensing measurements were carried out under normal atmospheric pressure.

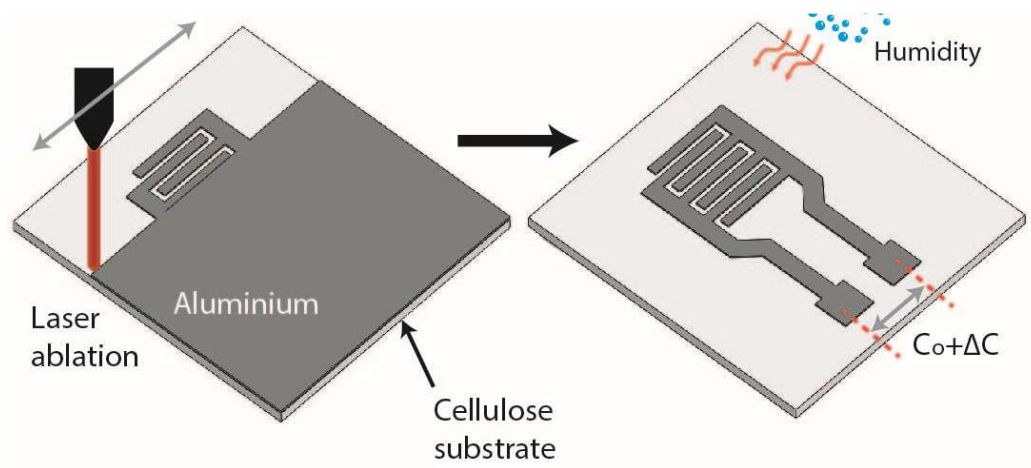


Figure 5.19. Schematic illustration of the fabrication procedure for the paper based humidity sensor

### 5.3.1.1 Results and discussion

Humidity sensing performance of three IDE designs (IDE1, IDE2, and IDE3) fabricated by both CO<sub>2</sub> and Nd:YAG laser ablation process were measured and compared in the range of 2%–85%RH. Figure 5.20(a) shows optical and close-up microscopic images of IDE1, IDE2, and IDE3 fabricated with optimized CO<sub>2</sub> laser settings (9 W, 4 m/s). Despite the fact the CO<sub>2</sub> laser beam used in the process was 60 μm the minimum width and gap achieved was  $98 \pm 5 \mu\text{m}$  and  $103 \pm 6 \mu\text{m}$ . The low selectivity and high energy absorbing by the paper substrate resulted in imperfect laser ablation which created non-uniform electrodes with rough edges. The high temperature applied to the paper substrate at high density ablation (e.g. IDE3 sensor) resulted in deformation/warping of the final electrodes. As shown in Figure 5.20(b), the humidity sensitivity of the sensors were evaluated on the basis of two regions of RH ranges: Region I (2–75%RH); and

Region II (75–85%RH). In region I, the sensors respond to the humidity changes are linear. As depicted in Figure 5.20(c) the three IDE designs had different sensitivities to changes in humidity: 1.2fF/%R.H, 5.6fF/%R.H. and 18.9fF/%R.H. for IDE1, IDE2, and IDE3, respectively. The result shows that as the number of electrodes increases the capacitance value of sensor and its sensitivity to humidity increases. The larger capacitance and sensitivity in IDEs with more dense electrodes is mainly due to the increase in effective surface area ( $A$ ) within the IDE capacitor. Therefore, under the same RH humidity conditions in either CO<sub>2</sub> and Nd:YAG laser ablation we always observed:

$$C_{IDE3} > C_{IDE2} > C_{IDE1} \quad (5.3)$$

The electrodes in the IDE capacitors generate an electric field beneath the paper substrate. The absorption/adsorption of water vapor changes its effective dielectric constant ( $\epsilon_r$ ), modifying the  $C$  value of the IDE sensor. Therefore, the change of the dielectric constant of the capacitive sensor is linearly proportional to the amount of absorbed water vapor. The large change in Region II reflects the region where capillary condensation occurs on the sensor. Figure 5.20(d) shows optical and close-up microscopic images of IDE1, IDE2, and IDE3 fabricated by optimized Nd:YAG laser settings (7.2W, 4m/s). The microscopic images exhibit more uniform and straight etched lines as compared to the CO<sub>2</sub> laser ablation process. The smallest achievable ablation gap was  $64 \pm 2 \mu\text{m}$  and the minimum electrode width was  $144 \pm 2 \mu\text{m}$ . The capacitance of the IDE sensors were measured and compared in the range 2–85%RH, Figure 5.20(e). The results were evaluated basis of two regions of RH ranges: Region I (2-68%RH), and (68-85%RH). In region I, the sensors react to the humidity changes with a linear response (without any capillary condensation effect). Region II describes a region where capillary condensation occurs with a non-linear response in all three sensors. As shown in Figure 5.20(d), the Nd:YAG laser process sensors show a higher linear response gain as compared to the CO<sub>2</sub> laser processed sensor at low RH (2-50%). The average linear sensitivity in Region I was 2.5fF/%RH, 45.7fF/%RH, and 83.2fF/%RH for IDE1, IDE2, and IDE3, respectively. With the change in RH from 40 to 85% the increase in capacitance of IDE1, IDE2, and IDE3 was respectively 471%, 1740%, 1804%. The abrupt onset of the capacitance response in Region II is caused by the capillary condensation inside the pores cellulose network of the paper. Porous structures facilitates condensation at a lower humidity level by increasing van der Waals interactions between the water vapor molecules and the surface of the porous material in a confined volume. The condensation of water vapor causes a big change in the

capacitive measurements from the IDE sensors due to the higher dielectric constant of water ( $\epsilon_r = 80$ ). In general, IDE sensors prepared by Nd:YAG laser ablation showed a higher capacitance response throughout all the regions (2-85% RH). The discrepancy between the Nd:YAG and CO<sub>2</sub> laser processed IDEs is mainly caused by the absorbent characteristic of the micro/nano-pores between the fabricated IDEs. The Nd:YAG laser processed MP provides a greater permeability of the water molecules, so water vapor molecules can easily pass through the pore openings and capillary condensation occurs throughout the thickness of the capillary porous structure, which provides a greater change in capacitance measurements. The sensing performance of humidity sensors are also measured by their response and recovery time to changing humidity. The time that is taken by a sensor to achieve ~90% of the total capacitance change is defined as the response or recovery time. High responsive humidity sensors have very small response time. In addition to response time performance, viable sensors have to be repeatable. This section characterizes the response time and repeatability performance of the Nd:YAG laser processed IDE sensors in upper and lower RH.

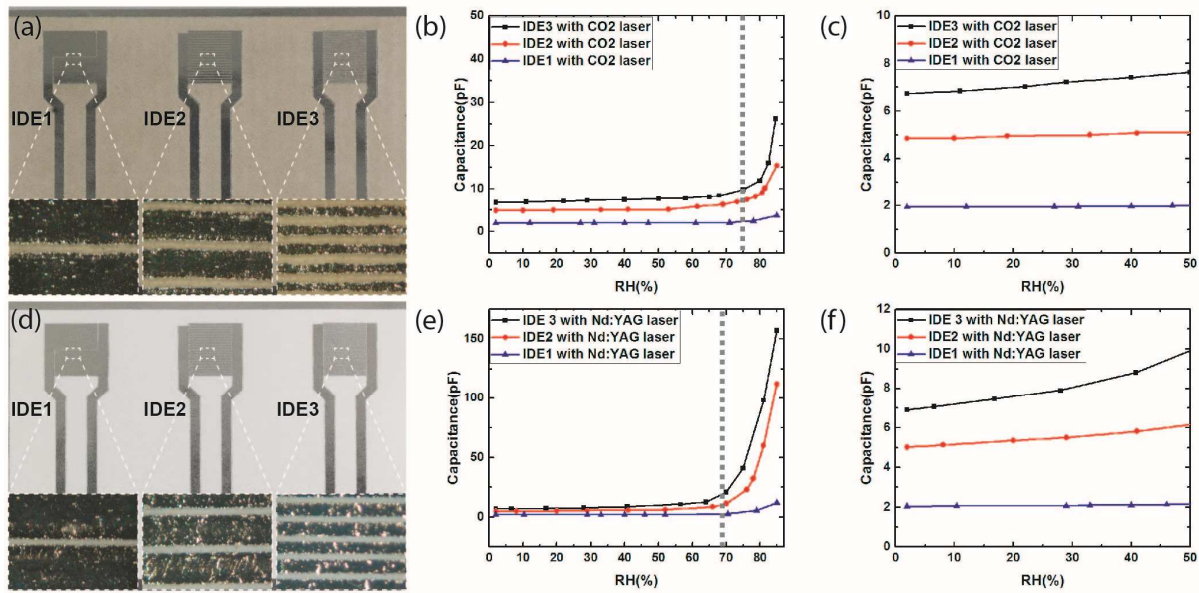


Figure 5.20. (a) Optical images of fabricated humidity sensors using CO<sub>2</sub> laser ablation, (b) capacitance variations versus relative humidity levels for the range 2–85%RH and (c) close up of capacitance variations versus relative humidity in range 2–50%RH. (a) Optical images of fabricated humidity sensors using Nd:YAG laser ablation, (b) capacitance variations versus relative humidity levels for the range 2–85%RH and (c) close up of capacitance variations versus relative humidity in range 2–50%RH.

The Nd:YAG laser processed sensors were chosen as they had the highest sensitivity. In the first experiment, the dynamic response of the three IDE humidity sensors under a testing cycle of 2% to 40% RH. Although the change in capacitance of the sensors were different (IDE1  $\sim 0.07$  pF, IDE2  $\sim 0.8$  pF, and IDE3  $\sim 1.8$  pF), their response and recovery time were comparable in performance. According to the results Figure 5.21(a) in the humidity range of 2%–40% RH (without any capillary condensation effect), the average response and recovery time increased with more sensors sensitivity.

The response time for the three designs IDE1, IDE2, and IDE3 was 45 s, 57 s, and 62 s, respectively. As shown in the Figure 5.21(b), all designs had a longer recovery process than the adsorption process. The approximate recovery time for IDE1, IDE2, and IDE3 was 86 s, 94 s, and 126 s, respectively. Figure 5.21(c) shows reversible changes in the capacitances as the RH was varied by four cycles between 2%–40%. The sensors show a high degree of repeatability with a capacitance variability of less than 4%. As for the second dynamic response test the sensors response and recovery behavior to capillary condensation were tested. In this test the RH in the chamber was abruptly changed from  $\sim 40\%$  to  $\sim 85\%$  by quickly supplying moisture, and the capacitance response was continuously recorded. The response and recovery curves for these tests are shown in Figure 5.21(d,e). For the IDE1 sensor, the response time was 215 s when increasing from 40% to 85% RH. However, the recovery time was about 43 s, and it reached a plateau quickly, indicating the short desorption time. For the IDE2 sensor, the response time was about 288 s, and the recovery time was about 13 s. With the high density electrodes in IDE3 the response time became 266 s, and the recovery time was about 10 s (Figure 5.21(e)).

Based on the above results, it is reasonable to get the conclusion that the capillary condensation will cost more time than evaporation of the water from the porous substrate. In addition, the faster recovery time in IDEs with smaller ratios of electrode width to inter-electrode gap can be explained by their higher exposed area which allows the easier escape of the condensed water molecules from the absorbent substrate. Figure 5.21(f) shows reversible changes in the three sensors capacitance as the relative humidity is varied cyclically between 40%–85% RH. The sensors showed good repeatability/stability with maximum variations of less than 6% for all designs.

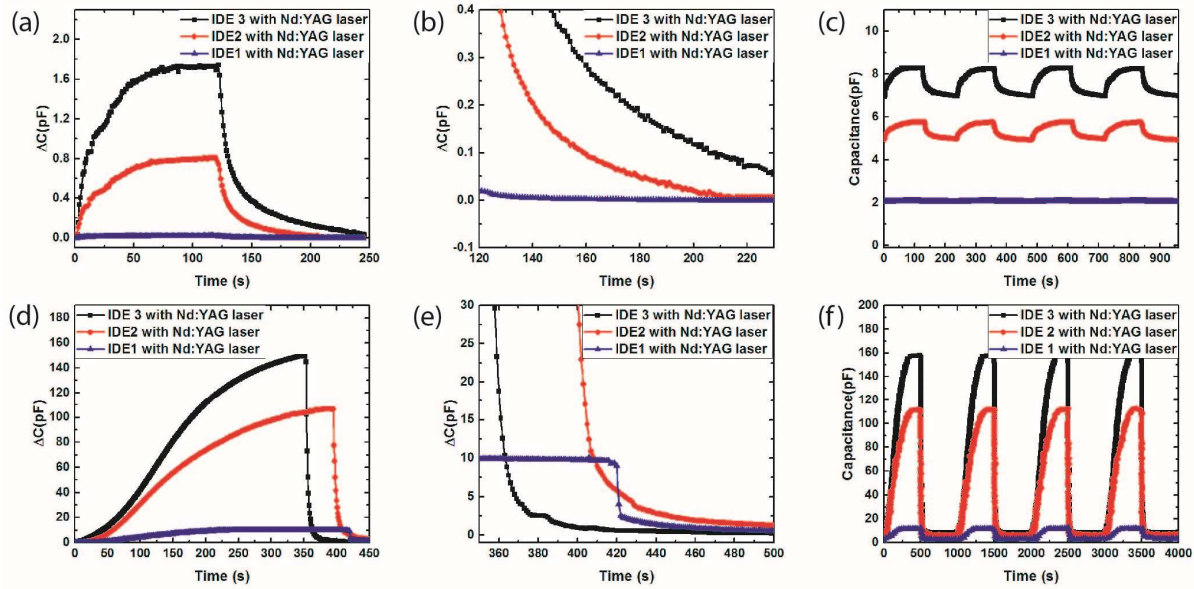


Figure 5.21. (a) Comparison of response time performance of different capacitive sensor designs to RH between 2% to 40%. (b) Close up of capacitance variation during desorption procedure from 40% to 2%RH. (c) Repeatabile capacitive responses of captive sensors during four cycles between 2% and 40% RH. (d) Comparison of response time performance of different capacitive sensor designs to RH between 40% to 85%RH. (e) Close up of capacitance variation during desorption procedure from 85% to 40%RH. (f) Repeatabile capacitive responses of captive sensors during four cycles between 40% and 85% RH.

### 5.3.2 Temperature sensor

Resistance Temperature Detectors (RTD) are contact based temperature sensors that change in resistance value as the environmental temperature changes. RTDs are often made of metallic materials (typically platinum, nickel, or copper). One of the significant characteristics of the metals used in RTDs is their approximate linear change in resistance versus temperature. This variation in resistance caused by the temperature change is used to detect the change in temperature which is calculated by the following equation:

$$R = R_{ref} [1 + \alpha(T - T_{ref})] \quad (5.4)$$

where  $R$  is the conductor resistance and temperature  $T$ ,  $R_{ref}$  is the conductor resistance at reference temperature  $T_{ref}$ ,  $\alpha$  is the temperature coefficient of the material, (and symbolizes the resistance change factor per degree of temperature change). The sensitivity ( $S$ ) of the temperature sensor is calculated by

$$S = \Delta R / \Delta T = \alpha R_{ref} \quad (5.5)$$

Here,  $\Delta R = R - R_{ref}$  is the change resistance of the temperature sensor with respect to changes in temperature  $\Delta T = T - T_{ref}$ . The equation shows that in ideal conditions, the RTDs sensitivity will be linearly dependence on the initial resistance ( $R_{ref}$ ) and temperature coefficient of the material ( $\alpha$ ). Using our proposed laser ablation technology (with optimized laser settings) aluminium based RTDs were devised with different sized meanders, Figure 5.22. Four different sized sensors were fabricated with same 1.5 mm widths and total lengths of 40, 80, 120, and 160 mm and were labelled as RTD 1, RTD 2, RTD 3, and RTD 4, respectively. The electrical characteristics of the samples were measured by two-point measurements using a digital multimeter (Agilent 34401A). Temperature tests from 21°C to 100°C were performed in a controlled temperature oven with a precision of 1°C. For the lower temperature measurements (from 4 to -20°C), the sensors were placed in a refrigerator.

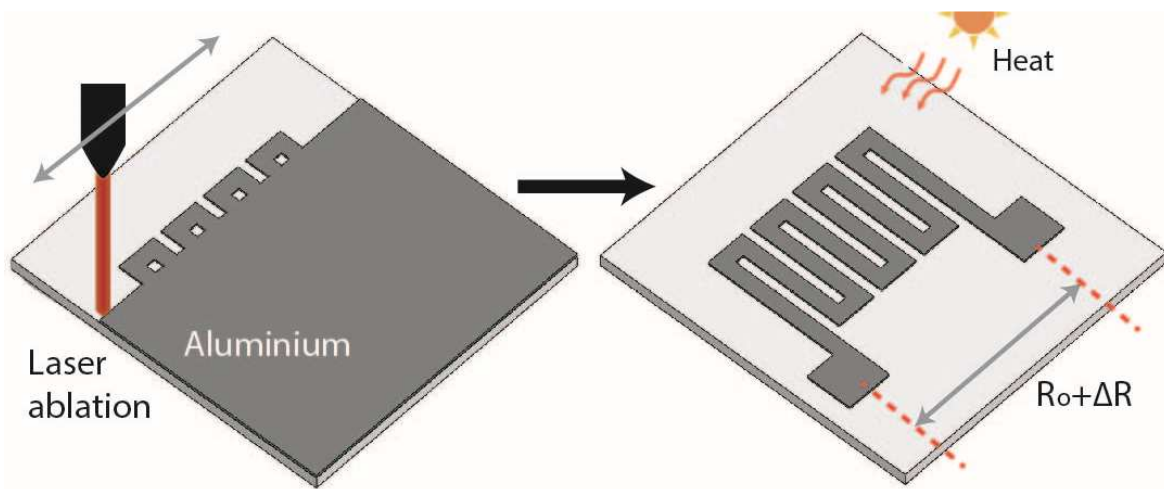


Figure 5.22. Schematic illustration of the fabrication procedure for the paper based temperature sensor

### 5.3.2.1 Results and discussion

RTD temperature sensors can play a double role in the developed low-cost sensing concept. The RTD sensor can provide information about the environment temperature, and also be used as a compensation sensor for other temperature depended sensors (e.g. humidity). Although this integrated design was not implemented, the compensation, calibration as well as proper interface wireless electronics can be integrated on a signal laser ablated MP substrate.

The four fabricated Nd:YAG laser ablated temperature sensors with different length are shown in Figure 5.23(a). By measuring electrical resistance of the RTDs at room temperature, and assuming a resistivity of  $2.65 \times 10^{-8} \Omega/\text{m}$  the estimated thickness of the evaporated aluminum was 25 nm, Figure 5.23(b).

The change in resistance of all four RTDs were measured and compared in the range of -20 to 80 °C. Figure 5.23(c) shows the linear resistance increases of the four RTDs as the temperature increases. The sensitivity extracted by the linear fit, showed a sensitivity of  $0.102 \Omega/^\circ\text{C}$  for RTD1,  $0.186 \Omega/^\circ\text{C}$  for RTD2,  $0.29 \Omega/^\circ\text{C}$  for RTD3, and  $0.451 \Omega/^\circ\text{C}$  for RTD4. As expected, the results showed a trend between the RTD sensitivity and length of the sensor: as the length increases, the linear sensitivity increases accordingly. Using eq. 5.4, the predicted sensitivity of the RTDs was a linear function of the initial resistance and equal to the temperature coefficient ( $0.0042 \text{K}^{-1}$ ) of pure aluminum. However the measurements from the four designs estimated an average the temperature coefficient of  $0.0036 \text{K}^{-1}$ , Figure 5.23(d). The small difference (14%) between the measurements and predicted theoretical estimate can be explained mainly by two reasons: the impurities in the conductive evaporated coating and thermodynamic limitation induced by the porous paper substrate and the isolating polymer coating.

To examine the stability of the sensors at temperatures above and below room temperature conditions we carried out continues readings from RTD sensors over the course of 24 hours at two temperatures of 21°C and 60°C. Figure 5.23(e) and f show the electrical resistance measurements from the four RTDs at 21°C and 60°C condition, respectively. The calculated maximum variations in resistance at both temperature condition for RTD1, RTD2, RTD3, and RTD4 were 6.5%, 4.4%, 2% and 3.1%, respectively. The results show that the smaller sensors (RTD1 and RTD2) had less sensitivity and higher relative variability output with long-term stability tests. Longer sensors (RTD3, and RTD4) showed higher temperature sensitivity with adequate stability performance at different temperatures.

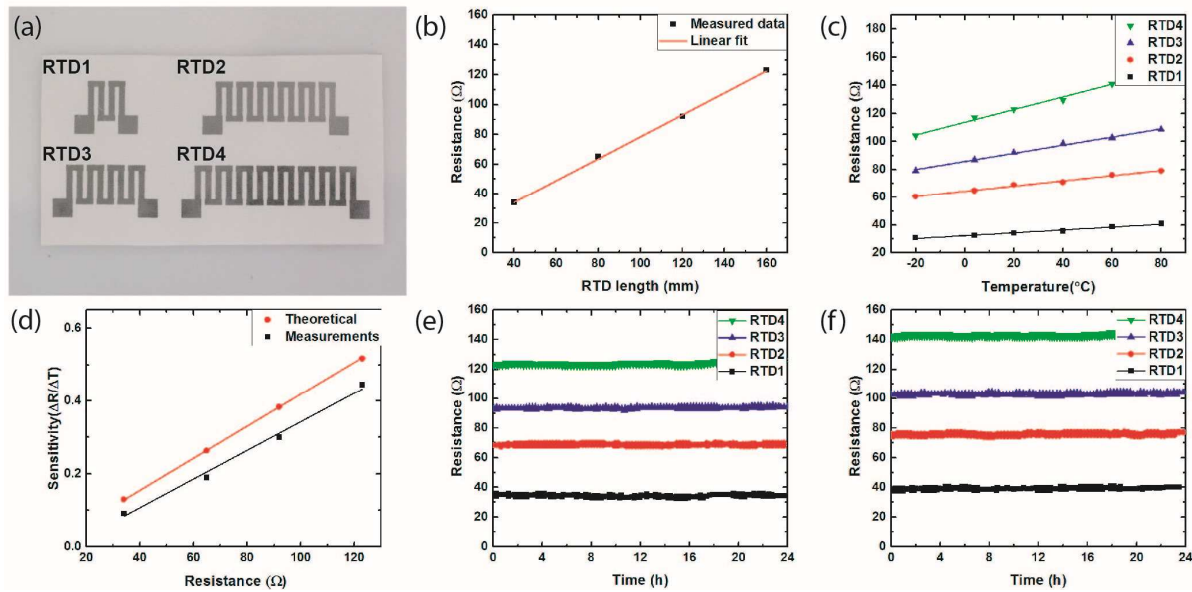


Figure 5.23. (a) Fabricated temperature sensors on the paper substrate through Nd:YAG laser ablating MP. (b) Electrical resistance of the four design temperature sensors and room temperature condition 21°C. (c) Resistance variation against temperature of four design RTDs sensors for temperature between -20°C to 80°C. (d) Sensitivity vs resistance curve. Stability test of four design RTDs continuously monitored at (e) 21°C and (f) 60°C conditions for 24h.

#### 5.4 Paper based *in-vitro* model for respiratory system

Respiratory epithelium (e.g., the lining of the lungs) is a highly-specialized vital tissue in mammals, serving as the interface between air and internal milieu (blood)[221], [222], Figure 5.24(a). Under normal conditions, this tissue exhibits remarkable multi-functional properties by providing a physical barrier to protect against pathogens and a medium for rapid (high flux) gas exchange, all while remaining strong and flexible. However, exposure to insults such as hazardous substances, allergens, pathogens, and smoking can alter the integrity of the epithelial cells, resulting in severely impaired respiratory function, which may lead to many life threatening respiratory diseases (e.g., viral respiratory tract infections, asthma, chronic obstructive pulmonary disease, and pneumonia)[223]. Treatment for these conditions is challenging, primarily due to an incomplete understanding of the disease etiologies and the fundamental underpinnings of epithelial tissue physiology[224]. Such scarcity of therapies urges the need for developing more clinically

relevant models of epithelial tissue that facilitate studying of the respiratory system and drug screening[225].

Current research relies on either animal models or *in-vitro* transwell plate setups which mimic epithelial tissue structure and function. The latter has the advantages of being more economical, easier to implement in many laboratories, and better experimental consistency (compared to animals, which introduce variations in many tissue parameters)[226]–[227]. The most common *in-vitro* approach is the use of commercially available semipermeable hanging film for creating an air liquid interface (ALI) in transwell flasks[228]–[229]. With this technique, the film is exposed to a liquid environment on one side and air on the other. The basal side provides moisture and growth medium, while the apical side provides exposure to air, thus mimicking airway epithelial tissue. The cell culture is then grown on the air side of the film, which still contains sufficient moisture (made available via diffusion from the liquid side) for supporting cellular growth. Despite mimicking the ALI condition, conventional transwell platforms have a number of limitations. These include their relative high cost, lack of proper distribution of nutrients and waste removal due to their static conditions, prolonged culture times (average 3 weeks) required for full cell differentiation, and their inability to faithfully recapitulate the mechanics of epithelial tissue (i.e., most films are too brittle, impermeable to gases, and incompatible with microfluidic systems) [230], [231]. Thus, there is a need for more cost effective, easy to use, and physiologically relevant (e.g. highly permeable for gas exchange and yet robust enough to support cell culture in liquid environment) ALI platforms[232].

As a more cost-effective approach, many researchers have successfully demonstrated the use of paper as an alternative material for conventional cell culture substrates (e.g., polystyrene, and PDMS)[125], [233]–[235]. In this work, we further expand the capabilities of paper-based cell-culture platforms by taking advantage of silicone-coated commercial hydrophobic papers (parchment paper) as the starting material to generate desired hydrophilic patterns, amenable to controlled cell attachment, using a CO<sub>2</sub> laser scrubbing process discussed in section 4.1, Figure 5.24(b). The hydrophilic patterns also regulate the permeability of both oxygen and nutrition through the hydrophobic paper.

### 5.4.1 Paper-based microfluidic ALI platform

A schematic of the *in-vitro* microfluidic airway system is shown in Figure 5.24(c). It consists of an upper and a lower laser-cut acrylic chamber (with 1.5 mm deep and 15 mm long channels) corresponding to the apical (airway lumen) and basal compartments of airway epithelium. The laser-treated paper provides support for cell attachment and diffusion of the fluid media to the cells. Figure 5.24(d, e) show the assembling process of the platform and the final device. The device can be easily disassembled and reloaded with a new paper/film membrane for multiple experiments. In order to develop the air liquid interface model for respiratory system, the CALU3 cells (American Type Culture Collection, HTB55), was used in our experiment, which has been extensively used in *in-vitro* studies focused on the functions of bronchial airway epithelium such as tight junction formation (Zona Occluden1), mucin secretion (MU5AC) and cilia formation ( $\beta$  tubulin)[230], [236]–[238].

Before assembling the ALI platform for *in-vitro* experiments, each component was ultraviolet (UV) sterilized at a distance of 8 cm for 15 min on each side. The appropriate length of inlet-outlet tubing was connected to the platform after sterilization with 70% ethanol. Upper and lower chambers were sterilized with 5x antibiotic/antimycotic solution (Sigma-Aldrich) overnight at room temperature inside the tissue culture hood. The sterilizing solution was removed and the chambers and tubing were washed with PBS.

For cell culture, the paper substrates were coated with fibronectin (10  $\mu$ g/ml) (Sigma) for 1hr and then conditioned with cell culture media for 1hr before cell seeding to facilitate cell attachment. CALU-3 cells, were seeded in upper open chamber at a density of  $2 \times 10^5$  cell in 200  $\mu$ l of media and the whole assembly was incubated at 37 °C, 5% CO<sub>2</sub> for 5hrs. The bottom chamber was then infused with media at a flow rate of 8  $\mu$ l/min using a syringe pump (Harvard Apparatus). The amount of media in collecting reservoir was checked every day for ensuring constant flow rate through the platform. On Day3 the cells exhibit a confluent monolayer coverage on the hydrophilic regions on the paper (5 mm x 15 mm). Next, an air-liquid interface is established for further differentiation by removing some of the medium from the top chamber while maintain the same constant flow of medium in the lower chamber for 7 days. The schematic procedure used of the ALI cell culture process is shown in Figure 5.25.

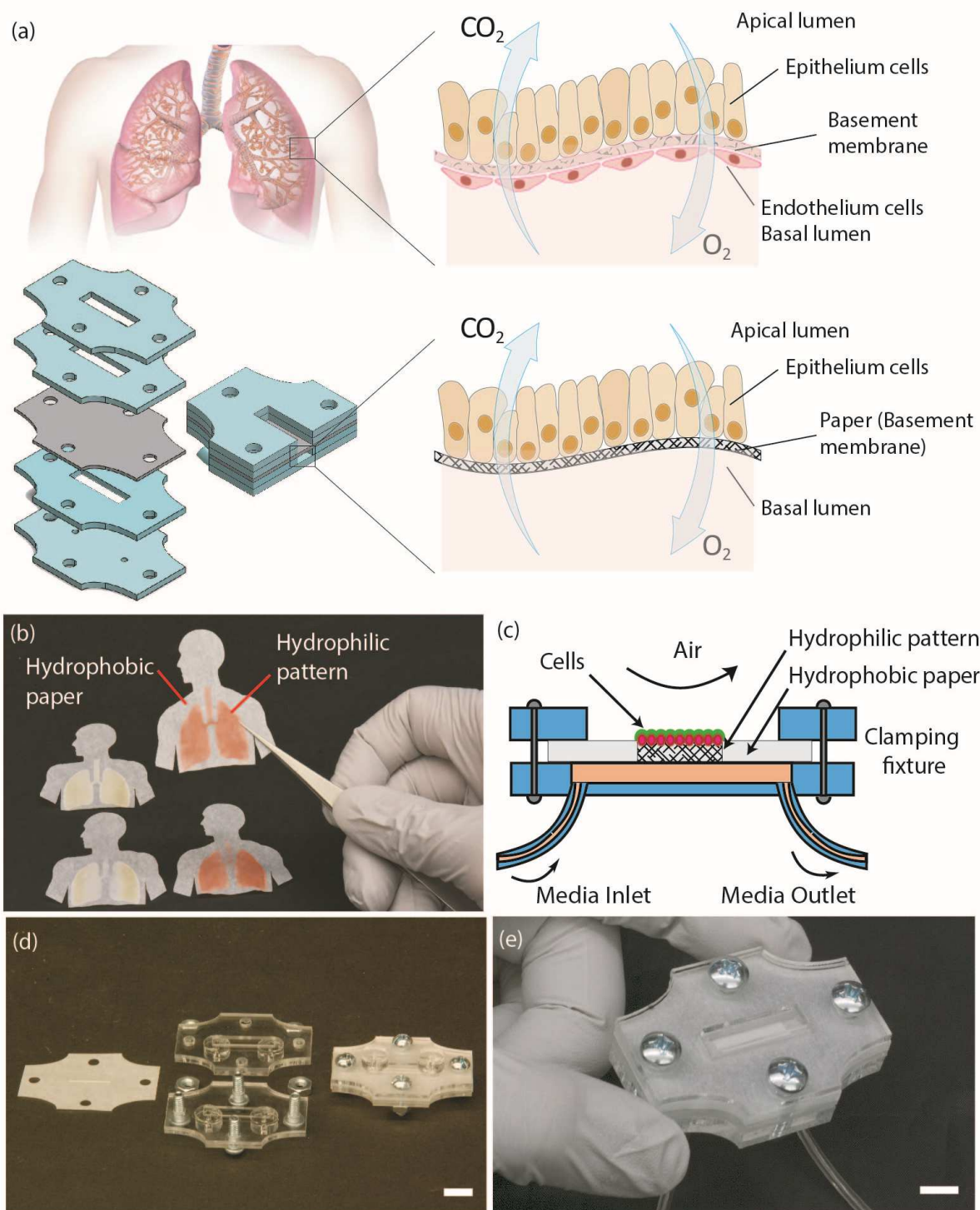


Figure 5.24. (a) Illustration of the respiratory epithelial tissue and paper-based microfabricated in-vitro lung device, (b) selective attachment of aqueous red dye on laser treated parchment paper, (c) schematic of the paper-based air-liquid-interface (ALI) platform, (d) photograph of components, and (e) assembled final device. All scale bars: 10 mm.

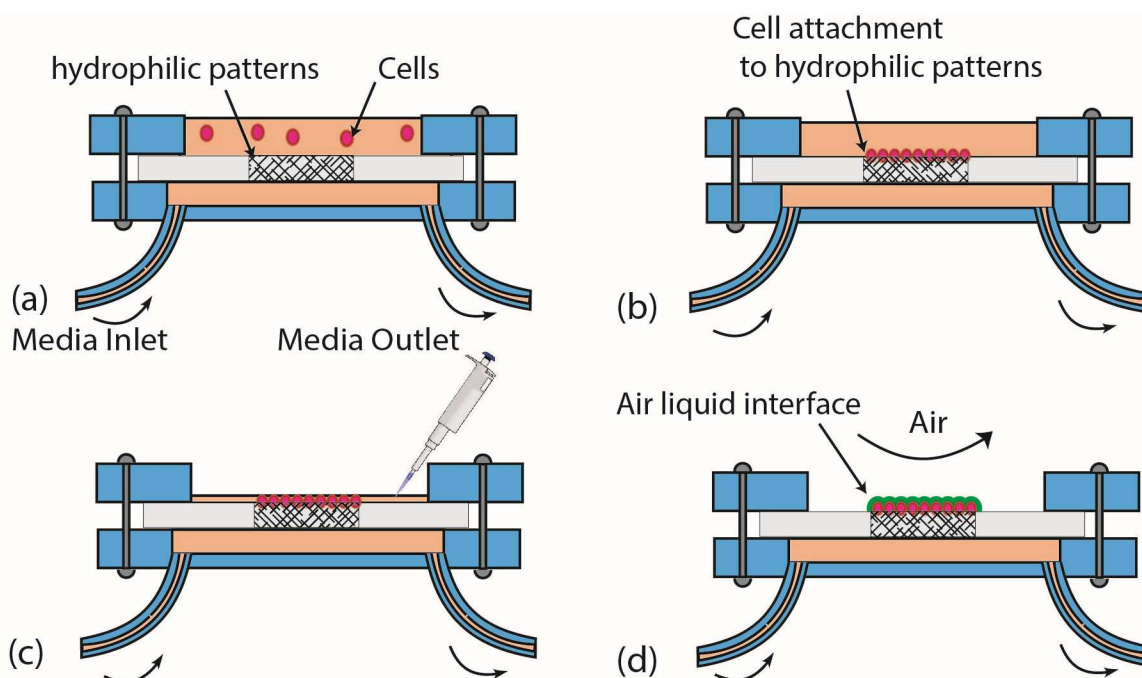


Figure 5.25. The procedure for airway cell culturing on the paper based platform; (a) cell seeding on the upper open chamber, (b) on day 3 the cells exhibit a confluent monolayer coverage on the laser ablated hydrophilic region on the parchment paper, (c) air-liquid interface is established by removing the medium from the top chamber while maintaining a constant flow of medium in the lower chamber for 7 days, (d) observation of ZO1 expression around the whole cell membrane that resembles the functional airway epithelium.

Given the importance of barrier formation in epithelium integrity and its relevance to drug delivery, allergen exposure and respiratory infection, we assessed barrier formation at air liquid interface on the paper based platform by quantifying the expression of Zona Occluden1 (ZO1), a key tight junction protein, commonly used as a surrogate for quantifying for barrier formation[224], [236], [239]–[241]. All results were compared with conventional static ALI transwell flasks. For conventional transwell ALI cultures, 12 well format transwells from Corning® with 0.4  $\mu\text{m}$  pore size were used as described before [224]. Same number of CALU-3 cells ( $2 \times 10^5$  cells in 200  $\mu\text{l}$ ) were seeded in both systems. For immunostaining, cells were fixed with 4% paraformaldehyde and permeabilized with 0.5% Triton X-100. Then the samples were blocked with 10% goat serum (Sigma-Aldrich) for 30 min and incubated with primary antibody rabbit ZO1 (Invitrogen, UK) for 1 hour at room temperature in 1:50 dilution. Secondary antibody-goat anti rabbit Alexa fluor 488 was allowed to conjugate for an hour at room temperature. Cell

nuclei were counterstained with DAPI for 15 minutes. All images are taken with Zeiss LSM710 confocal under 40x oil objective (SLIM imaging, University of Nottingham, UK).

#### 5.4.2 Airway epithelial cells on the paper platform

Figure 5.26 shows the cell viability on parchment paper stained by live-dead reduced biohazard cell viability assay (L7013-Life technologies) at Day1 and Day3 of cell seeding. The assay was performed according to the manufacturer's instruction. After staining, ALI platform was disassembled and the cells on parchment paper were mounted for confocal microscopy. As seen in, Figure 5.26 >90% of cells was viable on parchment paper at both Day1 and Day3 culture proving the compatibility of parchment paper to airway epithelium culture.

Fig.5 compares the barrier formation of airway epithelium between paper-based ALI platform under flow condition and conventional ALI method under stasis condition. The cells were stained for one of the tight junction proteins called Zonula occludens (ZO1) which was expressed as chicken wire appearance on cell membrane [236], [242]. The comparison was made at two time points Day5 and Day7 of ALI culture.

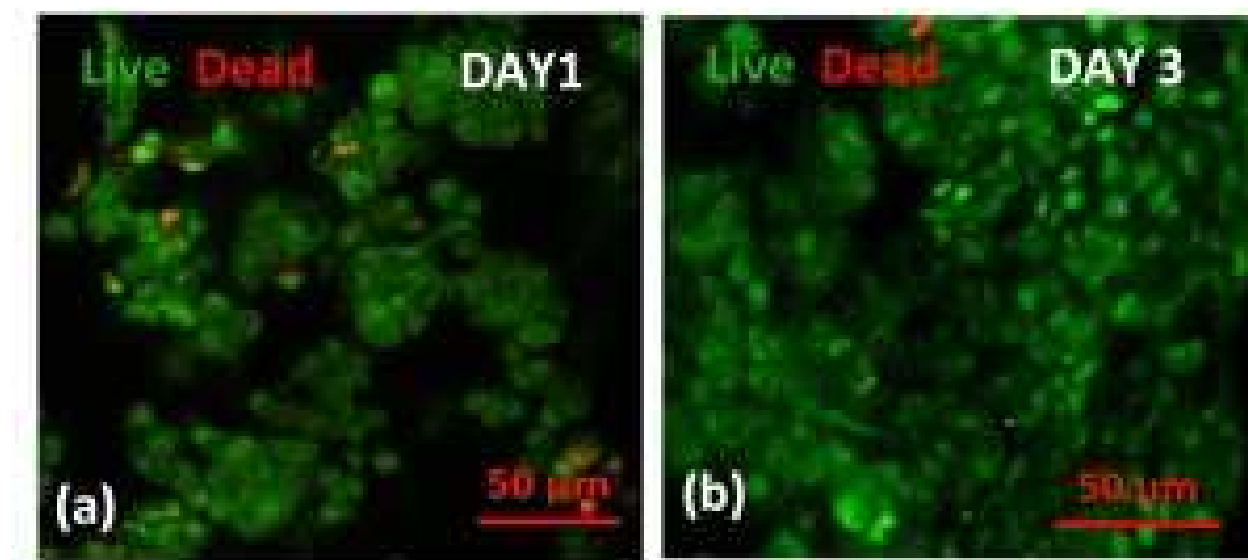


Figure 5.26. Assessment of cell viability of airway epithelium (CALU3) grown on parchment paper at day1 (a) and Day3 (b) by live-dead staining. CALU3 are stained with Syto10 (Live staining- green) and Ethidium Bromide (Dead staining- red). The images were captured using Zeiss LSM710 confocal microscope under 20x objectives. (scale bar= 50 μm, 20x objective)

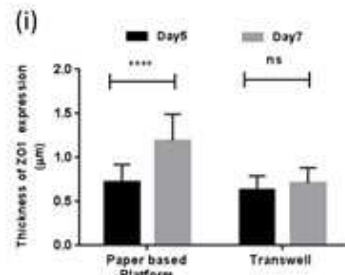
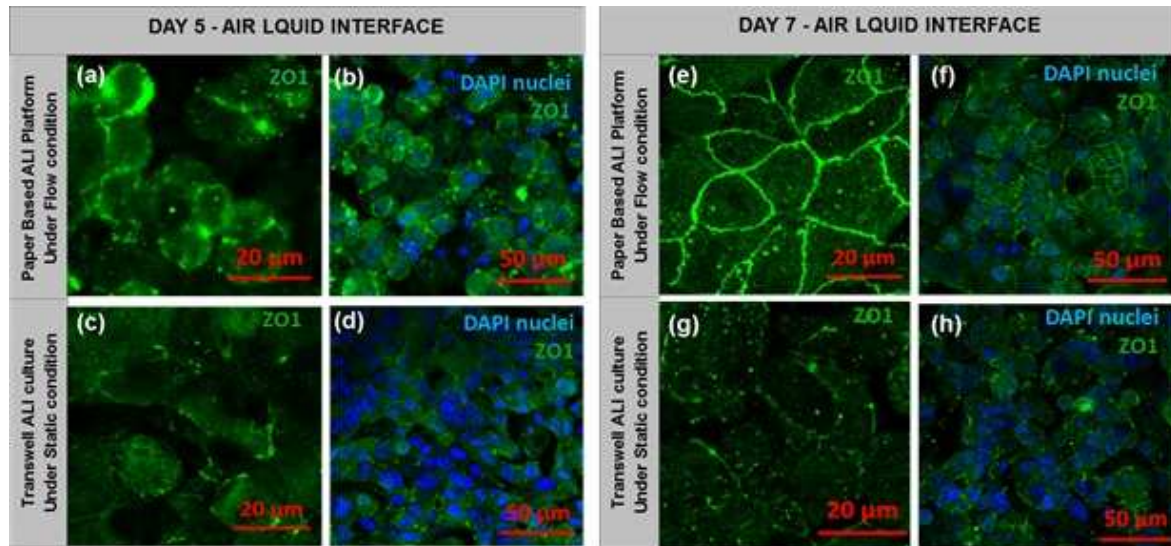


Figure 5.27. Comparison of airway epithelium integrity between paper-based ALI platform and conventional Transwell ALI. Tight junctional marker - ZO1 expression was compared between ALI platform (a,b,e,f) under flow condition and Transwell (c,d,g,h) under stasis at Day5 and Day7. The first column represents the ZO1 expression (green) at 60x magnification (scale bar = 20μm) and the second column represents the overlaid images of ZO1 (green) with DAPI nuclear staining (blue) at 40x magnification (scale bar = 50μm). The images were representative from 3 set of independent experiments. (i) Comparison of thickness of ZO1 expression between paper platform and Transwell at Day5 and Day7. Thickness of ZO1 was measured at 200% zoom of original image using Image J software. Mean was calculated from 100 random measurements from images of 3 independent experiments. \*\*\*\* $p < 0.0001$  and ns=not significant.

Unlike cells grown on transwell membranes that showed a patchy staining for ZO-1, we observed mature thick ZO1 expression (chicken wire appearance) around the whole cell membrane on day 7 ALI culture of epithelia cells grown on parchment paper under flow resembling the functional airway epithelium. On transwell system, it take about at least 3 weeks to one month to achieve the formation of mature ZO1 expression in chicken wire appearance[236], [237]. Regarding thickness of ZO1 expression, parchment paper ALI platform showed  $1.19 \mu\text{m} \pm 0.29$  thickness of ZO1 at Day7 of the ALI culture whereas transwell presented  $0.7 \mu\text{m} \pm 0.17$  thickness.

Moreover we excluded the potential influence of fibronectin coating on ZO1 formation by comparing ZO1 expression in fibronectin coated or un-coated membranes in transwell system. These experiments showed no additional effect of fibronectin on ZO1 expression at Day 5 and Day 7 of ALI culture (Figure 5.28).

In addition, we also compared the ZO1 expression between flow and static condition of the paper platform after Days 5 and 7 of ALI culture. Only small number of cells express ZO1 in immature form in static condition compared to flow condition showing the importance of the flow in air liquid interface model (Figure 5.29). Collectively, paper based ALI platform induced airway epithelium to form more efficient tight junctions under flow condition.

We suggest that the parchment paper ALI chip provides a valuable tool for cost and time efficient culture for respiratory system studies under physiologically relevant conditions. The relative small surface area, the speed in which cells can form tight junction, and the ability to perform experiments under flow are highly advantageous particularly when testing drugs uptake with different flow rates and working with small number of primary cells from patient groups (e.g. COPD and asthma) where typically very small amount of biological samples are available and testing the drug with different flow rates.

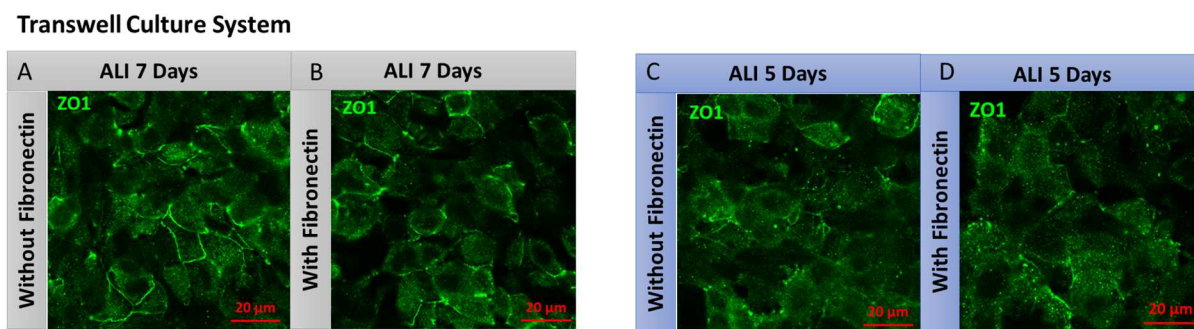


Figure 5.28. Comparison of airway epithelium integrity between with (B, D) and without fibronectin coating (A, C) on conventional Transwell ALI culture. Tight junctional marker - ZO1 expression (green colour) was compared at Day 5 and Day7. (Scale bar = 20μm).

### Paper Based Platform

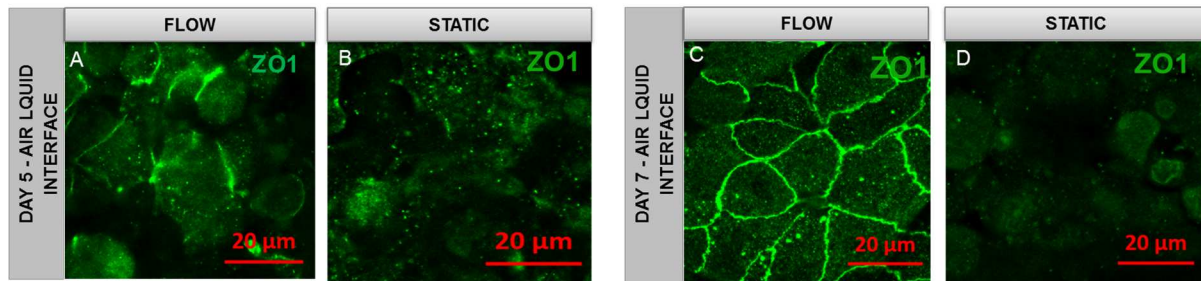


Figure 5.29. Comparison of ZO1 expression on differentiated CALU3 cells at Air Liquid Interface under flow and static condition of new ALI platform for 5days (A,B) and for 7 days (C,D). The CALU3 cells were fixed and stained with tight junction marker ZO1 (Zona Occluden1 –green) (scale bar = 20 μm)

## 6. CONCLUSION

This chapter brings together a summary of the presented laser processing techniques on multilayer films using CO<sub>2</sub> and Nd:YAG laser systems and all the designed biomedical devices described in the previous chapters. The devices include three mechanical, electrochemical, and environmental sensors along with an *in-vitro* cell culture platform for on-chip investigation of the human respiratory system. The first section covers the summary of all the achievements in this dissertation and following section provides a direction for future research.

### 6.1 Summary and Conclusions

Wearable health monitoring systems with integrated flexible sensing devices are considered to be the next generation of personal portable devices for remote health monitoring practices. The fabrication of such systems requires a deviation from traditional MEMS and transducer fabrication methods in order to create devices with satisfactory mechanical and electrical performances. Additionally, the techniques should be economical, adaptable for moderate-volume production, and preferably customizable (i.e., for a precision medicine approach). As a result, researchers have embraced the use of commercially available materials and rapid prototyping equipment for the development of low-cost, conformable, disposable devices for wound healing and other wearable applications. Processes such as inkjet printing, screen printing, micro-gravure coating, and laser machining are particularly suited for these applications due to their scalability and ease of implementation. Among these rapid fabrication technologies, laser machining offers a unique set of capabilities directly beneficial for the development of flexible/stretchable and low-cost systems. After describing the existing fabrication techniques in the introductory chapter, a brief overview of laser technologies with an emphasis on common types of laser systems CO<sub>2</sub> and Nd:YAG for flexible device manufacturing is presented in the second chapter. Chapter 3 discusses the selective carbonization process of thermoset polymers (e.g. polyimide) via CO<sub>2</sub> laser. In the process of carbonization, the polyimide is converted into a porous nano-scale carbonized layer with a very high surface area that can be used for creating functional carbon composite materials. Unlike bulk carbonization methods (e.g., furnaces), the laser-based technique offers unprecedented control over carbon nanoparticle deposition and patterning. The localized laser irradiation selectively

converts the polyimide to a highly porous and conductive carbonized structures with superhydrophilic wettability. The resulting change in surface wettability allows for selective trapping of aqueous based solutions into the carbonized regions. This chapter also describes the various ways of functionalizing the laser carbonized traces with electrically conductive materials such as silver nano particles and polyaniline. These functional composites can be used to create various carbon based sensors. Chapters 4 describes the unique capability of laser ablation for selective removal of material from multilayer films such as ITO coated PET, parchment paper and metalized paper. The use of such precise and selective removal of material can eliminate costly and time consuming processes associated with conventional photolithography and etching. Electrical, optical, mechanical, and surface analysis techniques were used to characterize the selective removal efficacy of the laser ablated area. Chapters 5 introduces novel low cost biomedical devices made by using laser processing techniques presented in the chapter 3 and 4. In chapter 5.1, we demonstrated the use of laser carbonization of polyimide to create a highly sensitive strain sensor and a wireless pressure sensor. The strain sensor fabrication is based on carbonizing conductive carbon patterns on the surface of a polyimide film using a CO<sub>2</sub> laser followed by its transfer to an elastomeric PDMS substrate. The carbonized material contain CNTs and multilayer graphene flakes that are aligned in the direction of the laser scanning, imparting anisotropy (directionality) to the sensors not achievable using reported conductive nanocomposite methods. The wireless pressure sensor uses a combination of CO<sub>2</sub> laser-induced carbonization and selective silver deposition on a polyimide sheet to create flexible highly conductive traces. The device consists of a pressure-sensitive capacitor with a variable spacing between its two electrodes that is connected in series with a planar spiral inductor. Applied pressure induces a change in the resonant frequency of the assembled LC circuit which can be detected wirelessly by an external readout coil. Section 5.2 demonstrates two pH sensing devices for wound assessment that are fabricated by using laser ablation and carbonization processes. The first pH sensors combines low-cost screen-printing with electro-polymerization of polyaniline on transparent electrodes that are fabricated by direct laser scribing of ITO films. The fabricated sensors are optically transparent, allowing visual inspection of the wound (a property highly desired by the caregivers) with an average sensitivity of  $-55$  mV/pH within physiologically relevant range of pH 4–10. The second pH sensing device is fabricated by combining irreversible bonding of PI to an Ecoflex substrate, followed by laser carbonization and micromachining serpentine traces to create highly stretchable

electrodes. This method produces highly porous carbonized 2D serpentine traces that are subsequently permeated with polyaniline as the conductive filler, binding material, and pH-sensitive membrane. The experimental and simulation results demonstrate that the stretchable serpentine PANI/C-PI interconnections with an optimal trace width of 0.3 mm can withstand elongations of up to 135% and are robust to more than 12000 stretch-and-release cycles at 20% strain without noticeable change in the resistance. The pH sensor displays a linear sensitivity in the physiological range of pH 4–10 with excellent stability to applied longitudinal and transverse strains up to 100% in different pH buffer solutions with a minimal deviation of less than  $\pm 4$  mV.

Section 5.3 describes a mask-free, and rapid process for creating low-cost humidity and temperature sensors on paper substrates by laser ablating commercially available metallized papers, a non-toxic and eco-friendly commodity often used for decorative and food packaging purposes. Humidity sensors show a linear sensitivity of about 45.7 fF/% RH at low moisture levels (2–68%RH) and an abrupt change of 1800% at higher humidity levels (85%), while the meander-pattern resistance temperature detector show an average sensitivity of 0.451  $\Omega/^{\circ}\text{C}$ . Lastly in section 5.4, we demonstrate the use of direct-patterned laser-ablating hydrophobic parchment paper as an effective semi-permeable membrane, ideal for ALI cell culture application. The surface properties of the paper are modified through a selective CO<sub>2</sub> laser-assisted treatment to create a unique porous substrate with hydrophilic regions that regulate fluid diffusion and cell attachment which can resemble the semi-permeable properties observed in the basement membrane of the human respiratory system. The final *in vitro* model, composed of parchment paper and acrylic microfluidics, was able to maintain long-term stability under a constant flow of media with faster barrier formation of airway epithelium than conventional transwell methods.

## 6.2 Future Directions

A key motivation for using laser processing is its ability to reduce the cost and time for fabricating inexpensive devices by processing commercially-available materials (e.g., polyimide, adhesive tape, paper, etc.). The effect of laser processing on any particular material depends on the physical and chemical properties of that material and the laser parameters (wavelength and energy). For instance, CO<sub>2</sub> laser ablation of thermoplastics (e.g., acrylic) can result in the evaporation of the materials without carbonization and formation of conductive traces. Thermosets, on the other hand, tend to burn/carbonize with laser ablation and form carbonic substances; however, not all

such traces are conductive. Suggested future work includes investigating the effect of various laser systems on different polymers, with a strong focus on several particularly promising ones, i.e., polyurethane, rubber, polyimide, photoresist, parylene, and dried hydrogel (agar, gelatin, and alginate). Our Preliminary experiments have shown the ability to carbonize rubber, but the resulting patterns exhibit a very high resistance. Nevertheless, by adjusting the laser parameters, it may be possible to create high-quality (and more conductive) stretchable traces, eliminating the need for transferring the carbonized material onto a stretchable elastomer. Parylene is another attractive material which has been extensively used in the fabrication of BioMEMS devices. Parylene is also a thermoset polymer that can be selective carbonized using a CO<sub>2</sub> laser. The implications of using parylene as the substrate include the unique opportunity to directly laser write conductive traces on 3D objects which are conformably coated with parylene, thus creating an easy method for imparting electrical conductivity on 3D surfaces. Parylene coating and carbonization can be performed sequentially on multiple layers to create a single 3D printed object with multiple layers of electronics. Furthermore, the electrical conductivity of the carbonized traces can enable electroplating highly conductivity traces that can be used in designing RF modules (e.g. antenna, and filters) on 3D printed objects. In this dissertation, we focused on carbonization and laser ablation with a CO<sub>2</sub> and Nd:YAG pulsed laser in a standard atmospheric environment (21% O<sub>2</sub> and 78% N<sub>2</sub>). Future work should include investigating the effect of various types of lasers and processing environments. It should also include investigating other commonly used lasers such as diode and UV lasers to understand their effects on material properties and their ability to generate conductive carbon nanoparticles. The quality of the carbonized film is also influenced by the atmosphere under which laser processing is performed. Previous research has shown that different gasses such as N<sub>2</sub> and H<sub>2</sub> can have effect on the quality and morphology of the pyrolyzed carbon. Another remaining task in the material laser processing area includes the characterization of laser carbonization process under controlled local micro-environments and investigating its effects on the carbonized material properties. Future investigations should study the effect of solvent treatment on carbonization process using various thermoset polymers and solvents. Polymers interact with solvents and can undergo dissolution, swelling, and sorption that could potentially influence the characteristic of the electrical and structural characteristic of the laser carbonized material.

## REFERENCES

- [1] J. Yeo, S. Hong, D. Lee, N. Hotz, M. T. Lee, C. P. Grigoropoulos, and S. H. Ko, "Next generation non-vacuum, maskless, low temperature nanoparticle ink laser digital direct metal patterning for a large area flexible electronics," *PLoS One*, vol. 7, no. 8, pp. 1–9, 2012.
- [2] Kenry, J. C. Yeo, and C. T. Lim, "Emerging flexible and wearable physical sensing platforms for healthcare and biomedical applications," *Microsystems Nanoeng.*, vol. 2, no. October 2015, p. 16043, 2016.
- [3] D.-H. Kim, R. Ghaffari, N. Lu, and J. A. Rogers, "Flexible and stretchable electronics for biointegrated devices.," *Annu. Rev. Biomed. Eng.*, vol. 14, pp. 113–28, Jan. 2012.
- [4] S. Wang, T. Chinnasamy, M. A. Lifson, F. Inci, and U. Demirci, "Flexible Substrate-Based Devices for Point-of-Care Diagnostics," *Trends Biotechnol.*, vol. xx, pp. 1–13, 2016.
- [5] D.-H. Kim, J. Xiao, J. Song, Y. Huang, and J. A. Rogers, "Stretchable, curvilinear electronics based on inorganic materials.," *Adv. Mater.*, vol. 22, no. 19, pp. 2108–24, May 2010.
- [6] R. Pelton, "Bioactive paper provides a low-cost platform for diagnostics," *TrAC Trends Anal. Chem.*, vol. 28, no. 8, pp. 925–942, Sep. 2009.
- [7] E. L. Tan, W. N. Ng, R. Shao, B. D. Pereles, and K. G. Ong, "A Wireless, Passive Sensor for Quantifying Packaged Food Quality," *Sensors*, vol. 7, no. 9, pp. 1747–1756, Sep. 2007.
- [8] S. Editor and D. J. Lockwood, *Environmental Analysis by Electrochemical Sensors and Biosensors*, vol. 2. New York, NY: Springer New York, 2015.
- [9] B. A. Nathan, F. Ieee, A. Ahnood, M. T. Cole, S. Lee, M. Ieee, Y. Suzuki, P. Hiralal, F. Bonaccorso, T. Hasan, L. Garcia-gancedo, A. Dyadyusha, S. Haque, P. Andrew, S. Hofmann, J. Moultrie, D. Chu, A. J. Flewitt, A. C. Ferrari, M. J. Kelly, J. Robertson, F. Ieee, G. A. J. Amaratunga, and W. I. Milne, "Flexible Electronics : The Next Ubiquitous Platform," vol. 100, no. Special Centennial Issue, pp. 1486 – 1517, 2012.
- [10] D. Zhang and Q. Liu, "Biosensors and bioelectronics on smartphone for portable biochemical detection," *Biosens. Bioelectron.*, vol. 75, pp. 273–284, 2016.

- [11] J. C. Yeo, K. Kenry, and C. T. Lim, “Emergence of the microfluidic wearable technologies,” *Lab Chip*, 2016.
- [12] E.-H. Yoo and S.-Y. Lee, “Glucose biosensors: an overview of use in clinical practice.,” *Sensors (Basel)*, vol. 10, no. 5, pp. 4558–76, Jan. 2010.
- [13] A. J. Bandonkar, V. W. S. Hung, W. Jia, G. Valdés-Ramírez, J. R. Windmiller, A. G. Martinez, J. Ramírez, G. Chan, K. Kerman, and J. Wang, “Tattoo-based potentiometric ion-selective sensors for epidermal pH monitoring.,” *Analyst*, vol. 138, no. 1, pp. 123–8, 2013.
- [14] W. Li, D. C. Rodger, A. Pinto, E. Meng, J. D. Weiland, M. S. Humayun, and Y. C. Tai, “Parylene-based integrated wireless single-channel neurostimulator,” *Sensors Actuators, A Phys.*, vol. 166, no. 2, pp. 193–200, 2011.
- [15] P. J. Rousche, D. S. Pellinen, D. P. Pivin, J. C. Williams, R. J. Vetter, and D. R. Kipke, “Flexible polyimide-based intracortical electrode arrays with bioactive capability.,” *IEEE Trans. Biomed. Eng.*, vol. 48, no. 3, pp. 361–71, Mar. 2001.
- [16] D.-H. Kim, N. Lu, R. Ma, Y.-S. Kim, R.-H. Kim, S. Wang, J. Wu, S. M. Won, H. Tao, A. Islam, K. J. Yu, T. Kim, R. Chowdhury, M. Ying, L. Xu, M. Li, H.-J. Chung, H. Keum, M. McCormick, P. Liu, Y. Zhang, F. G. Omenetto, Y. Huang, T. Coleman, and J. A. Rogers, “Epidermal electronics,” *Science (80-. )*, vol. 333, no. September, pp. 838–843, 2011.
- [17] M. Ying, A. P. Bonifas, N. Lu, Y. Su, R. Li, H. Cheng, A. Ameen, Y. Huang, and J. A. Rogers, “Silicon nanomembranes for fingertip electronics.,” *Nanotechnology*, vol. 23, no. 34, p. 344004, Aug. 2012.
- [18] D.-H. Kim, N. Lu, R. Ghaffari, Y.-S. Kim, S. P. Lee, L. Xu, J. Wu, R.-H. Kim, J. Song, Z. Liu, J. Viventi, B. de Graff, B. Elolampi, M. Mansour, M. J. Slepian, S. Hwang, J. D. Moss, S.-M. Won, Y. Huang, B. Litt, and J. A. Rogers, “Materials for multifunctional balloon catheters with capabilities in cardiac electrophysiological mapping and ablation therapy.,” *Nat. Mater.*, vol. 10, no. 4, pp. 316–23, Apr. 2011.
- [19] H. Lee, C. Song, Y. S. Hong, M. S. Kim, H. R. Cho, T. Kang, K. Shin, S. H. Choi, T. Hyeon, and D.-H. Kim, “Wearable/disposable sweat-based glucose monitoring device with multistage transdermal drug delivery module,” *Sci. Adv.*, vol. 3, no. 3, p. e1601314, 2017.

- [20] D.-H. Kim, S. Wang, H. Keum, R. Ghaffari, Y.-S. Kim, H. Tao, B. Panilaitis, M. Li, Z. Kang, F. Omenetto, Y. Huang, and J. A. Rogers, "Thin, flexible sensors and actuators as 'instrumented' surgical sutures for targeted wound monitoring and therapy.," *Small*, vol. 8, no. 21, pp. 3263–8, Nov. 2012.
- [21] J. Viventi, D.-H. Kim, L. Vigeland, E. S. Frechette, J. A. Blanco, Y.-S. Kim, A. E. Avrin, V. R. Tiruvadi, S.-W. Hwang, A. C. Vanleer, D. F. Wulsin, K. Davis, C. E. Gelber, L. Palmer, J. Van der Spiegel, J. Wu, J. Xiao, Y. Huang, D. Contreras, J. A. Rogers, and B. Litt, "Flexible, foldable, actively multiplexed, high-density electrode array for mapping brain activity in vivo," *Nat. Neurosci.*, vol. 14, no. 12, pp. 1599–1605, Nov. 2011.
- [22] J. Viventi, D.-H. Kim, J. D. Moss, Y. Kim, J. A. Blanco, N. Annetta, A. Hicks, J. Xiao, Y. Huang, D. J. Callans, J. A. Rogers, and B. Litt, "A conformal, bio-interfaced class of silicon electronics for mapping cardiac electrophysiology.," *Sci. Transl. Med.*, vol. 2, no. 24, p. 24ra22, Mar. 2010.
- [23] S. Il Park, D. S. Brenner, G. Shin, C. D. Morgan, B. A. Copits, H. U. Chung, M. Y. Pullen, K. N. Noh, S. Davidson, S. J. Oh, J. Yoon, K. Jang, V. K. Samineni, M. Norman, J. G. Grajales-reyes, S. K. Vogt, S. S. Sundaram, K. M. Wilson, J. S. Ha, R. Xu, T. Pan, T. Kim, Y. Huang, M. C. Montana, J. P. Golden, M. R. Bruchas, R. W. G. Iv, and J. A. Rogers, "letters Soft , stretchable , fully implantable miniaturized optoelectronic systems for wireless optogenetics," *Nat. Biotechnol.*, vol. 33, no. 12, pp. 1280–1286, 2015.
- [24] M. Ochoa, R. Rahimi, and B. Ziaie, "Flexible Sensors for Chronic Wound Management," *IEEE Rev. Biomed. Eng.*, vol. 7, pp. 73–86, Jan. 2014.
- [25] J.-H. Ahn and J. H. Je, "Stretchable electronics: materials, architectures and integrations," *J. Phys. D. Appl. Phys.*, vol. 45, no. 10, p. 103001, Mar. 2012.
- [26] G. M. Whitesides, N. Bowden, S. Brittain, A. G. Evans, and J. W. Hutchinson, "No Title," *Nature*, vol. 393, no. 6681, pp. 146–149, May 1998.
- [27] J. Jones, S. P. Lacour, S. Wagner, and Z. Suo, "Stretchable wavy metal interconnects," *J. Vac. Sci. Technol. A Vacuum, Surfaces, Film.*, vol. 22, no. 4, p. 1723, 2004.
- [28] S. P. Lacour, J. Jones, Z. Suo, and S. Wagner, "Design and Performance of Thin Metal Film Interconnects for Skin-Like Electronic Circuits," *IEEE Electron Device Lett.*, vol. 25, no. 4, pp. 179–181, Apr. 2004.

- [29] D.-H. Kim and J. A. Rogers, “Stretchable Electronics: Materials Strategies and Devices,” *Adv. Mater.*, vol. 20, no. 24, pp. 4887–4892, Dec. 2008.
- [30] D.-Y. Khang, H. Jiang, Y. Huang, and J. a Rogers, “A stretchable form of single-crystal silicon for high-performance electronics on rubber substrates.,” *Science*, vol. 311, no. 5758, pp. 208–12, Jan. 2006.
- [31] Y. Sun, W. M. Choi, H. Jiang, Y. Y. Huang, and J. a Rogers, “Controlled buckling of semiconductor nanoribbons for stretchable electronics.,” *Nat. Nanotechnol.*, vol. 1, no. 3, pp. 201–7, Dec. 2006.
- [32] Y. Zhang, S. Xu, H. Fu, J. Lee, J. Su, K.-C. Hwang, J. a Rogers, and Y. Huang, “Buckling in serpentine microstructures and applications in elastomer-supported ultra-stretchable electronics with high areal coverage.,” *Soft Matter*, vol. 9, no. 33, pp. 8062–8070, 2013.
- [33] Y. Hsu, M. Gonzalez, F. Bossuyt, J. Vanfleteren, and I. De Wolf, “Polyimide-Enhanced Stretchable Interconnects: Design, Fabrication, and Characterization,” *IEEE Trans. Electron Devices*, vol. 58, no. 8, pp. 2680–2688, Aug. 2011.
- [34] S. Xu, Y. Zhang, J. Cho, J. Lee, X. Huang, L. Jia, J. a Fan, Y. Su, J. Su, H. Zhang, H. Cheng, B. Lu, C. Yu, C. Chuang, T.-I. Kim, T. Song, K. Shigeta, S. Kang, C. Dagdeviren, I. Petrov, P. V Braun, Y. Huang, U. Paik, and J. a Rogers, “Stretchable batteries with self-similar serpentine interconnects and integrated wireless recharging systems,” *Nat. Commun.*, vol. 4, p. 1543, Feb. 2013.
- [35] D.-H. Kim, N. Lu, R. Ghaffari, Y.-S. Kim, S. P. Lee, L. Xu, J. Wu, R.-H. Kim, J. Song, Z. Liu, J. Viventi, B. de Graff, B. Elolampi, M. Mansour, M. J. Slepian, S. Hwang, J. D. Moss, S.-M. Won, Y. Huang, B. Litt, and J. A. Rogers, “Materials for multifunctional balloon catheters with capabilities in cardiac electrophysiological mapping and ablation therapy,” *Nat. Mater.*, vol. 10, no. 4, pp. 316–323, Apr. 2011.
- [36] S. Bocchini, A. Chiolerio, S. Porro, D. Accardo, N. Garino, K. Bejtka, D. Perrone, and C. F. Pirri, “Synthesis of polyaniline-based inks, doping thereof and test device printing towards electronic applications,” *J. Mater. Chem. C*, vol. 1, no. 33, p. 5101, 2013.
- [37] A. Zeumault, S. Ma, and J. Holbery, “Fully inkjet-printed metal-oxide thin-film transistors on plastic,” *Phys. status solidi*, vol. 7, pp. 1–7, Mar. 2016.

- [38] O.-S. Kwon, H. Kim, H. Ko, J. Lee, B. Lee, C.-H. Jung, J.-H. Choi, and K. Shin, "Fabrication and characterization of inkjet-printed carbon nanotube electrode patterns on paper," *Carbon N. Y.*, vol. 58, pp. 116–127, Jul. 2013.
- [39] R. Giardi, S. Porro, A. Chiolerio, E. Celasco, and M. Sangermano, "Inkjet printed acrylic formulations based on UV-reduced graphene oxide nanocomposites," *J. Mater. Sci.*, vol. 48, no. 3, pp. 1249–1255, Feb. 2013.
- [40] W. Shen, X. Zhang, Q. Huang, Q. Xu, and W. Song, "Preparation of solid silver nanoparticles for inkjet printed flexible electronics with high conductivity.," *Nanoscale*, vol. 6, no. 3, pp. 1622–8, 2014.
- [41] M. Singh, H. M. Haverinen, P. Dhagat, and G. E. Jabbour, "Inkjet printing-process and its applications.," *Adv. Mater.*, vol. 22, no. 6, pp. 673–85, Feb. 2010.
- [42] J. Weremczuk, G. Tarapata, and R. S. Jachowicz, "The ink-jet printing humidity sorption sensor—modelling, design, technology and characterization," *Meas. Sci. Technol.*, vol. 23, no. 1, p. 014003, Jan. 2012.
- [43] Y. Liu and M. Lee, "Laser Direct Synthesis and Patterning of Silver Nano/Microstructures on a Polymer Substrate," *ACS Appl. Mater. Interfaces*, vol. 6, no. 16, pp. 14576–14582, Aug. 2014.
- [44] A. Manshina, A. Povolotskiy, T. Ivanova, A. Kurochkin, Y. Tver'yanovich, D. Kim, M. Kim, and S. C. Kwon, "CuCl<sub>2</sub> -based liquid electrolyte precursor for laser-induced metal deposition," *Laser Phys. Lett.*, vol. 4, no. 3, pp. 242–246, Mar. 2007.
- [45] K. Kordás, K. Bali, S. Leppävuori, A. Uusimäki, and L. Nánai, "Laser direct writing of copper on polyimide surfaces from solution," *Appl. Surf. Sci.*, vol. 154–155, pp. 399–404, Feb. 2000.
- [46] V. A. Kochemirovsky, L. S. Logunov, S. V. Safonov, I. I. Tumkin, Y. S. Tver'yanovich, and L. G. Menchikov, "Sorbitol as an efficient reducing agent for laser-induced copper deposition," *Appl. Surf. Sci.*, vol. 259, pp. 55–58, Oct. 2012.
- [47] E. J. Bjerneld, K. V. G. K. Murty, J. Prikulis, and M. Käll, "Laser-Induced Growth of Ag Nanoparticles from Aqueous Solutions," *ChemPhysChem*, vol. 3, no. 1, pp. 116–119, Jan. 2002.

- [48] Y. Niidome, A. Hori, H. Takahashi, Y. Goto, and S. Yamada, "Laser-Induced Deposition of Gold Nanoparticles onto Glass Substrates in Cyclohexane," *Nano Lett.*, vol. 1, no. 7, pp. 365–369, Jul. 2001.
- [49] Y. F. Lu, M. Takai, T. Nakata, S. Nagatomo, and S. Namba, "Laser-induced deposition of Ni lines on ferrite in NiSO<sub>4</sub> aqueous solution," *Appl. Phys. A Solids Surfaces*, vol. 52, no. 2, pp. 129–134, Feb. 1991.
- [50] D. A. Willis and V. Grosu, "Microdroplet deposition by laser-induced forward transfer," *Appl. Phys. Lett.*, vol. 86, no. 24, pp. 1–3, 2005.
- [51] S. Winter, M. Zenou, and Z. Kotler, "Conductivity of laser printed copper structures limited by nano-crystal grain size and amorphous metal droplet shell," *J. Phys. D. Appl. Phys.*, vol. 49, no. 16, p. 165310, 2016.
- [52] C. B. Arnold, P. Serra, and A. Piqué, "Laser Direct-Write Techniques for Printing of Complex Materials," *MRS Bull.*, vol. 32, no. 01, pp. 23–32, 2007.
- [53] D. B. Chrisey, A. Piqué, R. A. McGill, J. S. Horwitz, B. R. Ringeisen, D. M. Bubb, and P. K. Wu, "Laser Deposition of Polymer and Biomaterial Films," *Chem. Rev.*, vol. 103, no. 2, pp. 553–576, Feb. 2003.
- [54] S. H. Ko, H. Pan, C. P. Grigoropoulos, C. K. Luscombe, J. M. J. Fréchet, and D. Poulidakos, "All-inkjet-printed flexible electronics fabrication on a polymer substrate by low-temperature high-resolution selective laser sintering of metal nanoparticles," *Nanotechnology*, vol. 18, no. 34, p. 345202, Aug. 2007.
- [55] I. Theodorakos, F. Zacharatos, R. Geremia, D. Karnakis, and I. Zergioti, "Selective laser sintering of Ag nanoparticles ink for applications in flexible electronics," *Appl. Surf. Sci.*, vol. 336, pp. 157–162, May 2015.
- [56] A. Chiolerio, G. Maccioni, P. Martino, M. Cotto, P. Pandolfi, P. Rivolo, S. Ferrero, and L. Scaltrito, "Inkjet printing and low power laser annealing of silver nanoparticle traces for the realization of low resistivity lines for flexible electronics," *Microelectron. Eng.*, vol. 88, no. 8, pp. 2481–2483, Aug. 2011.
- [57] S. Hong, J. Yeo, G. Kim, D. Kim, H. Lee, J. Kwon, H. Lee, P. Lee, and S. H. Ko, "Nonvacuum, maskless fabrication of a flexible metal grid transparent conductor by low-temperature selective laser sintering of nanoparticle ink," *ACS Nano*, vol. 7, no. 6, pp. 5024–5031, 2013.

- [58] Y. Son, J. Yeo, H. Moon, T. W. Lim, S. Hong, K. H. Nam, S. Yoo, C. P. Grigoropoulos, D. Y. Yang, and S. H. Ko, "Nanoscale electronics: Digital fabrication by direct femtosecond laser processing of metal nanoparticles," *Adv. Mater.*, vol. 23, pp. 3176–3181, 2011.
- [59] J. Lin, Z. Peng, Y. Liu, F. Ruiz-Zepeda, R. Ye, E. L. G. Samuel, M. J. Yacaman, B. I. Yakobson, and J. M. Tour, "Laser-induced porous graphene films from commercial polymers," *Nat. Commun.*, vol. 5, p. 5714, Dec. 2014.
- [60] R. Rahimi, M. Ochoa, W. Yu, and B. Ziaie, "Highly Stretchable and Sensitive Unidirectional Strain Sensor via Laser Carbonization," *ACS Appl. Mater. Interfaces*, vol. 7, no. 8, pp. 4463–4470, Mar. 2015.
- [61] S. Mueller, B. Kruck, and P. Baudisch, "LaserOrigami: laser-cutting 3D objects," in *Proceedings of the SIGCHI Conference on Human Factors in Computing Systems*, 2013, pp. 2585–2592.
- [62] A. Toossi, M. Daneshmand, and D. Sameoto, "A low-cost rapid prototyping method for metal electrode fabrication using a CO<sub>2</sub> laser cutter," *J. Micromechanics Microengineering*, vol. 23, no. 4, p. 047001, Apr. 2013.
- [63] J. Yuan, J. Chen, and C. He, "Research of micro removing copper foil of FCCL assisted with laser," in *2011 IEEE International Conference on Mechatronics and Automation*, 2011, pp. 749–754.
- [64] J. C. Ion, *Laser Processing of Engineering Materials: Principles, Procedure and Industrial Applications*. Oxford: Elsevier Butterworth-Heinemann, 2005.
- [65] D. Bäuerle, *Laser Processing and Chemistry*. .
- [66] N. B. Dahotre and S. P. Harimkar, *Laser Fabrication and Machining of Materials*. Springer, 2007.
- [67] C. Hallgren, H. Reimers, D. Chakarov, J. Gold, and A. Wennerberg, "An in vivo study of bone response to implants topographically modified by laser micromachining," *Biomaterials*, vol. 24, no. 5, pp. 701–710, 2003.
- [68] D. W. and J. B. G. J. R. Lawrence, C. Dowding, *Lasers in Surface Engineering, Surface Engineering Serires*. ASM International, 1998.

- [69] M. Psarski, J. Marczak, J. Grobelny, and G. Celichowski, "Superhydrophobic surface by replication of laser micromachined pattern in epoxy/alumina nanoparticle composite," *J. Nanomater.*, vol. 2014, 2014.
- [70] H. Klank, J. P. Kutter, and O. Geschke, "CO(2)-laser micromachining and back-end processing for rapid production of PMMA-based microfluidic systems.," *Lab Chip*, vol. 2, no. 4, pp. 242–246, Nov. 2002.
- [71] J. Lawrence and L. Li, *Laser modification of the wettability characteristics of engineering materials*. Professional Engineering, 2001.
- [72] G. Chitnis, Z. Ding, C.-L. Chang, C. a Savran, and B. Ziaie, "Laser-treated hydrophobic paper: an inexpensive microfluidic platform.," *Lab Chip*, vol. 11, no. 6, pp. 1161–5, Mar. 2011.
- [73] A. Qureshi, W. P. Kang, J. L. Davidson, and Y. Gurbuz, "Review on carbon-derived, solid-state, micro and nano sensors for electrochemical sensing applications," *Diam. Relat. Mater.*, vol. 18, no. 12, pp. 1401–1420, Dec. 2009.
- [74] S. Park, M. Vosguerichian, and Z. Bao, "A review of fabrication and applications of carbon nanotube film-based flexible electronics," *Nanoscale*, vol. 5, no. 5, p. 1727, Mar. 2013.
- [75] W.-J. Guan, Y. Li, Y.-Q. Chen, X.-B. Zhang, and G.-Q. Hu, "Glucose biosensor based on multi-wall carbon nanotubes and screen printed carbon electrodes.," *Biosens. Bioelectron.*, vol. 21, no. 3, pp. 508–12, Sep. 2005.
- [76] S. J. Leigh, R. J. Bradley, C. P. Purssell, D. R. Billson, and D. a Hutchins, "A simple, low-cost conductive composite material for 3D printing of electronic sensors.," *PLoS One*, vol. 7, no. 11, p. e49365, Jan. 2012.
- [77] S. Pyo, J.-I. Lee, M.-O. Kim, T. Chung, Y. Oh, S.-C. Lim, J. Park, and J. Kim, "Development of a flexible three-axis tactile sensor based on screen-printed carbon nanotube-polymer composite," *J. Micromechanics Microengineering*, vol. 24, no. 7, p. 075012, Jul. 2014.
- [78] J. Wang, B. Tian, V. B. Nascimento, and L. Angnes, "Performance of screen- printed carbon electrodes fabricated from different carbon inks," *Electrochim. Acta*, vol. 43, pp. 3459–3465, 1988.

- [79] K. Grennan, A. J. Killard, and M. R. Smyth, "Physical Characterizations of a Screen-Printed Electrode for Use in an Amperometric Biosensor System," *Electroanalysis*, vol. 13, no. 8–9, pp. 745–750, 2001.
- [80] A. J. Bandothkar, V. W. S. Hung, W. Jia, G. Valdés-Ramírez, J. R. Windmiller, A. G. Martinez, J. Ramírez, G. Chan, K. Kerman, and J. Wang, "Tattoo-based potentiometric ion-selective sensors for epidermal pH monitoring," *Analyst*, vol. 138, no. 1, pp. 123–8, Jan. 2013.
- [81] R. Rahimi, M. Ochoa, W. Yu, and B. Ziaie, "Highly Stretchable and Sensitive Unidirectional Strain Sensor via Laser Carbonization," *ACS Appl. Mater. Interfaces*, Feb. 2015.
- [82] M.-Y. Cheng, C.-M. Tsao, Y.-Z. Lai, and Y.-J. Yang, "The development of a highly twistable tactile sensing array with stretchable helical electrodes," *Sensors Actuators A Phys.*, vol. 166, no. 2, pp. 226–233, Apr. 2011.
- [83] J. Zhong, "Carbon Nanofibers and Their Composites: A Review of Synthesizing, Properties and Applications," *Materials (Basel)*, vol. 7, no. 5, pp. 3919–3945, 2014.
- [84] O. C. Jeong and S. Konishi, "Three-dimensionally combined carbonized polymer sensor and heater," *Sensors Actuators A Phys.*, vol. 143, no. 1, pp. 97–105, May 2008.
- [85] N. E. Hebert, B. Snyder, R. L. McCreery, W. G. Kuhr, and S. A. Brazill, "Performance of Pyrolyzed Photoresist Carbon Films in a Microchip Capillary Electrophoresis Device with Sinusoidal Voltammetric Detection," *Anal. Chem*, vol. 75, no. 16, pp. 4265–4271, 2003.
- [86] M. S. Kim, B. Hsia, C. Carraro, and R. Maboudian, "Flexible micro-supercapacitors with high energy density from simple transfer of photoresist-derived porous carbon electrodes," *Carbon N. Y.*, vol. 74, pp. 163–169, 2014.
- [87] H.-S. Min, B. Y. Park, L. Taherabadi, C. Wang, Y. Yeh, R. Zaouk, M. J. Madou, and B. Dunn, "Fabrication and properties of a carbon/polypyrrole three-dimensional microbattery," *J. Power Sources*, vol. 178, no. 2, pp. 795–800, Apr. 2008.
- [88] K. C. Morton, C. A. Morris, M. A. Derylo, R. Thakar, and L. A. Baker, "Carbon Electrode Fabrication from Pyrolyzed Parylene C," *Anal. Chem*, vol. 83, 13, pp. 5447–5452, 2011.
- [89] T. Lippert, E. Ortelli, J. Panitz, F. Raimondi, J. Wambach, J. Wei, and A. Wokaun, "Imaging-XPS / Raman investigation on the carbonization of polyimide after irradiation at 308 nm," *Appl. Phys. A*, vol. 69, pp. 651–654, 1999.

- [90] G. . Shafeev and P. Hoffmann, "Light-enhanced electroless Cu deposition on laser-treated polyimide surface," *Appl. Surf. Sci.*, vol. 138–139, pp. 455–460, Jan. 1999.
- [91] J. M. Ingram, M. Greb, J. a. Nicholson, and A. W. Fountain, "Polymeric humidity sensor based on laser carbonized polyimide substrate," *Sensors Actuators B Chem.*, vol. 96, no. 1–2, pp. 283–289, Nov. 2003.
- [92] M. Inagaki, S. Harada, T. Sato, T. Nakajima, Y. Horino, and K. Morita, "Carbonization of polyimide film 'Kapton,'" *Carbon N. Y.*, vol. 27, no. 2, pp. 253–257, 1989.
- [93] F. Raimondi, S. Abolhassani, R. Brüttsch, F. Geiger, T. Lippert, J. Wambach, J. Wei, and a. Wokaun, "Quantification of polyimide carbonization after laser ablation," *J. Appl. Phys.*, vol. 88, no. 6, p. 3659, 2000.
- [94] M. Park, L. N. Cella, W. Chen, N. V Myung, and A. Mulchandani, "Carbon nanotubes-based chemiresistive immunosensor for small molecules: detection of nitroaromatic explosives.," *Biosens. Bioelectron.*, vol. 26, no. 4, pp. 1297–301, Dec. 2010.
- [95] J. Li, Y. Lu, Q. L. Ye, J. Han, and M. Meyyappan, "Carbon Nanotube Based Chemical Sensors for Gas and Vapor Detection," *Chem. Phys. Lett*, vol. 313, no. 2, p. 91, 1999.
- [96] J. Bin In, B. Hsia, J.-H. Yoo, S. Hyun, C. Carraro, R. Maboudian, and C. P. Grigoropoulos, "Facile fabrication of flexible all solid-state micro-supercapacitor by direct laser writing of porous carbon in polyimide," *Carbon N. Y.*, vol. 83, 144–151, Mar. 2015.
- [97] S. Luo, P. T. Hoang, and T. Liu, "Direct laser writing for creating porous graphitic structures and their use for flexible and highly sensitive sensor and sensor arrays," *Carbon N. Y.*, vol. 96, pp. 522–531, Jan. 2016.
- [98] S. B. Walker and J. A. Lewis, "Reactive Silver Inks for Patterning High-Conductivity Features at Mild Temperatures," *J. Am. Chem. Soc.*, vol. 134, no. 3, pp. 1419–1421, Jan. 2012.
- [99] B. P. Vinayan, R. Nagar, V. Raman, N. Rajalakshmi, K. S. Dhathathreyan, and S. Ramaprabhu, "Synthesis of graphene-multiwalled carbon nanotubes hybrid nanostructure by strengthened electrostatic interaction and its lithium ion battery application," *J. Mater. Chem.*, vol. 22, no. 19, p. 9949, 2012.
- [100] H. Cheng, Z. Dong, C. Hu, Y. Zhao, Y. Hu, L. Qu, N. Chen, and L. Dai, "Textile electrodes woven by carbon nanotube–graphene hybrid fibers for flexible electrochemical capacitors," *Nanoscale*, vol. 5, no. 8, p. 3428, Apr. 2013.

- [101] W. Shen, X. Zhang, Q. Huang, Q. Xu, and W. Song, "Preparation of solid silver nanoparticles for inkjet printed flexible electronics with high conductivity.," *Nanoscale*, vol. 6, no. 3, pp. 1622–8, Jan. 2014.
- [102] R. Shankar, L. Groven, A. Amert, K. W. Whites, and J. J. Kellar, "Non-aqueous synthesis of silver nanoparticles using tin acetate as a reducing agent for the conductive ink formulation in printed electronics," *J. Mater. Chem.*, vol. 21, no. 29, p. 10871, 2011.
- [103] M. T. Byrne and Y. K. Gun'ko, "Recent advances in research on carbon nanotube-polymer composites.," *Adv. Mater.*, vol. 22, no. 15, pp. 1672–88, Apr. 2010.
- [104] S. R. Shin, R. Farzad, A. Tamayol, V. Manoharan, P. Mostafalu, Y. S. Zhang, M. Akbari, S. M. Jung, D. Kim, M. Comotto, N. Annabi, F. E. Al-Hazmi, M. R. Dokmeci, and A. Khademhosseini, "A Bioactive Carbon Nanotube-Based Ink for Printing 2D and 3D Flexible Electronics," *Adv. Mater.*, vol. 28, no. 17, pp. 3280–3289, 2016.
- [105] S. Park, M. Vosguerichian, and Z. Bao, "A review of fabrication and applications of carbon nanotube film-based flexible electronics.," *Nanoscale*, vol. 5, no. 5, pp. 52, 2013.
- [106] R. Rahimi, M. Ochoa, and B. Ziaie, "Direct Laser Writing of Porous-Carbon/Silver Nanocomposite for Flexible Electronics," *ACS Appl. Mater. Interfaces*, vol. 8, no. 26, pp. 16907–16913, 2016.
- [107] T. Yamada, Y. Hayamizu, Y. Yamamoto, Y. Yomogida, A. Izadi-Najafabadi, D. N. Futaba, and K. Hata, "A stretchable carbon nanotube strain sensor for human-motion detection.," *Nat. Nanotechnol.*, vol. 6, no. 5, pp. 296–301, May 2011.
- [108] J. Yu, W. Lu, S. Pei, K. Gong, L. Wang, L. Meng, Y. Huang, J. P. Smith, K. S. Booksh, Q. Li, J.-H. Byun, Y. Oh, Y. Yan, and T.-W. Chou, "Omnidirectionally Stretchable High-Performance Supercapacitor Based on Isotropic Buckled Carbon Nanotube Films," *ACS Nano*, vol. 10, no. 5, pp. 5204–5211, May 2016.
- [109] J. Zhou, X. Xu, H. Yu, and G. Lubineau, "Deformable and wearable carbon nanotube microwire-based sensors for ultrasensitive monitoring of strain, pressure and torsion," *Nanoscale*, pp. 604–612, 2017.
- [110] M. Sopronyi, F. Sima, C. Vaulot, L. Delmotte, A. Bahouka, and C. Matei Ghimbeu, "Direct synthesis of graphitic mesoporous carbon from green phenolic resins exposed to subsequent UV and IR laser irradiations," *Sci. Rep.*, vol. 6, no. October, p. 39617, 2016.

- [111] F. Clerici, M. Fontana, S. Bianco, M. Serrapede, F. Perrucci, S. Ferrero, E. Tresso, and A. Lamberti, “*In situ* MoS<sub>2</sub> Decoration of Laser-Induced Graphene as Flexible Supercapacitor Electrodes,” *ACS Appl. Mater. Interfaces*, p. acsami.6b00808, 2016.
- [112] Y. Lu, H. Lyu, A. G. Richardson, T. H. Lucas, and D. Kuzum, “Flexible Neural Electrode Array Based-on Porous Graphene for Cortical Microstimulation and Sensing,” *Sci. Rep.*, vol. 6, no. August, p. 33526, Sep. 2016.
- [113] A. Patole and G. Lubineau, “Carbon nanotubes with silver nanoparticle decoration and conductive polymer coating for improving the electrical conductivity of polycarbonate composites,” *Carbon N. Y.*, vol. 81, pp. 720–730, 2014.
- [114] L. M. Malard, M. A. Pimenta, G. Dresselhaus, and M. S. Dresselhaus, “Raman spectroscopy in graphene,” *Phys. Rep.*, vol. 473, no. 5–6, pp. 51–87, Apr. 2009.
- [115] M. Liu, Y.-E. Miao, C. Zhang, W. W. Tjiu, Z. Yang, H. Peng, and T. Liu, “Hierarchical composites of polyaniline-graphene nanoribbons-carbon nanotubes as electrode materials in all-solid-state supercapacitors,” *Nanoscale*, vol. 5, no. 16, pp. 7312–20, 2013.
- [116] J. Lin, Z. Peng, Y. Liu, F. Ruiz-Zepeda, R. Ye, E. L. G. Samuel, M. J. Yacaman, B. I. Yakobson, and J. M. Tour, “Laser-induced porous graphene films from commercial polymers,” *Nat. Commun.*, vol. 5, no. 5714, pp. 1–8, 2014.
- [117] R. Verplancke, F. Bossuyt, D. Cuypers, and J. Vanfleteren, “Thin-film stretchable electronics technology based on meandering interconnections: fabrication and mechanical performance,” *J. Micromechanics Microengineering*, vol. 22, no. 1, p. 015002, Jan. 2012.
- [118] F. Bossuyt, J. Guenther, T. Löher, M. Seckel, T. Sterken, and J. de Vries, “Cyclic endurance reliability of stretchable electronic substrates,” *Microelectron. Reliab.*, vol. 51, no. 3, pp. 628–635, Mar. 2011.
- [119] C. Yan, W. Kang, J. Wang, M. Cui, X. Wang, C. Y. Foo, K. J. Chee, and P. S. Lee, “Stretchable and wearable electrochromic devices,” *ACS Nano*, vol. 8, pp. 316–22, 2014.
- [120] G. D. Moon, G.-H. Lim, J. H. Song, M. Shin, T. Yu, B. Lim, and U. Jeong, “Highly stretchable patterned gold electrodes made of Au nanosheets,” *Adv. Mater.*, vol. 25, no. 19, pp. 2707–12, May 2013.
- [121] U. H. Shin, D. W. Jeong, S. H. Kim, H. W. Lee, and J. M. Kim, “Elastomer-infiltrated vertically aligned carbon nanotube film-based wavy-configured stretchable conductors,” *ACS Appl. Mater. Interfaces*, vol. 6, no. 15, pp. 12909–12914, 2014.

- [122] R. Derda, A. Laromaine, A. Mammoto, S. K. Y. Tang, T. Mammoto, D. E. Ingber, and G. M. Whitesides, "Paper-supported 3D cell culture for tissue-based bioassays," *Proc. Natl. Acad. Sci. U. S. A.*, vol. 106, no. 44, pp. 18457–62, Nov. 2009.
- [123] S. Ahmed, M. N. Bui, and A. Abbas, "Paper-based chemical and biological sensors: Engineering aspects," *Biosens. Bioelectron.*, vol. 77, pp. 249–263, Mar. 2016.
- [124] H. Juvonen, A. Määttänen, P. Laurén, P. Ihalainen, A. Urtti, M. Yliperttula, and J. Peltonen, "Biocompatibility of printed paper-based arrays for 2-D cell cultures," *Acta Biomater.*, vol. 9, no. 5, pp. 6704–6710, May 2013.
- [125] K. A. Simon, K. M. Park, B. Mosadegh, A. B. Subramaniam, A. D. Mazzeo, P. M. Ngo, and G. M. Whitesides, "Polymer-based mesh as supports for multi-layered 3D cell culture and assays," *Biomaterials*, vol. 35, no. 1, pp. 259–268, Jan. 2014.
- [126] B. Mosadegh, M. R. Lockett, K. Thu, K. A. Simon, K. Gilbert, S. Hillier, D. Newsome, H. Li, A. B. Hall, D. M. Boucher, B. K. Eustace, and G. M. Whitesides, "Biomaterials A paper-based invasion assay : Assessing chemotaxis of cancer cells in gradients of oxygen," *Biomaterials*, vol. 52, pp. 262–271, 2015.
- [127] L. Wang, C. Xu, Y. Zhu, Y. Yu, N. Sun, X. Zhang, K. Feng, and J. Qin, "Human induced pluripotent stem cell-derived beating cardiac tissues on paper," *Lab Chip*, vol. 15, no. 22, pp. 4283–4290, 2015.
- [128] L. Jeong, I. S. Yeo, H. N. Kim, Y. Il Yoon, D. H. Jang, S. Y. Jung, B. M. Min, and W. H. Park, "Plasma-treated silk fibroin nanofibers for skin regeneration," *Int. J. Biol. Macromol.*, vol. 44, no. 3, pp. 222–228, 2009.
- [129] S. C. Jin, H. S. Baek, Y. I. Woo, M. H. Lee, J.-S. Kim, J.-C. Park, Y. H. Park, D. K. Rah, K.-H. Chung, S. J. Lee, and I. H. Han, "Beneficial effects of microwave-induced argon plasma treatment on cellular behaviors of articular chondrocytes onto nanofibrous silk fibroin mesh," *Macromol. Res.*, vol. 17, no. 9, pp. 703–708, 2009.
- [130] V. P. Ribeiro, L. R. Almeida, A. R. Martins, I. Pashkuleva, A. P. Marques, A. S. Ribeiro, C. J. Silva, G. Bonifácio, R. a. Sousa, R. L. Reis, and A. L. Oliveira, "Influence of different surface modification treatments on silk biotextiles for tissue engineering applications," *J. Biomed. Mater. Res. Part B Appl. Biomater.*, p. n/a–n/a, 2015.

- [131] J. Yong, F. Chen, Q. Yang, D. Zhang, G. Du, J. Si, F. Yun, and X. Hou, "Femtosecond laser weaving superhydrophobic patterned PDMS surfaces with tunable adhesion," *J. Phys. Chem. C*, vol. 117, no. 47, pp. 24907–24912, 2013.
- [132] D. Tobjörk and R. Österbacka, "Paper electronics.," *Adv. Mater.*, no. 17, pp. 61, 2011.
- [133] J.-H. Kim, S. Mun, H.-U. Ko, G.-Y. Yun, and J. Kim, "Disposable chemical sensors and biosensors made on cellulose paper.," *Nanotechnology*, vol. 25, no. 9, p. 092001, 2014.
- [134] W. Kit-Anan, A. Olarnwanich, C. Sriprachuabwong, C. Karuwan, A. Tuantranont, A. Wisitsoraat, W. Srituravanich, and A. Pimpin, "Disposable paper-based electrochemical sensor utilizing inkjet-printed Polyaniline modified screen-printed carbon electrode for Ascorbic acid detection," *J. Electroanal. Chem.*, vol. 685, pp. 72–78, Oct. 2012.
- [135] W.-J. Lan, E. J. Maxwell, C. Parolo, D. K. Bwambok, A. B. Subramaniam, and G. M. Whitesides, "Paper-based electroanalytical devices with an integrated, stable reference electrode.," *Lab Chip*, vol. 13, no. 20, pp. 4103–8, 2013.
- [136] S. Ahmed, M. P. N. Bui, and A. Abbas, "Paper-based chemical and biological sensors: Engineering aspects," *Biosens. Bioelectron.*, vol. 77, pp. 249–263, 2016.
- [137] N. Lopez-Ruiz, V. F. Curto, M. M. Erenas, F. Benito-Lopez, D. Diamond, A. J. Palma, and L. F. Capitan-Vallvey, "Smartphone-Based Simultaneous pH and Nitrite Colorimetric Determination for Paper Microfluidic Devices," *Anal. Chem.*, vol. 86, no. 19, 9562, 2014.
- [138] M. Novell, M. Parrilla, G. a Crespo, F. X. Rius, and F. J. Andrade, "Paper-based ion-selective potentiometric sensors.," *Anal. Chem.*, vol. 84, no. 11, pp. 4695–702, Jun. 2012.
- [139] S. Mohammadi, M. Maeki, R. M. Mohamadi, A. Ishida, H. Tani, and M. Tokeshi, "An instrument-free, screen-printed paper microfluidic device that enables bio and chemical sensing.," *Analyst*, vol. 140, no. 19, pp. 6493–9, 2015.
- [140] A. K. Yetisen, M. S. Akram, and C. R. Lowe, "Paper-based microfluidic point-of-care diagnostic devices," *Lab Chip*, vol. 13, no. 12, pp. 2210–2251, 2013.
- [141] N. Meredith, C. Quinn, D. Cate, T. Reilly, J. Volckens, and C. Henry, "Paper-Based Analytical Devices for Environmental Analysis," *Analyst*, pp. 1874–1887, 2016.
- [142] A. V. Quintero, F. Molina-Lopez, E. C. P. Smits, E. Danesh, J. van den Brand, K. Persaud, A. Oprea, N. Barsan, U. Weimar, N. F. de Rooij, and D. Briand, "Smart RFID label with a printed multisensor platform for environmental monitoring," *Flex. Print. Electron.*, vol. 1, no. 2, p. 025003, 2016.

- [143] K. Yamada, H. Shibata, K. Suzuki, and D. Citterio, "Toward practical application of paper-based microfluidics for medical diagnostics: state-of-the-art and challenges," *Lab Chip*, vol. 17, no. 7, pp. 1206–1249, 2017.
- [144] A. Mills, "Oxygen indicators and intelligent inks for packaging food.," *Chem. Soc. Rev.*, vol. 34, no. 12, pp. 1003–1011, 2005.
- [145] T. Wang, R. C. Reid, and S. D. Minter, "A Paper-based Mitochondrial Electrochemical Biosensor for Pesticide Detection," *Electroanalysis*, vol. 28, no. 4, pp. 854–859, Apr. 2016.
- [146] P. Yang, Z. Lin, Z. L. Wang, K. C. Pradel, L. Lin, X. Li, X. Wen, J. He, M. Science, U. States, E. Engineering, M. Sciences, S. Arabia, B. Engineering, and C. Academy, "Paper-Based Origami Triboelectric," *ACS Nano*, vol. 9, no. 1, pp. 901–907, 2015.
- [147] A. W. Martinez, S. T. Phillips, M. J. Butte, and G. M. Whitesides, "Patterned paper as a platform for inexpensive, low-volume, portable bioassays," *Angew. Chemie - Int. Ed.*, vol. 46, no. 8, pp. 1318–1320, 2007.
- [148] C. G. Li, H.-A. Joung, H. Noh, M.-B. Song, M.-G. Kim, and H. Jung, "One-Touch-Activated Blood Multidiagnostic System using a Minimally Invasive Hollow Microneedle Integrated with a Paper-Based Sensor," *Lab Chip*, vol. 15, no. 16, pp. 3286–3292, 2015.
- [149] R. Rahimi, M. Ochoa, T. Parupudi, X. Zhao, I. K. Yazdi, M. R. Dokmeci, A. Tamayol, A. Khademhosseini, and B. Ziaie, "A low-cost flexible pH sensor array for wound assessment," *Sensors Actuators, B Chem.*, vol. 229, pp. 609–617, 2016.
- [150] N. Komuro, S. Takaki, K. Suzuki, and D. Citterio, "Inkjet printed (bio)chemical sensing devices.," *Anal. Bioanal. Chem.*, vol. 405, no. 17, pp. 5785–805, Jul. 2013.
- [151] S. H. Jeong, A. Hagman, K. Hjort, M. Jobs, J. Sundqvist, and Z. Wu, "Liquid alloy printing of microfluidic stretchable electronics.," *Lab Chip*, vol. 12, no. 22, pp. 4657–64, Nov. 2012.
- [152] S. Khan, L. Lorenzelli, R. Dahiya, and S. Member, "Technologies for Printing Sensors and Electronics over Large Flexible Substrates : A Review," vol. 15, no. c, pp. 3164–3185, 2014.
- [153] X. Liu, M. Mwangi, X. Li, M. O'Brien, and G. M. Whitesides, "Paper-based piezoresistive MEMS sensors.," *Lab Chip*, vol. 11, no. 13, pp. 2189–96, Jul. 2011.

- [154] J. Perelaer, P. J. Smith, D. Mager, D. Soltman, S. K. Volkman, V. Subramanian, J. G. Korvink, and U. S. Schubert, "Printed electronics: the challenges involved in printing devices, interconnects, and contacts based on inorganic materials," *J. Mater. Chem.*, vol. 20, no. 39, p. 8446, 2010.
- [155] E. Tekin, P. J. Smith, and U. S. Schubert, "Inkjet printing as a deposition and patterning tool for polymers and inorganic particles," *Soft Matter*, vol. 4, no. 4, pp. 703–713, 2008.
- [156] K. Park, D. Lee, A. Rai, D. Mukherjee, and M. R. Zachariah, "Size-resolved kinetic measurements of aluminum nanoparticle oxidation with single particle mass spectrometry," *J. Phys. Chem. B*, vol. 109, no. 15, pp. 7290–7299, 2005.
- [157] a. Rai, K. Park, L. Zhou, and M. R. Zachariah, "Understanding the mechanism of aluminium nanoparticle oxidation," *Combust. Theory Model.*, vol. 10, pp. 843, 2006.
- [158] A. Kamyshny and S. Magdassi, "Conductive nanomaterials for printed electronics," *Small*, vol. 10, no. 17, pp. 3515–3535, 2014.
- [159] M. Zhang, C. Wang, H. Wang, M. Jian, X. Hao, and Y. Zhang, "Carbonized Cotton Fabric for High-Performance Wearable Strain Sensors," *Adv. Funct. Mater.*, 2016.
- [160] B. Ziaie, "Hard and soft micromachining for BioMEMS: review of techniques and examples of applications in microfluidics and drug delivery," *Adv. Drug Deliv. Rev.*, vol. 56, no. 2, pp. 145–172, Feb. 2004.
- [161] S. E. Burns, K. Reynolds, W. Reeves, M. Banach, T. Brown, K. Chalmers, N. Cousins, M. Etchells, C. Hayton, K. Jacobs, a Menon, S. Siddique, P. Too, C. Ramsdale, J. Watts, P. Cain, T. von Werne, J. Mills, C. Curling, H. Sirringhaus, K. Amundson, and M. D. McCreary, "A scalable manufacturing process for flexible active-matrix e-paper displays," *J. Soc. Inf. Disp.*, vol. 13, no. 7, pp. 583–586, 2005.
- [162] R. Rahimi, M. Ochoa, A. Tamayol, S. Khalili, A. Khademhosseini, and B. Ziaie, "Highly Stretchable Potentiometric pH Sensor Fabricated via Laser Carbonization and Machining of Carbon–Polyaniline Composite," *ACS Appl. Mater. Interfaces*, vol. 9, no. 10, pp. 9015–9023, Mar. 2017.
- [163] M. F. El-kady, R. B. Kaner, L. Angeles, U. States, and M. Science, "Direct Laser Writing of Graphene," no. 9, pp. 8725–8729, 2014.
- [164] T. Lu, L. Finkenauer, J. Wissman, and C. Majidi, "Rapid Prototyping for Soft-Matter Electronics," *Adv. Funct. Mater.*, vol. 24, no. 22, pp. 3351–3356, Jun. 2014.

- [165] M. Ochoa, R. Rahimi, and B. Ziaie, "Laser-Enabled Fabrication Technologies for Low-Cost Flexible/Conformal Cutaneous Wound Interfaces," Springer International Publishing, 2016, pp. 207–226.
- [166] J. D. Majumdar and I. Manna, "Laser processing of materials," vol. 28, no. August, pp. 495–562, 2003.
- [167] C. Mattmann, F. Clemens, and G. Tröster, "Sensor for Measuring Strain in Textile," *Sensors*, vol. 8, no. 6, pp. 3719–3732, Jun. 2008.
- [168] L. M. Castano and A. B. Flatau, "Smart fabric sensors and e-textile technologies: a review," *Smart Mater. Struct.*, vol. 23, no. 5, p. 053001, May 2014.
- [169] R.-H. Kim, D.-H. Kim, J. Xiao, B. H. Kim, S.-I. Park, B. Panilaitis, R. Ghaffari, J. Yao, M. Li, Z. Liu, V. Malyarchuk, D. G. Kim, A.-P. Le, R. G. Nuzzo, D. L. Kaplan, F. G. Omenetto, Y. Huang, Z. Kang, and J. a Rogers, "Waterproof AllnGaP optoelectronics on stretchable substrates with applications in biomedicine and robotics.," *Nat. Mater.*, vol. 9, no. 11, pp. 929–37, Nov. 2010.
- [170] C. King, M. O. Culjat, M. L. Franco, C. E. Lewis, E. P. Dutton, W. S. Grundfest, and J. W. Bisley, "Tactile Feedback Induces Reduced Grasping Force in Robot-Assisted Surgery," *IEEE Trans. Haptics*, vol. 2, no. 2, pp. 103–110, Apr. 2009.
- [171] I. Kang, M. J. Schulz, J. H. Kim, V. Shanov, and D. Shi, "A carbon nanotube strain sensor for structural health monitoring," *Smart Mater. Struct.*, vol. 15, no. 3, pp. 737–748, 2006.
- [172] E. P. Scilingo, F. Lorussi, A. Mazzoldi, and D. De Rossi, "Strain-sensing fabrics for wearable kinaesthetic-like systems," *IEEE Sens. J.*, vol. 3, no. 4, pp. 460–467, Aug. 2003.
- [173] L. Cai, L. Song, P. Luan, Q. Zhang, N. Zhang, Q. Gao, D. Zhao, X. Zhang, M. Tu, F. Yang, W. Zhou, Q. Fan, J. Luo, W. Zhou, P. M. Ajayan, and S. Xie, "Super-stretchable, transparent carbon nanotube-based capacitive strain sensors for human motion detection.," *Sci. Rep.*, vol. 3, p. 3048, Jan. 2013.
- [174] S. M. Won, H.-S. Kim, N. Lu, D. Kim, C. Del Solar, T. Duenas, A. Ameen, and J. A. Rogers, "Piezoresistive Strain Sensors and Multiplexed Arrays Using Assemblies of Single-Crystalline Silicon Nanoribbons on Plastic Substrates," *IEEE Trans. Electron Devices*, vol. 58, no. 11, pp. 4074–4078, Nov. 2011.
- [175] Y. Kim, Y. Kim, C. Lee, and S. Kwon, "Thin Polysilicon Gauge for Strain Measurement of Structural Elements," *IEEE Sens. J.*, vol. 10, no. 8, pp. 1320–1327, Aug. 2010.

- [176] J. Park, S. Wang, M. Li, C. Ahn, J. K. Hyun, D. S. Kim, D. K. Kim, J. a Rogers, Y. Huang, and S. Jeon, “Three-dimensional nanonetworks for giant stretchability in dielectrics and conductors.,” *Nat. Commun.*, vol. 3, no. May, p. 916, Jan. 2012.
- [177] S. Cravanzola, G. Haznedar, D. Scarano, A. Zecchina, and F. Cesano, “Carbon-based piezoresistive polymer composites: Structure and electrical properties,” *Carbon N. Y.*, vol. 62, pp. 270–277, Oct. 2013.
- [178] R. Whitney, “The measurement of volume changes in human limbs,” *J Physiol*, vol. 121, pp. 1–27, 1953.
- [179] J.-H. So, J. Thelen, A. Qusba, G. J. Hayes, G. Lazzi, and M. D. Dickey, “Reversibly Deformable and Mechanically Tunable Fluidic Antennas,” *Adv. Funct. Mater.*, vol. 19, no. 22, pp. 3632–3637, Nov. 2009.
- [180] M. D. Dickey, R. C. Chiechi, R. J. Larsen, E. a. Weiss, D. a. Weitz, and G. M. Whitesides, “Eutectic Gallium-Indium (EGaIn): A Liquid Metal Alloy for the Formation of Stable Structures in Microchannels at Room Temperature,” *Adv. Funct. Mater.*, vol. 18, no. 7, pp. 1097–1104, Apr. 2008.
- [181] J. T. Muth, D. M. Vogt, R. L. Truby, Y. Mengüç, D. B. Kolesky, R. J. Wood, and J. a Lewis, “Embedded 3D Printing of Strain Sensors within Highly Stretchable Elastomers.,” *Adv. Mater.*, pp. 6307–6312, Jun. 2014.
- [182] A. P. A. Raju, A. Lewis, B. Derby, R. J. Young, I. a. Kinloch, R. Zan, and K. S. Novoselov, “Wide-Area Strain Sensors based upon Graphene-Polymer Composite Coatings Probed by Raman Spectroscopy,” *Adv. Funct. Mater.*, vol. 24, no. 19, pp. 2865–2874, May 2014.
- [183] K. S. Kim, Y. Zhao, H. Jang, S. Y. Lee, J. M. Kim, K. S. Kim, J.-H. Ahn, P. Kim, J.-Y. Choi, and B. H. Hong, “Large-scale pattern growth of graphene films for stretchable transparent electrodes.,” *Nature*, vol. 457, no. 7230, pp. 706–10, Feb. 2009.
- [184] M. Amjadi, A. Pichitpajongkit, S. Lee, S. Ryu, and I. Park, “Highly stretchable and sensitive strain sensor based on silver nanowire-elastomer nanocomposite.,” *ACS Nano*, vol. 8, no. 5, pp. 5154–63, May 2014.
- [185] X. Li, R. Zhang, W. Yu, K. Wang, J. Wei, D. Wu, A. Cao, Z. Li, Y. Cheng, Q. Zheng, R. S. Ruoff, and H. Zhu, “Stretchable and highly sensitive graphene-on-polymer strain sensors.,” *Sci. Rep.*, vol. 2, p. 870, Jan. 2012.

- [186] M. Park, J. Im, J. Park, and U. Jeong, "Micropatterned stretchable circuit and strain sensor fabricated by lithography on an electrospun nanofiber mat.," *ACS Appl. Mater. Interfaces*, vol. 5, no. 17, pp. 8766–71, Sep. 2013.
- [187] Y. Lee, S. Bae, H. Jang, S. Jang, S.-E. Zhu, S. H. Sim, Y. Il Song, B. H. Hong, and J.-H. Ahn, "Wafer-scale synthesis and transfer of graphene films.," *Nano Lett.*, vol. 10, no. 2, pp. 490–3, Feb. 2010.
- [188] C. Lee, L. Jug, and E. Meng, "High strain biocompatible polydimethylsiloxane-based conductive graphene and multiwalled carbon nanotube nanocomposite strain sensors," *Appl. Phys. Lett.*, vol. 102, no. 18, p. 183511, 2013.
- [189] M. Hempel, D. Nezich, J. Kong, and M. Hofmann, "A novel class of strain gauges based on layered percolative films of 2D materials.," *Nano Lett.*, vol. 12, no. 11, pp. 5714–8, Nov. 2012.
- [190] V. Correia, C. Caparros, C. Casellas, L. Francesch, J. G. Rocha, and S. Lanceros-Mendez, "Development of inkjet printed strain sensors," *Smart Mater. Struct.*, vol. 22, no. 10, p. 105028, Oct. 2013.
- [191] S. Yao and Y. Zhu, "Wearable multifunctional sensors using printed stretchable conductors made of silver nanowires.," *Nanoscale*, vol. 6, no. 4, pp. 2345–52, Feb. 2014.
- [192] C. Yan, J. Wang, W. Kang, M. Cui, X. Wang, C. Y. Foo, K. J. Chee, and P. S. Lee, "Highly stretchable piezoresistive graphene-nanocellulose nanopaper for strain sensors.," *Adv. Mater.*, vol. 26, no. 13, pp. 2022–7, Apr. 2014.
- [193] O. Akar, T. Akin, and K. Najafi, "A wireless batch sealed absolute capacitive pressure sensor," *Sensors Actuators A Phys.*, vol. 95, no. 1, pp. 29–38, Dec. 2001.
- [194] M. Luo, A. W. Martinez, C. Song, F. Herrault, and M. G. Allen, "A Microfabricated Wireless RF Pressure Sensor Made Completely of Biodegradable Materials," *J. Microelectromechanical Syst.*, vol. 23, no. 1, pp. 4–13, Feb. 2014.
- [195] F. H. Epstein, A. J. Singer, and R. A. F. Clark, "Cutaneous Wound Healing," *N. Engl. J. Med.*, vol. 341, no. 10, pp. 738–746, Sep. 1999.
- [196] M. a Fonder, G. S. Lazarus, D. a Cowan, B. Aronson-Cook, A. R. Kohli, and A. J. Mamelak, "Treating the chronic wound: A practical approach to the care of nonhealing wounds and wound care dressings.," *J. Am. Acad. Dermatol.*, vol. 58, no. 2, pp. 185–206, Feb. 2008.

- [197] R. W. Tarnuzzer and G. S. Schultz, "Biochemical analysis of acute and chronic wound environments," *Wound Repair Regen.*, vol. 4, no. 3, pp. 321–325, Jul. 1996.
- [198] C. K. Sen, G. M. Gordillo, S. Roy, R. Kirsner, L. Lambert, T. K. Hunt, F. Gottrup, G. C. Gurtner, and M. T. Longaker, "Human skin wounds: a major and snowballing threat to public health and the economy.," *Wound Repair Regen.*, vol. 17, no. 6, pp. 763–71, 2010.
- [199] X. Liu, W. Kim, R. Schmidt, B. Drerup, and J. Song, "Wound measurement by curvature maps: a feasibility study.," *Physiol. Meas.*, vol. 27, no. 11, pp. 1107–23, Nov. 2006.
- [200] J. E. Grey, "Wound assessment," *Bmj*, vol. 332, no. 7536, pp. 285–288, 2006.
- [201] E. A. A. Sharon Baranoski, *Wound care essentials: Practice principles*. Lippincott Williams & Wilkins, 2008.
- [202] G. Dow, A. Browne, and R. G. Sibbald, "Infection in chronic wounds: controversies in diagnosis and treatment.," *Ostomy. Wound. Manage.*, vol. 45, no. 8, pp. 23–7, 1999.
- [203] S. M. O'Meara, N. a Cullum, M. Majid, and T. a Sheldon, "Systematic review of antimicrobial agents used for chronic wounds," *British Journal of Surgery*, vol. 88, no. 1. pp. 4–21, Jan-2001.
- [204] S. Schreml, R. M. Szeimies, S. Karrer, J. Heinlin, M. Landthaler, and P. Babilas, "The impact of the pH value on skin integrity and cutaneous wound healing," *J. Eur. Acad. Dermatology Venereol.*, vol. 24, no. 4, pp. 373–378, 2010.
- [205] S. L. Percival, S. McCarty, J. A. Hunt, and E. J. Woods, "The effects of pH on wound healing, biofilms, and antimicrobial efficacy," *Wound Repair Regen.*, no. 2, 174, 2014.
- [206] L. A. Schneider, A. Korber, S. Grabbe, and J. Dissemond, "Influence of pH on wound-healing: a new perspective for wound-therapy?," *Arch. Dermatol. Res.*, vol. 298, no. 9, pp. 413–420, Jan. 2007.
- [207] E. M. Jones, C. A. Cochrane, and S. L. Percival, "The Effect of pH on the Extracellular Matrix and Biofilms.," *Adv. wound care*, vol. 4, no. 7, pp. 431–439, 2015.
- [208] G. Gethin, "The significance of surface pH in chronic wounds," *Wounds UK*, vol. 3, no. 3, pp. 52–56, 2007.
- [209] D. A. Jankowska, M. B. Bannwarth, C. Schulenburg, G. Faccio, K. Maniura-Weber, R. M. Rossi, L. Scherer, M. Richter, and L. F. Boesel, "Simultaneous detection of pH value and glucose concentrations for wound monitoring applications," *Biosens. Bioelectron.*, vol. 87, pp. 312–319, Jan. 2017.

- [210] S. Pasche, B. Schyrr, B. Wenger, E. Scolan, R. Ischer, and G. Voirin, “Smart Textiles with Biosensing Capabilities,” *Adv. Sci. Technol.*, vol. 80, pp. 129–135, 2012.
- [211] D. Jeon, W. J. Yoo, J. K. Seo, S. H. Shin, K. T. Han, S. G. Kim, J. Y. Park, and B. Lee, “Fiber-optic pH sensor based on sol-gel film immobilized with neutral red,” *Opt. Rev.*, vol. 20, no. 2, pp. 209–213, Mar. 2013.
- [212] A. Nocke, A. Schröter, C. Cherif, and G. Gerlach, “Miniaturized textile-based multi-layer ph-sensor for wound monitoring applications,” *Autex Res. J.*, vol. 12, no. 1, pp. 20–22, Jan. 2012.
- [213] V. Sridhar and K. Takahata, “A hydrogel-based passive wireless sensor using a flex-circuit inductive transducer,” *Sensors Actuators A Phys.*, vol. 155, no. 1, pp. 58–65, 2009.
- [214] G. Urban, G. Jobst, F. Keplinger, E. Aschauer, O. Tilado, R. Fasching, and F. Kohl, “Miniaturized multi-enzyme biosensors integrated with pH sensors on flexible polymer carriers for in vivo applications,” *Biosens. Bioelectron.*, vol. 7, no. 10, pp. 733–739, 1992.
- [215] R. Sheybani and A. Shukla, “Highly Sensitive Label-Free Dual Sensor Array for Rapid Detection of Wound Bacteria,” *Biosens. Bioelectron.*, no. October, pp. 1–9, 2016.
- [216] E. Song, R. P. Tortorich, T. H. Da Costa, and J. W. Choi, “Inkjet printing of conductive polymer nanowire network on flexible substrates and its application in chemical sensing,” *Microelectron. Eng.*, vol. 145, pp. 143–148, 2015.
- [217] T. Guinovart, G. Valdés-Ramírez, J. R. Windmiller, F. J. Andrade, and J. Wang, “Bandage-Based Wearable Potentiometric Sensor for Monitoring Wound pH,” *Electroanalysis*, no. Suite 400, p. n/a–n/a, Mar. 2014.
- [218] N. Mehmood, A. Hariz, R. Fitridge, and N. H. Voelcker, “Applications of modern sensors and wireless technology in effective wound management,” *J. Biomed. Mater. Res. - Part B Appl. Biomater.*, vol. 102, no. 4, pp. 885–895, 2014.
- [219] W.-D. Huang, H. Cao, S. Deb, M. Chiao, and J. C. Chiao, “A flexible pH sensor based on the iridium oxide sensing film,” *Sensors Actuators A Phys.*, vol. 169, pp. 1–11, 2011.
- [220] H.-J. Chung, M. S. Sulkin, J.-S. Kim, C. Goudeseune, H.-Y. Chao, J. W. Song, S. Y. Yang, Y.-Y. Hsu, R. Ghaffari, I. R. Efimov, and J. a Rogers, “Stretchable, multiplexed pH sensors with demonstrations on rabbit and human hearts undergoing ischemia,” *Adv. Healthc. Mater.*, vol. 3, no. 1, pp. 59–68, Jan. 2014.

- [221] C. A. Pope, “Cardiovascular Mortality and Long-Term Exposure to Particulate Air Pollution: Epidemiological Evidence of General Pathophysiological Pathways of Disease,” *Circulation*, vol. 109, no. 1, pp. 71–77, Dec. 2003.
- [222] W. W. Thompson, “Mortality Associated With Influenza and Respiratory Syncytial Virus in the United States,” *JAMA*, vol. 289, no. 2, p. 179, Jan. 2003.
- [223] P. a Martorana, B. Lunghi, M. Lucattelli, G. De Cunto, R. Beume, and G. Lungarella, “Effect of roflumilast on inflammatory cells in the lungs of cigarette smoke-exposed mice.,” *BMC Pulm. Med.*, vol. 8, p. 17, 2008.
- [224] H. Harrington, P. Cato, F. Salazar, M. Wilkinson, A. Knox, J. W. Haycock, F. Rose, J. W. Aylott, and A. M. Ghaemmaghami, “Immunocompetent 3D Model of Human Upper Airway for Disease Modeling and In Vitro Drug Evaluation.,” *Mol. Pharm.*, vol. 11, no. 7, pp. 2082–91, Jul. 2014.
- [225] D. Huh, H. J. Kim, J. P. Fraser, D. E. Shea, M. Khan, A. Bahinski, G. a Hamilton, and D. E. Ingber, “Microfabrication of human organs-on-chips.,” *Nat. Protoc.*, vol. 8, no. 11, pp. 2135–57, Nov. 2013.
- [226] C. Y. Chan, P.-H. Huang, F. Guo, X. Ding, V. Kapur, J. D. Mai, P. K. Yuen, and T. J. Huang, “Accelerating drug discovery via organs-on-chips.,” *Lab Chip*, vol. 13, no. 24, pp. 4697–710, 2013.
- [227] D. Huh, G. a Hamilton, and D. E. Ingber, “From 3D cell culture to organs-on-chips.,” *Trends Cell Biol.*, vol. 21, no. 12, pp. 745–54, Dec. 2011.
- [228] P. Gangatirkar, S. Paquet-Fifield, A. Li, R. Rossi, and P. Kaur, “Establishment of 3D organotypic cultures using human neonatal epidermal cells.,” *Nat. Protoc.*, vol. 2, no. 1, pp. 178–86, Jan. 2007.
- [229] M. B. Esch, T. L. King, and M. L. Shuler, “The role of body-on-a-chip devices in drug and toxicity studies.,” *Annu. Rev. Biomed. Eng.*, vol. 13, pp. 55–72, Aug. 2011.
- [230] Y. Zhu, A. Chidekel, and T. H. Shaffer, “Cultured Human Airway Epithelial Cells (Calu-3): A Model of Human Respiratory Function, Structure, and Inflammatory Responses,” *Crit. Care Res. Pract.*, vol. 2010, pp. 1–8, 2010.
- [231] D. Huh, B. D. Matthews, A. Mammoto, M. Montoya-Zavala, H. Y. Hsin, and D. E. Ingber, “Reconstituting Organ-Level Lung Functions on a Chip,” *Science (80-. )*, vol. 328, no. 5986, pp. 1662–1668, 2010.

- [232] S. Kumar Mahto, J. Tenenbaum-Katan, and J. Sznitman, “Respiratory Physiology on a Chip,” *Scientifica (Cairo)*., vol. 2012, pp. 1–12, 2012.
- [233] J. a Potkay, “The promise of microfluidic artificial lungs,” *Lab Chip*, vol. 14, no. 21, pp. 4122–4138, 2014.
- [234] H.-J. Park, S. J. Yu, K. Yang, Y. Jin, A.-N. Cho, J. Kim, B. Lee, H. S. Yang, S. G. Im, and S.-W. Cho, “Paper-based bioactive scaffolds for stem cell-mediated bone tissue engineering,” *Biomaterials*, vol. 35, no. 37, pp. 9811–23, Dec. 2014.
- [235] Y. Chen, Z. Kuo, and C. Cheng, “Paper – a potential platform in pharmaceutical development,” *Trends Biotechnol.*, vol. 33, no. 1, pp. 4–9, Jan. 2015.
- [236] C. E. Stewart, E. E. Torr, N. H. Mohd Jamili, C. Bosquillon, and I. Sayers, “Evaluation of Differentiated Human Bronchial Epithelial Cell Culture Systems for Asthma Research,” *J. Allergy*, vol. 2012, no. di, pp. 1–11, 2012.
- [237] M. E. Kreft, U. D. Jerman, E. Lasič, N. Hevir-Kene, T. L. Rižner, L. Peternel, and K. Kristan, “The characterization of the human cell line Calu-3 under different culture conditions and its use as an optimized in vitro model to investigate bronchial epithelial function,” *Eur. J. Pharm. Sci.*, vol. 69, pp. 1–9, Mar. 2015.
- [238] G. E. Morris, J. C. Bridge, L. a Brace, a J. Knox, J. W. Aylott, C. E. Brightling, a M. Ghaemmaghami, and F. R. a J. Rose, “A novel electrospun biphasic scaffold provides optimal three-dimensional topography for in vitro co-culture of airway epithelial and fibroblast cells,” *Biofabrication*, vol. 6, no. 3, p. 035014, 2014.
- [239] K. Khoufache, O. Cabaret, C. Farrugia, D. Rivollet, A. Alliot, E. Allaire, C. Cordonnier, S. Bretagne, and F. Botterel, “Primary in vitro culture of porcine tracheal epithelial cells in an air-liquid interface as a model to study airway epithelium and *Aspergillus fumigatus* interactions,” *Med. Mycol.*, vol. 48, no. 8, pp. 1049–1055, 2010.
- [240] S. Dekali, C. Gamez, T. Kortulewski, K. Blazy, P. Rat, and G. Lacroix, “Assessment of an in vitro model of pulmonary barrier to study the translocation of nanoparticles,” *Toxicol. Reports*, vol. 1, pp. 157–171, 2014.
- [241] J. L. Harcourt, M. McDonald, P. Svoboda, J. Pohl, K. Tatti, and L. M. Haynes, “Human cathelicidin, LL-37, inhibits respiratory syncytial virus infection in polarized airway epithelial cells,” *BMC Res. Notes*, vol. 9, no. 1, p. 11, 2016.

- [242] I. George, S. Vranic, S. Boland, A. Courtois, and A. Baeza-Squiban, “Development of an in vitro model of human bronchial epithelial barrier to study nanoparticle translocation,” *Toxicol. Vitro.*, vol. 29, no. 1, pp. 51–58, 2015.

## VITA

Rahim Rahimi received the B.S. degree in electrical engineering from the Iran University of Science and Technology, Tehran in 2009. In 2012, he began his graduate studies at Purdue University in West Lafayette, IN in the department of electrical and computer engineering. Since then, he has been a research assistant with the Ziaie Biomedical Microdevices Laboratory at Purdue University while pursuing a PhD degree. His research focuses on the development of low-cost flexible and stretchable microsystems for biomedical applications, including monitoring and treatment of chronic dermal wounds.